

## SHOCK LAYERS AND BOUNDARY LAYERS IN HYPERSONIC FLOWS

J. COUSTEIX, D. ARNAL, B. AUPOIX, J. PH. BRAZIER and A. LAFON

*Centre d'Etudes et de Recherches de Toulouse (CERT), Office National d'Etudes et de Recherches Aérospatiales (ONERA), 2 Avenue Edouard Belin, 31055 Toulouse Cedex, France*

(Received 26 July 1993)

**Abstract**—This paper presents an overview of the physical and numerical aspects of flows encountered around a vehicle in hypersonic flight. These problems are typically related to the reentry phase of a space shuttle into the atmosphere. Nonetheless, it is believed that the material given here is a good background for other applications. Compared with the standard aerodynamic problems on an aircraft in transonic or supersonic flight, hypersonic flows are characterized by a much higher level of energy. The high temperature of the flow can lead to thermochemical non-equilibrium, with chemical reactions and vibrational relaxation. These effects are of prime importance in the evaluation of the heating of the body and they may affect general flow features, including the wall pressure. Basic elements are discussed to understand the physics of these phenomena. Applications are given in the framework of boundary layer calculations and of numerical solutions of the Navier-Stokes equations. In the front of the vehicle, a strong bow shock wave forms and the boundary layer is fed by a rotational flow. A discussion is given concerning how a boundary layer theory can account for these effects. At lower altitudes, the velocity of the flow remains large, the Reynolds number increases and the flow becomes turbulent. In this context, laminar-turbulent transition and turbulence modelling are discussed.

### CONTENTS

1. INTRODUCTION	97
2. GENERAL CONSIDERATIONS	98
2.1. Characteristics of hypersonic flows	98
2.1.1. Typical trajectory of a shuttle	98
2.1.2. High energy flows	99
2.1.3. Relaxing flows	100
2.1.4. Effects on wall pressure	101
2.1.5. Viscous interaction	103
2.1.6. Shock wave effects	104
2.2. Continuum and molecular approaches	105
2.2.1. Various flow regimes	105
2.2.2. Molecular approach	106
2.2.3. Continuum approach	106
2.3. Characteristics of the flow of a gas mixture	107
2.3.1. Enthalpy, internal energy and temperature	109
2.3.2. Equation of state	110
2.3.3. Specific heats	111
2.3.4. Flow velocity and diffusion velocity	112
2.4. Vibrational nonequilibrium	112
2.5. Chemical reactions	113
2.5.1. Species production rates	113
2.5.2. Chemical model for air at high temperature	114
2.5.3. Chemical time scale	115
2.5.4. Chemical equilibrium	116
2.6. Flow equations of a gas mixture	118
2.6.1. Equation of state	118
2.6.2. Species equations and continuity equation	119
2.6.3. Momentum equation	122
2.6.4. Vibrational rate equation	123
2.6.5. Energy equation	124
3. LAMINAR BOUNDARY LAYERS	126
3.1. Boundary layer equations	126
3.2. Boundary conditions	127
3.2.1. Boundary conditions at the wall	127
3.2.2. Boundary conditions at the boundary layer outer edge	128
3.3. The atom/molecule approximation	129
3.3.1. Basic relations	129
3.3.2. Chemistry	129
3.3.3. Transport	129

3.4. Two-dimensional stagnation point solutions for atom/molecule approach	130
3.4.1. Fay–Riddell solutions	130
3.4.2. Goulard's extension to finite catalysis	131
3.5. Sensitivity study of two-dimensional boundary layers computations to the high temperature gas model for dissociating air	132
3.5.1. Influence of wall catalytic efficiency	133
3.5.2. Influence of the chemical reaction rates	133
3.5.3. Influence of the wall temperature	135
3.5.4. Model reduction	136
3.5.5. Influence of ionization in re-entry flows	137
3.6. Three-dimensional boundary layer flows	137
3.6.1. Stagnation point solutions	137
3.6.2. Attachment line solutions	138
3.6.3. Sensitivity study to the high temperature gas model	139
<b>4. ENTROPY GRADIENT EFFECTS</b>	<b>139</b>
4.1. Entropy levels in the shock layer	139
4.2. Van Dyke's theory	141
4.3. Defect approach	146
4.4. Applications	149
4.5. Conclusion	152
<b>5. SHOCK LAYER COMPUTATION</b>	<b>154</b>
5.1. Approximation levels for the shock layer computation	154
5.1.1. VSL and PNS equations	155
5.1.2. NS and TLNS equations	156
5.2. A numerical algorithm for NS and TLNS equations	157
5.2.1. Conservation-law form	157
5.2.2. Basic features of the numerical method	158
5.2.3. Inviscid flux discretization	161
5.2.4. Linearization and relaxation algorithm	165
5.3. Results for TLNS computations	166
5.3.1. Flat plate	166
5.3.2. Double ellipse	168
5.3.3. Hyperboloid	169
<b>6. TURBULENCE MODELS</b>	<b>174</b>
6.1. Foreword	174
6.2. Mean and turbulent motions	174
6.2.1. The decomposition problem	174
6.2.2. Mean flow equations	174
6.2.3. Boundary layer equations	175
6.3. The three models of turbulence	176
6.4. Experimental knowledge of compressible turbulent flows	176
6.4.1. Homogeneous flows	176
6.4.2. Free sheared flows	177
6.4.3. Boundary layer flows: the wall region	177
6.4.4. Boundary layer flows: the outer region	178
6.4.5. Evolution of the turbulent Prandtl number	180
6.5. Turbulence models for compressible turbulent flows	181
6.5.1. Model classification	181
6.5.2. Transport equations for compressible turbulence	183
6.5.3. Strong Reynolds analogy	184
6.5.4. Alternatives to the strong Reynolds analogy	184
6.5.5. Modelling the pressure/dilatation term	185
6.5.6. Modelling the dissipation	186
6.5.7. Closure of the Reynolds-stress transport equations	187
6.6. Examples of model predictions	188
6.6.1. Evolution of the skin friction coefficient versus Mach number	188
6.6.2. Evolution of the skin friction coefficient versus wall temperature/adiabatic temperature ratio	189
6.6.3. Prediction of the mixing layer spreading rate evolution	189
<b>7. TRANSITION</b>	<b>190</b>
7.1. Linear stability theory	191
7.1.1. Assumptions. Eigenvalue problem	191
7.1.2. Temporal and spatial theories	192
7.1.3. Relation between spatial and temporal theories	193
7.1.4. PSE approach	194
7.1.5. Inviscid theory	194
7.2. Results for zero pressure gradient flows on adiabatic walls	195
7.2.1. Two-dimensional waves, $\psi = 0$	195
7.2.2. Oblique waves ( $\psi \neq 0$ )	197
7.3. Receptivity, secondary instability, nonlinear effects	198
7.3.1. Receptivity	198
7.3.2. Nonlinear evolution and breakdown	198

7.4. Factors acting on the stability properties	199
7.4.1. Streamwise pressure gradient	199
7.4.2. Wall temperature	199
7.4.3. Real gas effects	200
7.5. Transition prediction	200
7.5.1. The $\epsilon^*$ -method	200
7.5.2. First application: flat plate with adiabatic wall	201
7.5.3. Wind tunnel simulation. Empirical criteria	202
7.5.4. Further applications of the $\epsilon^*$ -method	204
7.6. Concluding remarks	205
8. CONCLUSION	205
REFERENCES	207

## 1. INTRODUCTION

Compared with the flow around a transport aircraft in transonic or supersonic regime, the flow around a space plane along the reentry trajectory into the atmosphere differs in several ways. The body of the vehicle and its trajectory are designed in such a way that the vehicle decelerates in the atmosphere from a high velocity (several kilometers per second) to a very low velocity for landing on a runway. This deceleration is produced by purely aerodynamic phenomena with the help of a rounded vehicle shape, large angles of attack (typically 30°) and a particular trajectory. In front of the vehicle, a strong bow shock wave compresses the flow; this compression enables the vehicle to decelerate.

A hypersonic flow is primarily characterized by a very high level of energy. Across the shock wave, the kinetic energy is transformed into enthalpy. The temperature of the flow between the shock wave and the body—the shock layer—is very large. In these conditions, the properties of air are deeply modified. Indeed, phenomena like vibrational excitation and dissociation of the molecules of oxygen and nitrogen occur. The energy is stored under a thermochemical form and the temperature of the flow is strongly reduced compared to the value which would be obtained if the gas were perfect. Obviously, the effect on the heating of the body is very large. There is also a nonnegligible effect on the pressure distribution along the body.

Another feature of the flow around a space plane during the reentry is that the density of air changes by several orders of magnitude. At the very beginning, the density of air is very low and increases gradually. At low densities, the gas cannot be considered as a continuum and the study of the flow pertains to the field of rarefied gas dynamics; the mean free path between two molecular collisions is of the same order of magnitude as the length scale of the body, or even larger. At lower altitudes, the density increases, the mean free path decreases; the gas behaves as a continuum. As the density of air increases, the velocity of the vehicle is reduced, but the net result is an increase of the Reynolds number. At the beginning of the reentry, the Reynolds number is low and the flow is laminar. At a certain altitude, the Reynolds number is large enough for the laminar-turbulent transition of the boundary layer to take place. Clearly, this adds another degree of complexity. The modelling of transition must be performed with care because if transition occurs too early along the trajectory, a dramatic overheating of the body can result.

A complete presentation of all the material needed to study the various phenomena encountered in the flow during an atmospheric reentry requires several books and exceeds the scope of this paper. As required by Professor A. D. Young who invited us to write a review on boundary layers in hypersonic flow, this paper intends ‘to provide an informative survey in some depth, embracing current and future developments, primarily aimed at the young engineer who is not yet a specialist in the field’. In fact, the subject has not been restricted to boundary layers; the word “shock layers” is in the title because it has been considered interesting to present the modern numerical treatment of Navier-Stokes equations which enable us to calculate the shock layer. In addition, it is assumed that the reader is familiar with aerodynamics at more standard conditions.

Following this introduction, Section 2 describes the main characteristics of hypersonic flows which are studied. Section 2 also presents the models used to describe these flows:

equations and transport properties. Section 3 is an application of these concepts to the study of laminar hypersonic boundary layers; in this section, the emphasis is placed on the influence of the chemical reactions on the behavior of the boundary layer flow. Section 4 treats the problem of entropy swallowing effects. Briefly, these effects are due to the fact that the bow shock wave induces a rotational flow in the shock layer even in the regions where the flow can be considered as inviscid. The result is that the boundary layer is fed with streamlines of varying entropy and the characteristics of the inviscid flow are not at all constant in the direction normal to the wall. These effects are especially sensitive at low Reynolds number, when the boundary layer is thick. In these conditions, the standard boundary layer theory does not apply and it is shown that a new theory—called the defect boundary layer theory—can take these effects into account. Section 5 describes a numerical procedure to calculate the flow in the shock layer. Nowadays, CFD (Computational Fluid Dynamics) plays a key role in aerodynamics. This is particularly true in the field of hypersonic flows where it is impossible to simulate in wind tunnels all the flight parameters to obtain a true similarity. Finally, Sections 6 and 7 describe the models employed to reproduce the turbulence effects and the transition process. In these fields, very little is known about the effects of high temperature and the presentation is almost entirely limited to air considered as a perfect gas. This does not mean that the problem is simple because the compressibility of the flow has large effects on turbulence and on transition.

In this paper, the problem of shock wave-boundary layer and shock-shock interactions is not discussed. Indeed, it is a very important topic and the reader is referred to excellent reviews which can be found in various papers.<sup>(51,52,92)</sup> The experimental simulation of hypersonic flows is also an important topic which is not discussed in this paper (see for example Refs 29, 93 and 174).

## 2. GENERAL CONSIDERATIONS

### 2.1. CHARACTERISTICS OF HYPERSONIC FLOWS

#### 2.1.1. Typical Trajectory of a Shuttle

In order to illustrate the point, Table 1 and Fig. 1 give the STS-2 flight reentry trajectory<sup>(171)</sup> along which the typical flows discussed in this paper are encountered. The reference time ( $t = 0$ ) corresponds to an altitude of 400,000 ft. In these data,  $Z$  and  $V$  are the altitude and the velocity of the shuttle,  $\rho_\infty$  and  $T_\infty$  are the freestream density and temperature (upstream of the front shock wave), the Mach number is calculated with the shuttle velocity and the freestream temperature, the Reynolds number  $R_L$  and the Knudsen number  $Kn$  are also calculated with the freestream conditions and a reference length  $L = 1$  m which is the order of magnitude of the nose radius.

TABLE I. STS-2 FLIGHT—REENTRY TRAJECTORY (FROM REF. 171)

$t$ (s)	$Z$ (km)	$V$ ( $\text{km s}^{-1}$ )	$\rho_\infty$ ( $\text{kg m}^{-3}$ )	$T_\infty$ (K)	$M_\infty$	Angle of attack (°)	$R_L$ $L = 1$ m	$Kn$ $L = 1$ m
200	92.35	7.50	$2.184 \cdot 10^{-6}$	324	20.8	40.4	$8.39 \cdot 10^2$	$3.69 \cdot 10^{-2}$
250	85.74	7.53	$6.365 \cdot 10^{-6}$	199	26.6	41.0	$3.63 \cdot 10^3$	$1.09 \cdot 10^{-2}$
330	77.91	7.42	$2.335 \cdot 10^{-5}$	199	26.2	40.2	$1.31 \cdot 10^4$	$2.98 \cdot 10^{-3}$
460	74.98	7.20	$3.185 \cdot 10^{-5}$	198	25.5	40.0	$1.75 \cdot 10^4$	$2.18 \cdot 10^{-3}$
480	74.62	7.16	$4.055 \cdot 10^{-5}$	198	25.4	40.3	$2.21 \cdot 10^4$	$1.71 \cdot 10^{-3}$
540	73.33	7.03	$4.794 \cdot 10^{-5}$	200	24.8	40.4	$2.54 \cdot 10^4$	$1.45 \cdot 10^{-3}$
650	71.29	6.73	$6.824 \cdot 10^{-5}$	205	23.4	39.4	$3.39 \cdot 10^4$	$1.03 \cdot 10^{-3}$
770	68.67	6.31	$9.669 \cdot 10^{-5}$	219	21.3	38.5	$4.26 \cdot 10^4$	$7.44 \cdot 10^{-4}$
830	66.81	6.05	$1.216 \cdot 10^{-4}$	230	19.9	41.4	$4.94 \cdot 10^4$	$6.01 \cdot 10^{-4}$
1000	60.56	4.99	$2.621 \cdot 10^{-4}$	253	15.6	42.0	$8.12 \cdot 10^4$	$2.87 \cdot 10^{-4}$
1120	52.97	3.87	$6.762 \cdot 10^{-4}$	262	11.9	38.3	$1.58 \cdot 10^5$	$1.13 \cdot 10^{-4}$
1215	47.67	2.96	$1.344 \cdot 10^{-3}$	260	9.2	34.8	$2.42 \cdot 10^5$	$5.65 \cdot 10^{-5}$
1270	45.10	2.49	$1.907 \cdot 10^{-3}$	258	7.7	32.9	$2.90 \cdot 10^5$	$3.97 \cdot 10^{-5}$
1295	43.10	2.29	$2.478 \cdot 10^{-3}$	253	7.2	30.1	$3.52 \cdot 10^5$	$3.04 \cdot 10^{-5}$
1320	41.50	2.27	$3.399 \cdot 10^{-3}$	268	6.9	28.0	$4.58 \cdot 10^5$	$2.25 \cdot 10^{-5}$

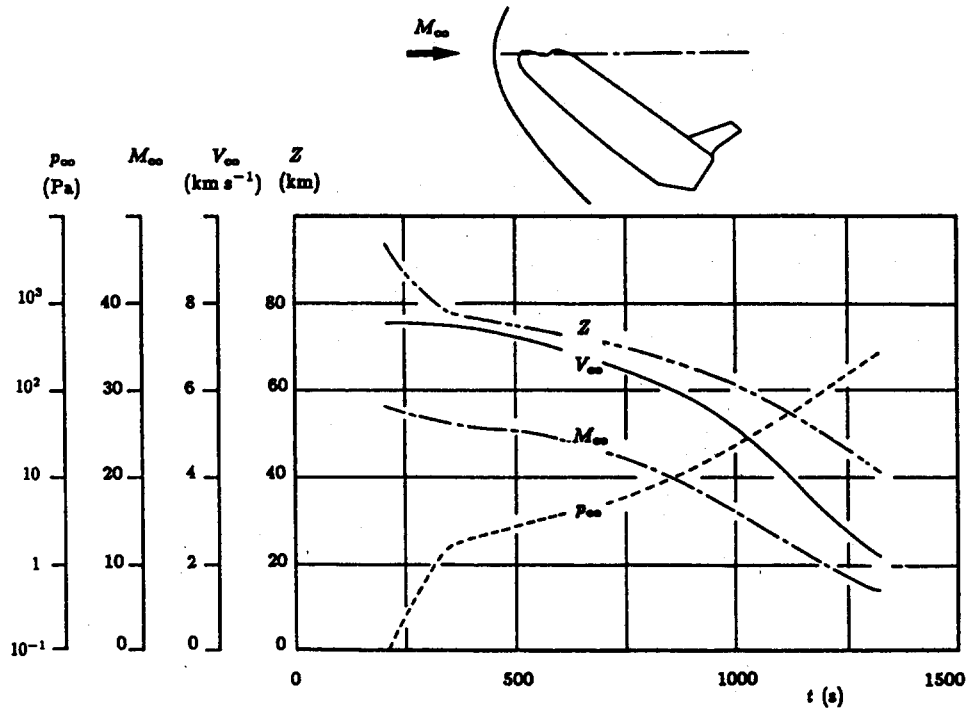


FIG. 1. STS-2 flight—Reentry trajectory (from Ref. 171).

From these data, one observes that the flow conditions vary greatly along the trajectory. In particular, the density varies by several orders of magnitude between the sea level and an altitude of 90 km; the pressure follows roughly the same variations since the temperature has the same order of magnitude throughout the trajectory. Consequently, the Reynolds number varies by several orders of magnitude. It follows that laminar-turbulent transition occurs during reentry: for example, on the lower surface, the boundary layer is laminar above an altitude of 46 km. The Knudsen number also varies greatly; its significance is discussed in Section 2.2.1. It is also interesting to note the value of the velocity which is around several kilometers per second.

### 2.1.2. High Energy Flows

At the beginning of an atmospheric reentry, the velocity of a shuttle is typically  $7.6 \text{ km s}^{-1}$ . Assuming a normal shock wave in front of the vehicle, practically all of this mechanical energy is transformed into enthalpy. In a coordinate system associated with the body, the flow velocity in front of the shock wave,  $V_\infty$ , is equal to the velocity of the body. Across the shock wave, the total enthalpy  $h_t = h + V^2/2$  is constant

$$h_\infty + \frac{V_\infty^2}{2} = h_{sw} + \frac{V_{sw}^2}{2}$$

where the index "sw" signifies the state just downstream of the shock wave. In the above equation  $h_\infty \ll V_\infty^2$  and since the intensity of the shock wave is very strong,  $V_{sw} \ll V_\infty$ . Therefore, across the shock wave, a first approximation is

$$h_{sw} = \frac{V_\infty^2}{2}.$$

This equation shows that the flow is characterized, first of all, by a transformation of mechanical energy into enthalpy. Across the shock wave, the *high speed flow is transformed into a hyperenthalpic flow*.

If the air behaved like a perfect gas, as it does at standard conditions, the temperature would be of the order of 29,000 K! Clearly, this is not realistic. Indeed, the gas undergoes physical and chemical transformations. At high temperatures, the degrees of freedom of the molecules are excited (translation, rotation, vibration ...); the molecules can dissociate: atomic oxygen and atomic nitrogen are produced; the electrons can change orbits and subsequently emit quanta of energy when they recover their initial orbit (radiation). At very large temperatures, ionization may also be present. Phenomena such as dissociation are endothermic: energy is needed to transform a molecule into atoms and this energy is stored in the form of chemical energy. Therefore, *a part of the available energy (enthalpy) is transformed into chemical energy*. As far as it is possible to speak of the temperature of the flow, its value is of the order of 6000 K instead of 29,000 K. The reader understands now why it is important to take into account these *high temperature effects*. In particular, the wall heat flux is very sensitive to these effects which must therefore be accounted for in order to properly calculate the heating of the body. The effects on the wall pressure distribution will be discussed below in Section 2.1.4.

### 2.1.3. Relaxing Flows

As stated above, the increase of enthalpy across the shock wave excites certain phenomena (depending on the level of available energy) and leaves the flow in nonequilibrium. The nonequilibrium can be thermal or chemical. The return to equilibrium occurs after a certain time, i.e. after a sufficient number of molecular collisions.

For example, let us consider the excitation of the vibrational degree of freedom which can occur downstream of the shock wave. The corresponding energy is characterized by a temperature which is not equal to the translational temperature (this temperature is directly associated with the average translational velocity of the particles—molecules or atoms). In the state of thermal equilibrium, the two temperatures are equal but this is no longer the case in the presence of vibrational excitation. The equality of the two temperatures is recovered after a large number of molecular collisions. For example, a characteristic number of collisions for oxygen at a pressure of 1 atm and a temperature of 2000 K is 18,000.<sup>(195)</sup> If the density of the gas is low, the process may take place over a large timespan. In other words, in the equilibrium state, the energy is distributed over the various modes (translation, rotation, vibration) according to the Boltzmann distribution and a unique temperature can be defined. In nonequilibrium, the distribution of energy is modified and a unique temperature is no longer sufficient to characterize this distribution. Before reaching the equilibrium state, it is said that *the flow is relaxing*.

Another example of nonequilibrium is due to the chemical reactions between the different species comprising the gas. A chemical reaction can occur if a molecular collision takes place with a sufficiently high level of energy. Obviously, the high levels of enthalpy downstream of the shock wave encourage these reactions. Here again, it takes a certain number of molecular collisions to recover a new equilibrium.

These phenomena (vibrational or chemical relaxation) are characterized by a time scale,  $t_c$ , which is an order of magnitude of the time needed to establish the equilibrium. To describe the flow, this characteristic time is compared to a mechanical time,  $t_m$ , which is associated with the convection phenomena:  $t_m$  is the time needed for a particle to travel over the characteristic length of the problem being considered. The ratio  $t_c/t_m$  is called a Damköhler number<sup>(13)</sup> (sometimes the Damköhler number is defined as the inverse ratio).

Let us consider a flow with chemical reactions (a similar discussion may be done for a flow with vibrational relaxation). When  $t_c/t_m$  is very small, the chemical reactions are very fast compared with the flow time scale and the new equilibrium is reached over a very short timespan. In other words, the chemical composition of the gas adapts immediately to the variations of pressure and temperature of the flow according to the laws of chemical equilibrium; at each point of the flow, the composition of the flow is determined by the chemical equilibrium. This situation occurs when the density is large enough in order to assure a large number of molecular collisions over a short distance.

On the other hand, if the ratio  $t_c/t_m$  is very large, the chemical reactions do not have any time to develop over the length of development of the flow. This means that the rate of production of species can be neglected; the flow is said to be *frozen*. If diffusion phenomena are neglected, the composition of the flow does not change along a streamline. This situation occurs across a shock wave where the variation of the flow conditions are so fast that the chemical reactions have no time to develop. At the molecular scale, the shock wave is spread out over a few mean free paths, but if the gas is considered as a continuum, the shock wave is a discontinuity line. The situation of frozen flow is also encountered in the core of the flow when the density of the gas is very low. In this case, the number of molecular collisions is so small that the rate of production of species is negligible over the characteristic length of the flow.

Downstream of the shock wave, the return to equilibrium of the translational degree of freedom is very fast, since only a few molecular collisions are required (an order of magnitude is 10 or even less); the return to equilibrium of the rotation is slightly longer and the return to equilibrium of the vibration is very much longer (several thousands of molecular collisions may be necessary). The return to chemical equilibrium is even much longer.

An example of the evolution of different temperatures behind a normal shock wave is given in Fig. 2.<sup>(33)</sup> As discussed in Section 2.4, the various modes of energy are characterized by different temperatures and  $T$  is the trans-rotational temperature (Section 2.3.1). At a short distance downstream of the shock wave, the various temperatures are very different because the flow is at nonequilibrium. Further downstream, these differences vanish as the flow returns to equilibrium.

Figure 3 shows a velocity-altitude map with the domains of dissociation and ionization of air assuming vibrational and chemical equilibrium.<sup>(102)</sup> The percentages at the top of the figure represent the effective beginning and end of various zones with significant effects. A typical shuttle trajectory is also shown in Fig. 3, but it is important to note that the flow is *not* at equilibrium along a large portion of the trajectory. To give a rough estimate, let us say that equilibrium is reached below  $Z = 40$  km. From Fig. 3, it is expected that the vibrational and dissociation effects are very important during a shuttle reentry.

#### 2.1.4. Effects on Wall Pressure

To illustrate the high temperature effects on the wall pressure distribution, let us consider the flow on a flat plate with an angle of attack  $\alpha$  and let us assume that the viscous effects are negligible (in reality this hypothesis is not justified).

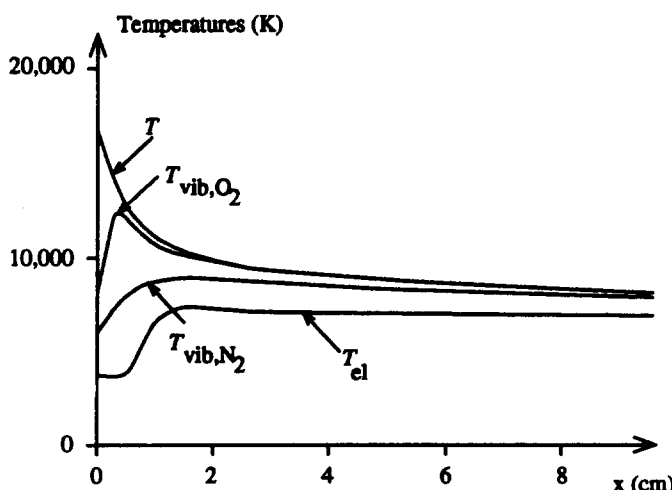


FIG. 2. Evolution of temperatures downstream of a normal shock wave in air.<sup>(33)</sup>

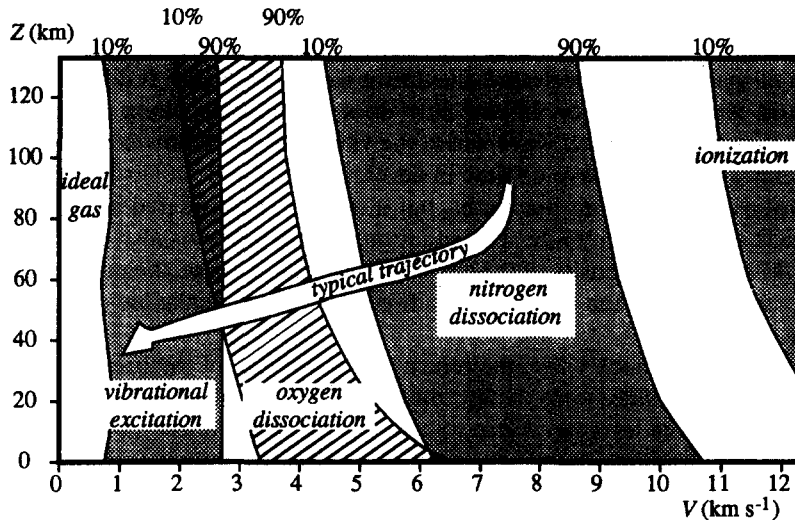


FIG. 3. Velocity-altitude map with the domains of dissociation and ionization of air, assuming vibrational and chemical equilibrium.<sup>(102)</sup> The trajectory is given as a reference: equilibrium is reached only at the end of the trajectory.

Three cases are considered (Fig. 4). Downstream of the shock wave, (i) air behaves as a perfect gas, (ii) air is in chemical equilibrium, and (iii) air is in chemical nonequilibrium. In the following discussion, only the windward side of the plate is considered.

In the first case, the shock wave is rectilinear and makes an angle  $\theta_i$  with the wall. Downstream of the shock wave, the flow is uniform. At the wall, the pressure is constant and equal to the pressure everywhere in the shock layer. The resultant of the pressure forces is exerted exactly in the middle of the plate.

In the second case, the composition of the gas is different downstream of the shock wave—as compared to its upstream composition. If the temperature is high enough, air is partially or totally dissociated; the local composition of the gas is calculated from the laws of chemical equilibrium and depends only on the local values of pressure and temperature. This situation is close to the first one except that the composition of the gas is not known *a priori* since this composition depends on the conditions of the flow downstream of the shock wave and vice-versa. The shock wave is rectilinear and makes an angle  $\theta_e < \theta_i$  with the wall. In the shock layer, the flow is uniform. At the wall, the pressure is constant but lower than with the perfect gas hypothesis.

In the third case, the composition of the gas varies along a streamline downstream of the shock wave; it is no longer a local function of pressure and temperature but depends also on the history of the flow along the streamlines. Downstream of the shock wave, there is a region of relaxation and equilibrium is reached only at the end of this region. Very near the leading edge of the plate the distance between the shock wave and the wall is so small that the equilibrium cannot be obtained. On the contrary, in this region the correct approximation is to assume that the flow is frozen. Therefore, at the leading edge the angle between the shock wave and the wall is equal to  $\theta_i$ , i.e. the value calculated with the perfect gas hypothesis. Far away from the leading edge, the thickness of the relaxation layer is small compared with the shock layer thickness and the angle of the shock wave tends towards the value  $\theta_e$ . The shock wave is no longer rectilinear and the shock layer flow is not uniform. At the wall, the pressure is not constant; the value near the leading edge is larger and the center of pressure is displaced towards the leading edge. This means that the moment of pressure forces is modified.

On a reentry vehicle, the high temperature effects on the value of wall pressure at a given point are not very large. However, the wall pressure distribution can be altered and the effects on the moments of forces can be significant.

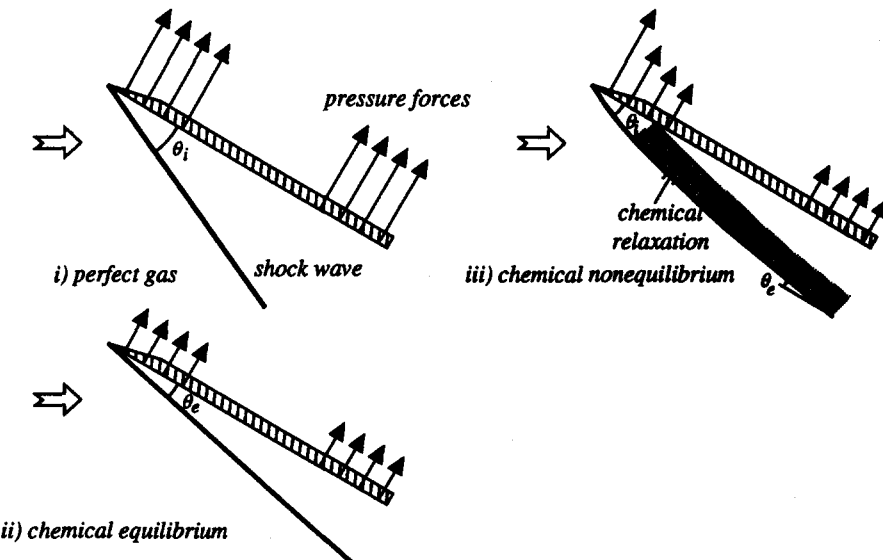


FIG. 4. Flat plate at incidence.

### 2.1.5. Viscous Interaction

The interaction between the viscous flow and the non-viscous flow in the shock layer is due to the mixing of several phenomena. Firstly, the shock layer is thin. In front of a bluff body, the shock wave detachment distance is about one tenth of the radius of curvature of the nose of the body. For a typical radius of 1 m, the location of the shock wave is about 10 cm in front of the body. On the other hand, the inclination of the shock wave with respect to the body is very small. For example, let us consider a symmetrical wedge with an included angle of 10°. For air considered as a perfect gas, the angle between the wall and the shock wave is 34° at a Mach number of 2; this angle is 11° at a Mach number of 10 and tends towards 6° when the Mach number tends towards infinity. Therefore, at high Mach numbers, the shock layer is thin all along the body.

Secondly, the thickness of the boundary layer increases greatly with the Mach number. At the beginning of the reentry, the Reynolds number is low enough for the flow to remain laminar. On a flat plate, using the reference enthalpy method (see for example Ref. 44), the displacement thickness is given by

$$\delta_1 = \frac{0.664 f H x}{\mathcal{R}_x^{1/2}}$$

where the shape parameter  $H$  is given by

$$H = 2.59 + 2.9 \frac{h_w - h_{aw}}{h_e} + 0.667 M_e^2.$$

In these formulae,  $\mathcal{R}_x$  is the Reynolds number based on the development length,  $x$ , of the boundary layer;  $h_w$  is the wall enthalpy;  $h_{aw}$  is the recovery enthalpy, i.e. the enthalpy which would be obtained at the wall under adiabatic conditions;  $h_e$  and  $M_e$  are the enthalpy and the Mach number of the flow at the edge of the boundary layer;  $f$  is a compressibility function defined as

$$f = \left( \frac{\mu^*/\mu_e}{h^*/h_e} \right)^{1/2}$$

where  $\mu^*/\mu_e$  is calculated from the reference enthalpy  $h^*$

$$h^* - h_e = 0.54(h_w - h_e) + 0.16(h_{aw} - h_e).$$

From the expression for  $H$ , it is noted that the shape parameter varies with  $M_e^2$  for large Mach numbers.

Due to its relatively large thickness, the boundary layer deviates (or displaces) the inviscid flow and a pressure variation is induced. The deviation  $d\alpha$  of the flow produced by the boundary layer is equal to  $\frac{d\delta_1}{dx}$ , the derivative of the boundary layer displacement thickness.

This problem has been analyzed by decomposing the plate into two regions (see for example Ref. 3). One region is close to the leading edge where the slope of the displacement thickness is large. This is the strong interaction region: the boundary layer displaces the inviscid flow which in turn affects the boundary layer development. Far away from the leading edge, in the weak interaction region, the slope of the displacement thickness is smaller. The boundary layer displaces the inviscid flow but the boundary layer development is only slightly affected. For the present purposes, it suffices to analyze this region. As a first approximation, it is assumed that the pressure variation is related to the flow deviation by the small perturbation theory (in principle, this theory is not valid at very large Mach numbers)

$$\frac{dp}{p} = \gamma M_e^2 \frac{d\alpha}{\sqrt{M_e^2 - 1}}$$

where  $\gamma$  is the ratio of specific heats ( $\gamma = 1.4$  for air in standard conditions). Therefore, at high Mach numbers, the relative pressure variation is proportional to  $f M_e^3 / R_x^{1/2}$ . This parameter is called *the viscous interaction parameter*. At the beginning of the reentry, the interaction is strong because the Mach number is large and because the Reynolds number is small. Indeed, at the very beginning, the shock layer is entirely filled with viscous flow and even the boundary layer concept is not applicable.

#### 2.1.6. Shock Wave Effects

Shock wave interference phenomena and shock wave/boundary layer interactions also occur in supersonic flows, but they are of special importance in hypersonic flows because they are generally characterized by wall pressure peaks and heat transfer peaks. These phenomena can occur on control surfaces inducing a loss of control efficiency.

Schematically, shock wave/boundary layer interactions are classified in four basic configurations: flow over a ramp, impingement of a shock wave on a wall, flow over a forward facing step, and flow over a backward facing step. Such interactions are encountered near wing-body junctions, near a flap hinge or in air intakes of air breathing propulsive vehicles. Compared with the supersonic case, there are no fundamental differences (at least, as far as high temperature effects are not concerned). However, in hypersonic flow, the boundary layer is frequently laminar at the onset of the interaction.

Shock interference phenomena are more common in hypersonic flow than in supersonic flow since the inclination of the shock waves with the body is smaller. For example, such interference phenomena are produced by the front bow shock wave which interacts with the shock wave created by a fin. The intersection of shock waves can lead to the formation of shocks, shear layers or jets which can impinge on a wall and interact with a boundary layer. In particular, a shear layer is formed where, in non-viscous flow, a slip line would be present. In certain configurations, the shear layer can impinge on a wall inducing a large pressure peak and a large heat transfer peak because the compression along the shear layer can be very strong.

The study of shock/shock and shock wave/boundary layer interactions constitutes a very broad field of investigation, but this topic is not included in this paper. The interested reader is referred to very complete reviews Refs 51, 52 and 92.

## 2.2. CONTINUUM AND MOLECULAR APPROACHES

### 2.2.1. Various Flow Regimes

At the very beginning of the reentry in the atmosphere, the density is very low and there are few molecules in the flow around the vehicle. If a molecule collides with the nose of the vehicle, the next collision is in the tail region, and even this collision may not occur at all. Therefore, it is possible to follow a given particle along its path in the flow. On the other hand, at lower altitudes, the number of particles in an even very small volume is so large that it is out of the question to identify a given particle. Clearly, the study of the flow for these two extreme cases is not performed using the same methods.

The relevant parameter used to classify the various flow regimes is the *Knudsen number*

$$Kn = \frac{\lambda}{L}$$

where  $\lambda$  is the mean free path and  $L$  is a characteristic length of the flow. To be more accurate, a local length could be used to define a scale over which a significant variation of the flow occurs.

An interesting expression of the Knudsen number, obtained from the kinetic theory of gases, is

$$Kn = 1.26 \sqrt{\gamma} \frac{M}{\mathcal{R}_L}$$

where  $M$  is the Mach number of the flow,  $\mathcal{R}_L$  is the Reynolds number based on the length  $L$  and  $\gamma$  is the ratio of specific heats.

If the Knudsen number is small ( $Kn < 0.1$ ), the gas can be considered as a continuum and the standard fluid mechanics approach is used.

On the contrary, when the Knudsen number is large ( $Kn > 10$ ), we are in the *free molecular regime*. From the above expression of the Knudsen number, this flow regime is likely to occur at large Mach numbers and low Reynolds numbers. Before colliding with the wall, the molecules are not influenced by the presence of the body. The forces acting on the vehicle can be calculated locally from the properties of molecules in the freestream.

The range of Knudsen numbers between these two extreme cases corresponds to the *transitional regime*. Here, the transitional regime has nothing to do with the laminar-turbulent transition.

For all values of the Knudsen number, the flow is represented by the Boltzmann equation which describes the evolution of the distribution function of the molecules. In practice, the numerical solution of the Boltzmann equation can only be obtained at large Knudsen numbers. At small Knudsen numbers, too many variables are involved in the numerical solution. In the latter case, the relevant equations are the Navier-Stokes equations which simplify into the Euler equations when the Knudsen number tends towards zero (i.e. when the Reynolds number goes to infinity). In the transitional regime, the *Direct Simulation Monte Carlo* method is used to simulate the flow.<sup>(20,115)</sup> This method describes the evolution of representative samples of molecules so that the history of only a limited number of molecules is followed. A representative molecule is not a real molecule but it represents a certain number of real molecules. The numerical method uses a discretization of time. During a time step  $\Delta t$ , a representative molecule is displaced over a certain distance based on its velocity. During the displacement, the molecule does not undergo any collision. At the new location of the representative molecule, the effects of the collisions which would have occurred during  $\Delta t$  are taken into account (the collisions can be with another molecule or with a wall). Obviously, the calculated collisions must be representative of real collisions.

### 2.2.2. Molecular Approach

In the framework of the theory of molecular gas dynamics, the gas is described by the *distribution function* of the molecules. In a gas consisting of an ensemble of species  $I$  with an internal degree of freedom, the state of a molecule is represented by a point  $S(\varepsilon_I^i, r, c, t)$  in the phase space:  $\varepsilon_I^i$  represents the internal energy of a molecule of species  $I$  corresponding to the energy level  $i$ ,  $r$  is its position vector,  $c$  is its velocity, and  $t$  is the time. The distribution function  $f_I^i(\varepsilon_I^i, r, c, t)$  is defined such that, at a given time  $t$ , the probable number of molecules of species  $I$  having the energy  $\varepsilon_I^i$  in a volume  $drdc$  is  $f_I^i drdc$  where  $dr$  is a volume element around the location  $r$  and  $dc$  is a volume element around the velocity  $c$ .

The evolution of the distribution function is obtained from the calculation of the number of particles of species  $I$  with energy  $\varepsilon_I^i$  which deplete or replenish the number of particles contained in the volume element  $drdc$  at instant  $t$ . The result is the *Boltzmann equation*<sup>(32,38,90,195)</sup> which reads symbolically

$$\frac{\partial f_I^i}{\partial t} + c_j \frac{\partial f_I^i}{\partial r_j} = J.$$

In this equation, the effects of external forces (for example, due to gravity or to an electric field) are not taken into account.

The Boltzmann equation describes the total variation of the probable number of particles due to collisions. The collisional term  $J$  is comprised of various contributions

$$J = J_{\text{trans}} + J_{\text{rot}} + J_{\text{vib}} + J_{\text{chem}} + J_{\text{ion}}$$

which correspond to physical processes in which different modes of energy are exchanged: translation, rotation, vibration, chemical reactions, ionization.

For small values of the Knudsen number, solutions of the Boltzmann equation can be obtained using the Chapman–Enskog expansion. The zeroth order solution corresponds to equilibrium ( $f_I^i$  is stationary) and is the solution of

$$J_{\text{trans}}^0 + J_{\text{rot}}^0 = 0$$

because the characteristic times of translation and rotation are smaller than the other time scales. For the translational mode, the solution is a Maxwellian distribution function and for the rotational mode, the solution is a Boltzmannian distribution function.

From the distribution function, various moments can be calculated and the characteristics of the macroscopic flow are deduced: density, velocity, energy, concentrations of each species, etc. By taking the moments of the Boltzmann equation, the corresponding conservation equations are obtained. At the zeroth order, the Euler equations are obtained for the standard case of a flow at ordinary temperatures and pressures. At high temperatures, in the presence of vibrational relaxation, chemical reactions and ionization, the Euler equations are joined by the equations describing the evolution of species and the evolution of each mode of energy: these equations contain convective terms and production terms but no diffusion terms.

Starting from the zeroth order solution of the Boltzmann equation, the first order solution can be obtained. The formal result is the Navier–Stokes system of equations joined by the equations for the evolution of species concentration and for the evolution of each mode of energy (for example the vibrational energy).

### 2.2.3. Continuum Approach

The continuum approach is precisely based on the first order solution described above, i.e. the Navier–Stokes equations joined by the species equations and the equations for the various modes of energy. At high Reynolds numbers, the equations are simplified into two subsets of equations: (i) the boundary layer equations which apply near walls or in

wakes, and (ii) the Euler equations elsewhere (plus the corresponding species equations and the equations for the modes of energy).

Compared with the Euler equations (and the associated equations for species and modes of energy), the Navier-Stokes equations (and the associated equations) contain additional terms which are fluxes of diffusion. For example, the momentum equations contain viscous stresses which are momentum diffusion fluxes; the energy equation contains an energy flux and the species equations contain a mass diffusion flux. These terms are associated with transport phenomena: transport of momentum, energy, mass of species, etc. From the series expansion of the Boltzmann equation, these terms are related to gradients of velocity, enthalpy, species concentration, etc. by means of transport coefficients: viscosity, thermal conductivity, mass diffusivity, etc. In principle, these transport coefficients are a result of the series expansion of the Boltzmann equation but their calculation is extremely difficult. The calculations express the transport coefficients by means of collision integrals which can be calculated when the properties of molecules are known from a model describing the intermolecular forces.

Let us note that the conservation equations (of momentum, energy, mass of species) can also be obtained formally by a more direct approach, reasoning at the macroscopic scale and assuming the existence of diffusion fluxes. These fluxes are then empirically modelled. This is in contrast with the approach described above in which a theoretical basis is used to express the diffusion fluxes.

### 2.3. CHARACTERISTICS OF THE FLOW OF A GAS MIXTURE

In this paper, it is assumed that each gas of the mixture behaves as a *perfect gas*.

By definition, a *perfect gas* is one where the intermolecular forces are negligible. This hypothesis is valid for dilute gases. This is in contrast with a real gas, where intermolecular forces must be taken into account (the difference between perfect and real gases appears, in particular, in the equation of state).

By definition, a *thermally perfect gas* is one where the enthalpy and the internal energy are functions of temperature only. It follows that the specific heats  $c_p$  and  $c_v$  are function of temperature only. In an *ideal gas* (sometimes called a *calorically perfect gas*), the specific heats  $c_p$  and  $c_v$  are constant.

It is also assumed that in a mixture of gases, *the mixing is ideal*. This means that the interactions between particles of different species are negligible. It follows that the enthalpy of the mixture is the sum of the enthalpies of the constituents; the internal energy of the mixture is the sum of the internal energies of the constituents. It is also assumed that the mixture satisfies the relation:  $h = e + p/\rho$ .

In the more general case, the mixture is in *chemical nonequilibrium* and in *thermodynamic nonequilibrium*.

Let us recall that a chemical reaction is in equilibrium when the forward reaction is exactly balanced by the backward reaction. The rate of production of species is zero. A flow is in *local chemical equilibrium* when at each point in the flow, all the chemical reactions are in equilibrium. Then, at each point in the flow, the composition of the gas is a function of the local values of pressure and temperature. Let us note that the composition can vary from point to point.

A flow is *locally in thermodynamic equilibrium* when the local population distribution of the particles is given by a local Maxwell-Boltzmann distribution at the local temperature, according to the results of statistical thermodynamics. This means, in particular, that each mode of energy is characterized by the same temperature. The hypothesis of local thermodynamic equilibrium is not valid, in particular, when the vibrational mode is excited.

The Navier-Stokes equations imply a small departure from local equilibrium of translational and rotational modes;<sup>(195)</sup> the viscous stresses and the thermal heat flux are associated with this nonequilibrium. The sum of the energies of the translational and rotational modes is represented by a temperature which will be noted  $T$  (see Section 2.3.1). Sometimes,

the energies of the vibrational modes are represented by temperatures  $T_{\text{vib},I}$  (Section 2.4), but these temperatures are different from  $T$  and one needs as many temperatures  $T_{\text{vib},I}$  as there are species  $I$  in vibrational nonequilibrium.

Finally, the contribution of electrons is neglected because it is assumed that the flow can be only slightly ionized.

A few definitions are needed before giving the characteristics of a gas mixture and the laws of mixing.

$V$ —volume of the system.

$M$ —total mass of the system.

$M_I$ —total mass of species  $I$  contained in the system.

$\rho$ —density of the mixture.

$\rho_I$ —density of species  $I$  in the mixture, i.e. mass of species  $I$  per unit volume of mixture.

$Y_I$ —mass fraction of species  $I$ ;  $Y_I = \frac{M_I}{M} = \frac{\rho_I}{\rho}$ .

$\mathcal{M}_I$ —mass per mole of species  $I$ .

$\mathcal{M}$ —mass per mole of mixture.

$N_I$ —number of moles of species  $I$  in the mixture per unit volume.

$N$ —total number of moles of mixture per unit volume.

$X_I$ —mole fraction of species  $I$ ;  $X_I = \frac{N_I}{N}$ .

$p_I$ —partial pressure of species  $I$ .

$p$ —pressure of mixture.

$h_I$ —enthalpy of species  $I$  per unit mass of species  $I$ .

$h$ —enthalpy of mixture per unit mass of the mixture.

$\mathcal{N}_A$ —Avogadro's number =  $6.02252 \cdot 10^{23}$ :  $\mathcal{N}_A$  is the number of particles per mole.

$h_p$ —Planck constant:  $h_p = 6.6256 \cdot 10^{-34}$  J s.

$k_B$ —Boltzmann constant:  $k_B = 1.38054 \cdot 10^{-23}$  J K $^{-1}$ .

$\mathcal{R}$ —universal gas constant:  $\mathcal{R} = k_B \mathcal{N}_A$ ;  $\mathcal{R} = 8.3143 \text{ J mol}^{-1} \text{ K}^{-1}$ .

$R_I$ —specific gas constant of species  $I$ :  $R_I = \frac{\mathcal{R}}{\mathcal{M}_I}$ .

$R$ —specific gas constant of the mixture:  $R = \frac{\mathcal{R}}{\mathcal{M}}$ .

For air at standard conditions,  $R_0 = 287.1 \text{ J kg}^{-1} \text{ K}^{-1}$ .

From the above definitions, several relationships can be deduced. First, the densities are given by

$$\rho = \frac{M}{V}; \quad \rho_I = \frac{M_I}{V}$$

so that

$$\rho = \sum_I \rho_I$$

and for the mass fractions we have

$$Y_I = \frac{\rho_I}{\rho}; \quad \sum_I Y_I = 1.$$

The densities are also given by

$$\rho = \mathcal{M}N; \quad \rho_I = \mathcal{M}_I N_I$$

and, taking into account

$$N = \sum_I N_I$$

the mass per mole of the mixture can be calculated as function of the mass per mole of

species

$$\frac{\rho}{M} = \sum_I \frac{\rho_I}{M_I} \quad \text{or} \quad \frac{1}{M} = \sum_I \frac{Y_I}{M_I}.$$

For the mole fractions  $X_I$ , we have the following relations

$$\sum_I X_I = 1$$

$$Y_I = \frac{M_I}{M} X_I$$

$$M = \sum_I M_I X_I.$$

### 2.3.1. Enthalpy, Internal Energy and Temperature

The enthalpy  $h_I$  of species  $I$ , per unit mass of species  $I$ , is<sup>(3)</sup>

$$h_I = (h - e_0)_I + (\Delta h_f)_I^0$$

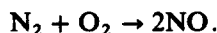
where

$$(h - e_0)_I = h_{\text{sens}, I}$$

is called the sensible enthalpy.

The quantity  $(e_0)_I$  is the zero-point energy and  $(\Delta h_f)_I^0$  is the heat of formation of species  $I$  at a temperature of absolute zero, which is interpreted as the effective zero-point energy; at absolute zero, the sensible energy is zero.

In fact, the absolute level of enthalpy is not involved in calculations. Only the changes of enthalpy are important and the enthalpy is known to within an additive constant. Conventionally, the heat of formation of species is defined from a reaction involving stable species at reference conditions (at a pressure of one atmosphere and at a temperature of 298.15 K). For example, the heat of formation of NO is defined from the (fictitious) reaction



The heat of formation is given by

$$2(\Delta h_f)_{\text{NO}} M_{\text{NO}} = 2h_{\text{NO}} M_{\text{NO}} - h_{\text{N}_2} M_{\text{N}_2} - h_{\text{O}_2} M_{\text{O}_2}.$$

This is a relation for the molar enthalpies ( $h_I M_I$  is the molar enthalpy of species  $I$ ) because the chemical reaction tells us that one mole of  $\text{N}_2$  and one mole of  $\text{O}_2$  produce two moles of NO.

These calculations are valid to define the heat of formation at any temperature. In particular at absolute zero, this enables us to calculate  $(\Delta h_f)_I^0$ .

If the same calculation is performed for  $\text{N}_2$ , it is readily shown that the heat of formation is zero because the reaction involved is simply



It is recalled that the enthalpy is related to the internal energy by

$$h_I = e_I + \frac{p_I}{\rho_I}.$$

The internal energy is decomposed into four contributions: translational, rotational, vibrational and electronic energies

$$e_I = (e_{\text{trans}})_I + (e_{\text{rot}})_I + (e_{\text{vib}})_I + (e_{\text{el}})_I$$

or

$$e_I = (e_{\text{trans}})_{\text{sens}, I} + (e_{\text{rot}})_{\text{sens}, I} + (e_{\text{vib}})_{\text{sens}, I} + (e_{\text{el}})_{\text{sens}, I} + (\Delta h_f)_I^0. \quad (1)$$

At *thermodynamic equilibrium*, statistical thermodynamics enable us to determine the various contributions. For monatomic species  $I$ , the sensible translational energy is

$$(e_{\text{trans}})_{\text{sens}, I} = \frac{3 \mathcal{R}}{2 M_I} T$$

and the rotational and vibrational energies are zero.

For a diatomic molecule  $I$ , considered as a harmonic oscillator, in *thermodynamic equilibrium*, the sensible translational, rotational and vibrational energies are

$$(e_{\text{trans}})_{\text{sens}, I} = \frac{3 \mathcal{R}}{2 M_I} T \quad (2a)$$

$$(e_{\text{rot}})_{\text{sens}, I} = \frac{\mathcal{R}}{M_I} T \quad (2b)$$

$$(e_{\text{vib}})_{\text{sens}, I} = \frac{\frac{\Theta_I}{T}}{\exp\left(\frac{\Theta_I}{T}\right) - 1} \frac{\mathcal{R}}{M_I} T \quad (2c)$$

where  $\Theta_I$  is a characteristic temperature for vibration

$$\Theta_I = \frac{h_P v_I}{k_B}$$

In this relation,  $v_I$  is the fundamental vibrational frequency of the molecule  $I$ ,  $h_P$  is the Planck constant,  $k_B$  is the Boltzmann constant.

No equivalent simple formula exists for the electronic energy but, for our applications, it does not matter since the electronic energy is negligible.

The above results are obtained directly from the theory of statistical thermodynamics. Interpolation polynomial formulae are also available and can be interesting for numerical calculations.<sup>(11,78)</sup>

In a *nonequilibrium flow*, it is assumed that the temperature  $T$  is associated with the trans-rotational energy as follows:

- for monatomic species:

$$(e_{\text{tr-rot}})_{\text{sens}, I} = (e_{\text{trans}})_{\text{sens}, I} = \frac{3 \mathcal{R}}{2 M_I} T$$

- for diatomic species:

$$(e_{\text{tr-rot}})_{\text{sens}, I} = (e_{\text{trans}})_{\text{sens}, I} + (e_{\text{rot}})_{\text{sens}, I} = \frac{5 \mathcal{R}}{2 M_I} T.$$

### 2.3.2. Equation of State

The partial pressure  $p_I$  of species  $I$  is the pressure which would exist in the system if the same quantity of species  $I$  were the only matter in the system.

For an ideal mixture of gases, the internal energy per unit mass is

$$e = \sum_I Y_I e_I$$

and the enthalpy per unit mass is

$$h = \sum_I Y_I h_I.$$

We also have

$$p_I = \rho_I h_I - \rho_I e_I.$$

By summing this relation we obtain

$$\sum_I p_I = \rho h - \rho e.$$

The total pressure satisfies

$$p = \rho h - \rho e$$

and Dalton's law expresses the total pressure as the sum of the partial pressures

$$p = \sum_I p_I.$$

Since each species behaves like a perfect gas, the equation of state for each species reads

$$p_I = \rho_I \frac{R}{M_I} T$$

or

$$p_I = N_I R T.$$

Using Dalton's law, the equation of state for the mixture is obtained

$$p = N R T$$

or

$$p = \rho \frac{R}{M} T.$$

It is also deduced that

$$p_I = p \frac{N_I}{N} = p X_I.$$

Let us note that, in these equations, the temperature  $T$  is the trans-rotational temperature (the same for all species).

### 2.3.3. Specific Heats

Let us recall that for an ideal mixture of gases, the internal energy per unit mass is

$$e = \sum_I Y_I e_I$$

and the enthalpy per unit mass is

$$h = \sum_I Y_I h_I.$$

In a flow in chemical nonequilibrium, this relationship shows that the enthalpy of the mixture is a function of the temperature and of the gas composition. This composition is not a local function because it depends on the history of the flow. Only in the case of chemical equilibrium, the composition of the gas is a function of the local values of pressure and temperature.

If  $h_I = h_I(T)$  (this is the case of a thermally perfect gas), the specific heat of species  $I$  at constant pressure is

$$c_{pI} = \left( \frac{\partial h_I}{\partial T} \right)_p = \frac{dh_I}{dT}.$$

In general, it is not possible to define the specific heat of the mixture in the same way since  $h$  depends on the history of the flow through the composition of the gas. Sometimes, the specific heat of the frozen gas is used as

$$c_{pf} = \left( \frac{\partial h}{\partial T} \right)_{p, Y_I}$$

where the derivative is taken at constant pressure and at constant mass fractions (the composition of the gas is frozen). Using the definition of the enthalpy of the mixture, we obtain

$$c_{pf} = \sum_I Y_I \left( \frac{\partial h_I}{\partial T} \right)_p$$

or

$$c_{pf} = \sum_I Y_I c_{pI}.$$

Obviously, similar considerations hold for the specific heats at constant volume.

### 2.3.4. Flow Velocity and Diffusion Velocity

For each species  $I$ , it is possible to define an average velocity  $u_I$  at a point  $P$  as

$$u_I = \langle c_I \rangle$$

where  $c_I$  is a sample of the instantaneous velocity of a particle of species  $I$  at point  $P$  and the sign  $\langle \rangle$  stands for the statistical average of these samples.

The flow velocity at a point is defined as a mass weighted average

$$\rho u = \sum_I \rho_I u_I$$

or

$$u = \sum_I Y_I u_I.$$

The diffusion velocity  $u_I^D$  of species  $I$  is defined as

$$u_I^D = u_I - u.$$

## 2.4. VIBRATIONAL NONEQUILIBRIUM

Let us imagine that a large amount of energy is suddenly brought to all the parts of a gas system. The sudden increase of energy creates nonequilibrium phenomena because the excess of energy cannot be redistributed instantaneously amongst the various modes. The redistribution of energy is performed by means of collisions between particles. The number of collisions needed to reach the new equilibrium state depends on the mode of energy. In particular, the return to vibrational and chemical equilibrium requires a large number of collisions and so it is important to take into account the associated exchanges of energy during the relaxation towards the new equilibrium. The case of chemical nonequilibrium is discussed in Section 2.5.

From a study based on the theory of statistical mechanics, simple results are obtained for diatomic molecules. Let  $\dot{\omega}_{vib,I}$  be the rate of change of the sensible vibrational energy of species  $I$ , i.e. the variation of vibrational energy of species  $I$  per unit time and unit volume.

The rate of change  $\dot{\omega}_{\text{vib},I}$  is given by a relaxation equation<sup>(3,13,32,195)</sup>

$$\dot{\omega}_{\text{vib},I} = \frac{\rho_I}{\tau_I} [(e_{\text{vib}}^{\text{eq}})_{\text{sens},I} - (e_{\text{vib}})_{\text{sens},I}]. \quad (3)$$

This equation implies a relaxation towards the equilibrium value  $(e_{\text{vib}}^{\text{eq}})_{\text{sens},I}$  which is given by Eq. 2c.

In Eq. 3,  $\tau_I$  is a relaxation time. For most diatomic species, a good approximation of  $\tau_I$  is given by

$$\tau_I = \frac{C}{p_I} \exp \left[ \left( \frac{K_2}{T} \right)^{1/3} \right]$$

where  $C$  and  $K_2$  are constants which depend on the properties of the molecules.

The above approach is only a first approximation to calculate the evolution of the vibrational energy. Several simplifying hypotheses have been introduced to yield Eq. 3. In particular, it is assumed that molecules behave like harmonic oscillators and only transition from one energy level to the next level is considered. More elaborate models have been proposed to account for energy transfer between different modes: translation–vibration, vibration–vibration, vibration–chemistry.<sup>(32,33,181)</sup>

A vibrational temperature  $T_{\text{vib},I}$  can be defined from

$$(e_{\text{vib}})_{\text{sens},I} = \frac{\Theta_I}{\exp \left( \frac{\Theta_I}{T_{\text{vib},I}} \right) - 1} \frac{\mathcal{M}_I}{\mathcal{M}_I}. \quad (4)$$

In the presence of vibrational relaxation, the vibrational temperatures  $T_{\text{vib},I}$  are not equal to the temperature  $T$ . In this case, one needs as many vibrational temperatures as species in vibrational nonequilibrium in order to describe the flow. At vibrational equilibrium,  $T_{\text{vib},I} = T$  and Eq. 2c is recovered.

## 2.5. CHEMICAL REACTIONS

### 2.5.1. Species Production Rates

Let us consider an *elementary reaction*



The production rate  $\dot{\omega}_{AB}$  of species  $AB$  is the mass of  $AB$  produced by the chemical reaction per unit time and per unit volume. So,  $\dot{\omega}_{AB}/\mathcal{M}_{AB}$  represents the variation per unit time of  $N_{AB}$  due to chemical reactions. The production rates  $\dot{\omega}_A$  and  $\dot{\omega}_B$  are defined in the same way, but obviously for the above reaction these quantities are negative.

A molecule of  $AB$  is made of elements of  $A$  and  $B$ . The chemical reaction does not alter either the mass of elements of  $A$  or  $B$ . Therefore, the mass conservation of elements  $A$  and  $B$  yields

$$\begin{aligned} N_A + N_{AB} &= \text{cst} \\ N_B + N_{AB} &= \text{cst} \end{aligned}$$

and we deduce

$$\frac{\dot{\omega}_{AB}}{\mathcal{M}_{AB}} = - \frac{\dot{\omega}_A}{\mathcal{M}_A} = - \frac{\dot{\omega}_B}{\mathcal{M}_B}.$$

The production rate  $\dot{\omega}_{AB}$  is proportional to the number of possible collisions between reacting particles and we have<sup>(3,13,148)</sup>

$$\frac{\dot{\omega}_{AB}}{\mathcal{M}_{AB}} = k N_A N_B. \quad (5)$$

The coefficient  $k$  in Eq. 5 is called the *specific reaction rate coefficient*. Assuming the *vibrational equilibrium*, this coefficient is given by a law of the form

$$k = KT^\alpha e^{-\frac{E_a}{RT}}. \quad (6)$$

When  $\alpha = 0$ , this is Arrhenius' law. The quantity  $E_a$  is the activation energy. Sometimes, a characteristic temperature  $T_a$  of formation of species  $AB$  is introduced as:  $T_a = E_a/\mathcal{R}$ .

In the case of vibrational nonequilibrium, the expression of the reaction rate coefficient is more complicated; the influence of the vibrational temperatures has to be taken into account.<sup>(129,145,183)</sup>

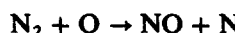
In a flow of a mixture, there is a set of *elementary* chemical reactions represented using Penner notation as

$$\sum_I v'_I A_I \xrightleftharpoons{f} \sum_I v''_I A_I \quad (7)$$

where "f" represents the forward reaction and "b" the backward reaction. The coefficients  $v'_I$  and  $v''_I$  are called the stoichiometric coefficients. We let

$$v_I = v''_I - v'_I.$$

For example, the reaction



is represented using Penner notation with the coefficients:  $v'_{\text{NO}} = 0$ ,  $v'_{\text{N}} = 0$ ,  $v'_{\text{N}_2} = 1$ ,  $v'_\text{O} = 1$ ,  $v''_{\text{NO}} = 1$ ,  $v''_{\text{N}} = 1$ ,  $v''_{\text{N}_2} = 0$ ,  $v''_\text{O} = 0$ .

The generalization of Eq. 5 for the forward reaction 7 is

$$\left( \frac{\dot{\omega}_I}{\mathcal{M}_I} \right)_f = k_f v_I \prod_j N_j^{v'_j} \quad \text{with} \quad k_f = K_f T^{\alpha_f} e^{-T_f/T}$$

where  $\prod_j$  represents a product over all possible values of  $J$ .

For the backward reaction we have

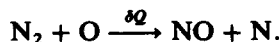
$$\left( \frac{\dot{\omega}_I}{\mathcal{M}_I} \right)_b = -k_b v_I \prod_j N_j^{v''_j} \quad \text{with} \quad k_b = K_b T^{\alpha_b} e^{-T_b/T}.$$

Finally, the production rate of species  $I$  in reaction 7 is

$$\frac{\dot{\omega}_I}{\mathcal{M}_I} = v_I \left( k_f \prod_j N_j^{v'_j} - k_b \prod_j N_j^{v''_j} \right). \quad (8)$$

Let us stress again that the above relation is valid only for an elementary reaction, i.e. a reaction which takes place in a single step.

Generally, a chemical reaction is associated with a heat exchange: the reaction is *exothermic* if heat is produced, the reaction is *endothermic* if heat is absorbed by the formation of products. This heat exchange is included in the calculation of enthalpies and can be calculated from the laws of classical thermodynamics. For example, consider the reaction



The heat  $\delta Q$  produced by the reaction of one mole of  $\text{N}_2$  and one mole of  $\text{O}$  at constant pressure, for example, is

$$\delta Q = h_{\text{NO}} \mathcal{M}_{\text{NO}} + h_{\text{N}} \mathcal{M}_{\text{N}} - h_{\text{O}} \mathcal{M}_{\text{O}} - h_{\text{N}_2} \mathcal{M}_{\text{N}_2}.$$

### 2.5.2. Chemical Model for Air at High Temperature

For air at temperatures below 9000 K, the following detailed kinetic mechanism is used





Species present are  $\text{N}_2$ ,  $\text{O}_2$ ,  $\text{N}$ ,  $\text{O}$ ,  $\text{NO}$ ,  $\text{NO}^+$  and free electrons  $e^-$ . In the above chemical reactions,  $\text{M}$  is a collision partner which can be any species among the species present.

For specific problems, it is not useful to consider all the chemical reactions. For example, to study the heating of a shuttle during an atmospheric reentry using a boundary layer approach, it seems sufficient to use a simplified model



A subset of the above reactions constituted of the first three reactions can even be sufficient: it is the Zeld'ovich process.

Applications to the calculations of boundary layers on a shuttle will be given in Section 3.

### 2.5.3. Chemical Time Scale

According to the formula given in Section 2.5.1, the chemical time scale for e.g. the forward reaction in Eq. 8 reads

$$\tau_{\text{chem}} \propto N_I \left( k_f \prod_j N_J^{v'_j} \right)^{-1}$$

or, introducing the density of species  $I$ ,  $\rho_I = N_I M_I$

$$\tau_{\text{chem}} \propto \rho_I \left( k_f \prod_j N_J^{v'_j} \right)^{-1}.$$

Introducing the quantity

$$v' = \sum_j v'_j$$

and the species mass fractions  $Y_I$ , the chemical time scale reads

$$\tau_{\text{chem}} \propto Y_I \left( k_f \rho^{v'-1} \prod_j Y_J^{v'_j} \right)^{-1}$$

i.e. the chemical time scale decreases when the chemical reaction rate or the density increases (if  $v' > 1$ ).

Let us now consider the reentry trajectory of the STS-2 flight (Fig. 1 and Table 1<sup>(171)</sup>).

As the shuttle goes deeper into the atmosphere, the density increases by roughly three orders of magnitude. As  $v'$  is usually two or three, this implies a variation of three or six orders of magnitude of the  $\rho^{v'-1}$  term. At the same time, the shuttle slows down so that the flow enthalpy and the temperature level decrease. In the outer region of the boundary layer, near the stagnation point, the temperature decreases from about 6000 K to about 3000 K. The variation of reaction rate coefficients with temperature can be very steep. For example,

for the atomic oxygen dissociation reaction, the forward reaction rate coefficient decreases by four orders of magnitude between 6000 K and 3000 K while the backward reaction rate coefficient hardly changes. Hence, the chemical time scale depends strongly on both the considered chemical reaction via the reaction rate coefficient and the altitude via the density.

For the boundary layer flow, air is highly dissociated in the stagnation point region and tends to recombine downstream as the flow acceleration leads to a decrease in the temperature level. For the recombination reactions  $v' = 3$ , and so the variation of the density is the leading term and the chemical time scale decreases with the altitude. On the other hand, the mean motion time scale, e.g. the length of the shuttle divided by the upstream velocity, varies weakly. This results in an important variation of the chemical relaxation time scale with regard to the mean motion time scale during reentry. The flow is chemically frozen at the beginning of the reentry (high altitudes, low densities) and near equilibrium at the end of the laminar regime (lower altitudes, higher densities).

#### 2.5.4. Chemical Equilibrium

If the forward and backward reactions balance exactly, there is *chemical equilibrium*. The species production rate is zero. Then, we have

$$\prod_j N_j^{v_j} = \frac{k_f}{k_b}$$

with

$$v_j = v_j'' - v_j'.$$

Using the equation of state  $p_j = N_j \mathcal{R} T$ , we deduce

$$\prod_j p_j^{v_j} = \frac{k_f}{k_b} (\mathcal{R} T)^{\sum_j v_j} = K_p(T). \quad (11)$$

This law is known as the law of *mass action*. This result can also be obtained from the thermodynamic study of the mixture.<sup>(59)</sup> Indeed, the state of chemical equilibrium corresponds to a minimum of the Gibbs free energy of the mixture. This means that the equilibrium coefficient  $K_p(T)$  results from the thermodynamic properties of gases contained in the mixture. The composition of the gas mixture in chemical equilibrium is therefore determined only from the thermodynamic properties of species, no chemical model is needed to study chemical equilibrium flows. Conversely, the forward and backward reaction rate constants for a chemical reaction are related by the equilibrium constant which is known to within a good accuracy since it depends only upon the thermodynamic properties of the species involved in the reaction. Therefore, only one of these reaction rate constants has to be determined. Spectroscopic measurements are used to determine the forward or backward reaction rate. Unfortunately, for certain chemical reactions, the accuracy is still very poor and uncertainties result in the calculation of wall heat flux in nonequilibrium flow.

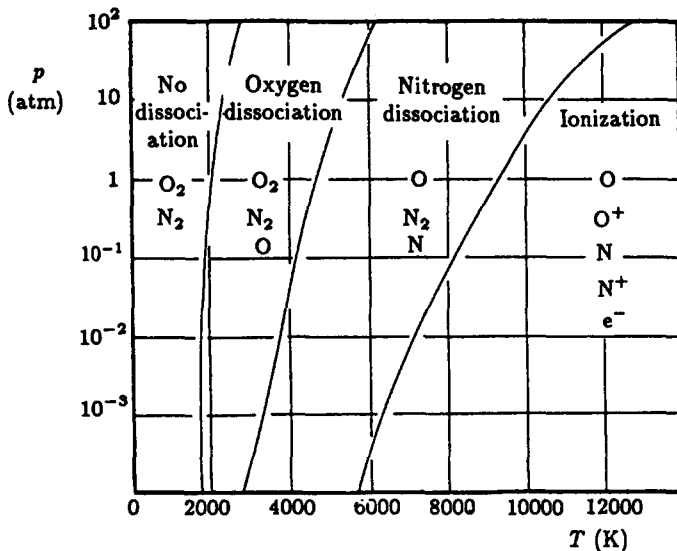
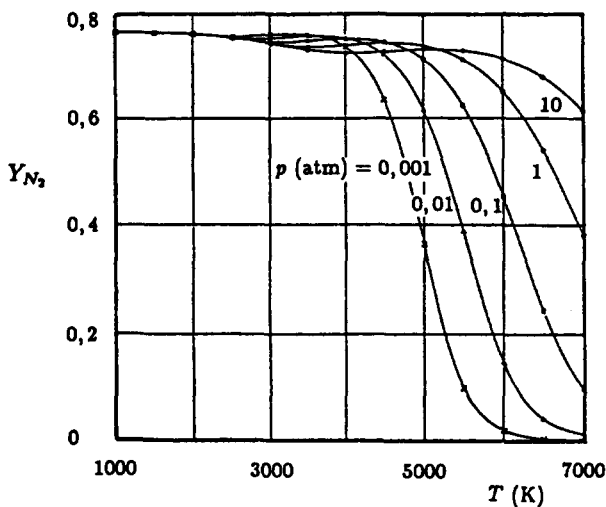
The state and composition of a gas mixture in chemical equilibrium are function of only two parameters: for example, the pressure and the temperature. The characteristics of the mixture can be determined using the following equations:

- (1) conservation of mass of each basic element (for example: air contains roughly 21% of oxygen and 79% of nitrogen);
- (2) law of mass action (or minimization of the Gibbs free energy);
- (3) conservation of electric charges (if ionization is present).

Figure 5 gives a global view of various chemical reactions in air for a wide range of pressure and temperature as calculated by Hansen.<sup>(82)</sup>

Figures 6–13 give results obtained in a range of temperature and of pressure without ionization: air is assumed to be composed of  $\text{N}_2$ ,  $\text{O}_2$ ,  $\text{N}$ ,  $\text{O}$ ,  $\text{NO}$ .<sup>(58)</sup>

For a given pressure and for an increasing temperature, dissociation of  $\text{O}_2$  occurs before dissociation of  $\text{N}_2$ ; dissociation of  $\text{N}_2$  occurs when dissociation of  $\text{O}_2$  is nearly complete

FIG. 5. Dissociation and ionization domains for air in chemical equilibrium.<sup>(82)</sup>FIG. 6. Mass fraction of N<sub>2</sub> for air in chemical equilibrium.<sup>(58)</sup>

(Figs 6–10). At a given temperature, the lower the pressure is, the more pronounced the dissociation is. The mass fraction of NO is always small but not negligible.

Figures 11–13 give the evolution of the reduced enthalpy  $h/R_0 T$  ( $R_0$  is the constant of non-dissociated air:  $R_0 = 287.1 \text{ J kg}^{-1} \text{ K}^{-1}$ ) and the evolution of the specific heat coefficients  $c_p$  (at constant pressure) and  $c_v$  (at constant volume). Let us emphasize once again that the specific heats are well defined quantities at equilibrium.

For temperatures below 2000 K, air behaves practically like a thermally perfect gas:  $c_p$  and  $c_v$  are function of  $T$  only.

The curves of  $h/R_0 T$  have two plateaux: the first one corresponds to the complete dissociation of O<sub>2</sub> and the second one to the complete dissociation of N<sub>2</sub>.

At a given pressure, the curves of  $c_p$  and  $c_v$  have two peaks where the slopes of the  $Y_{O_2}$ -curves and  $Y_{N_2}$ -curves are maximum.

It is important to note that the above described properties are valid at *chemical equilibrium*. In the case of nonequilibrium the state of the mixture depends on the history of the flow.

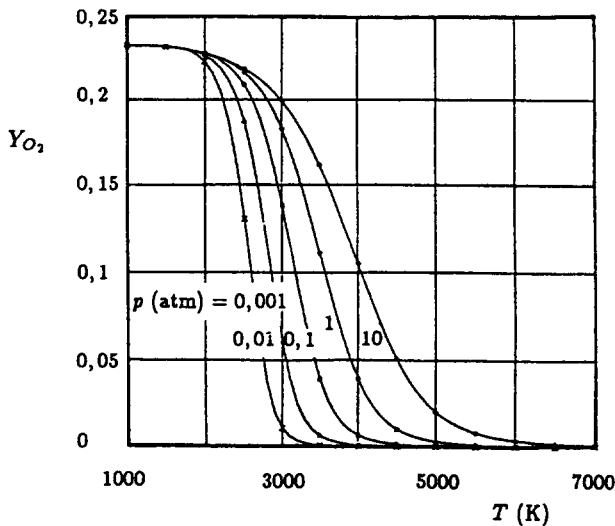


FIG. 7. Mass fraction of  $O_2$  for air in chemical equilibrium.<sup>(58)</sup>

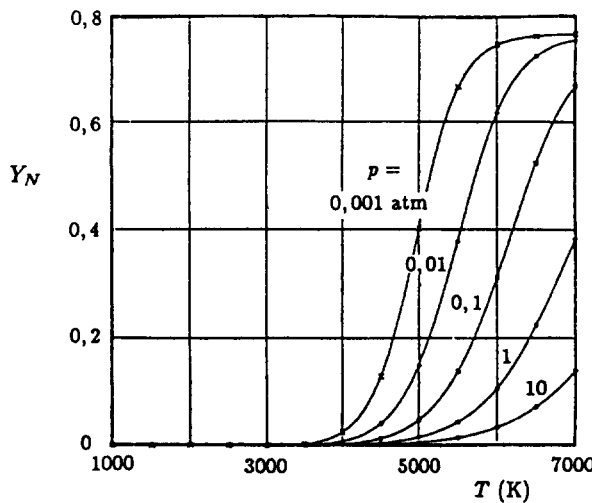


FIG. 8. Mass fraction of N for air in chemical equilibrium.<sup>(58)</sup>

## 2.6. FLOW EQUATIONS OF A GAS MIXTURE

The flow equations can be derived from kinetic theory. These developments and the equations can be found in the literature.<sup>(6,13,32,38,90,195)</sup>

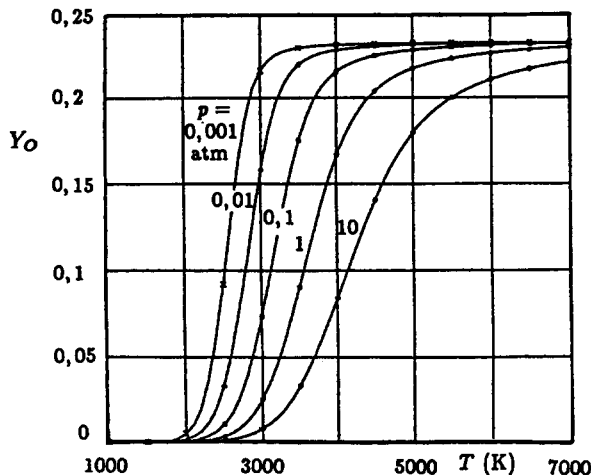
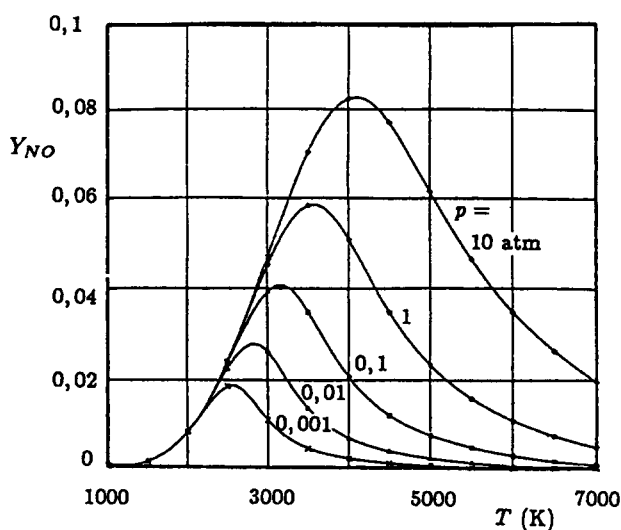
In this section, the equations are based on the following main hypotheses:

- The gas behaves like an ideal mixture of perfect gases.
- The trans-rotational energy is characterized by the temperature  $T$ .
- Vibrational and chemical nonequilibrium are possible.
- There are no radiative effects in the gas. The wall can emit or absorb energy by radiation.
- There are no external force effects (due to gravity or electric fields).
- The energy of the electronic mode is neglected.

### 2.6.1. Equation of State

The equation of state has already been discussed in Section 2.3.2. This equation is

$$p = \rho \frac{\mathcal{R}}{\mathcal{M}} T \quad (12)$$

FIG. 9. Mass fraction of O for air in chemical equilibrium.<sup>(58)</sup>FIG. 10. Mass fraction of NO for air in chemical equilibrium.<sup>(58)</sup>

with

$$\frac{1}{\mathcal{M}} = \sum_I \frac{Y_I}{\mathcal{M}_I}.$$

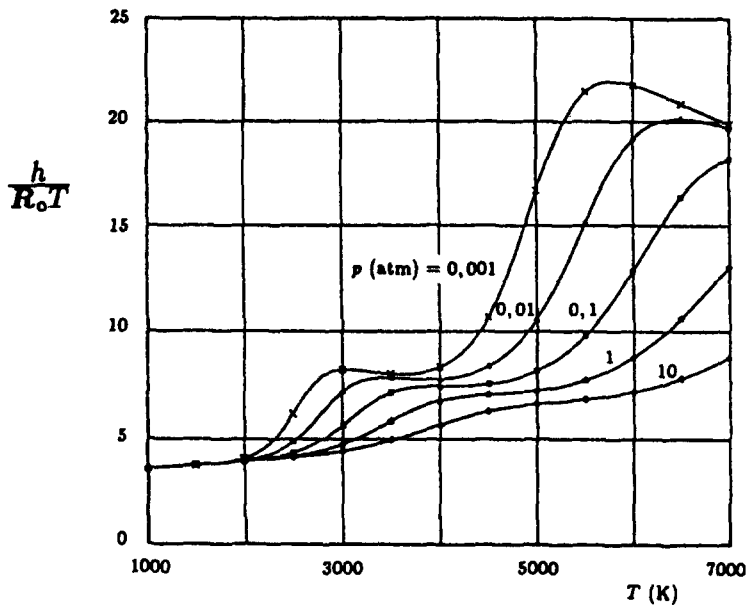
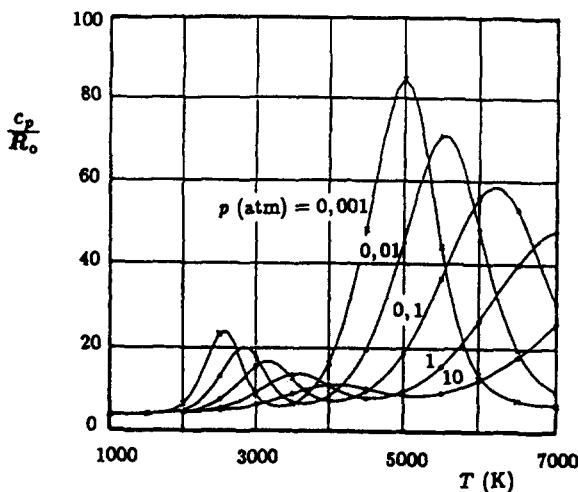
### 2.6.2. Species Equations and Continuity Equation

The variation of mass of each species due to chemical reactions is

$$\frac{\partial \rho_I}{\partial t} + \operatorname{div}(\rho_I u_I) = \dot{\omega}_I \quad (13)$$

where  $u_I$  is the average velocity of each species (Section 2.3.4) and  $\dot{\omega}_I$  is the production rate of species  $I$  due to all the chemical reactions "r" involving species  $I$

$$\dot{\omega}_I = \sum_r v_{Ir} \left( k_{fr} \prod_j N_j^{v_{jr}} - k_{br} \prod_j N_j^{v_{br}} \right) \mathcal{M}_I.$$

FIG. 11. Enthalpy vs temperature for air in chemical equilibrium.<sup>(58)</sup>FIG. 12. Specific heat coefficient  $c_p/R_o$  at constant pressure for air in chemical equilibrium.<sup>(58)</sup>

Using the definitions of the mass fractions and of the diffusion velocities, Eq. 13 becomes

$$\frac{\partial \rho Y_I}{\partial t} + \operatorname{div}(\rho Y_I(u_I^D + u)) = \dot{\omega}_I \quad (14)$$

or

$$\frac{\partial \rho Y_I}{\partial t} + \operatorname{div}(\rho Y_I u) = \dot{\omega}_I - \operatorname{div} q_I \quad (15)$$

where the *mass diffusion flux* of species  $I$  is defined as

$$q_I = \rho Y_I u_I^D = \rho_I u_I^D.$$

Equation 15 describes the evolution of the mass fraction of species  $I$  contained in a fluid particle during its displacement; the evolution of the mass fraction is due to chemical

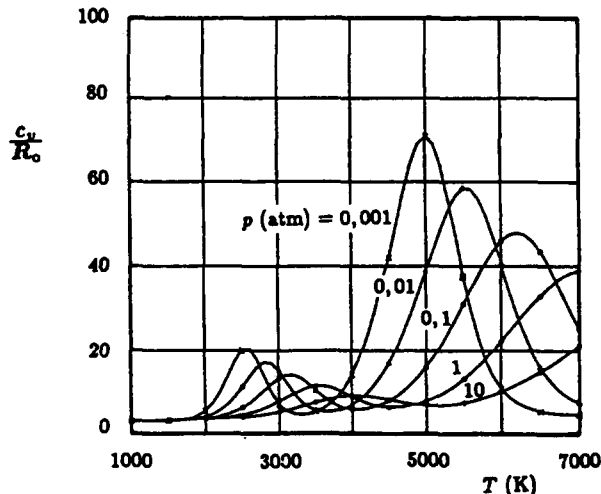


FIG. 13. Specific heat coefficient  $c_v/R_0$  at constant volume for air in chemical equilibrium.<sup>(58)</sup>

production and to mass diffusion phenomena. Here, a fluid particle, by definition, is displaced with the flow at the velocity  $u$ .

The conservation of the total mass implies that the production rate of the total mass is zero

$$\sum_I \dot{\omega}_I = 0$$

and by definition we have

$$\sum_I Y_I = 1; \quad \sum_I \mathbf{q}_I = 0.$$

The sum of Eq. 15 gives the equation of mass conservation or the *continuity equation*

$$\frac{\partial \rho}{\partial t} + \operatorname{div}(\rho \mathbf{u}) = 0. \quad (16)$$

Using this equation, the species equation can be written as

$$\frac{\partial Y_I}{\partial t} + \rho \mathbf{u} \cdot \operatorname{grad}(Y_I) = \dot{\omega}_I - \operatorname{div} \mathbf{q}_I. \quad (17)$$

In this form, Eq. 17 are not independent (their sum gives a trivial result  $0 = 0$ ). In a numerical method, according to the numerical scheme used, either one equation is discarded and all the round-off errors are accumulated on discarded species (usually, species with the higher mass fraction), or all equations are solved and the identity  $\sum_I Y_I = 1$  is forced.

In the species equations, the mass diffusion flux needs to be modelled. To a first approximation, the influence of the vibrational nonequilibrium is neglected and, from the gas kinetic theory, we have

$$\begin{aligned} \mathbf{q}_I &= \rho \sum_{J \neq I} \frac{M_I M_J}{M^2} D_{IJ} d_J - D_I^T \frac{1}{T} \operatorname{grad} T \\ d_I &= \operatorname{grad} \frac{N_I}{N} + \left( \frac{N_I}{N} - \frac{\rho_I}{\rho} \right) \frac{1}{p} \operatorname{grad} p \end{aligned}$$

where  $D_{IJ}$  and  $D_I^T$  are, respectively, the multicomponent and thermal diffusion coefficients. These coefficients can be calculated, at least theoretically, from a model describing the intermolecular forces (for example, the Lennard-Jones potential). Generally, the effect of

thermal diffusion (known as the Soret effect) is very small and is neglected. The effects of the pressure gradient term are also generally small; for boundary layer calculations this term is usually neglected.

For a binary mixture of species *A* and *B*, a simpler expression is available according to Fick's law

$$\mathbf{q}_A = -\mathbf{q}_B = -\rho \mathcal{D}_{AB} \mathbf{grad}(Y_A)$$

where  $\mathcal{D}_{AB}$  is the binary diffusion coefficient given by

$$\mathcal{D}_{AB} = \frac{3}{16} \frac{\sqrt{4\pi N_A k_B^3 T^3 \left( \frac{M_A + M_B}{2M_A M_B} \right)}}{\pi p (\sigma_{AB})^2 \Omega_{AB}^{(1,1)*}}.$$

In this equation,  $\sigma_{AB}$  is a molecular potential energy parameter and the quantity  $\Omega_{AB}^{(1,1)*}$  is a collision integral. Tabulated values of functions involved in the expression of the diffusion coefficient can be found in the literature.<sup>(3,21,90)</sup>

For a multicomponent gas, Fick's law can still be used as<sup>(3)</sup>

$$\mathbf{q}_I = -\rho \mathcal{D}_I^m \mathbf{grad}(Y_I)$$

with

$$\mathcal{D}_I^m = \frac{1 - X_I}{\sum_J \frac{X_J}{\mathcal{D}_{IJ}}}.$$

Another possible expression of the mass diffusion fluxes is<sup>(91)</sup>

$$\mathbf{q}_I = -\rho \frac{M_I}{M} \mathcal{D}_I^m \mathbf{grad}(X_I)$$

where the multicomponent diffusion coefficient  $\mathcal{D}_I^m$  is related to binary diffusion coefficient by the following approximate formula

$$\mathcal{D}_I^m = \frac{1 - Y_I}{\sum_{J \neq I} \frac{X_J}{\mathcal{D}_{IJ}}}.$$

Let us note that with the above expressions, the identity  $\sum_I \mathbf{q}_I = 0$  is not satisfied. A possible solution is to correct the mass diffusion flux as follows<sup>(42)</sup>

$$\mathbf{q}_I^* = \mathbf{q}_I - Y_I \sum_I \mathbf{q}_I$$

which implies

$$\sum_I \mathbf{q}_I^* = 0.$$

### 2.6.3. Momentum Equation

Neglecting external force fields (such as gravitation or electric forces due to ionization), the momentum equation reads

$$\rho \frac{\partial \mathbf{u}}{\partial t} + (\mathbf{grad} \mathbf{u}) \cdot \rho \mathbf{u} = \operatorname{div} [ -p \underline{\delta} + \underline{\tau}] \quad (18)$$

where  $p$  is the pressure and  $\underline{\tau}$  is the viscous stress tensor. The tensor  $\underline{\delta}$  is the second order identity tensor.

The momentum equation can be obtained by evaluating the statistical fluxes of momentum across a surface. The quantity  $[p\underline{\delta} - \underline{\tau}]$  is the thermal momentum flux, i.e. the flux

calculated from the thermal velocities of particles (the velocity seen by an observer moving with the flow velocity). The pressure is the average of the normal components of the thermal momentum flux and is related to the average kinetic energy of the particles.

Formally, the momentum equation is the same for a nonequilibrium flow as for the flow of a simple gas.

The viscous stress tensor is expressed by the kinetic theory from the Boltzmann equation as

$$\tau = \mu(\mathbf{grad} \mathbf{u} + ' \mathbf{grad} \mathbf{u} - \frac{2}{3} \delta \operatorname{div} \mathbf{u}) + \eta \delta \operatorname{div} \mathbf{u}.$$

In this formula,  $\mu$  and  $\eta$  are the viscosity and bulk viscosity coefficients and ' $\mathbf{grad}$ ' denotes the transpose of the operator  $\mathbf{grad}$ .

Generally, the bulk viscosity coefficient is assumed to be zero, according to Stokes' hypothesis. The viscosity coefficient  $\mu$  can be expressed as a function of the viscosities  $\mu_I$  of the individual species by means of a mixture rule.<sup>(90)</sup> A simplified form is provided using Wilke's rule<sup>(200)</sup>

$$\mu = \sum_I \frac{X_I \mu_I}{\sum_J X_J \phi_{IJ}}$$

with

$$\phi_{IJ} = \frac{1}{\sqrt{8}} \left( 1 + \frac{\mathcal{M}_I}{\mathcal{M}_J} \right)^{-1/2} \left[ 1 + \left( \frac{\mu_I}{\mu_J} \right)^{1/2} \left( \frac{\mathcal{M}_J}{\mathcal{M}_I} \right)^{1/4} \right]^2.$$

For a pure gas, the viscosity coefficient is given by

$$\mu_I = \frac{5}{16} \frac{\sqrt{\pi \mathcal{M}_I k_B T / \mathcal{N}_A}}{\pi \sigma_{II}^2 \Omega_{II}^{(2,2)*}}$$

where  $\sigma_{II}$  is the collision diameter and  $\Omega_{II}^{(2,2)*}$  is a collision integral for which tabulated values can be found in the literature.<sup>(3,21,90)</sup>

#### 2.6.4. Vibrational Rate Equation

The equation for the evolution of the sensible vibrational energy of a species has the general form of a conservation equation which expresses the variation of the vibrational energy due to production and diffusion terms

$$\rho \frac{\partial}{\partial t} [Y_I(e_{\text{vib}})_{\text{sens}, I}] + \rho \mathbf{u} \cdot \mathbf{grad} [Y_I(e_{\text{vib}})_{\text{sens}, I}] = \dot{\omega}_{\text{vib}, I} - \operatorname{div} [\mathbf{q}_I(e_{\text{vib}})_{\text{sens}, I} + \mathbf{q}_{\text{vib}, I}]. \quad (19)$$

This equation includes the relaxation effect (the first term on the right hand side), the transport of vibrational energy by mass diffusion (the second term on the right hand side) and by heat conduction (the third term on the right hand side).

The relaxation effect is expressed as discussed in Section 2.4

$$\dot{\omega}_{\text{vib}, I} = \frac{\rho Y_I}{\tau_I} [(e_{\text{vib}}^{\text{eq}})_{\text{sens}, I} - (e_{\text{vib}})_{\text{sens}, I}].$$

The transport by mass diffusion is modelled according to the expressions given in Section 2.6.2.

The vibrational heat flux can be expressed by Fourier's law

$$\mathbf{q}_{\text{vib}, I} = - Y_I \lambda_{\text{vib}, I} \mathbf{grad} T_{\text{vib}, I}.$$

In this relation  $\lambda_{\text{vib}, I}$  is the *vibrational thermal conductivity* and  $T_{\text{vib}, I}$  is the vibrational temperature defined by Eq. 4.

The vibrational thermal conductivity is related to the viscosity  $\mu_I$  of species  $I$  by Eucken's relation

$$\lambda_{\text{vib},I} = \mu_I c_{v\text{ vib},I} \quad (20)$$

where the specific heat  $c_{v\text{ vib},I}$  is calculated by using Eq. 4 as

$$c_{v\text{ vib},I} = \frac{d(e_{\text{vib}})_{\text{sens},I}}{dT_{\text{vib},I}}$$

### 2.6.5. Energy Equation

Let us recall that the internal energy is decomposed as follows

$$e = (e_{\text{trans}})_{\text{sens}} + (e_{\text{rot}})_{\text{sens}} + (e_{\text{vib}})_{\text{sens}} + (e_{\text{el}})_{\text{sens}} + (\Delta h_f)^0$$

and

$$e = \sum_I Y_I e_I.$$

Based on our assumptions, the trans-rotational energy is characterized by the temperature  $T$  and is expressed by the following relations:

- for monatomic species:

$$(e_{\text{tr-rot}})_{\text{sens},I} = (e_{\text{trans}})_{\text{sens},I} = \frac{3}{2} \frac{\mathcal{R}}{\mathcal{M}_I} T$$

- for diatomic species:

$$(e_{\text{tr-rot}})_{\text{sens},I} = (e_{\text{trans}})_{\text{sens},I} + (e_{\text{rot}})_{\text{sens},I} = \frac{5}{2} \frac{\mathcal{R}}{\mathcal{M}_I} T.$$

The vibrational energy is calculated using Eq. 19. Since the electronic mode is neglected, the calculation of the evolution of the energy  $e$  has yet to be determined.

Neglecting the effects of external forces, the equation for the internal energy has the standard general form

$$\rho \frac{\partial e}{\partial t} + \rho \mathbf{u} \cdot \mathbf{grad} e = - p \text{div } \mathbf{u} - \text{div} \mathbf{q}_t + \Phi_D \quad (21)$$

where  $\mathbf{q}_t$  is the energy flux and  $\Phi_D$  is the viscous dissipation, i.e. the deformation work of viscous stresses

$$\Phi_D = \mathbf{I} : \mathbf{grad} \mathbf{u}.$$

The energy equation can also be expressed for the enthalpy  $h = e + p/\rho$  as

$$\rho \frac{\partial h}{\partial t} + \rho \mathbf{u} \cdot \mathbf{grad} h = \frac{\partial p}{\partial t} + \mathbf{u} \cdot \mathbf{grad} p - \text{div} \mathbf{q}_t + \Phi_D. \quad (22)$$

The energy equation can be obtained by evaluating the statistical flux of energy across a surface. The flux of energy is due to the thermal flux of kinetic and internal energies.

Let us note that the energy equation does not display explicitly the heat of reactions (the energy exchange due to chemical reactions). In fact, this contribution is taken into account in the definition of the enthalpy via the heat of formation. The heats of reaction would appear explicitly by writing the energy equation for the sensible enthalpy.

The flux of energy is given by kinetic theory as

$$\mathbf{q}_t = \mathbf{q}_{th} = \sum_I h_I \mathbf{q}_I + \mathcal{R} T \sum_I \sum_J \frac{N_J}{N} \frac{1}{\mathcal{M}_I \mathcal{D}_{IJ}} \left( \frac{\mathbf{q}_I}{\rho_I} - \frac{\mathbf{q}_J}{\rho_J} \right). \quad (23)$$

The first term in expression 23 of the flux of energy represents the transport by conduction due to the translational, rotational and vibrational modes. The second term in

Eq. 23 represents the transport by mass diffusion. The third term is a coupling between mass and thermal diffusions: this term is known as the Dufour effect and is generally neglected. The coefficient  $\mathcal{D}_I^T$  is the same as in the term representing the Soret effect (Section 2.6.2). In Eq. 23,  $\mathcal{D}_{IJ}$  is the binary diffusion coefficient, i.e. the diffusion coefficient of species  $I$  in species  $J$  for a mixture consisting of only these two species.

In Eq. 23, the radiative effects in the gas are neglected; these effects would appear as an additional term  $\mathbf{q}_R$  in the expression of  $\mathbf{q}_t$ . Neglecting the radiative effects is valid below a temperature of 10,000 K. However, at temperatures below 10,000 K, the effects of *wall radiation* can be significant and must be taken into account in the calculation of the wall heating. For temperatures below 10,000 K the assumption is made that the energy radiated by the wall is not absorbed by the fluid; it is also assumed that the fluid does not emit or absorb any radiated energy ( $\mathbf{q}_R = 0$ ).

Assuming the *vibrational equilibrium* of species, the thermal heat flux is expressed as

$$\mathbf{q}_{th} = -\lambda \mathbf{grad} T.$$

The thermal conductivity coefficient  $\lambda$  can be expressed as a function of the coefficients  $\lambda_I$  of individual species by means of a mixture rule. As for the viscosity, Wilke's rule is

$$\lambda = \sum_I \frac{X_I \lambda_I}{\sum_J X_J \psi_{IJ}} \quad (24)$$

with

$$\psi_{IJ} = \frac{1}{\sqrt{8}} \left( 1 + \frac{\mathcal{M}_I}{\mathcal{M}_J} \right)^{-1/2} \left[ 1 + \left( \frac{\lambda_I}{\lambda_J} \right)^{1/2} \left( \frac{\mathcal{M}_J}{\mathcal{M}_I} \right)^{1/4} \right]^2.$$

For a monatomic gas, the thermal conductivity coefficient is<sup>(90)</sup>

$$\lambda_I = \frac{5}{2} \mu_I c_{v \text{ trans}, I}$$

with

$$c_{v \text{ trans}, I} = \frac{de_{\text{trans}, I}}{dT} = \frac{3 \mathcal{R}}{2 \mathcal{M}_I}.$$

For a diatomic or polyatomic gas, the coefficient of thermal conductivity can be related to the coefficient of viscosity by means of Eucken's relation. According to the decomposition of the internal energy

$$e_I = (e_{\text{trans}})_{\text{sens}, I} + (e_{\text{rot}})_{\text{sens}, I} + (e_{\text{vib}})_{\text{sens}, I} + (e_{\text{el}})_{\text{sens}, I} + (\Delta h_f)_I^0$$

and, if thermodynamic equilibrium is assumed, the specific heat of species  $I$  at constant volume is

$$c_{vI} = c_{v \text{ trans}, I} + c_{v \text{ rot}, I} + c_{v \text{ vib}, I} + c_{v \text{ el}, I}.$$

Eucken's method expresses the thermal conductivity coefficient as follows

$$\lambda_I = \mu_I (\frac{5}{2} c_{v \text{ trans}, I} + c_{v \text{ rot}, I} + c_{v \text{ vib}, I} + c_{v \text{ el}, I}).$$

With *vibrational nonequilibrium*, the thermal heat flux is expressed by

$$\mathbf{q}_{th} = -\lambda_{\text{trans, rot}} \mathbf{grad} T + \sum_I \mathbf{q}_{\text{vib}, I}. \quad (25)$$

The vibrational heat fluxes  $\mathbf{q}_{\text{vib}, I}$  have already been discussed in Section 2.6.4.

A first approximation of the transport coefficient  $\lambda_{\text{trans, rot}}$  is

$$\lambda_{\text{trans, rot}} = \lambda(T) - \sum_I Y_I \lambda_{\text{vib}, I}$$

where  $\lambda_{\text{vib},I}$  is calculated from Eq. 20

$$\lambda_{\text{vib},I} = \mu_I c_{\nu, \text{vib},I} = \mu_I \frac{d(e_{\text{vib}})_{\text{sens},I}}{dT_{\text{vib},I}}$$

and  $\lambda$  is calculated from a mixture law such as Eq. 24, at temperature  $T$ .

### 3. LAMINAR BOUNDARY LAYERS

Laminar boundary layers are first addressed since the maximum heat loads during the re-entry occur in the laminar regime. Only chemical non-equilibrium will be accounted for as thermal relaxation is assumed to be more rapid and to occur between the shock wave and the outer edge of the boundary layer. Turbulent boundary layers, which appear at the end of the re-entry, will be addressed in Section 6.

#### 3.1. BOUNDARY LAYER EQUATIONS

Boundary layer equations can be deduced from the complete flow equations presented in Section 2. For two-dimensional, plane or axisymmetric flows, the boundary layer equations read, with  $x$  along the body,  $y$  along the normal,  $u$  and  $v$  the velocity components in these two directions:

- State equation

$$p = \rho \frac{\mathcal{R}}{M} T. \quad (26)$$

- Continuity equation

$$\frac{\partial \rho}{\partial t} + \frac{1}{R^j} \frac{\partial \rho u R^j}{\partial x} + \frac{\partial \rho v}{\partial y} = 0. \quad (27)$$

This form holds either for plane ( $j = 0$ ) or for axisymmetric flows ( $j = 1$ ).  $R$  is the distance of a point of the wall to the body axis in axisymmetric flow as shown on Fig. 14.

- Species equations

$$\rho \frac{\partial Y_I}{\partial t} + \rho u \frac{\partial Y_I}{\partial x} + \rho u \frac{\partial Y_I}{\partial y} = \dot{\omega}_I - \frac{\partial q_{Iy}}{\partial y} \quad (28)$$

$$q_{Iy} = \sum_{J \neq I} \rho \frac{M_I M_J}{M^2} D_{IJ} \frac{\partial}{\partial y} \left( \frac{N_J}{N} \right) - \frac{D_I^T}{T} \frac{\partial T}{\partial y}.$$

- Momentum equations

$$\rho \frac{\partial u}{\partial t} + \rho u \frac{\partial u}{\partial x} + \rho v \frac{\partial u}{\partial y} = - \frac{\partial p}{\partial x} + \frac{\partial \tau}{\partial y}; \quad \tau = \mu \frac{\partial u}{\partial y} \quad (29)$$

$$0 = \frac{\partial p}{\partial y}. \quad (30)$$

- Energy equation for the enthalpy

$$\rho \frac{\partial h}{\partial t} + \rho u \frac{\partial h}{\partial x} + \rho v \frac{\partial h}{\partial y} = - \frac{\partial q_{ty}}{\partial y} + \frac{\partial p}{\partial t} + u \frac{\partial p}{\partial x} + \mu \left( \frac{\partial u}{\partial y} \right)^2 \quad (31)$$

$$q_{ty} = - \lambda \frac{\partial T}{\partial y} \sum_I q_{Iy} h_I + \mathcal{R} T \sum_I \sum_J \frac{N_J}{N} \frac{1}{M_I} \frac{D_I^T}{\mathcal{D}_{IJ}} \left( \frac{q_{Iy}}{\rho_I} - \frac{q_{Jy}}{\rho_J} \right).$$

Or, using the stagnation enthalpy  $H = h + \frac{u^2}{2}$ , the energy equation reads

$$\rho \frac{\partial H}{\partial t} + \rho u \frac{\partial H}{\partial x} + \rho v \frac{\partial H}{\partial y} = \frac{\partial p}{\partial t} + \frac{\partial}{\partial y} (u \tau - q_{ty}). \quad (32)$$

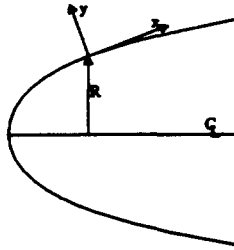


FIG. 14. Reference frame for the boundary layer approach.

For three-dimensional flows, the boundary layer equations are similar to Eqs 26–32 with now two momentum equations along directions parallel to the wall, a more complex form of the advection term in the species, momentum and energy equations and a modification of the source term in the energy equation. The final form of the equations strongly depends upon the choice of a surface coordinate system. Readers are referred to Ref. 89 for a discussion of surface coordinate systems and to Ref. 27 for an example of three-dimensional boundary layer equation set.

### 3.2. BOUNDARY CONDITIONS

The boundary layer equations form a set of parabolic equations which can be integrated marching along the body once initial and boundary conditions have been prescribed.

For two-dimensional flows, boundary layer profiles at the initial station and boundary conditions at the wall and at the outer edge of the boundary layer are required.

For three-dimensional boundary layers, information diffuses along the normal to the wall and is advected downstream by all the streamlines crossing this wall normal. A given point influences a large downstream domain. Therefore, boundary layer profiles should be prescribed everywhere flow enters the computation domain.

#### 3.2.1. Boundary Conditions at the Wall

If the velocity slip is neglected, the velocity is null at the wall. If the temperature jump is neglected, the fluid temperature can either be prescribed equal to the imposed wall temperature, or determined from an imposed wall heat flux. The heat flux the wall is submitted to is the sum of the convective heat flux  $q_{t,y_w}$  due to the boundary layer flow and other sources or sinks, mainly radiation effects. The gas radiation can be neglected so that the global flux is the difference between the convective flux due to the boundary layer and the wall radiation

$$\Phi = q_{t,y_w} - \varepsilon\sigma T_w^4 \quad (33)$$

where  $\varepsilon$  is the wall emissivity factor and  $\sigma$  the Stefan–Boltzmann constant ( $\sigma = 5.67 \cdot 10^{-8} \text{ W m}^{-2} \text{ K}^{-4}$ ). It has been observed during a long period in the space shuttle re-entry that the wall temperature remains constant, i.e. if heat conduction inside the wall is neglected, this flux is null. This is known as *radiative equilibrium* when the radiated flux balances the boundary layer flux. When radiative equilibrium is imposed as boundary condition, both the wall temperature and the convective flux are results of the computation.

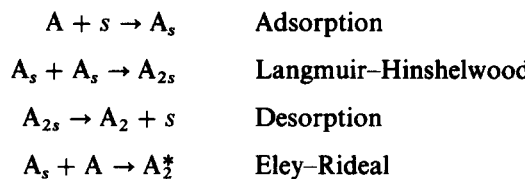
The wall boundary conditions for the species equations reflect the interactions between the gas and the surface material which can act as a catalyst and promote chemical reactions at the interface. As the wall temperature is moderate ( $T_w < 1500 \text{ K}$ ), chemical reactions will tend to recombine atoms at the wall. The heterogeneous catalysis phenomenon includes the following steps:

- Atoms which diffuse towards the surface may be adsorbed at the surface. This first step depends upon both the impinging atom and the surface: this is the surface selectivity. For

example, metal surfaces can easily adsorb oxygen atoms while metal oxide surfaces are more reluctant to adsorb oxygen.

- In the Langmuir–Hinshelwood process, an atom adsorbed in a site of the surface reacts with another atom adsorbed in another site. The wall atoms the adsorbed atoms are bound with act as third bodies as they dissipate the excess energy for the recombination reaction.
- The last step in the Langmuir–Hinshelwood process is the desorption of the molecule from the wall, the surface site is now free and the process can occur again.
- In the Eley–Rideal process, atoms adsorbed in a site of the surface react by collision with a free atom in the gas. The so-formed molecule is in an excited state and quickly leaves the surface. The excess energy of the molecule is however eventually transmitted to the wall by quenching in the wall region.

These various steps can be written as chemical reactions where  $s$  denotes a site and \* an excited state.



Goulard<sup>(79)</sup> has proposed to model the wall catalysis with the help of an Arrhenius law. The flux of atoms at the wall due to catalysis is expressed as

$$q_{I\text{ cat}} = k_{Iw}(\rho_w Y_{Iw})^m \quad (34)$$

where the subscript  $w$  indicates wall values and the reaction order  $m$  should be between one and two. Scott<sup>(169)</sup> assumes the reaction order to be equal to one, the reaction rate constant  $k_{Iw}$  has thus the dimension of a velocity.

When the coefficients  $k_{Iw}$  tend towards zero, the species are not modified at the wall. The wall is thus said to be *non-catalytic*. On the contrary, when the coefficients tend towards infinity, the atoms impinging the wall recombine very quickly. The wall is said to be *catalytic*. As the atom dissociation energy is transferred at the wall, wall catalytic efficiency increases the wall heat flux. The non-catalytic and catalytic wall cases are extreme cases which are not encountered practically; real materials have a *finite catalytic efficiency*.

Concerning ionized species, it is taken for granted that they are neutralized at the wall, whatever the wall catalytic efficiency.

The boundary condition at the wall expresses that the species diffusion flux at the wall must balance the flux due to chemical reactions at the interface in a steady state regime

$$q_{Iy_w} = q_{I\text{ cat}} \quad (35)$$

where the flux  $q_{I\text{ cat}}$  is given by Eq. 34 for atoms. Extra relations can be deduced from the fact that interface reactions do not create or destroy chemical elements so that the flux of chemical elements is null at the wall. For air dissociation problems, only five species ( $N_2, O_2, NO, N, O$ ) are taken into account. This yields two element conservation relations for nitrogen and oxygen. Therefore, only three interface reaction rates are independent. It is usually assumed that nitrogen monoxide is not modified at the interface, and only the interface reaction rates for atomic nitrogen and oxygen are specified. For a catalytic wall, it is possible to impose either complete atom recombination with no modification of the nitrogen monoxide or chemical equilibrium at the wall. This is discussed at length in Ref. 170.

### 3.2.2. Boundary Conditions at the Boundary Layer Outer Edge

The flow outside of the boundary layer must match with the inviscid flow solution at the wall. Outside of the boundary layer, where all gradients along the wall normal vanish, the species (28), momentum (29) and energy (31) equations reduce to their inviscid form at the

wall. The outer pressure, velocity, temperature and species distributions could be imposed as the solution at the wall of an inviscid flow calculation.

It must be pointed out that the inviscid solution at the stagnation point is in thermal and chemical equilibrium as the flow velocity is locally zero and the mean motion time scale is therefore infinite. According to the matching principle, the flow outside the boundary layer must be at equilibrium *at the stagnation point*. It is therefore expected that thermal non-equilibrium will be weaker than chemical non-equilibrium in the boundary layer and can be neglected.

### 3.3. THE ATOM/MOLECULE APPROXIMATION

The atom/molecule approximation was a convenient way to simplify computations of dissociated air. As it has been used in some important references, it will be quickly introduced.

As can be seen from Figs 6–10, oxygen dissociation is almost complete when nitrogen dissociation starts to proceed. Moreover, only small amounts of nitrogen monoxide are observed. The gas is roughly a mixture of molecular nitrogen, atomic and molecular oxygen at “low” temperatures; of atomic oxygen, atomic and molecular nitrogen at “high” temperatures. Moreover, oxygen and nitrogen have similar molar masses, transport and thermodynamical properties. The problem can be simplified by considering a mixture of only two species: atoms  $A$  and molecules  $A_2$ .

#### 3.3.1. Basic Relations

The following relationships can easily be checked

- $M_{A_2} = 2M_A$ .
- $Y_{A_2} = 1 - Y_A$  so that most of the following variables will be expressed in terms of  $Y_A$ .
- The mixture pressure reads

$$p = p_A + p_{A_2} = (1 + Y_A) \rho \frac{\mathcal{R}}{M_{A_2}} T = Z \rho R_0 T \quad \text{where } Z = 1 + Y_A; \quad R_0 = \frac{\mathcal{R}}{M_{A_2}}. \quad (36)$$

- Since  $C_{PA} \sim C_{PA_2}$ , the mixture enthalpy reads

$$h = h_{A_2} + Y_A h_A^0 + Y_A \int_0^T (C_{PA} - C_{PA_2}) dT \sim h_{A_2} + Y_A h_A^0. \quad (37)$$

#### 3.3.2. Chemistry

The chemistry of the atom/molecule mixture can be represented with a single chemical reaction



where the third body  $M$  stands for both the molecule  $A_2$  and the atom  $A$ .

#### 3.3.3. Transport

For a binary mixture, the mass diffusion can be represented with the help of a Fick law provided thermal diffusion effects are negligible and pressure gradients are small. The transport properties of the mixture are thus usually represented by assuming constant Prandtl ( $\mathcal{P} = \frac{\mu C_{PF}}{\lambda}$ ) and Lewis ( $\mathcal{L} = \frac{\rho D C_{PF}}{\lambda}$ ) numbers. The Sutherland law is sometimes used to compute the viscosity, as it leads to about 10% error for chemical equilibrium air.<sup>(66)</sup>

The various fluxes thus read

$$q_A = -\rho D \mathbf{grad} Y_A; \quad \rho D = \frac{\mathcal{L}}{\varphi} \mu \quad (39)$$

$$\tau = p\dot{\varphi} - \mu \left( \mathbf{grad} u + ' \mathbf{grad} u - \frac{2}{3} \dot{\varphi} \operatorname{div} u \right) - \eta \operatorname{div} u \quad (40)$$

$$q_t = -\frac{\mu}{\varphi} (\mathbf{grad} h + (\mathcal{L} - 1)(h_A - h_{A_2}) \mathbf{grad} Y_A) \quad \text{with } h_A - h_{A_2} \sim h_A^0. \quad (41)$$

It must be pointed out that this model is however a very crude one which requires some tuning to give good results according to the considered range of temperature. The formation enthalpies are different as  $h_N^0 \sim 2h_O^0$  as well as the reaction rate coefficients for oxygen and nitrogen dissociations.

### 3.4. TWO-DIMENSIONAL STAGNATION POINT SOLUTIONS FOR ATOM/MOLECULE APPROACH

#### 3.4.1. Fay–Riddell Solutions

As heat transfer is often maximum at the stagnation point, axisymmetric stagnation point solutions were investigated by Fay and Riddell<sup>(66)</sup> using an atom/molecule approach. The boundary layer equations were transformed with the help of the Levy–Lees–Dorodnitsyn space coordinate transformation<sup>(53)</sup>

$$\xi = \int_0^x \rho_w \mu_w u_e R^2 dx; \quad \eta = \frac{Ru_e}{\sqrt{2\xi}} \int_0^y \rho dy \quad (42)$$

where  $u_e$  is the velocity outside the boundary layer. With this set of space variables, the boundary layer equations are written for the reduced velocity  $f' = \frac{u}{u_e}$ , enthalpy  $S = \frac{H}{H_e}$  and

mass fraction  $Z_A = \frac{C_A}{C_{Ae}}$  profiles. Self similar solutions can be obtained at the stagnation point, and the boundary layer equations reduce to a set of coupled ordinary differential equations.

A reaction rate  $k_0 \sim T^{1.5}$  was used and both frozen and equilibrium flows were also investigated.

All the results presented herein are for the same conditions, i.e. a Lewis number of 1.4, a Prandtl number of 0.71, a wall temperature of 300 K and a wall enthalpy/external enthalpy ratio of 0.0123.

Along the stagnation line, only the velocity component normal to the wall is not null, the species mass fraction profiles thus result from a balance between advection towards the wall, chemistry and diffusion. The atom mass fraction profiles for a frozen flow on a catalytic wall are given on Fig. 15. For a frozen flow on a non-catalytic wall, the atom mass fraction is constant throughout the boundary layer and equal to the external value. The wall catalytic efficiency modifies the boundary condition at the wall and strongly affects the whole atom mass fraction profile.

The wall heat flux is also affected by the wall catalysis. From a study over a wide range of altitudes from 7.5 to 36 km and velocities from 1.8 to 7 km s<sup>-1</sup>, and for different values of the Prandtl and Lewis numbers, Fay and Riddell proposed fits for the wall heat flux as

$$\frac{\Phi_w}{h_w - H_e} = A \left( 1 + [\mathcal{L}^{0.52} - 1] \frac{h_{De}}{H_e} \right) \quad \text{Chemical equilibrium flow}$$

$$\frac{\Phi_w}{h_w - H_e} = A \left( 1 + [\mathcal{L}^{0.63} - 1] \frac{h_{De}}{H_e} \right) \quad \text{Frozen flow—Catalytic wall}$$

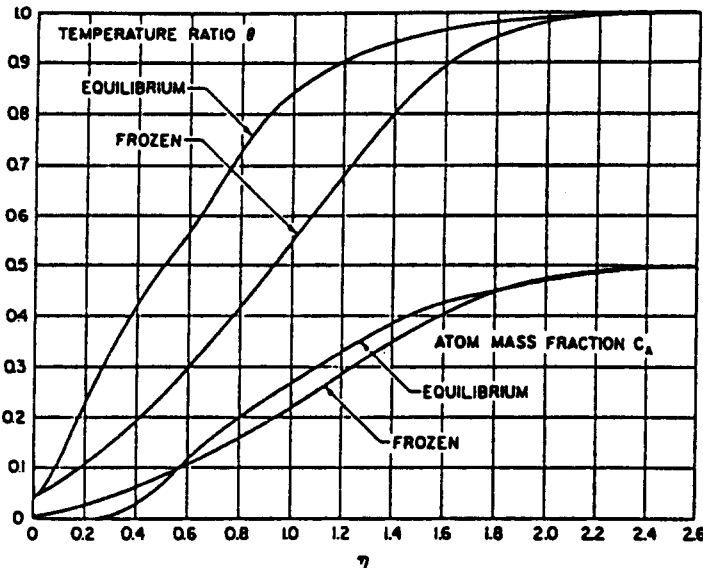


FIG. 15. Temperature and atom mass fraction profiles for frozen and equilibrium flows (from Ref. 66).

$$\frac{\Phi_w}{h_w - H_e} = A \left( 1 - \frac{h_{De}}{H_e} \right) \quad \text{Frozen flow—Non-catalytic wall}$$

$$\text{with } A = 0.76 \left( \frac{\rho_e \mu_e}{\rho_w \mu_w} \right)^{0.4} \frac{1}{\mathcal{P}} \sqrt{\rho_w \mu_w \left( \frac{du_e}{dx} \right)_0}$$

where the subscript 0 indicates values at the stagnation point and  $h_{De}$  is the dissociation enthalpy per mass unit, i.e. the atom formation enthalpy times their mass fraction.

These formulae bring into evidence the influence of wall catalysis upon heat flux. Atoms diffuse towards the wall and, for a catalytic wall, recombine and release their formation energy. This leads to a higher wall heat flux for the catalytic wall. As the wall heat flux can be expressed as

$$\Phi_w = -\lambda \frac{\partial T}{\partial y} - \rho D(h_A - h_{A_2}) \frac{\partial Y_A}{\partial y} \quad (43)$$

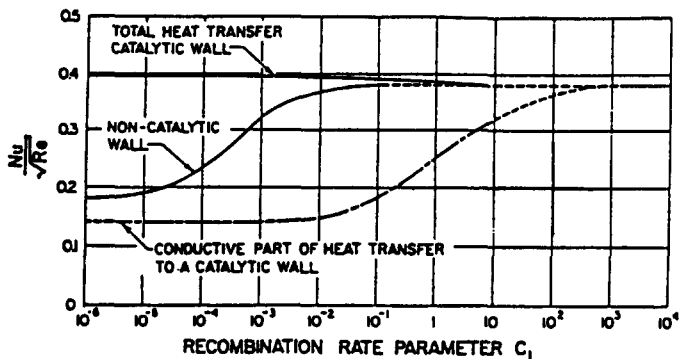
the flux on a non-catalytic wall is only due to the temperature gradient while both terms intervene for a catalytic wall. The contribution of both terms is given in Fig. 16 in which the frozen flow corresponds to a zero recombination rate parameter.

The larger the recombination rate parameter, the more atoms recombine in the boundary layer as shown in Fig. 17. On a non-catalytic wall, as the recombination rate increases, more atoms recombine in the boundary layer in the cold region close to the wall and release their formation energy so that the wall heat flux increases.

### 3.4.2. Goulard's Extension to Finite Catalysis

The study of frozen flow axisymmetric stagnation point was extended by Goulard<sup>(79)</sup> to account for finite catalytic recombination rate at the wall. Figure 18 shows the influence of finite wall catalytic efficiency and flight velocity upon the stagnation point heat flux for a sphere of 1 m diameter at 76 km altitude.

In order to compare the different cases, the wall heat flux is presented in reduced form, divided by its value for a catalytic wall. The faster the wall recombination, i.e. the more catalytic the wall, the higher the heat flux as more atoms can recombine at the wall and release their formation enthalpy. As the velocity increases, the gas is more and more



$$\frac{N_u}{\sqrt{Re}} = \frac{-\Phi_w P}{(h_w - H_e) \sqrt{\rho_w \mu_w \left(\frac{du_w}{dz}\right)_0}}$$

FIG. 16. Heat transfer parameter as function of the recombination rate parameter (from Ref. 66).

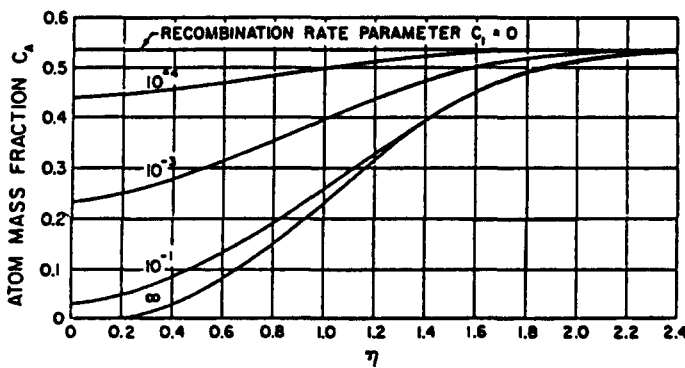


FIG. 17. Atom mass fraction profile at the stagnation point on a non-catalytic wall as function of the recombination rate parameter (from Ref. 66).

dissociated outside of the boundary layer so that the energy release due to atom recombination on a catalytic wall is more and more important. The heat flux reduction due to a non-catalytic wall so increases with velocity.

For a shuttle re-entry at  $7 \text{ km s}^{-1}$ , a non-catalytic wall leads to a heat flux reduction of 70% and the reaction-cured glass used for the space shuttle thermal protection system, with a recombination rate constant of about  $1 \text{ m s}^{-1}$ , to a reduction of about 50% with respect to a catalytic wall.

Goulard pointed out that, on a wall with finite catalytic efficiency, the catalytic rate coefficient increases with temperature; as the wall temperature increases the wall becomes more and more catalytic so that the wall heat flux may increase with the wall temperature.

### 3.5. SENSITIVITY STUDY OF TWO-DIMENSIONAL BOUNDARY LAYERS COMPUTATIONS TO THE HIGH TEMPERATURE GAS MODEL FOR DISSOCIATING AIR

Thanks to computer power increase, the dissociating air boundary layer has been computed since the late sixties.<sup>(23)</sup> A sensitivity study of boundary layer to the gas model was performed by Eldem<sup>(6,45,58)</sup> for the STS-2 flight re-entry.

Only the five main neutral species ( $N_2$ ,  $O_2$ ,  $NO$ ,  $N$ ,  $O$ ) are accounted for. The chemical model is made with the 17 reactions 9a–9e. Computations have been performed over axisymmetric hyperboloids at zero degree incidence which are supposed to represent the

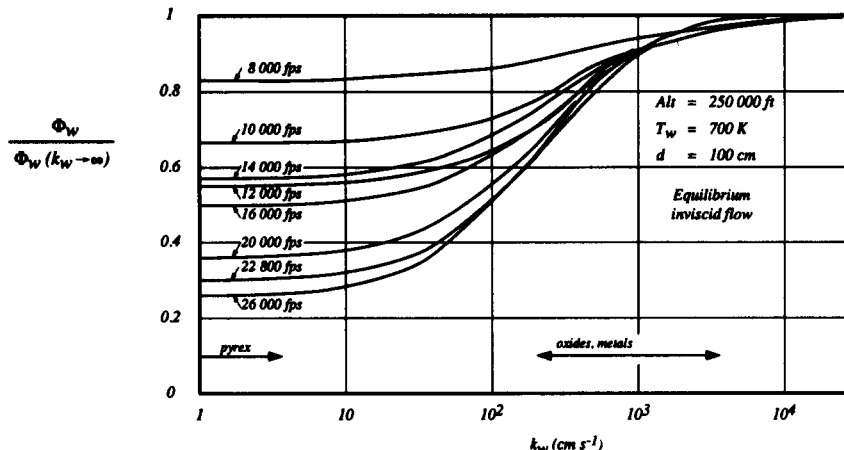


FIG. 18. Reduced heat transfer as function of catalytic recombination rate and flight velocity at 76 km altitude (from Ref. 79).

space shuttle windward symmetry line during the STS-2 re-entry.<sup>(171)</sup> A constant wall temperature of 1500 K is used in all the computations presented herein.

### 3.5.1. Influence of Wall Catalytic Efficiency

The stagnation point wall heat flux evolution during the re-entry is plotted in Fig. 19 for a catalytic wall, a non-catalytic wall and a wall with finite catalytic efficiency according to Scott's data.<sup>(168)</sup> The agreement with Goulard results is fair as the maximum wall heat flux is reduced by about 70% for a non-catalytic wall and 40% for a wall with finite catalytic efficiency. These reductions remain important during all of the re-entry, not only at the stagnation point but also all along the body as shown on Fig. 20. Comparisons with Navier-Stokes solutions (e.g. Ref. 171) shows that the influence of the wall catalytic efficiency is more important in boundary layer computations. This is due to the fact that chemical equilibrium is assumed at the outer edge of the boundary layer at the stagnation point which is not verified in Navier-Stokes solutions. Therefore, the gas dissociation at the boundary layer edge is overestimated and the flux on a non-catalytic wall is underestimated. The solution of this problem requires a more elaborate boundary layer approach which will be the topic of Section 4.

### 3.5.2. Influence of the Chemical Reaction Rates

Reaction rate constants are known with little accuracy, especially at high temperatures. Non-Arrhenius expressions for the reaction rate constants can be found either from reviews of data for combustion<sup>(14,72,198)</sup> or from papers dealing with re-entry problem.<sup>(28,80,98,140,143)</sup>

Various sets of reaction rate constants, namely one due to Oertel,<sup>(140)</sup> one due to Park,<sup>(143)</sup> one due to Bortner,<sup>(28)</sup> the one recommended by the National Bureau of Standard<sup>(198)</sup> i.e. the one due to Baulch<sup>(14)</sup> and, lastly, the review due to R. H. Hanson and S. Salimian in Gardiner's textbook<sup>(72)</sup> have been compared. For the oxygen dissociation reaction which is one of the most important reactions, a very large scatter is observed. There is one order of magnitude discrepancy between the most reliable models. The ratio of reaction rate constants to the value recommended by the National Bureau of Standard is plotted in Fig. 21 for a shuffle reaction. The dotted lines indicate the uncertainty range as evaluated by the N.B.S.<sup>(198)</sup> Since Gardiner's data are the most recent ones, the scatter is larger than estimated, a ratio of about three between extreme values can be observed.

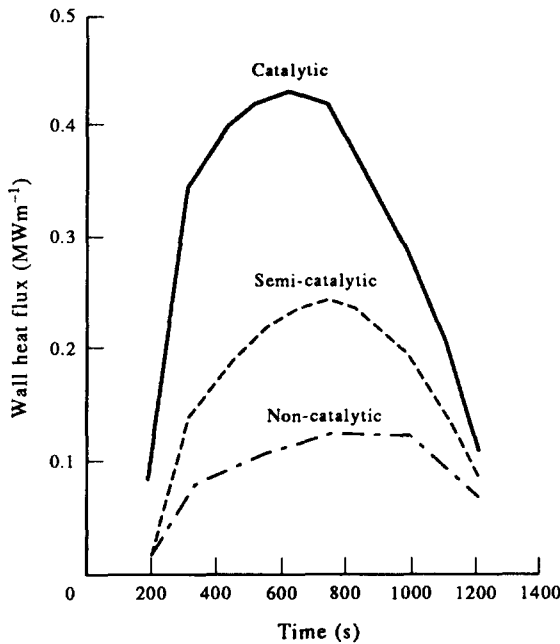


FIG. 19. Stagnation point wall heat flux during STS-2 flight re-entry.

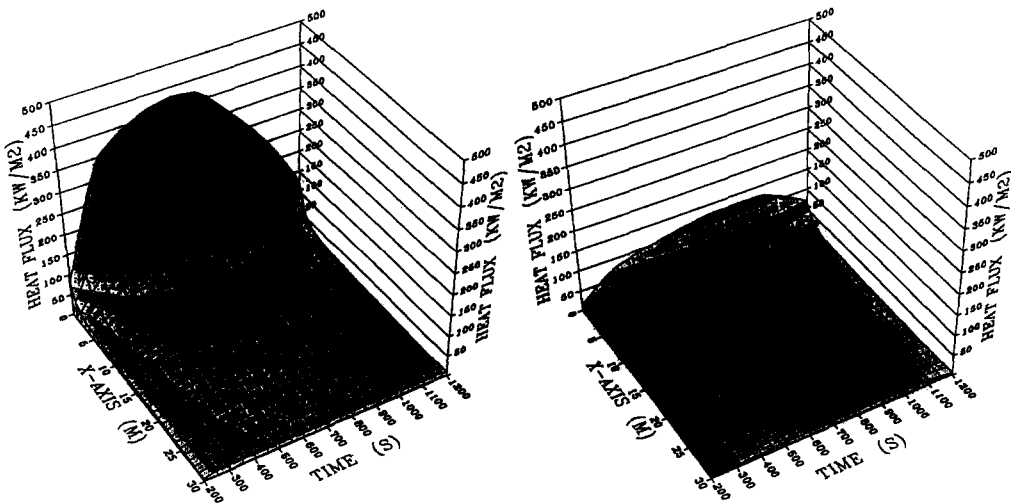


FIG. 20. Wall heat flux along the body centerline versus time during the STS-2 flight re-entry for a catalytic (left) and a non-catalytic (right) wall.

The influence of three chemical models on boundary layer predictions is presently investigated. The selected models are the sets of reaction rate constants published by Bortner,<sup>(28)</sup> Gardiner<sup>(72)</sup> and Oertel.<sup>(140)</sup> Gardiner data are the same as Baulch's<sup>(14)</sup> which are the N.B.S. recommended rate constants,<sup>(198)</sup> except for the two shuffle reactions. A fourth result is obtained assuming infinite reaction rate constants, i.e. chemical equilibrium flow.

The variation of the stagnation point wall heat flux prediction with the chemical reaction rate constants is shown in Fig. 22. For a catalytic wall, the wall heat flux does not depend upon the reaction rate as atom recombination energy is transferred to the wall. A slightly larger wall heat flux is obtained for flow at chemical equilibrium.

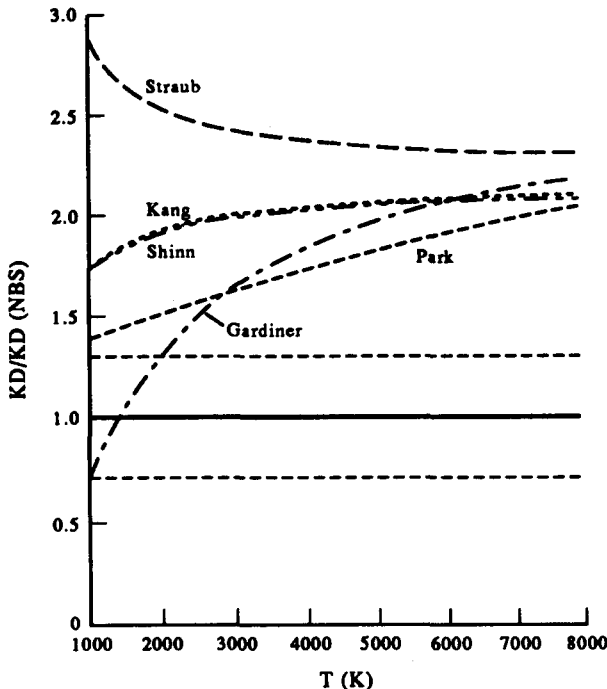


FIG. 21. Comparison of reaction rate constant determinations for the  $\text{NO} + \text{O} \rightarrow \text{N} + \text{O}_2$  shuffle reaction.

For a non-catalytic wall, a large discrepancy is observed. The wall heat flux depends only upon the wall temperature gradient, hence upon the energy release due to chemical reactions inside the boundary layer. Oertel's chemical model yields too fast dissociation rates for oxygen and hence a faster recombination rate in the cold region close to the wall. A higher wall heat flux is also predicted. Gardiner and Bortner models, which are within the present uncertainty range, lead to a 12% difference in wall heat flux.

The influence of the chemical rate constant on the wall heat flux predictions along the shuttle centerline is similar.<sup>(6,45,58)</sup>

### 3.5.3. Influence of the Wall Temperature

For catalytic and non-catalytic walls, it is observed as foreseeable that the wall heat flux is higher when the temperature is lower. The effect of wall temperature is more important for a non-catalytic wall than for a catalytic wall. The effect is also more important when the altitude decreases.

These results are consistent with the idea that the wall heat flux is proportional to the difference between the wall enthalpy  $h_w$  and the recovery enthalpy  $h_{aw}$ :

$$\phi_w \sim h_w - h_{aw}.$$

For hypersonic flows, the recovery enthalpy  $h_{aw}$  can be approximated by the inviscid flow stagnation enthalpy  $H_e$ . When the difference  $H_e - h_w$  is small, changes in the wall temperature and hence in  $h_w$  have more influence on the wall heat flux. The difference  $H_e - h_w$  decreases when the velocity decreases as the stagnation enthalpy becomes smaller. The difference  $H_e - h_w$  is also smaller when the wall enthalpy is larger: for a given wall temperature, the wall enthalpy is larger when the dissociation is more advanced which is the case for a non-catalytic wall.

Let us recall here the plausible more complex temperature dependency pointed out by Goulard for semi-catalytic walls.

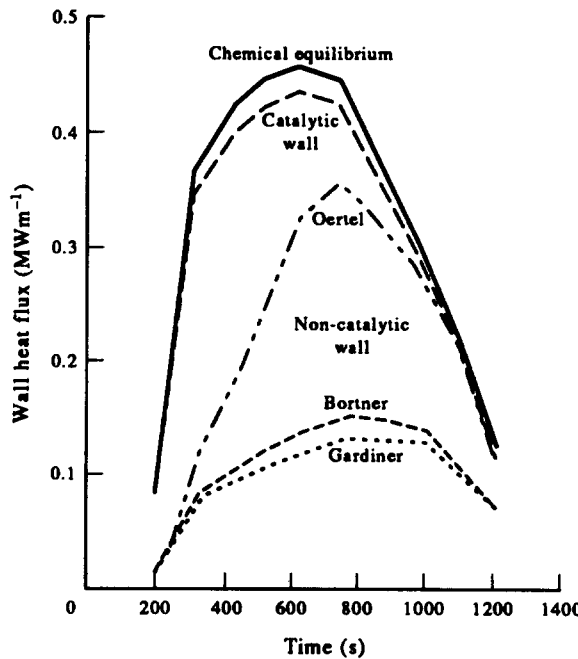


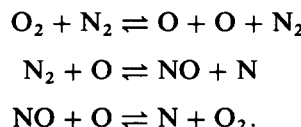
FIG. 22. Influence of the chemical reaction rate on the stagnation point wall heat flux.

### 3.5.4. Model Reduction

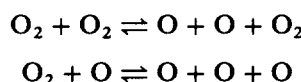
In order to decrease the computational cost, it is important to identify the key features of the high temperature gas model and to discard unimportant phenomena which may require large computational time.

A systematic study of model simplifications from the analysis of "complete" model computations has been performed for boundary layer flows on the STS-2 re-entry.<sup>(6,45,58)</sup>

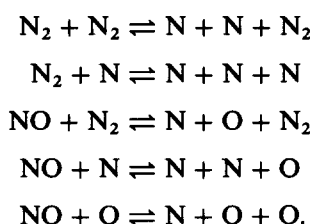
Concerning chemical models, a good approximation to represent all the process with a reduced set of chemical reactions is the Zeld'ovich model



At low altitudes, the prediction can be improved by taking into account two more oxygen dissociation reactions



as only oxygen dissociates at the end of the re-entry due to the decrease of the velocity. These results are in agreement with previous results obtained by Blottner<sup>(23)</sup> who brought into evidence the major rôle of the oxygen dissociation and the shuffle reactions. To get a perfect agreement with the complete computations over the re-entry trajectory, five more reactions of nitrogen and nitrogen monoxide dissociation are needed.



The other seven reactions play no rôle and can be neglected.

Concerning the transport model, the thermal diffusion is a second order effect and can be neglected. Moreover, the Prandtl number remains quite constant throughout the boundary layer during the whole re-entry so that a constant Prandtl number about 0.72 can be assumed without modifying model predictions. At last, analysis of the species diffusion flux shows that the species diffusion flux can be modelled by a Fick law with a Lewis number about 1.2.

Concerning the thermodynamical model, polynomial fits to thermodynamic functions<sup>(78,99)</sup> give the same results as the use of more complex (and computationally time consuming since they involve exponentials) expressions for the energy partition function to compute thermodynamical functions.

### 3.5.5. Influence of Ionization in Re-entry Flows

Boundary layer computations with and without ionized species and ionization chemistry have been compared.<sup>(9)</sup> For shuttle re-entry flows, i.e. for velocity about  $7000 \text{ m s}^{-1}$ , ionization is weak. Only about one per cent of nitrogen monoxide is ionized so that ionization hardly affects the energy budget. Ionization can therefore be neglected for such flows in the aerothermodynamic study. It may however play an important rôle in the attenuation of radiocommunications (the "black-out" phenomenon).

## 3.6. THREE-DIMENSIONAL BOUNDARY LAYER FLOWS

### 3.6.1. Stagnation Point Solutions

Since Howarth's works,<sup>(94,134)</sup> it is customary to study three-dimensional stagnation points in a cartesian coordinate system in a plane osculating the stagnation point. As the pressure is maximum at the stagnation point, a Taylor expansion of the pressure field near the stagnation point shows that the iso-pressure contours near the stagnation point are ellipses of identical symmetry axes and hence the axes of the ellipses are two orthogonal directions along which the inviscid flow is radial; these directions and the associated velocity gradients can be determined from the knowledge of the pressure field.

An extension of the Levy-Lees-Dorodnitsyn space variable transformation Eq. 42 which takes advantage of the existence of two principal directions and also reduces to the standard form for two-dimensional flows has been looked for as

$$\xi = \int_0^x \rho_w \mu_w u_e dx; \quad \zeta = \int_0^z \rho_w \mu_w w_e dz; \quad \eta = \alpha(x, z) \int_0^y \rho dy. \quad (44)$$

The self-similarity conditions together with the identity with the Levy-Lees-Dorodnitsyn transformation for two-dimensional, plane and axisymmetric, flows impose<sup>(9,58)</sup>

$$\alpha = \sqrt{\frac{\left(\frac{\partial u_e}{\partial x}\right)_0 + \left(\frac{\partial w_e}{\partial z}\right)_0}{\rho_w \mu_w}}. \quad (45)$$

For axisymmetric stagnation points, the wall heat flux is proportional to the square root of the stagnation point velocity gradient, or if the pressure distribution is given by a Newtonian law, to the inverse of the square root of the nose radius. The proportionality constant accounts for gas properties, external flow dissociation level and wall catalytic efficiency.

For three-dimensional stagnation points, the stagnation point heat transfer can be expressed as

$$q_{t,w} \sim \sqrt{\frac{1}{2} \left[ \left( \frac{\partial u_e}{\partial x} \right)_0 + \left( \frac{\partial w_e}{\partial z} \right)_0 \right]} \quad \text{or} \quad q_{t,w} \sim \sqrt{\frac{R_1 + R_2}{2R_1 R_2}} \quad (\text{Newtonian pressure distribution}) \quad (46)$$

where  $R_1$  and  $R_2$  are the principal curvature radii at the stagnation point. Of course, the proportionality constants are the same as for axisymmetric flows.

An interesting point is that, for three-dimensional flows, the maximum heat flux is no longer at the stagnation point but by its sides. This is due to the fact that, near the stagnation point, the wall heat flux is directly related to the velocity gradient. Since, at the stagnation point, the wall heat flux depends upon the mean of the velocity gradient in the two principal directions, it may increase in the direction of the maximum velocity gradient.

### 3.6.2. Attachment Line Solutions

Important heat loads can be encountered along the attachment lines on the leading edges of wings or winglets where the curvature radii are small.

This problem can be tackled by modelling the leading edge as an infinite swept cylinder. Self-similar solutions are used to study the flow along the attachment line. The inviscid flow velocity along the attachment line  $w_e$  is constant while there exists a velocity gradient normal to the attachment line ( $u_e = kx$ ). A space variable transformation analog to the Levy-Lees-Dorodnitsyn is used again

$$\xi = \int_0^x \rho_w \mu_w u_e dx; \quad \zeta = z; \quad \eta = \frac{u_e}{\sqrt{2\xi}} \int_0^y \rho dy, \quad (47)$$

and self-similarity along the attachment line is sought for the dimensionless velocities  $f' = \frac{u}{u_e}$ ,  $g' = \frac{w}{w_e}$  enthalpy  $S = \frac{H}{H_e}$  and mass fraction  $Z_I = \frac{C_I}{C_{Ie}}$  profiles.

An example of the wall heat flux evolution with the sweep angle for flows with high temperature effects is given in Fig. 23 for a cylinder of 0.3 m radius. For a catalytic wall, the

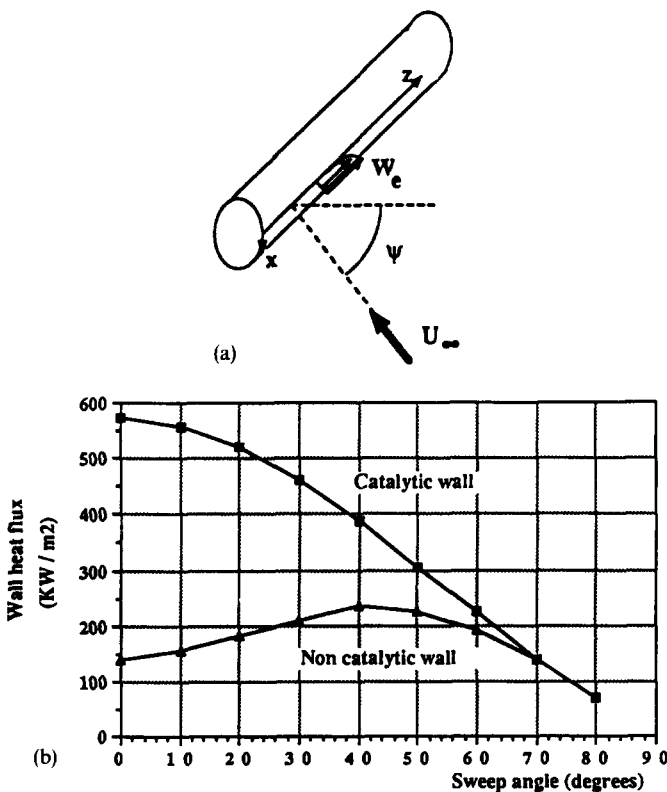


FIG. 23. Wall heat flux along an infinite swept cylinder attachment line.

$\cos^{3/2}\psi$  evolution is observed as for perfect gas flows while an unexpected behaviour is observed on non-catalytic walls.

The increase of the wall heat flux on a non-catalytic wall for intermediate sweep angles results from a decrease due to the sweep angle and an increase due to changes of the wall enthalpy as discussed in Refs 9 and 27.

### 3.6.3. Sensitivity Study to the High Temperature Gas Model

The sensitivity study of boundary layer computations to the high temperature gas model has been extended to three-dimensional flows.<sup>(7,9,27)</sup> The phenomena observed in two-dimensional flows, namely the importance of wall catalytic efficiency, of the chemical model or of the wall temperature, together with the evolution of the wall heat flux along the re-entry trajectory are retrieved in three-dimensional boundary layers.

## 4. ENTROPY GRADIENT EFFECTS

### 4.1. ENTROPY LEVELS IN THE SHOCK LAYER

A blunt body in a hypersonic flow is preceded by a strong shock wave. For an inviscid flow, the entropy remains constant along the streamlines except across a shock wave, where the entropy jump depends on the local slope of the shock. Because of the curved shape of the shock wave, the entropy level varies in the shock layer from one streamline to one another. Thus, there exists an entropy gradient orthogonal to the streamlines within the inviscid shock layer, mainly for the streamlines which crossed the shock wave in the nose region, where the strongest curvature is encountered. These streamlines remain near the body wall, constituting the "entropy layer".

This entropy gradient is related to the vorticity of the flowfield through the Crocco equation

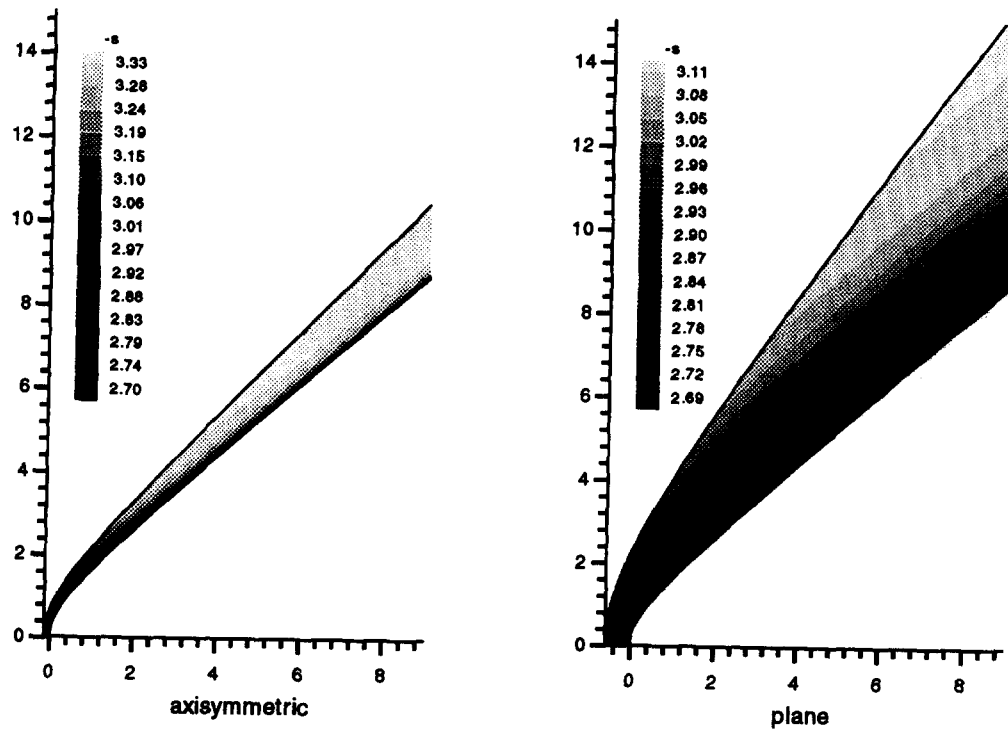
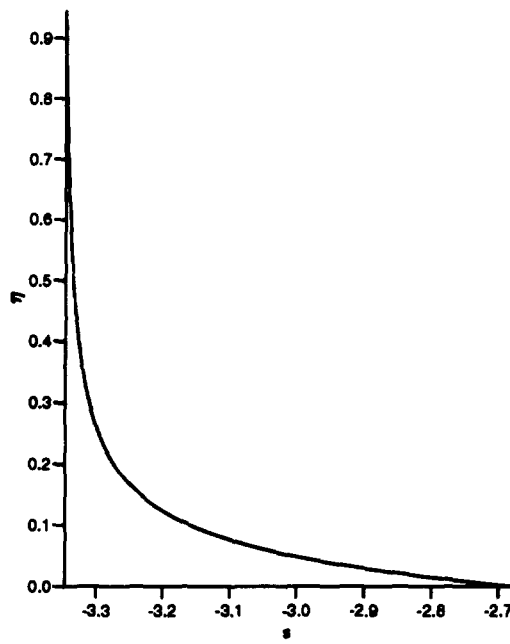
$$\overline{\text{curl}} \vec{V} \wedge \vec{V} = -\overline{\text{grad}} H + T \overline{\text{grad}} S$$

where  $H$  is the total enthalpy. The vorticity appears in the inviscid flow as a tangential velocity gradient across the entropy layer, and, since in most of the applications the total enthalpy remains constant, a negative temperature gradient normal to the wall.

For two-dimensional planar or axisymmetric flows, a fundamental difference appears concerning the normal entropy gradient at the wall. The streamlines along the wall stem from the stagnation line. Van Dyke<sup>(186)</sup> showed that the entropy gradient is null on the stagnation line in a planar flow, because the shock wave is locally normal, but is not null for the stagnation line of an axisymmetric flow. Let us consider for example a hypersonic flow past a hyperboloid. Figure 24 shows the entropy levels in the shock layer for both planar and axisymmetric bodies, whereas Figs 25 and 26 show the entropy profiles across the shock layer along the normal to the wall.

In the flow past an axisymmetric hyperboloid, the shock wave curvature decreases rapidly and the entropy field tends to be uniform, except for the streamlines near the wall, which cross the strongly curved shock wave in the nose region. In this case, the entropy gradient remains non-null at the wall, and the entropy layer thickness decreases towards the rear of the body, since the mass flow is constant in the entropy layer and the circumference of the body increases (Fig. 24 left). The entropy values at the wall and at the edge of the entropy layer remain constant because the wall is a streamline and outside of the entropy layer the flow is quasi-isentropic. So the normal entropy gradient at the wall strongly increases downstream. Far from the nose, the flow is similar to a flow past a sharp cone except in the entropy layer, whose aspect is quite similar to a viscous boundary layer (Fig. 25).

For a planar hyperbola at the same conditions (Fig. 24 right), the entropy gradient vanishes at the wall. The entropy layer is thus located at a short distance above the wall

FIG. 24. Entropy level in the shock layer ( $M = 23.4$ ).FIG. 25. Entropy profile—axisymmetric case ( $M = 23.4, \xi = 9$ ).

(Fig. 26). So the velocity and temperature gradients in the inviscid flow are null at the wall as well, and their influence will be significant only with a very thick boundary layer. Moreover, far downstream, the flow can be assimilated to a parallel flow and the entropy layer thickness remains constant. Thus the entropy gradient remains bounded. Since it is null at the wall, its influence on the skin friction and the heat flux will now be far less important.

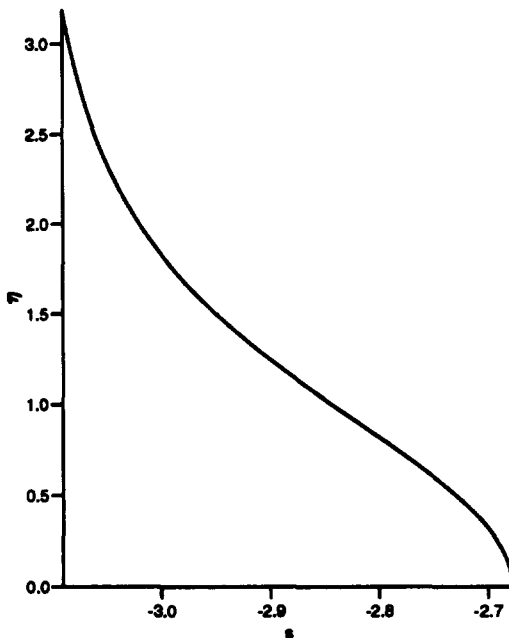


FIG. 26. Entropy profile—planar case ( $M = 23.4, \xi = 9$ ).

A reliable computational method for viscous hypersonic flows must include the influence of the inviscid flow vorticity on the boundary layer. Solving the complete Navier-Stokes equations remains expensive, especially when real gas models are involved, and is not convenient for design applications. This is necessary however when the whole shock layer is viscous; but for large enough Reynolds numbers, the boundary layer is sufficiently small compared to the shock layer to assume that viscous effects are negligible near the shock wave. One can then consider some distinct calculations for the inviscid shock layer and the viscous boundary layer.

#### 4.2. VAN DYKE'S THEORY

The standard boundary layer theory of Prandtl cannot take into account normal gradients outside of the boundary layer. Van Dyke<sup>(184-186)</sup> proposed an enlarged theory called higher-order boundary layer theory based on matched asymptotic expansions for high Reynolds numbers. The main advantage of this systematic method is to give not only the equations but also the matching conditions between the different zones.

We consider a steady flow of perfect gas past a convex blunt body. The equations for a reactive gas could be obtained using the same method. To derive boundary layer equations, one must use curvilinear coordinates  $(\xi, \eta)$ , where  $\xi$  is the distance along the body and  $\eta$  is normal to the body surface (Fig. 27). The longitudinal curvature of the body is

$$\kappa(\xi) = 1/R(\xi).$$

The symbol  $r$  represents the distance from the wall to the symmetry axis. All the variables are divided by reference values in order to get dimensionless variables.

Two approximations of the Navier-Stokes solutions will be sought: one far from the wall, in the region where the viscous effects are weak, and another one near the wall, where the viscous effects are important. These approximations are looked for as expansions in powers of a small perturbation parameter

$$\varepsilon = \frac{1}{\sqrt{Re}}.$$

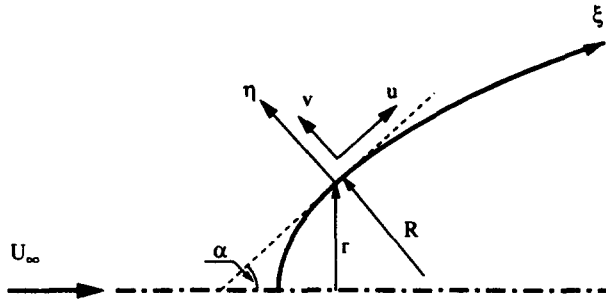


FIG. 27. Coordinates system.

The outer expansions read

$$\begin{aligned} u(\xi, \eta) &= U_1(\xi, \eta) + \varepsilon U_2(\xi, \eta) + \dots \\ v(\xi, \eta) &= V_1(\xi, \eta) + \varepsilon V_2(\xi, \eta) + \dots \\ p(\xi, \eta) &= P_1(\xi, \eta) + \varepsilon P_2(\xi, \eta) + \dots \\ \rho(\xi, \eta) &= R_1(\xi, \eta) + \varepsilon R_2(\xi, \eta) + \dots \\ h(\xi, \eta) &= H_1(\xi, \eta) + \varepsilon H_2(\xi, \eta) + \dots \\ T(\xi, \eta) &= T_1(\xi, \eta) + \varepsilon T_2(\xi, \eta) + \dots \end{aligned}$$

In the inner region, a stretched normal coordinate  $\bar{\eta} = \eta/\varepsilon$  is used according to the principle of least degeneracy (Van Dyke<sup>(187)</sup>). In this way, the normal coordinate is referred to a quantity of the same order of magnitude as the boundary layer thickness, so that the new normal coordinate is of order unity in the boundary layer. Similarly, a special expansion must be written for the normal velocity because this quantity is of order  $\varepsilon$  in the boundary layer, according to the continuity equation. Therefore, the inner expansions have the form

$$\begin{aligned} u(\xi, \eta) &= u_1(\xi, \bar{\eta}) + \varepsilon u_2(\xi, \bar{\eta}) + \dots \\ v(\xi, \eta) &= \varepsilon \bar{v}_1(\xi, \bar{\eta}) + \varepsilon^2 \bar{v}_2(\xi, \bar{\eta}) + \dots \\ p(\xi, \eta) &= p_1(\xi, \bar{\eta}) + \varepsilon p_2(\xi, \bar{\eta}) + \dots \\ \rho(\xi, \eta) &= \rho_1(\xi, \bar{\eta}) + \varepsilon \rho_2(\xi, \bar{\eta}) + \dots \\ h(\xi, \eta) &= h_1(\xi, \bar{\eta}) + \varepsilon h_2(\xi, \bar{\eta}) + \dots \\ T(\xi, \eta) &= t_1(\xi, \bar{\eta}) + \varepsilon t_2(\xi, \bar{\eta}) + \dots \end{aligned}$$

All the coefficients and their derivatives are assumed to be of order unity.

These expansions are brought in the dimensionless Navier-Stokes equations and like powers of  $\varepsilon$  are equated. This leads to the following equations:

– outer region, first order

$$\left\{ \begin{array}{l} \frac{\partial}{\partial \xi} [(r + \eta \cos \alpha)^j R_1 U_1] + \frac{\partial}{\partial \eta} [(1 + \kappa \eta)(r + \eta \cos \alpha)^j R_1 V_1] = 0 \\ R_1 U_1 \frac{1}{1 + \kappa \eta} \frac{\partial U_1}{\partial \xi} + R_1 V_1 \frac{\partial U_1}{\partial \eta} + \frac{\kappa}{1 + \kappa \eta} R_1 U_1 V_1 = - \frac{1}{1 + \kappa \eta} \frac{\partial P_1}{\partial \xi} \\ R_1 U_1 \frac{1}{1 + \kappa \eta} \frac{\partial V_1}{\partial \xi} + R_1 V_1 \frac{\partial V_1}{\partial \eta} - \frac{\kappa}{1 + \kappa \eta} R_1 U_1^2 = - \frac{\partial P_1}{\partial \eta} \\ R_1 U_1 \frac{1}{1 + \kappa \eta} \frac{\partial H_1}{\partial \xi} + R_1 V_1 \frac{\partial H_1}{\partial \eta} = U_1 \frac{1}{1 + \kappa \eta} \frac{\partial P_1}{\partial \xi} + V_1 \frac{\partial P_1}{\partial \eta} \end{array} \right.$$

with  $j = 0$  for planar and  $j = 1$  for axisymmetric bodies. These are the well-known Euler equations for an inviscid flow. Because of the loss of second order derivatives, all the boundary conditions can no longer be satisfied. That's why a boundary layer must be looked for.

– inner region, first order

$$\left\{ \begin{array}{l} \frac{\partial}{\partial \xi}(r^j \rho_1 u_1) + \frac{\partial}{\partial \bar{\eta}}(r^j \rho_1 \bar{v}_1) = 0 \\ \rho_1 u_1 \frac{\partial u_1}{\partial \xi} + \rho_1 \bar{v}_1 \frac{\partial u_1}{\partial \bar{\eta}} = - \frac{\partial p_1}{\partial \xi} + \frac{\partial}{\partial \bar{\eta}} \left( \mu_1 \frac{\partial u_1}{\partial \bar{\eta}} \right) \\ 0 = - \frac{\partial p_1}{\partial \bar{\eta}} \\ \rho_1 u_1 \frac{\partial h_1}{\partial \xi} + \rho_1 \bar{v}_1 \frac{\partial h_1}{\partial \bar{\eta}} = u_1 \frac{\partial p_1}{\partial \xi} + \bar{v}_1 \frac{\partial p_1}{\partial \bar{\eta}} + \frac{\partial}{\partial \bar{\eta}} \left( \frac{\mu_1}{Pr} \frac{\partial t_1}{\partial \bar{\eta}} \right) + \mu_1 \left( \frac{\partial u_1}{\partial \bar{\eta}} \right)^2. \end{array} \right.$$

These are the usual Prandtl equations. They are thus found to be just the first term of a perturbation expansion. Note that the curvature radius only appears in the continuity equation.

– outer region, second order  
continuity

$$\frac{\partial}{\partial \xi}[(r + \eta \cos \alpha)^j(R_1 U_2 + R_2 U_1)] + \frac{\partial}{\partial \eta}[(1 + \kappa \eta)(r + \eta \cos \alpha)^j(R_1 V_2 + R_2 V_1)] = 0$$

$\xi$ -momentum

$$(R_1 U_2 + R_2 U_1) \frac{1}{1 + \kappa \eta} \frac{\partial U_1}{\partial \xi} + R_1 U_1 \frac{1}{1 + \kappa \eta} \frac{\partial U_2}{\partial \xi} + (R_1 V_2 + R_2 V_1) \frac{\partial U_1}{\partial \eta} + R_1 V_1 \frac{\partial U_2}{\partial \eta} + \frac{\kappa}{1 + \kappa \eta} [(R_1 V_2 + R_2 V_1) U_1 + R_1 V_1 U_2] = - \frac{1}{1 + \kappa \eta} \frac{\partial P_2}{\partial \xi}$$

$\eta$ -momentum

$$(R_1 U_2 + R_2 U_1) \frac{1}{1 + \kappa \eta} \frac{\partial V_1}{\partial \xi} + R_1 U_1 \frac{1}{1 + \kappa \eta} \frac{\partial V_2}{\partial \xi} + (R_1 V_2 + R_2 V_1) \frac{\partial V_1}{\partial \eta} + R_1 V_1 \frac{\partial V_2}{\partial \eta} - \frac{\kappa}{1 + \kappa \eta} (R_2 U_1^2 + 2R_1 U_1 U_2) = - \frac{\partial P_2}{\partial \eta}$$

energy

$$(R_1 U_2 + R_2 U_1) \frac{1}{1 + \kappa \eta} \frac{\partial H_1}{\partial \xi} + R_1 U_1 \frac{1}{1 + \kappa \eta} \frac{\partial H_2}{\partial \xi} + (R_1 V_2 + R_2 V_1) \frac{\partial H_1}{\partial \eta} + R_1 V_1 \frac{\partial H_2}{\partial \eta} = U_1 \frac{1}{1 + \kappa \eta} \frac{\partial P_2}{\partial \xi} + U_2 \frac{1}{1 + \kappa \eta} \frac{\partial P_1}{\partial \xi} + V_1 \frac{\partial P_2}{\partial \eta} + V_2 \frac{\partial P_1}{\partial \eta}$$

These are just the Euler equations linearized for small perturbations. No viscous terms appear until third order in the outer region.

– inner region, second order  
continuity

$$\begin{aligned} & \frac{\partial}{\partial \xi} [r^j (\rho_1 u_2 + \rho_2 u_1) + \bar{\eta} j \cos \alpha \rho_1 u_1] \\ & + \frac{\partial}{\partial \bar{\eta}} [r^j (\rho_1 \bar{v}_2 + \rho_2 \bar{v}_1) + \bar{\eta} (j \cos \alpha + \kappa r^j) \rho_1 \bar{v}_1] = 0 \end{aligned}$$

**$\xi$ -momentum**

$$\begin{aligned}
 & (\rho_1 u_2 + \rho_2 u_1) \frac{\partial u_1}{\partial \xi} + \rho_1 u_1 \frac{\partial u_2}{\partial \xi} + (\rho_1 \bar{v}_2 + \rho_2 \bar{v}_1) \frac{\partial u_1}{\partial \bar{\eta}} + \rho_1 \bar{v}_1 \frac{\partial u_2}{\partial \bar{\eta}} \\
 &= - \frac{\partial p_2}{\partial \xi} + \kappa \bar{\eta} \frac{\partial p_1}{\partial \xi} + \frac{\partial}{\partial \bar{\eta}} \left( \mu_1 \frac{\partial u_2}{\partial \bar{\eta}} + \mu_2 \frac{\partial u_1}{\partial \bar{\eta}} \right) \\
 &+ \rho_1 u_1 \kappa \left( \bar{\eta} \frac{\partial u_1}{\partial \xi} - \bar{v}_1 \right) - \kappa \frac{\partial}{\partial \bar{\eta}} (\mu_1 u_1) + \mu_1 \left( j \frac{\cos \alpha}{r} + 2\kappa \right) \frac{\partial u_1}{\partial \bar{\eta}}
 \end{aligned}$$

 **$\eta$ -momentum**

$$\frac{\partial p_2}{\partial \bar{\eta}} = \kappa \rho_1 u_1^2$$

**energy**

$$\begin{aligned}
 & (\rho_1 u_2 + \rho_2 u_1) \frac{\partial h_1}{\partial \xi} + \rho_1 u_1 \frac{\partial h_2}{\partial \xi} + (\rho_1 \bar{v}_2 + \rho_2 \bar{v}_1) \frac{\partial h_1}{\partial \bar{\eta}} + \rho_1 \bar{v}_1 \frac{\partial h_2}{\partial \bar{\eta}} \\
 &= u_1 \frac{\partial p_2}{\partial \xi} + u_2 \frac{\partial p_1}{\partial \xi} + \bar{v}_1 \frac{\partial p_2}{\partial \bar{\eta}} + \bar{v}_2 \frac{\partial p_1}{\partial \bar{\eta}} + \frac{\partial}{\partial \bar{\eta}} \left[ \frac{\mu_1 \partial t_2}{Pr \partial \bar{\eta}} + \frac{\mu_2 \partial t_1}{Pr \partial \bar{\eta}} \right] \\
 &+ \mu_2 \left( \frac{\partial u_1}{\partial \bar{\eta}} \right)^2 + 2\mu_1 \frac{\partial u_1}{\partial \bar{\eta}} \frac{\partial u_2}{\partial \bar{\eta}} + \kappa \bar{\eta} u_1 \left( \rho_1 \frac{\partial t_1}{\partial \xi} - \frac{\partial p_1}{\partial \xi} \right) \\
 &+ \left( j \frac{\cos \alpha}{r} + \kappa \right) \frac{\mu_1 \partial t_1}{Pr \partial \bar{\eta}} - 2\kappa \mu_1 u_1 \frac{\partial u_1}{\partial \bar{\eta}}.
 \end{aligned}$$

In these equations the advection terms for small perturbations appear, in addition to several source terms due to the longitudinal and transverse curvatures, and particularly a normal pressure gradient.

The second-order boundary layer equations are linear and thus the source terms and the boundary conditions can be split into several parts corresponding to different second order effects (Van Dyke<sup>(186)</sup>):

- longitudinal curvature (terms proportional to  $\kappa$ )
- transverse curvature (terms proportional to  $j \cos \alpha$ )
- displacement
- entropy gradient
- total enthalpy gradient
- slip velocity
- temperature jump.

These effects can be solved separately, except the displacement and entropy gradient effects which are coupled, since in the second-order outer equations appears the term

$$V_2 \frac{\partial U_1}{\partial \bar{\eta}}$$

which is the product of the displacement velocity by the shear of the first order inviscid flow. Thus, for a given first-order boundary layer, the second-order flow will be different depending on whether the external flow is sheared or not.

The boundary conditions are not sufficient to solve both the inner and outer problems. The missing conditions are obtained by matching the two expansions, i.e. writing that they are equivalent in an intermediate region. Matching conditions are given by Van Dyke using his matching principle:

The  $m$ -term inner expansion of the  $n$ -term outer expansion is equal to the  $n$ -term outer expansion of the  $m$ -term inner expansion.

For the longitudinal component of the velocity, the two-term outer expansion is

$$u = U_1(\xi, \eta) + \varepsilon U_2(\xi, \eta) + \dots$$

Rewritten in internal coordinates

$$u = U_1(\xi, \varepsilon\bar{\eta}) + \varepsilon U_2(\xi, \varepsilon\bar{\eta}) + \dots$$

and expanded for  $\varepsilon \rightarrow 0$ , it yields

$$u = U_1(\xi, 0) + \varepsilon\bar{\eta} \frac{\partial U_1}{\partial \eta}(\xi, 0) + \varepsilon U_2(\xi, 0) + \dots$$

This must be equivalent to the limit of the inner expansion for  $\bar{\eta} \rightarrow \infty$

$$u_1(\xi, \bar{\eta}) + \varepsilon u_2(\xi, \bar{\eta}) \underset{\bar{\eta} \rightarrow \infty}{\sim} U_1(\xi, 0) + \varepsilon \left( U_2(\xi, 0) + \bar{\eta} \frac{\partial U_1}{\partial \eta}(\xi, 0) \right).$$

Equating the like powers of  $\varepsilon$  leads to

$$\begin{cases} u_1(\xi, \bar{\eta}) \underset{\bar{\eta} \rightarrow \infty}{\sim} U_1(\xi, 0) \\ u_2(\xi, \bar{\eta}) \underset{\bar{\eta} \rightarrow \infty}{\sim} U_2(\xi, 0) + \bar{\eta} \frac{\partial U_1}{\partial \eta}(\xi, 0). \end{cases} \quad (48)$$

The second-order inner term is thus matched with the wall value of the second-order outer term, plus the slope at the wall of the first-order outer term. The slope at the wall of the second-order term arises only in third-order expansion, with the wall value of the second-order derivative of the first-order term. The same argument is also valid with  $p$ ,  $\rho$  and  $T$ . The case of  $v$  is slightly different

$$\varepsilon \bar{v}_1(\xi, \bar{\eta}) + \varepsilon^2 \bar{v}_2(\xi, \bar{\eta}) \underset{\bar{\eta} \rightarrow \infty}{\sim} V_1(\xi, 0) + \varepsilon \left( V_2(\xi, 0) + \bar{\eta} \frac{\partial V_1}{\partial \eta}(\xi, 0) \right).$$

So,

$$\begin{cases} 0 = V_1(\xi, 0) \\ \bar{v}_1(\xi, \bar{\eta}) \underset{\bar{\eta} \rightarrow \infty}{\sim} V_2(\xi, 0) + \bar{\eta} \frac{\partial V_1}{\partial \eta}(\xi, 0) \end{cases}$$

or

$$\begin{cases} V_1(\xi, 0) = 0 \\ V_2(\xi, 0) = \lim_{\bar{\eta} \rightarrow \infty} \left[ \bar{v}_1(\xi, \bar{\eta}) - \bar{\eta} \frac{\partial V_1}{\partial \eta}(\xi, 0) \right]. \end{cases}$$

This gives the boundary conditions at the wall for the external inviscid flow. The first one is the usual slip-condition at the wall for an inviscid flow. The second represents the displacement of the second-order external flow by the first-order boundary layer. The normal velocity of the inviscid flow is no longer zero, but has a fixed value, as if the wall was not a solid line but a blowing was performed across it. This last condition is used for coupling inner and outer calculations. So the first-order boundary layer must be solved before the second-order external flow. Due to these boundary conditions, the calculations must be done in the following order

- outer flow, first order (Euler)
- boundary layer, first order (Prandtl)
- outer flow, second order (perturbed Euler)
- boundary layer, second order.

According to the equation

$$\frac{\partial p_1}{\partial \bar{\eta}} = 0$$

we get  $p_1(\xi, \eta) = P_1(\xi, 0)$ . The pressure is thus constant across the boundary layer and equal to the inviscid flow pressure at the wall.

The matched asymptotic expansions technique provides complete matching conditions between the inner and outer expansions, for all the variables at any order, with a more

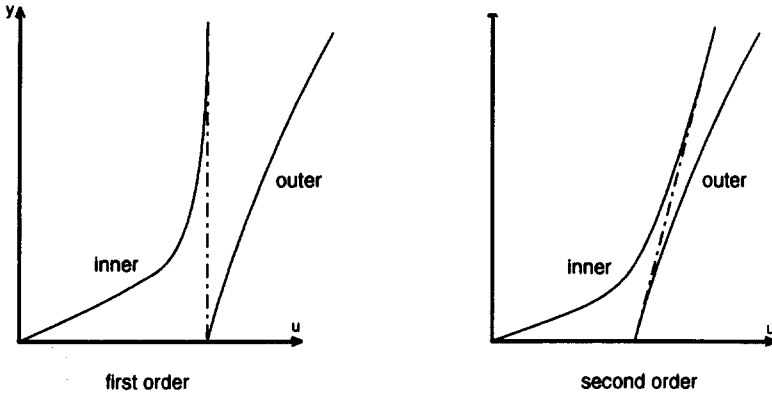


FIG. 28. Matching schemes.

rigorous argumentation than in Prandtl's theory. Figure 28 summarizes the matching schemes for first- and second-order expansions. The matching between the boundary layer and the external flow with second-order expansions is not perfect when the external flow departs from a linear profile with constant slope. For hypersonic reentry flows, the Reynolds number is often moderate at high altitudes, because of the low density of air. The boundary layers are thus thick and can be of the same order of magnitude as the entropy layer, and the inviscid flow quantities can undergo important variations between the wall and the edge of the boundary layer. Because of the hypothesis of Reynolds number tending towards infinity, the boundary layer is assumed to be very thin in Van Dyke's theory and the inviscid flow gradients are represented only by their wall value. So the second order expansion cannot ensure a good matching of the boundary layer with the inviscid flow if the inviscid profiles are not linear, and the influence of the external vorticity on the skin friction and the wall heat flux is not estimated correctly.

A single composite expansion valid in the whole domain can be written as the sum of the internal and external expansions minus the common part

$$u^c = u^e + u^i - (u^e)^i.$$

Thus the second-order composite expansion is

$$u^c = U_1 + u_1 - U_1(\xi, 0) + \varepsilon \left( U_2 + u_2 - U_2(\xi, 0) - \bar{\eta} \frac{\partial U_1}{\partial \eta}(\xi, 0) \right).$$

This development is equivalent to each expansion in the corresponding region. The slope at the wall of the velocity and temperature profiles is now equal to the boundary layer slope plus the inviscid flow slope.

To improve the results of the second order expansions, several authors like Monnoyer<sup>(132)</sup> or Sawley and Wüthrich<sup>(201)</sup> have modified the matching relation. They first compute an ordinary first order boundary layer, and determine the boundary layer thickness  $\delta$ . Then they solve combined first and second order boundary layer equations and match the boundary layer profile with the inviscid flow value at  $\delta$ . The results obtained with this method are rather good, but the definition of  $\delta$  remains somewhat ambiguous, since different values can be obtained, depending on the variable considered.

#### 4.3. DEFECT APPROACH

To ensure a smooth matching at any order whatever the external flow, a defect approach has been proposed, coupled with asymptotic expansions.<sup>(8)</sup> In the boundary layer region, the variables are no longer the physical variables, but the difference between them and the

external solution (Le Balleur<sup>(11,12)</sup>). So we write

$$\begin{aligned}\rho &= \rho_E + \rho_D \\ u &= u_E + u_D \\ v &= v_E + v_D - v_E(\xi, 0) \\ p &= p_E + p_D \\ h &= h_E + h_D \\ T &= T_E + T_D\end{aligned}$$

where the subscript  $E$  stands for the external variables and the defect variables are labelled  $D$ . The term  $v_E(\xi, 0)$  has been added to keep the condition  $v_D(\xi, 0) = 0$  at the wall whatever the value of  $v_E$ .

The outer expansions are identical to Van Dyke's. Using the stretched normal variable  $\bar{\eta}$ , the defect expansions read

$$\begin{aligned}u_D(\xi, \eta) &= u_1(\xi, \bar{\eta}) + \varepsilon u_2(\xi, \bar{\eta}) + \dots \\ v_D(\xi, \eta) &= \varepsilon \bar{v}_1(\xi, \bar{\eta}) + \varepsilon^2 \bar{v}_2(\xi, \bar{\eta}) + \dots \\ p_D(\xi, \eta) &= p_1(\xi, \bar{\eta}) + \varepsilon p_2(\xi, \bar{\eta}) + \dots \\ \rho_D(\xi, \eta) &= \rho_1(\xi, \bar{\eta}) + \varepsilon \rho_2(\xi, \bar{\eta}) + \dots \\ h_D(\xi, \eta) &= h_1(\xi, \bar{\eta}) + \varepsilon h_2(\xi, \bar{\eta}) + \dots \\ T_D(\xi, \eta) &= t_1(\xi, \bar{\eta}) + \varepsilon t_2(\xi, \bar{\eta}) + \dots.\end{aligned}$$

In the outer region, the defect variables are null and the equations for the outer flow are exactly the same as for Van Dyke's theory, i.e. the Euler equations. In the inner region, one must first bring the above expansions into the Navier–Stokes equations, then subtract the external equations, and at last equate like powers of  $\varepsilon$ . For practical reasons, the inner equations can then be rewritten in outer coordinates, using  $\eta$  instead of  $\bar{\eta}$ , and replacing  $\bar{v}_1$  and  $\bar{v}_2$  by

$$v_1(\xi, \eta) = \varepsilon \bar{v}_1(\xi, \bar{\eta}) \quad v_2(\xi, \eta) = \varepsilon \bar{v}_2(\xi, \bar{\eta}).$$

Then the following first-order equations are obtained:

– continuity

$$\frac{\partial}{\partial \xi} [r^j \rho_1 U_1 + r^j (R_1 + \rho_1) u_1] + \frac{\partial}{\partial \eta} [r^j \rho_1 (V_1 + v_1)] + r^j R_1 \frac{\partial v_1}{\partial \eta} = 0$$

–  $\xi$ -momentum

$$\begin{aligned}(R_1 + \rho_1)(U_1 + u_1) \frac{\partial u_1}{\partial \xi} + [\rho_1 U_1 + (R_1 + \rho_1) u_1] \frac{\partial U_1}{\partial \xi} + (R_1 + \rho_1)(V_1 + v_1) \frac{\partial u_1}{\partial \eta} \\ = - \frac{\partial p_1}{\partial \xi} + \frac{1}{Re} \frac{\partial}{\partial \eta} \left( \mu_1 \frac{\partial u_1}{\partial \eta} \right)\end{aligned}$$

–  $\eta$ -momentum

$$0 = - \frac{\partial p_1}{\partial \eta}$$

– energy

$$\begin{aligned}(R_1 + \rho_1)(U_1 + u_1) \frac{\partial h_1}{\partial \xi} + [\rho_1 U_1 + (R_1 + \rho_1) u_1] \frac{\partial H_1}{\partial \xi} + (R_1 + \rho_1)(V_1 + v_1) \frac{\partial h_1}{\partial \eta} \\ = u_1 \frac{\partial P_1}{\partial \xi} + (U_1 + u_1) \frac{\partial p_1}{\partial \xi} + \frac{\partial}{\partial \eta} \left( \frac{\mu_1}{Pr Re} \frac{\partial t_1}{\partial \eta} \right) + \frac{\mu_1}{Re} \left( \frac{\partial u_1}{\partial \eta} \right)^2.\end{aligned}$$

As in the Prandtl equations, the wall curvature appears in the first-order equations only through the transverse curvature radius in the continuity equation. The second-order equations are small-perturbations of the above ones plus source terms due to curvature effects, as in Van Dyke's theory.

From a theoretical point of view, it can be shown that the defect equations are consistent with those of Van Dyke by the fact that at a given order they differ only by terms which are higher-order in Van Dyke's theory. For example, if the first order defect equations are rewritten for the physical variables, replacing  $u_D$  by  $u - u_E$  and so on, the Prandtl equations are obtained plus terms of order  $\varepsilon$ .

Each expansion must satisfy the boundary conditions corresponding to its own domain of validity. The upstream conditions are to be applied to the outer expansion and the wall conditions to the inner one. The missing conditions are obtained by matching the inner and outer expansions. At the edge of the boundary layer, we can write

$$\begin{aligned} u &\rightarrow u_E \quad u_D \rightarrow 0 \\ v &\rightarrow v_E \quad v_D \rightarrow v_E(\xi, 0) \\ \rho &\rightarrow \rho_E \quad \rho_D \rightarrow 0 \\ p &\rightarrow p_E \quad p_D \rightarrow 0 \\ T &\rightarrow T_E \quad T_D \rightarrow 0. \end{aligned}$$

Thus at first order

$$\lim_{\bar{\eta} \rightarrow \infty} u_1 = 0$$

$$V_1(\xi, 0) = 0$$

$$\lim_{\bar{\eta} \rightarrow \infty} p_1 = 0$$

$$\lim_{\bar{\eta} \rightarrow \infty} t_1 = 0$$

$$\lim_{\bar{\eta} \rightarrow \infty} \rho_1 = 0.$$

The conditions on  $p$ ,  $\rho$  and  $T$  are not independent since they are linked through the state equation. The condition on  $v$  is not a boundary condition for the inner expansion but it gives the wall condition for the outer flow.

The wall conditions for the inner flow are

$$\begin{aligned} u &= U_1 + u_1 + \varepsilon(U_2 + u_2) = 0 \\ v &= \varepsilon \bar{v}_1 + \varepsilon^2 \bar{v}_2 = 0 \\ T &= T_1 + t_1 + \varepsilon(T_2 + t_2) = T_w \end{aligned}$$

hence

$$u_1(\xi, 0) = -U_1(\xi, 0)$$

$$v_1(\xi, 0) = 0$$

$$t_1(\xi, 0) = T_w - T_1(\xi, 0).$$

Using the above conditions, the first order  $\eta$ -momentum equation reduces to

$$p_1 = 0.$$

So, the pressure in the first-order boundary layer is everywhere equal to the local inviscid flow pressure, instead of its wall value as in Van Dyke's theory.

#### 4.4. APPLICATIONS

To investigate the defect approach, several cases have been selected for a blunt body in a hypersonic flow of ideal gas. The general shape of the body is a planar or axisymmetric hyperboloid, defined by the nose radius and the angle of the asymptotes, at zero degree incidence. The numerical data are given by Shinn, Moss and Simmonds<sup>(171)</sup> for a hyperboloid equivalent to the windward symmetry line of the U.S. space shuttle. Two points of the re-entry trajectory of the STS-2 flight are considered here.

The Prandtl number is assumed to be constant and equal to 0.725. The ratio of specific heats  $\gamma$  is 1.4. The wall temperature is fixed and equal to 1500 K. Sutherland's viscosity law is used. No comparison with experimental data is possible since the real gas effects are not yet included. So Navier-Stokes solutions<sup>(104)</sup> have been taken as reference, to compare the standard and the defect Euler + boundary layer methods. Euler calculations are made with a code from ONERA.<sup>(191)</sup> Only first-order boundary layer solutions are presented here since second-order outer flow solutions are not yet available. Several second-order calculations using Van Dyke's theory have been made on a hypersonic blunt body.<sup>(2,50,49,62,63)</sup>

Boundary layer profiles are displayed on Figs 29–32 for the Mach 23.4 case. Longitudinal velocity profiles are plotted in Fig. 29 at a distance of nine nose radii from the stagnation point. One can see on this figure the important velocity gradient at the wall in the inviscid flow. This gradient diminishes distinctly between the wall and the boundary layer edge. So even with a second-order expansion, Van Dyke's method could not give a good matching, since it considers only the wall value of the gradient. In this case, it would widely overestimate the skin friction (Adams<sup>(2)</sup>). Due to the very low wall temperature compared to the inviscid flow, the displacement effect is quasi-null and the Navier-Stokes solution recasts exactly the inviscid profile in the outer region. In this case, the agreement is quite good with the first-order defect boundary layer. A composite profile has also been plotted, using the additive composite expansion (Van Dyke<sup>(187)</sup>) constructed with the first order inner and outer expansions. It gives good results for the longitudinal velocity, slightly different from the defect ones.

The corresponding profiles for the temperature are shown in Fig. 30. The defect profile is in rather good agreement with the Navier-Stokes solution, but in this case the composite expansion written with Van Dyke's first order solutions gives disappointing results and does not improve the inner solution. This is due to the negative slope at the wall for the inviscid temperature. Figures 31 and 32 show the velocity and temperature profiles at

Reentry trajectory—Flight STS-2

Mach $M_\infty$	26.6	23.4
Time (s)	250	650
Altitude (km)	85.74	71.29
Nose radius $R_0$ (m)	1.322	1.253
Asymptotes half-angle ( $^\circ$ )	41.7	40.2
Pressure $p_\infty$ (Pa)	0.3634	4.0165
Temperature $T_\infty$ (K)	199	205
Velocity $U_\infty$ ( $m \cdot s^{-1}$ )	7530	6730
Density $\rho_\infty$ ( $kg \cdot m^{-3}$ )	$6.35 \cdot 10^{-6}$	$6.80 \cdot 10^{-5}$
Reference temperature $T_0$ (K)	56321	44900
Reynolds number $Re = \frac{\rho_\infty U_\infty R_0}{\mu(T_0)}$	183.55	1865.65
Small parameter $\varepsilon = Re^{-1/2}$	0.074	0.023
Reynolds number $Re_\infty = \frac{\rho_\infty U_\infty R_0}{\mu_\infty}$	4792	42374

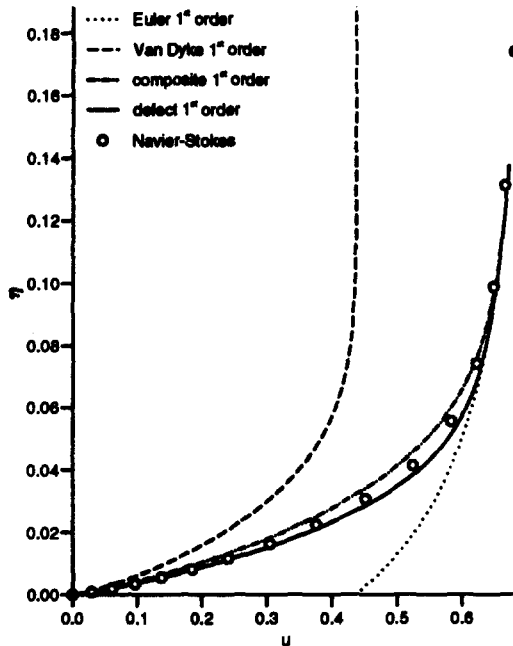


FIG. 29. Longitudinal velocity profiles  $M = 23.4$ ,  $T_w = 1500\text{ K}$ ,  $\xi = 9$ , axisymmetric.

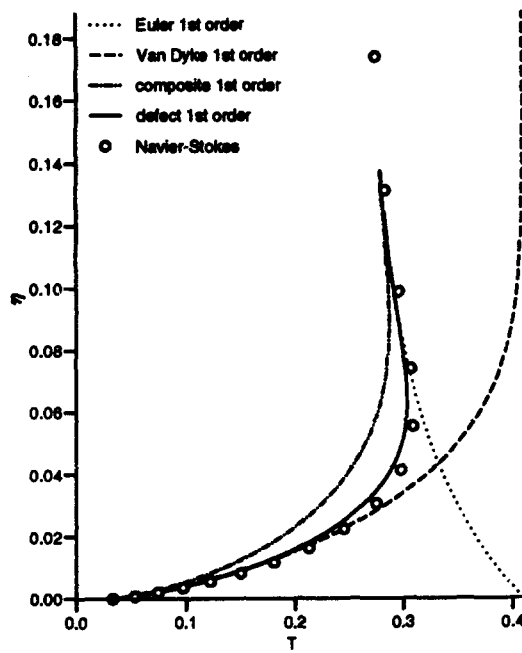


FIG. 30. Temperature profiles  $M = 23.4$ ,  $T_w = 1500\text{ K}$ ,  $\xi = 9$ , axisymmetric.

21 nose radii. The growing boundary layer has overlapped a larger part of the entropy layer. Because of the constant total enthalpy, the positive velocity gradient at the wall induces a negative temperature gradient. In spite of this, the wall heat flux is increased by the vorticity, as well as the skin friction, as can be seen in Figs 33 and 34. But the increase is far more important for the wall friction than for the flux. The defect approach underestimates slightly these quantities but gives better predictions than the standard boundary layer.

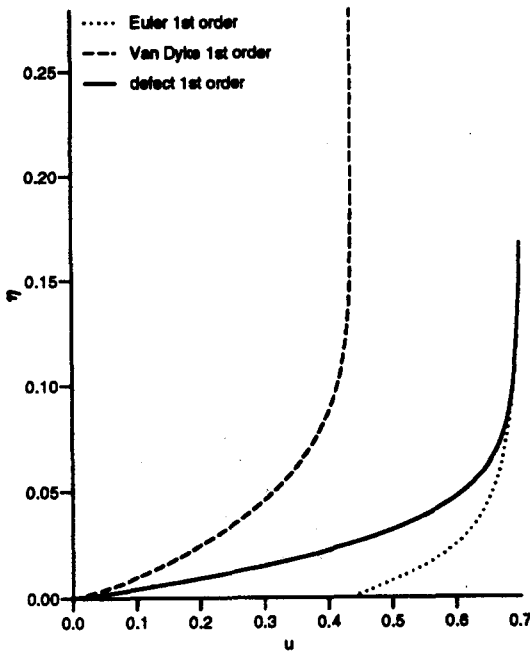


FIG. 31. Velocity profiles  $M = 23.4$ ,  $T_w = 1500$  K,  $\xi = 21$ , axisymmetric.

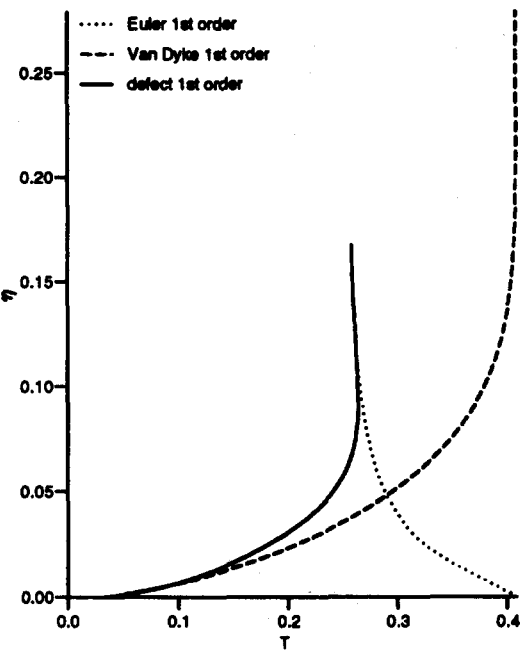


FIG. 32. Temperature profiles  $M = 23.4$ ,  $T_w = 1500$  K,  $\xi = 21$ , axisymmetric.

Let us now consider a planar hyperbola in the same conditions of hypersonic flows. In Figs 35 and 36 are plotted the velocity and temperature profiles on the Mach 23.4 hyperbola at nine nose radii abscissa. The inviscid gradients are hardly visible outside the boundary layer and all the methods give the same results.

When the Reynolds number is lower, the matching of the boundary layer with the inviscid flow takes place in the gradient region, as can be seen in Figs 37 and 38 for the case

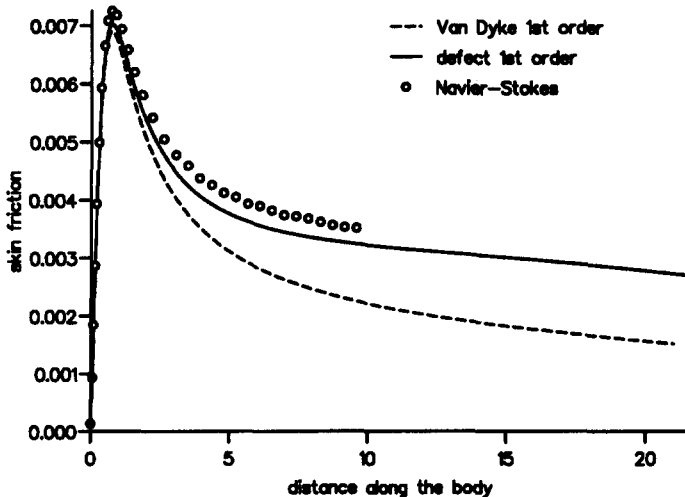


FIG. 33. Skin friction on the hyperboloid— $M = 23.4$ ,  $T_w = 1500$  K, axisymmetric.

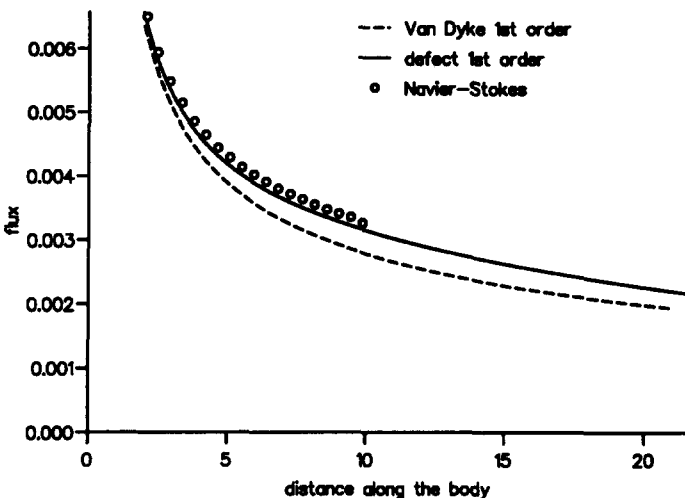


FIG. 34. Wall heat flux on the hyperboloid— $M = 23.4$ ,  $T_w = 1500$  K, axisymmetric.

of Mach 26.6. The defect method gives a good matching and a correct agreement with Navier-Stokes solutions, but the two boundary layer methods give similar results near the wall. Thus no significant difference is visible on the skin friction and the wall heat flux shown in Figs 39 and 40.

#### 4.5. CONCLUSION

The few examples presented here showed on the one hand the validity of boundary layer methods to compute hypersonic flows and on the other hand the importance of taking into account the second order effects when calculating boundary layers at low Reynolds numbers. The most important of them are the entropy gradient effect and the displacement effect. They can deeply modify the wall quantities such as the skin friction or the wall heat flux, which is essential in the design of the thermal protection of the vehicle.

Using the matched asymptotic expansions technique, the defect approach allows us to improve the standard higher-order boundary layer theory of Van Dyke, for a similar cost.

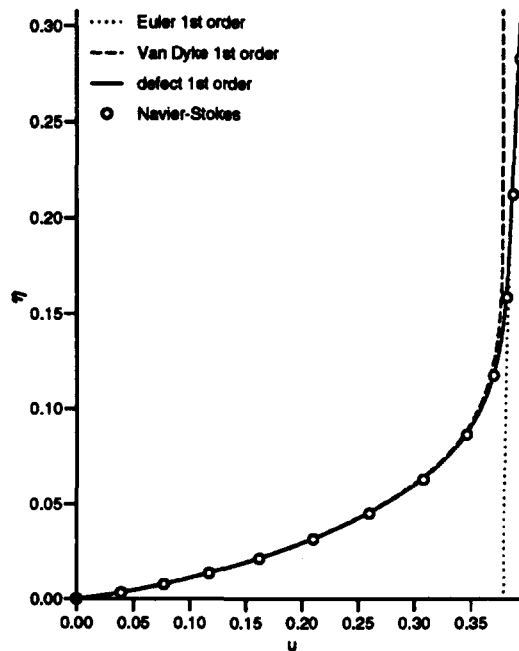


FIG. 35. Longitudinal velocity profiles  $M = 23.4$ ,  $T_w = 1500$  K,  $\xi = 9$ , planar flow.

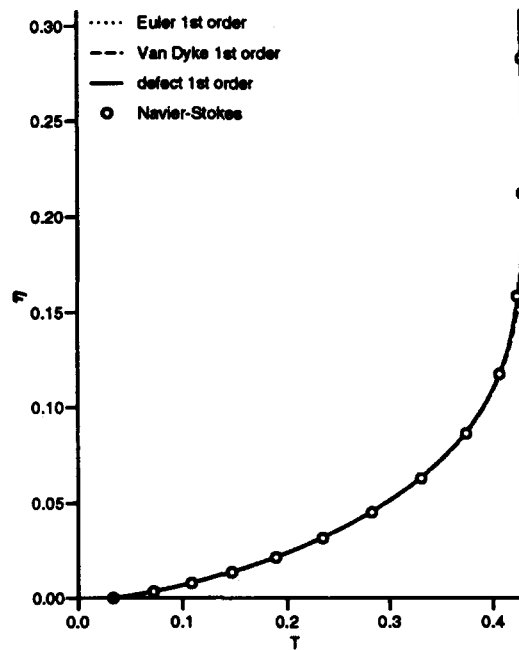


FIG. 36. Temperature profiles  $M = 23.4$ ,  $T_w = 1500$  K,  $\xi = 9$ , planar flow.

In particular, it ensures a smooth matching of the viscous and inviscid flows, even when the inviscid profiles vary significantly across the boundary layer. When the wall temperature is low and thus the displacement effect is negligible, first-order defect calculations can give good results and reproduce Navier-Stokes solutions with a reasonable accuracy at a lower cost. It could then be a valuable tool for design tasks.

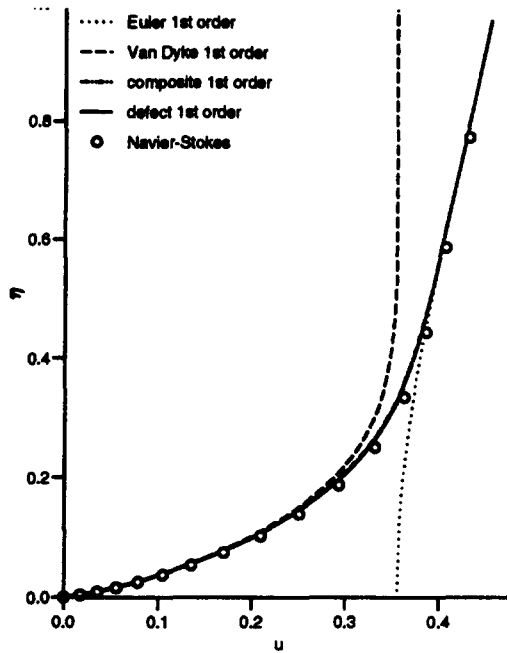


FIG. 37. Longitudinal velocity profiles  $M = 26.6$ ,  $T_w = 1500$  K,  $\xi = 9$ , planar flow.

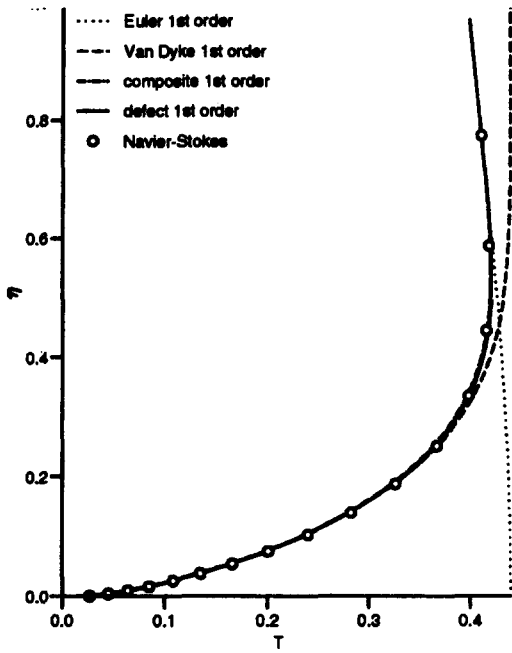


FIG. 38. Temperature profiles  $M = 26.6$ ,  $T_w = 1500$  K,  $\xi = 9$ , planar flow.

## 5. SHOCK LAYER COMPUTATION

### 5.1. APPROXIMATION LEVELS FOR THE SHOCK LAYER COMPUTATION

Computation of the hypersonic flow in the shock layer can be performed by solving the full set of equations given in Section 2.6, and that will be called hereafter Navier-Stokes equations (NS). However, solving the NS equations requires a very large amount of

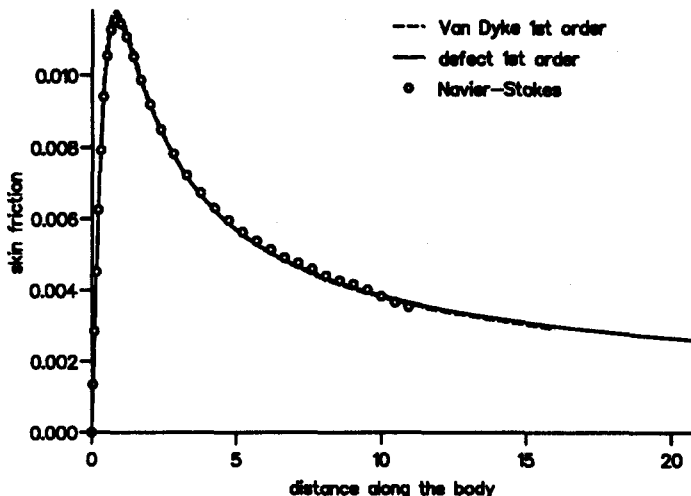


FIG. 39. Skin friction on the hyperbola— $M = 26.6$ ,  $T_w = 1500$  K, planar flow.

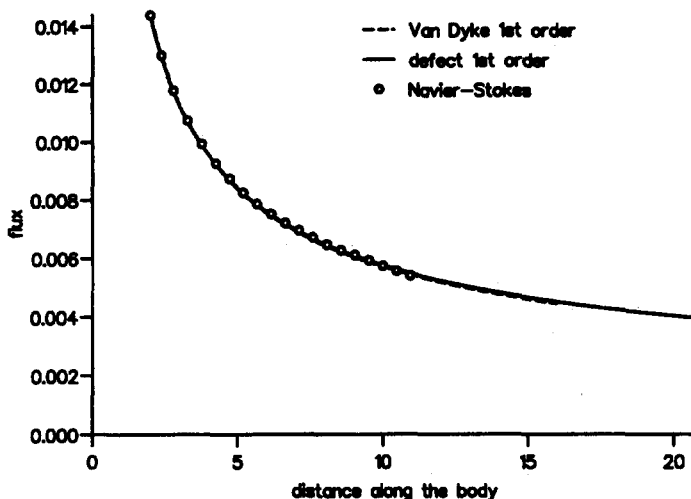


FIG. 40. Wall heat flux on the hyperbola— $M = 26.6$ ,  $T_w = 1500$  K, planar flow.

computer time and storage. It must be recalled that when solving the NS equations for a steady flow, a time marching method is usually retained since the steady NS equations are a mixed set of elliptic-parabolic equations while the unsteady form is a mixed set of hyperbolic-parabolic equations. It means that the unsteady NS equations are integrated in time till convergence to the steady-state solution. To reduce the computation time and storage, it has been proposed to “parabolize” the NS equations in the streamwise direction in order that the resulting set of equations can be solved using a space-marching technique. Since the method is aimed to compute the full shock layer, this simplified set of equations has to be applicable both to viscous and inviscid regions. Several sets of equations have been proposed that fall between the NS equations and the boundary layer equations, but all share a common feature: for steady flows, they are a mixed set of hyperbolic-parabolic equations in the streamwise direction.

### 5.1.1. VSL and PNS Equations

Historically, the first such set of equations is the viscous shock layer equations (VSL) introduced by Davis in 1970 for blunt body computations.<sup>(48)</sup> The VSL equations are

obtained by first splitting the shock layer into an inner viscous region and an outer inviscid region. The flow in each region is described by a set of equations derived from the NS equations by introducing variables which are of order one in that region and retaining terms up to second order in  $\epsilon = Re^{-1/2}$ , where  $Re$  is the Reynolds number based on the freestream quantities and the radius of the blunt body nose. The VSL equations are then obtained by combining the two sets of equations, in order to get a single set of equations uniformly valid in the shock layer up to second order in  $\epsilon$ . Originally derived under the perfect gas assumption, the VSL equations have been extended to take into account real gas effects (see Ref. 180 for example). Although the applicability domain of the VSL equations is limited (in particular, they cannot be used to compute flowfields with crossflow separation), they provide a valuable and efficient model to test complex real gas effects (chemistry scheme, nonequilibrium effects, wall catalicity).

A more complex set of equations in this class of hyperbolic-parabolic equations in the streamwise direction is known as the Parabolized Navier-Stokes equations (PNS), obtained in 1973 by Lubard and Helliwell<sup>(116)</sup> from the steady NS equations by dropping all viscous terms containing partial derivatives with respect to the streamwise coordinate. This set of equations is actually a mixed set of hyperbolic-parabolic equations provided that certain conditions are ensured. First, the outer inviscid flow must be supersonic. Second, the streamwise velocity component must be positive everywhere (precluding the simulation of reverse flow, but flowfields with crossflow separation may be computed). Third, the streamwise pressure gradient must be properly treated in order to avoid upstream influence through subsonic portions of the flowfield such as boundary layers. Indeed, if the full streamwise pressure gradient is retained, a space-marching procedure is not well posed and stability problems are generally encountered, leading to exponentially growing solutions, also known as "departure solutions". The precise influence of the streamwise pressure gradient on the mathematical nature of the PNS equations has been analyzed by Vigneron *et al.*<sup>(194)</sup> Introducing a coefficient  $\omega$  in front of the streamwise pressure gradient term in the streamwise momentum equations, it follows from the analysis that the PNS equations are indeed a mixed set of hyperbolic-parabolic equations in the streamwise direction, provided only a fraction  $\omega$  of the streamwise pressure gradient is retained in subsonic layers, with

$$\omega = \min\left(1, \frac{\gamma M_{sw}^2}{1 + (\gamma - 1)M_{sw}^2}\right)$$

where  $M_{sw}$  denotes the streamwise Mach number. The analysis of Vigneron *et al.* has greatly contributed to clarify the stability problems often encountered with the PNS equations when the full streamwise pressure gradient is retained. Following this work, the numerical computation of the PNS equations has gained a lot of popularity. Much of the studies are performed by retaining, in the subsonic layer, only the fraction  $\omega$  of the streamwise pressure gradient and neglecting the remaining part. Progress has been made from a numerical point of view by implementing sophisticated upwind type schemes in the discretization process allowing for a better capture of strong discontinuities that may occur in hypersonic flows.<sup>(110,178,105)</sup> Real gas effects have also been introduced using the PNS concept, leading to very efficient methods for the computation of complex three-dimensional nonequilibrium flowfields.<sup>(152)</sup> For a more complete account on PNS solvers, the reader is referred to the review paper by Lawrence.<sup>(109)</sup>

### 5.1.2. NS and TLNS Equations

The other main avenue for the computation of the shock layer for hypersonic flows is to solve the complete Navier-Stokes equations or a very similar set of equations, namely the thin layer Navier-Stokes equations (TLNS), which are obtained from the NS equations by dropping all viscous terms containing derivatives parallel to the body surface. Both NS and TLNS equations allow the computation of separated and reverse flows. Also, both systems are a mixed elliptic-parabolic set of equations for steady flows and thus are usually solved by using a time marching procedure. However, due both to the increase in computer

resources and progress in the discretization techniques, numerical solutions of NS and TLNS equations are now available. It must be stressed that development of efficient and accurate NS solvers is a key aspect in the field of hypersonic flows, since wind tunnel tests cannot simulate the flow conditions for the complete reentry trajectory of a space vehicle.

Section 5.2 is devoted to the exposure of a modern numerical method to compute the TLNS equations for hypersonic flows in chemical nonequilibrium. The choice has been made to give a detailed presentation of one such algorithm rather than an overview of the variety of algorithms that can be used for this purpose, ranging from finite element to finite volume type schemes. Indeed, due to space limitations, such an overview would have been limited to a very general presentation with poor informative and comprehensive interest for the reader. Contrary to this, it is felt that the current choice would give the reader a clear idea of the potential (efficiency and accuracy) of a modern finite volume type scheme for hypersonic flow computations for solving the TLNS equations.

## 5.2. A NUMERICAL ALGORITHM FOR NS AND TLNS EQUATIONS

### 5.2.1. Conservation-law Form

#### 5.2.1.1. Conservation-law form in cartesian coordinates

The Navier–Stokes equations for a mixture of perfect gases in chemical nonequilibrium are given in Section 2.6. They may be written in a form that is more suitable for the derivation of the numerical method. That is the conservation law form of the differential equation, where the time rate of change of the vector of conserved quantities is balanced by the gradients of the inviscid and viscous flux vectors as well as the source term vector. In two-dimensions, the governing equations are

$$\frac{\partial U}{\partial t} + \frac{\partial E_i}{\partial x} + \frac{\partial F_i}{\partial y} = \frac{\partial E_v}{\partial x} + \frac{\partial F_v}{\partial y} + S \quad (49)$$

where the following notations have been used:  $U$  vector of conservative variables,  $E_i$  inviscid flux vector along the  $x$  coordinate,  $F_i$  inviscid flux vector along the  $y$  coordinate,  $E_v$  viscous flux vector along the  $x$  coordinate,  $F_v$  viscous flux vector along the  $y$  coordinate, and  $S$  source term vector.

The expression of the vectors  $U$ ,  $E_i$ ,  $F_i$ ,  $E_v$ ,  $F_v$  is given below

$$U = [\rho_1, \rho_2, \dots, \rho_n, \rho u, \rho v, E]^T$$

$$E_i = [\rho_1 u, \rho_2 u, \dots, \rho_n u, \rho u^2 + p, \rho uv, u(E + p)]^T$$

$$F_i = [\rho_1 v, \rho_2 v, \dots, \rho_n v, \rho uv, \rho v^2 + p, v(E + p)]^T$$

$$E_v = \begin{bmatrix} -q_1^x \\ \vdots \\ -q_n^x \\ \tau_{xx} \\ \tau_{xy} \\ u\tau_{xx} + v\tau_{xy} - \sum_{I=1}^n h_I q_I^x - q_{th}^x \end{bmatrix} \quad F_v = \begin{bmatrix} -q_1^y \\ \vdots \\ -q_n^y \\ \tau_{xy} \\ \tau_{yy} \\ u\tau_{xy} + v\tau_{yy} - \sum_{I=1}^n h_I q_I^y - q_{th}^y \end{bmatrix}$$

$$S = [\dot{\omega}_1, \dot{\omega}_2, \dots, \dot{\omega}_n, 0, 0, 0]^T$$

with the following notations:  $n$  number of species in the mixture,  $u$  mass-averaged velocity component in the  $x$  direction,  $v$  mass-averaged velocity component in the  $y$  direction,  $E$  total energy per unit volume;  $E = \rho e + \rho(u^2 + v^2)/2$ ,  $q_I^x$  mass diffusion flux of species  $I$  in the  $x$  direction,  $q_I^y$  mass diffusion flux of species  $I$  in the  $y$  direction,  $q_{th}^x$  thermal heat flux in the  $x$  direction,  $q_{th}^y$  thermal heat flux in the  $y$  direction.

The modelisation of the mass diffusion fluxes  $q_i$ , thermal heat flux  $q_{th}$  has been discussed in Section 2.6. The evaluation of the chemical production rates  $\dot{\omega}_i$  was discussed in Section 2.5.

### 5.2.1.2. Conservation-law form in curvilinear coordinates

Equation 49 is written in cartesian coordinates. To compute flows around arbitrary geometries, it is more appropriate to use a more general coordinate system  $(\xi, \eta)$ . Let us introduce the Jacobian  $J$  of this coordinate transformation  $J = \partial(\xi, \eta)/\partial(x, y)$ . The transformed equation now reads

$$\frac{\partial \hat{U}}{\partial t} + \frac{\partial \hat{E}_i}{\partial \xi} + \frac{\partial \hat{F}_i}{\partial \eta} = \frac{\partial \hat{E}_v}{\partial \xi} + \frac{\partial \hat{F}_v}{\partial \eta} + \frac{S}{J} \quad (50)$$

where

$$\hat{U} = U/J; \quad \hat{E}_i = \left( \frac{\partial \xi}{\partial x} E_i + \frac{\partial \xi}{\partial y} F_i \right) / J; \quad \hat{F}_i = \left( \frac{\partial \eta}{\partial x} E_i + \frac{\partial \eta}{\partial y} F_i \right) / J$$

and similar formulae for  $\hat{E}_v$  and  $\hat{F}_v$ .

### 5.2.1.3. Thin-layer Navier–Stokes equations

For body-fitted coordinates, with  $\eta$  denoting the direction normal to the wall, the thin layer approximation consists of neglecting all  $\xi$  derivatives occurring in the viscous terms.<sup>(154)</sup> This approximation, valid for sufficiently high Reynolds numbers (typically  $Re > 10^4$ ) is supported both by the fact that viscous gradients parallel to the body are substantially smaller than those normal to the body but also by the fact that, generally, for such flows, the mesh is made dense only in the direction normal to the body and therefore the neglected terms would not be adequately resolved if retained. Upon simplifying the complete NS Eq. 50 using the thin layer approximation, the TLNS are given by

$$\frac{\partial \hat{U}}{\partial t} + \frac{\partial \hat{E}_i}{\partial \xi} + \frac{\partial \hat{F}_i}{\partial \eta} = \frac{\partial \hat{F}_v^*}{\partial \eta} + \frac{S}{J} \quad (51)$$

where  $\hat{F}_v^*$  is derived from  $\hat{F}_v$  by dropping all  $\xi$  derivatives.

## 5.2.2. Basic Features of the Numerical Method

### 5.2.2.1. Coupling between fluid motion and chemical reactions

One approach to compute the NS or TLNS equations for a chemically nonequilibrium flow is to uncouple the fluid equations and the species equations. Such an approach is easier to implement for extending an existing perfect gas solver to include nonequilibrium chemistry effects. However the uncoupled procedure has deficiencies. First, the set of  $n$  species equations is replaced by the global continuity equation plus  $n - 1$  species equations: the solution of the absent species will suffer a loss of numerical accuracy and it may happen that negative values of the corresponding species density are obtained since it is equal to the total density minus the sum of the  $n - 1$  other species densities. Second, it must be stressed that the coupling between species equations and fluid equations is crucial when energy transfer between the translational and chemical modes is important. A small variation in the species concentrations may induce a relatively large variation in the internal energy. Further, a small temperature variation may cause a large change in chemical production rates due to the exponential dependance of the rate coefficients on the temperature. Because of these deficiencies, a fully coupled strategy has been preferred, where all the equations are solved simultaneously. Another advantage of the fully coupled strategy when modern shock-capturing schemes are used is that better capture of discontinuities is expected since one uses the true eigenvalues and eigenvectors.<sup>(204)</sup>

### 5.2.2.2. Explicit versus implicit schemes

Equations 50 and 51 can be thought of as a convection–diffusion-reaction type system. The relative magnitudes of these three phenomena (that is convection, diffusion, reaction) can be measured in terms of dimensionless numbers. Let us remind ourselves that the Reynolds number represents the ratio of the diffusion time scale to the convection and the Damköhler number represents the ratio of the reaction time scale to the convection (Section 2.1.3). An important feature of nonequilibrium flows is that the time scale associated to the various reactions may differ from several orders of magnitude and, more importantly, some of the reactions time scales (e.g. those near equilibrium) can be much smaller than the convection time scale. This phenomenon, known as the stiffness problem, has an important consequence on the stability of time integration schemes to be used for solving Eqs 50 or 51. To illustrate the point, let us consider the linear model reaction–convection equation

$$v_t + av_x = \mu v. \quad (52)$$

The constant  $\mu$  is assumed negative, to satisfy the stability condition for the equilibrium state  $v = 0$ . This assumption is consistent with the general fact that chemical reactions always drive the chemical variables towards their equilibrium values.<sup>(146)</sup> Let us then consider a simple spatial discretization for Eq. 52: first order upwind for the convection and pointwise evaluation for the reaction. It reads

$$\frac{dv_j}{dt} = -\frac{a}{\Delta x}(v_j - v_{j-1}) + \mu v_j$$

where spatial nodes are indexed with the subscript  $j$  and the mesh spacing  $\Delta x$  is assumed constant. Using an explicit type time integration (e.g. explicit Euler), the fully discrete counterpart of 52 is

$$v_j^{n+1} - v_j^n = -\frac{a\Delta t}{\Delta x}(v_j^n - v_{j-1}^n) + \mu\Delta t v_j^n$$

where the superscript  $n$  is the time index. Using an implicit type time integration (e.g. implicit Euler) for the reaction term, the fully discrete counterpart of 52 is

$$v_j^{n+1} - v_j^n = -\frac{a\Delta t}{\Delta x}(v_j^n - v_{j-1}^n) + \mu\Delta t v_j^{n+1}.$$

From a classical Von Neumann stability analysis,<sup>(88)</sup> one easily obtains the expression of the amplification factor  $G(\phi, \Delta t, \Delta x)$ , where  $\phi$  denotes the phase angle of the linearized perturbation. For the explicit scheme, it is given by

$$G(\phi, \Delta t, \Delta x) = 1 - \frac{a\Delta t}{\Delta x}[1 - \exp(-I\phi)] + \mu\Delta t$$

while, for the implicit case, one has

$$G(\phi, \Delta t, \Delta x) = \left[ 1 - \frac{a\Delta t}{\Delta x}[1 - \exp(-I\phi)] \right] / [1 - \mu\Delta t].$$

The restriction on the time step value follows from the requirement that the amplification factor should be less than unity for any phase angle. This implies, for the explicit scheme

$$\frac{a\Delta t}{\Delta x} < \frac{1}{1 + 2D_a} \quad (53)$$

while, for the implicit case,

$$\frac{a\Delta t}{\Delta x} < 1 \quad (54)$$

where the number  $D_a = -\mu\Delta x/a$  has been introduced ( $\mu < 0$ ). Condition 54 is the classical CFL condition for the pure convection equation. Thus, using an implicit scheme for the

reaction term in Eq. 52 results in no further restriction on the time step. On the opposite, with an explicit time integration, a severe constraint exists for large values of the number  $D_a$  (see condition 53). The conclusion of this simple analysis is that implicit treatment of the source term  $S$  in Eqs 50, 51 is expected to speed up the solution procedure. When the stiffness is entirely dominated by the source terms (inviscid case), semi-implicit methods have been proposed where the convective part is treated explicitly while the source term is treated implicitly. However, for solving viscous flows as described by Eqs 50 and 51, stiffness may also arise from the viscous terms and implicit treatment of the viscous terms would be more efficient. Further, for steady-state computations, a fully implicit method is advised since it will reduce the time step constraints resulting from an explicit treatment of the inviscid part (see Eq. 54) without significant increase in the computational cost if an appropriate implicit strategy technique is used for the inviscid terms. This will be discussed in Section 5.2.4.

### 5.2.2.3. Classical versus modern shock-capturing schemes

An important characteristic of hypersonic flows is the existence of strong discontinuities (shock waves, contact discontinuities). The existence of such discontinuities is linked to the hyperbolic nature of the inviscid part of Eqs 50 and 51. Historically, space-centred schemes have been first used for the discretization of the inviscid terms. Since they do not reflect the physical propagation of perturbations along the characteristics, typical of hyperbolic problems, some type of artificial dissipation must be introduced to damp out oscillations and, in particular, allow the capture of discontinuities. However, the appropriate amount of artificial dissipation to add in order to get stable and accurate results is not easy to devise. These so-called classical shock-capturing schemes usually give oscillatory solutions across strong discontinuities. Such deficiencies can be eliminated by using modern shock-capturing schemes based on upwinding techniques. Upwind techniques aim to introduce in the design of the schemes physical properties of the Euler equations (inviscid part of Eqs 50 and 51). In the class of upwind type schemes, one can distinguish flux vector splitting (FVS) and flux difference splitting (FDS) methods. FVS methods introduce a first level of physical properties in the discretization process since the flux are split and discretized according to the signs of the propagation speeds (that is the eigenvalues of the flux Jacobian matrix). With FDS methods, a higher level of physical properties is taken into account since such schemes are based locally on the exact or approximate solution of the Euler equations. The exposure of the most popular such FDS scheme, namely Roe approximate Riemann solver, will be given in Section 5.2.3. For a very complete account on space-centred and upwind schemes for the discretization of the Euler equations (perfect gas case) the reader is referred to Ref. 88.

### 5.2.2.4. Finite volume formulation

The use of finite volume formulation for the discretization of conservation laws has become very popular, since it ensures at the discrete level the conservation of basic quantities such as mass, momentum and energy. Such formulation is obtained by integrating the conservation law equation on a discrete volume. Using Green theorem, the associated discrete counterpart of Eq. 51 is thus

$$\begin{aligned} \frac{\hat{U}_{j,k}^{n+1} - \hat{U}_{j,k}^n}{\Delta t} + \hat{E}_{i_{j+1/2},k}^{n+1} - \hat{E}_{i_{j-1/2},k}^{n+1} + \hat{F}_{i_{j,k+1/2}}^{n+1} - \hat{F}_{i_{j,k-1/2}}^{n+1} = \\ = \hat{F}_{v_{j,k+1/2}}^{n+1} - \hat{F}_{v_{j,k-1/2}}^{n+1} + \frac{S_{j,k}^{n+1}}{J_{j,k}} \end{aligned} \quad (55)$$

where  $j$  and  $k$  denote the indices along the  $\xi$  and  $\eta$  directions, while  $n$  is the time level index,  $\Delta t$  being the time step. According to the previous discussion about explicit versus implicit schemes, an implicit Euler time discretization is used. To complete the discretization

process, one must provide the formulae for the inviscid and viscous numerical fluxes as well as for the source term evaluation. The viscous terms being associated to a parabolic type problem, a standard centered scheme is used for the numerical viscous flux. The source term is evaluated at the center of the control volume. With regard to the inviscid numerical fluxes, the two-dimensional problem is split into two one-dimensional problems which are separately treated. Section 5.2.3 is devoted to the exposure of the discretization technique for the inviscid numerical flux  $\hat{E}_{i,j+1/2,k}$  along the  $\xi$  direction. A similar formula is derived for the inviscid numerical flux along the  $\eta$  direction.

### 5.2.3. Inviscid Flux Discretization

#### 5.2.3.1. Roe first-order FDS scheme

For the sake of simplicity, in this section, the inviscid flux  $E_i$  will be denoted  $\mathcal{E}$  and the index  $k$  will be omitted in the discretization formulae. That is,  $\mathcal{E}_{j+1/2}$  stands for  $E_{i,j+1/2,k}$ . Also, the detailed derivation of the inviscid numerical flux evaluation is carried out in the cartesian case. The formulation in the curvilinear case follows easily and will be given at the end of the present section.

The use of FDS schemes for the discretization of hyperbolic conservation laws (e.g. Euler equations) can be traced back to Godunov.<sup>(76)</sup> Godunov proposed to approximate the solution, at each time level, by a piecewise constant function (two constant states being separated by the cell interfaces) and then advance the solution by solving, at each interface, the resulting Riemann problem. Such strategy introduces a great amount of physics into the discretization process. However, it is time consuming since the exact solution of the Riemann problem requires solving in an iterative manner a non linear equation. Godunov ideas have thus been further extended by replacing the exact Riemann solver by an approximate Riemann solver, requiring less computational work. Roe<sup>(156,157)</sup> proposed to use a linearized approximate Riemann problem at cell interface  $j + 1/2$

$$\frac{\partial U}{\partial t} + \bar{A} \frac{\partial U}{\partial x} = 0 \quad (56)$$

where  $\bar{A} = \bar{A}_{j+1/2}(U_j, U_{j+1})$  is a constant matrix to be evaluated at cell interface  $j + 1/2$ . The average matrix  $A_{j+1/2}$  is sought with the following properties<sup>(157)</sup>

- (1)  $\mathcal{E}_{j+1} - \mathcal{E}_j = \bar{A}_{j+1/2}(U_{j+1} - U_j)$ ,
- (2)  $\bar{A}_{j+1/2}$  has real eigenvalues with linearly independent eigenvectors,
- (3)  $\bar{A}_{j+1/2}(U, U) = A(U)$ ,

where  $A = \partial \mathcal{E} / \partial U$  is the Jacobian matrix associated to the inviscid flux  $\mathcal{E}$ . The main feature of the Roe approximate Riemann solver is that it gives the exact solution whenever  $U_j$  and  $U_{j+1}$  lie on opposite sides of a shock wave or contact discontinuity. The expression of the matrix  $\bar{A}_{j+1/2}$  is discussed in the next paragraph. Roe averaging is an attractive way to define a characteristic field decomposition. This method, sometimes referred to as the “local characteristic approach”, allows an effective approximate local decoupling of the original non-linear system, providing a convenient framework to extend high order Total Variation Diminishing (TVD) schemes, developed for scalar hyperbolic laws, to non-linear systems of equations (see Ref. 203 and below). Indeed, let us denote  $\bar{\Lambda}_{j+1/2}$  the diagonal matrix whose diagonal elements are the eigenvalues  $\bar{a}_{j+1/2}^l$  of  $\bar{A}_{j+1/2}$ ,  $\bar{R}_{j+1/2}$  the matrix whose columns are the associated eigenvectors of  $\bar{A}_{j+1/2}$  and  $\bar{R}_{j+1/2}^{-1}$  its invert. Then, defining the local characteristic variables  $W = \bar{R}_{j+1/2}^{-1} U$ , Eq. 56 is transformed into a system of uncoupled scalar equations

$$\frac{\partial W}{\partial t} + \bar{\Lambda}_{j+1/2} \frac{\partial W}{\partial x} = 0. \quad (57)$$

Applying a first-order upwind scheme to each of the scalar characteristic equations and

transforming back to the original variables  $U$ , one gets

$$\mathcal{E}_{j+1/2} = \frac{1}{2}[\mathcal{E}_j + \mathcal{E}_{j+1} + \Phi_{j+1/2}] \quad (58)$$

with

$$\Phi_{j+1/2} = -\bar{R}_{j+1/2}|\bar{\Lambda}_{j+1/2}|\bar{R}_{j+1/2}^{-1}\Delta_{j+1/2}U; \quad \Delta_{j+1/2}U = U_{j+1} - U_j \quad (59)$$

where  $|\bar{\Lambda}|$  is the diagonal matrix whose diagonal elements are the absolute values of the diagonal elements of  $\bar{\Lambda}$ . The numerical flux evaluation  $\mathcal{E}_{j+1/2}$  given by Eq. 58 leads to a first-order upwind scheme, known as Roe scheme. It is made up of a second-order centered part plus the first-order upwind correction  $\Phi_{j+1/2}$ , that can be considered as some dissipative corrective term. The extension of Roe scheme to second-order accuracy is discussed below. A well-known deficiency of Roe scheme is that it is not consistent with an entropy inequality and might converge to a non-physical solution (e.g. expansion shock). A classical fix to this problem has been proposed by Harten,<sup>(85)</sup> where in Eq. 59  $|\bar{\Lambda}|$  is replaced by the diagonal matrix  $\psi(\bar{\Lambda})$  whose diagonal elements are  $\psi(\bar{a}_{j+1/2}^l)$ . The function  $\psi$  is given by

$$\psi(z) = \begin{cases} |z| & \text{if } |z| \geq \delta; \\ (z^2 + \delta^2)/2\delta & \text{if } |z| < \delta \end{cases}$$

where  $\delta$  is a small positive parameter. One can see the magnitude of  $\delta$  as a measure of the amount of numerical dissipation of the scheme: the larger  $\delta$  is, the more dissipative the scheme becomes.

### 5.2.3.2. Roe average

The matrix  $\bar{A}_{j+1/2}$  associated with the Roe linearized approximate Riemann problem is obtained as the Jacobian matrix  $A$  of the flux, evaluated at some average state  $\bar{U}$ . For a perfect gas, the first property to be satisfied by the matrix (see above) uniquely defines this average state. One gets<sup>(157)</sup>

$$\bar{u} = \frac{u_j + Du_{j+1}}{1 + D}; \quad \bar{v} = \frac{v_j + Dv_{j+1}}{1 + D}; \quad \bar{H} = \frac{H_j + DH_{j+1}}{1 + D}$$

with  $D = \sqrt{\rho_{j+1}/\rho_j}$ . For a mixture of gases, the above relations are completed by

$$\bar{Y}_I = \frac{Y_{I,j} + DY_{I,j+1}}{1 + D} \quad 1 \leq I \leq n$$

plus the condition

$$\sum_{I=1}^n \bar{\chi}_I \Delta \rho_I + \bar{\kappa} \Delta(\rho e) = \Delta p \quad (60)$$

where  $\Delta(.) = (.)_{j+1} - (.)_j$  denotes the jump across the interface  $j + 1/2$ . The coefficients  $\chi_I$  and  $\kappa$  are the partial derivatives of the pressure  $p$  with regard to the species densities  $\rho_I$  and the internal energy  $\rho e$

$$dp = \sum_{I=1}^n \chi_I d\rho_I + \kappa d(\rho e). \quad (61)$$

For a perfect gas,  $\chi_I = 0$ ,  $\kappa = \gamma - 1$  and Eq. 60 is automatically satisfied. It is no longer true for a mixture of gases where condition 60 does not give a unique way to determine Roe average state. Various formulations have thus been proposed to extend Roe average state for a mixture of gases. Following Montagné *et al.*<sup>(133, 196)</sup> the values  $\bar{\chi}_I$  and  $\bar{\kappa}$  are obtained by integrating Eq. 61 along the straight line path between states  $U_j$  and  $U_{j+1}$  in the  $\rho_I, \rho e$  space

$$\bar{\chi}_I = \int_0^1 \chi_I[\rho_I(\tau), \rho e(\tau)] d\tau; \quad \bar{\kappa}_I = \int_0^1 \kappa_I[\rho_I(\tau), \rho e(\tau)] d\tau \quad (62)$$

where

$$\rho_I(\tau) = \rho_{I,j} + \tau \Delta \rho_I; \quad \rho e(\tau) = (\rho e)_j + \tau \Delta(\rho e).$$

Numerical integration of Eq. 62 provides approximate values  $\hat{\chi}_I$  and  $\hat{\kappa}$ . For example, using the trapezoidal rule, one has:  $\hat{\chi}_I = (\chi_{I,j} + \chi_{I,j+1})/2$ ,  $\hat{\kappa} = (\kappa_j + \kappa_{j+1})/2$ . These approximate values no longer satisfy condition 60 and this approximate state is thus projected onto the straight line defined by Eq. 60. The resulting state is

$$\bar{\chi}_I = \frac{b\hat{\chi}_I + s^2 \Delta \rho_I \delta p}{b - \Delta p \delta p}; \quad \bar{\kappa} = \frac{b\hat{\kappa}}{b - \Delta p \delta p}$$

with

$$b = \Delta p^2 + \sum_{I=1}^n (s \Delta \rho_I)^2; \quad \delta p = \Delta p - \hat{\kappa} \Delta(\rho e) - \sum_{I=1}^n \hat{\chi}_I \Delta \rho_I; \quad s = [a_{f,j}^2 + a_{f,j+1}^2]/2$$

where  $a_f$  denotes the frozen speed of sound:  $a_f^2 = \sum_{I=1}^n Y_I \chi_I + kh$ .

With the above expression of Roe average state for a mixture of gases, the expression of the matrices  $\bar{A}_{j+1/2}$ ,  $\bar{\Lambda}_{j+1/2}$ ,  $\bar{R}_{j+1/2}$  and  $\bar{R}_{j+1/2}^{-1}$  are

$$\bar{A}_{j+1/2} = \begin{pmatrix} (1 - \bar{Y}_1)\bar{u} & -\bar{Y}_1\bar{u} & \dots & -\bar{Y}_1\bar{u} & \bar{Y}_1 & 0 & 0 \\ -\bar{Y}_2\bar{u} & (1 - \bar{Y}_2)\bar{u} & \dots & -\bar{Y}_2\bar{u} & \bar{Y}_2 & 0 & 0 \\ \vdots & \vdots & \ddots & \vdots & \vdots & \vdots & \vdots \\ -\bar{Y}_n\bar{u} & -\bar{Y}_n\bar{u} & \dots & (1 - \bar{Y}_n)\bar{u} & \bar{Y}_n & 0 & 0 \\ (-\bar{u}^2 + \bar{\alpha}_1) & (-\bar{u}^2 + \bar{\alpha}_2) & \dots & (-\bar{u}^2 + \bar{\alpha}_n) & (2 - \bar{\kappa})\bar{u} & -\bar{\kappa}\bar{v} & \bar{\kappa} \\ -\bar{u}\bar{v} & -\bar{u}\bar{v} & \dots & -\bar{u}\bar{v} & \bar{v} & \bar{u} & 0 \\ \bar{u}(\bar{\alpha}_1 - \bar{H}) & \bar{u}(\bar{\alpha}_2 - \bar{H}) & \dots & \bar{u}(\bar{\alpha}_n - \bar{H}) & (\bar{H} - \bar{\kappa}\bar{u}^2) & -\bar{\kappa}\bar{u}\bar{v} & \bar{u}(1 + \bar{\kappa}) \end{pmatrix}$$

$$\bar{\Lambda}_{j+1/2} = [\bar{u}, \bar{u}, \dots, \bar{u}, \bar{u} + \bar{a}_f, \bar{u}, \bar{u} - \bar{a}_f]^T$$

$$\bar{R}_{j+1/2} = \frac{1}{\bar{a}_f^2} \begin{pmatrix} 1 & 0 & \dots & 0 & \bar{Y}_1 & 0 & \bar{Y}_1 \\ 0 & 1 & \dots & 0 & \bar{Y}_2 & 0 & \bar{Y}_2 \\ \vdots & \vdots & \ddots & \vdots & \vdots & \vdots & \vdots \\ 0 & 0 & \dots & 1 & \bar{Y}_n & 0 & \bar{Y}_n \\ \bar{u} & \bar{u} & \dots & \bar{u} & \bar{u} + \bar{a}_f & 0 & \bar{u} - \bar{a}_f \\ 0 & 0 & \dots & 0 & \bar{v} & 1 & \bar{v} \\ -\frac{\bar{\chi}_1}{\bar{\kappa}} + \bar{u}^2 & -\frac{\bar{\chi}_2}{\bar{\kappa}} + \bar{u}^2 & \dots & -\frac{\bar{\chi}_n}{\bar{\kappa}} + \bar{u}^2 & \bar{H} + \bar{u}\bar{a}_f & \bar{v} & \bar{H} - \bar{u}\bar{a}_f \end{pmatrix}$$

$$\bar{R}_{j+1/2}^{-1} = \begin{pmatrix} \bar{a}_f^2 - \bar{Y}_1\bar{\alpha}_1 & -\bar{Y}_1\bar{\alpha}_2 & \dots & -\bar{Y}_1\bar{\alpha}_n & \bar{Y}_1\bar{\kappa}\bar{u} & \bar{Y}_1\bar{\kappa}\bar{v} & -\bar{Y}_1\bar{\kappa} \\ -\bar{Y}_2\bar{\alpha}_1 & \bar{a}_f^2 - \bar{Y}_2\bar{\alpha}_2 & \dots & -\bar{Y}_2\bar{\alpha}_n & \bar{Y}_2\bar{\kappa}\bar{u} & \bar{Y}_2\bar{\kappa}\bar{v} & -\bar{Y}_2\bar{\kappa} \\ \vdots & \vdots & \ddots & \vdots & \vdots & \vdots & \vdots \\ -\bar{Y}_n\bar{\alpha}_1 & -\bar{Y}_n\bar{\alpha}_2 & \dots & \bar{a}_f^2 - \bar{Y}_n\bar{\alpha}_n & \bar{Y}_n\bar{\kappa}\bar{u} & \bar{Y}_n\bar{\kappa}\bar{v} & -\bar{Y}_n\bar{\kappa} \\ \frac{(-\bar{u}\bar{a}_f + \bar{\alpha}_1)}{2} & \frac{(-\bar{u}\bar{a}_f + \bar{\alpha}_2)}{2} & \dots & \frac{(-\bar{u}\bar{a}_f + \bar{\alpha}_n)}{2} & \frac{(\bar{a}_f - \bar{u}\bar{\kappa})}{2} & \frac{-\bar{\kappa}\bar{v}}{2} & \frac{\bar{\kappa}}{2} \\ -\bar{v}\bar{\alpha}_1 & -\bar{v}\bar{\alpha}_2 & \dots & -\bar{v}\bar{\alpha}_n & \bar{\kappa}\bar{u}\bar{v} & \bar{a}_f^2 + \bar{\kappa}\bar{v}^2 & -\bar{\kappa}\bar{v} \\ \frac{(\bar{u}\bar{a}_f + \bar{\alpha}_1)}{2} & \frac{(\bar{u}\bar{a}_f + \bar{\alpha}_2)}{2} & \dots & \frac{(\bar{u}\bar{a}_f + \bar{\alpha}_n)}{2} & \frac{(-\bar{a}_f - \bar{u}\bar{\kappa})}{2} & \frac{-\bar{\kappa}\bar{v}}{2} & \frac{\bar{\kappa}}{2} \end{pmatrix}$$

where  $\bar{\alpha}_I = \bar{\chi}_I + \bar{\kappa}(\bar{u}^2 + \bar{v}^2)/2$  and  $\bar{H} = \bar{h} + (\bar{u}^2 + \bar{v}^2)/2$  is the total enthalpy.

### 5.2.3.3. Second-order TVD extension

Roe scheme, as defined by relations 58, 59, is first-order accurate due to the first-order upwind correction. Improving the accuracy while maintaining the oscillation free shock-capturing properties of the scheme can be done in the framework of TVD schemes. The theory of TVD schemes has been developed by Harten<sup>(84, 85)</sup> for scalar hyperbolic conservation laws and can be formally extended to systems by using the local characteristic approach. Let us consider a scalar hyperbolic conservation law

$$u_t + f_x(u) = 0 \quad (63)$$

and let  $(u_j^n)$  denote the discrete solution. The total variation of the discrete solution  $u^n$  is defined as

$$TV(u^n) = \sum_j |u_{j+1}^n - u_j^n|.$$

A scheme for the scalar Eq. 63 is said to be TVD if

$$TV(u^{n+1}) \leq TV(u^n).$$

The TVD property is compatible with the behavior of the exact solution of 63 and ensures that the scheme will not introduce oscillations near discontinuities. TVD schemes thus have excellent shock-capturing capabilities. Following the work of Harten, a large number of studies have been devoted to the construction and improvement of TVD schemes (see Ref. 203 for a review). Most of the resulting TVD schemes can be viewed as a spatially three-point central difference scheme with an added appropriate numerical dissipation mechanism ensuring the TVD property. A popular procedure to get second-order TVD schemes is to modify an existing first-order upwind TVD scheme. This procedure usually involves some kind of limiting techniques called limiters in order to satisfy the TVD property. Let us thus first start with Roe first-order upwind scheme for the scalar Eq. 63 (see also formulae 58 and 59)

$$f_{j+1/2} = \frac{1}{2} [f_j + f_{j+1} + \phi_{j+1/2}]; \quad \phi_{j+1/2} = -\psi(a_{j+1/2})\Delta_{j+1/2}u$$

with

$$a_{j+1/2} = \begin{cases} (f_{j+1} - f_j)/\Delta_{j+1/2}u & \text{if } u_j \neq u_{j+1}; \\ \frac{df}{du}(u_j) & \text{if } u_j = u_{j+1}; \end{cases} \quad \Delta_{j+1/2}u = u_{j+1} - u_j.$$

Second-order extension is obtained by modifying the numerical dissipation term  $\phi_{j+1/2}$ . Various formulations have been proposed, among which a good compromise between accuracy and efficiency is obtained with the so-called Yee–Roe–Davis TVD scheme<sup>(203)</sup> where

$$\phi_{j+1/2} = -\psi(a_{j+1/2})[\Delta_{j+1/2} - Q_{j+1/2}]$$

and

$$Q_{j+1/2} = \minmod(\Delta_{j-1/2}, \Delta_{j+1/2}, \Delta_{j+3/2}).$$

The minmod function of a list of arguments is equal to the smallest number in absolute value if the list of arguments is of the same sign, or is equal to zero if any arguments are of opposite sign. Other forms for the limiting function  $Q$  are available.

Going back to the system case and using the local characteristic approach, the present second-order TVD scheme is applied to each of the scalar characteristic equations (see Eq. 57). Transforming back to the original variables  $U$ , one gets

$$\mathcal{E}_{j+1/2} = \frac{1}{2} [\mathcal{E}_j + \mathcal{E}_{j+1} + \Phi_{j+1/2}];$$

$$\Phi_{j+1/2} = -\bar{R}_{j+1/2}\psi(\bar{\Lambda}_{j+1/2})[\bar{R}_{j+1/2}^{-1}\Delta_{j+1/2}U - Q_{j+1/2}] \quad (64)$$

where the components of  $Q_{j+1/2}$  are

$$Q_{j+1/2}^l = \text{minmod}(\alpha_{j-1/2}^l, \alpha_{j+1/2}^l, \alpha_{j+3/2}^l) \quad (65)$$

with  $\alpha_{j+1/2} = \bar{R}_{j+1/2}^{-1} \Delta_{j+1/2} U$ .

#### 5.2.3.4. Final form

The expression of the inviscid flux discretization in the curvilinear case is easily obtained from the previous expression 64 in the cartesian case, since the linearized approximate Riemann problem now involves the matrix  $\hat{A} = \partial \hat{E}_i / \partial \hat{U}$ . It gives

$$\hat{E}_{i,j+1/2} = \frac{1}{2} \left[ \left( \frac{\xi_x}{J} \right)_{j+1/2} (E_{i,j} + E_{i,j+1}) + \left( \frac{\xi_y}{J} \right)_{j+1/2} (F_{i,j} + F_{i,j+1}) + \left( \frac{|\text{grad } \xi|}{J} \right)_{j+1/2} \hat{\Phi}_{j+1/2} \right] \quad (66)$$

with

$$\hat{\Phi}_{j+1/2} = -\bar{R}_{j+1/2} \psi(\bar{\Lambda}_{j+1/2}) [\bar{R}_{j+1/2}^{-1} \Delta_{j+1/2} U - \hat{Q}_{j+1/2}] \quad (67)$$

where  $|\text{grad } \xi| = \sqrt{\xi_x^2 + \xi_y^2}$  and  $\hat{Q}$  has the same expression as 65 with  $\alpha_{j+1/2} = \bar{R}_{j+1/2}^{-1} \Delta_{j+1/2} U$ . The matrices  $\bar{\Lambda}$  and  $\bar{R}$  are associated to the eigenvalues and eigenvectors of the matrix  $\hat{A}/|\text{grad } \xi|$ . Introducing the rotation matrix  $T$ , the variables  $\tilde{U}$  and the flux  $\tilde{E}_i$ , such that

$$T = \begin{pmatrix} 1 & 0 & \cdots & 0 & 0 & 0 & 0 \\ 0 & 1 & \cdots & 0 & 0 & 0 & 0 \\ \vdots & \vdots & \ddots & \vdots & \vdots & \vdots & \vdots \\ 0 & 0 & \cdots & 1 & 0 & 0 & 0 \\ 0 & 0 & \cdots & 0 & \cos \theta & \sin \theta & 0 \\ 0 & 0 & \cdots & 0 & -\sin \theta & \cos \theta & 0 \\ 0 & 0 & \cdots & 0 & 0 & 0 & 1 \end{pmatrix}; \quad \cos \theta = \frac{\xi_x}{|\text{grad } \xi|}; \quad \sin \theta = \frac{\xi_y}{|\text{grad } \xi|}$$

$$\tilde{U} = TU = \begin{pmatrix} \rho_1 \\ \rho_2 \\ \vdots \\ \rho_n \\ \rho \tilde{u} \\ \rho \tilde{v} \\ E \end{pmatrix} \quad \tilde{E}_i = \frac{J}{|\text{grad } \xi|} T \hat{E}_i = \begin{pmatrix} \rho_1 \tilde{u} \\ \rho_2 \tilde{u} \\ \vdots \\ \rho_n \tilde{u} \\ \rho \tilde{u}^2 + p \\ \rho \tilde{u} \tilde{v} \\ \tilde{u}(E + p) \end{pmatrix}$$

one gets

$$\frac{1}{|\text{grad } \xi|} \hat{A} = T^{-1} \tilde{A} T; \quad \tilde{A} = \frac{\partial \tilde{E}_i}{\partial \tilde{U}}.$$

It follows

$$\hat{\Lambda} = \tilde{\Lambda}; \quad \hat{R} = T^{-1} \tilde{R}$$

where  $\tilde{\Lambda}$  and  $\tilde{R}$  are the matrices respectively defined with the eigenvalues and eigenvectors associated to the matrix  $\tilde{A}$ . They are given by expressions identical to those derived above in the cartesian case with  $u$  and  $v$  replaced by  $\tilde{u}$  and  $\tilde{v}$ .

#### 5.2.4. Linearization and Relaxation Algorithm

The value of  $U^{n+1}$  is obtained as the solution of a system of nonlinear algebraic equations (see Eq. 55). To approximately solve this set of nonlinear equations in a noniterative

manner, a linearized version of this nonlinear system is considered. Using a so-called delta formulation, where the unknown is the increment  $D = U^{n+1} - U^n$  between two time levels, we get

$$(LHS)^n D = -(RHS)^n. \quad (68)$$

The right-hand-side  $RHS$  in Eq. 68 is evaluated at the old time level  $n$ . It contains the inviscid, viscous and source term contributions as given by the above discussed discretization process. The left-hand-side  $LHS$  coefficient matrix is also evaluated from time level  $n$ . Since we are only interested in steady-state solutions, the  $LHS$  term may be some kind of approximation of the exact Jacobian associated to the  $RHS$  term. Indeed, when convergence is attained, the converged steady-state solution exactly satisfies  $RHS = 0$ .

The  $LHS$  matrix is obtained from a Taylor development around time level  $n$ . The source term gives only a contribution to the central coefficient (associated to  $D_{j,k}$ ), while the viscous terms involve coefficients to  $D_{j-1,k}$ ,  $D_{j,k}$ ,  $D_{j+1,k}$  since they have been discretized with a three point central difference scheme. For the inviscid numerical fluxes, only the first order contribution is implicitly treated. It gives contributions to the central term  $D_{j,k}$  and its immediate neighbors  $D_{j-1,k}$ ,  $D_{j+1,k}$ ,  $D_{j,k-1}$  and  $D_{j,k+1}$  while the second-order inviscid flux discretization involves a five point stencil in each space direction.

Finally, the resulting linear system can be written

$$A^W D_{j-1,k} + A^S D_{j,k-1} + A^P D_{j,k} + A^N D_{j,k+1} + A^E D_{j+1,k} = -(RHS)_j^n, \quad (69)$$

where  $A^W$ ,  $A^S$ ,  $A^P$ ,  $A^N$ ,  $A^E$  are  $(n+3) \times (n+3)$  matrices. This linear system is solved using a line relaxation algorithm along the  $\xi$  direction. Such strategy allows a fully implicit treatment of viscous terms. System 69 is thus written

$$\mathcal{A}_j^n \mathcal{D}_j = -(RHS)_j^n - \mathcal{B}_j^n \mathcal{D}_{j-1} - \mathcal{C}_j^n \mathcal{D}_{j+1} \quad (70)$$

where  $\mathcal{D}_j = (D_{j,k})_k$ ;  $\mathcal{A}_j^n$  is a block tri-diagonal matrix whose non-zero diagonals are filled with the coefficient matrices  $A^S$ ,  $A^P$ ,  $A^N$ , and  $\mathcal{B}_j^n$  (resp.  $\mathcal{C}_j^n$ ) is a block diagonal matrix whose diagonal elements are the coefficient matrices  $A^W$  (resp.  $A^E$ ). The tri-diagonal matrix  $\mathcal{A}_j^n$  is inverted using the classical Thomas algorithm. The relaxation method thus consists of solving system 70 by backward and forward sweeps across the computational domain until convergence.

### 5.3. RESULTS FOR TLNS COMPUTATIONS

To conclude this section on shock layer computations, a few sample results are given to illustrate the ability of the above described TLNS solver to compute a wide range of flow conditions and to give accurate predictions of viscous dominated regions (e.g. boundary layer) as well as to accurately capture strong discontinuities (e.g. shock waves).

#### 5.3.1. Flat Plate

Results for the flowfield relaxation along a flat plate of 1 m length with various non-equilibrium upstream conditions are first presented. This purely theoretical test case has been investigated in order to validate the ability of the present solver to give an accurate prediction of the boundary layer and to compute a wide range of flow conditions (from equilibrium to frozen type). The chosen free stream temperature and velocity are  $T_\infty = 8000$  K and  $U_\infty = 3000$  m s $^{-1}$  while three different values of the pressure are considered ( $P_\infty = 10^4$ ,  $10^3$ ,  $10^2$  Pa). Upstream of the plate, non-dissociated air is assumed. Since the chemical characteristic time is inversely proportional to the pressure, the ratio of the convective time and the chemical time is divided by 100 between case 1 ( $P_\infty = 10^4$  Pa) and case 3 ( $P_\infty = 10^2$  Pa). Indeed, the free stream conditions are such that the three cases are respectively associated to near-equilibrium, non-equilibrium and frozen type flow (with respect to O<sub>2</sub> chemical characteristic time). The computations are carried out using Park's data for the chemical rates.<sup>(144)</sup> For the diffusive terms modeling, constant Lewis and

Prandtl are assumed, respectively equal to 1.4 and 0.725. The wall is assumed to be fully catalytic with a prescribed temperature of 1500 K. Upstream of the plate, air is nondissociated (made up of  $N_2$  and  $O_2$ ). Due to the high temperature level ( $T_\infty = 8000$  K), the gas is in a non-equilibrium state and endothermic dissociation phenomena occur along the plate, leading to a decrease of both temperature and pressure towards their equilibrium values. A simplified analysis of the inviscid flowfield behavior at the edge of the boundary layer can be done using the one-dimensional Euler equations for reacting flows.<sup>(149)</sup> The evolutions of the temperature and NO mass fraction along the plate are plotted on Figs 41 and 42. One can see the relaxation phenomena towards equilibrium: the relaxation length is smaller for case 1 ( $P_\infty = 10^4$  Pa, near-equilibrium type flow) than for the other two cases. For case 1, NO is first created near the leading edge of the plate and then becomes unstable when the temperature decreases downstream: through exchange reactions  $N_2$  is then created and one can notice the typical maximum value occurring in the evolution of NO mass fraction. For the other two cases, the dissociation processes are slower and the temperature levels are higher.

The results given by the present TLNS solver have been compared with results from a boundary layer code.<sup>(158)</sup> For this flat plate test case, the two methods are expected to give similar results inside the boundary layer. The Reynolds number based on the free stream conditions and the length of the plate is equal respectively to 70,000, 7000 and 700 for cases 1, 2 and 3. In all three cases, good agreement has been observed between the two methods (see Ref. 149 for a detailed account): the largest discrepancies are obtained for case 3,

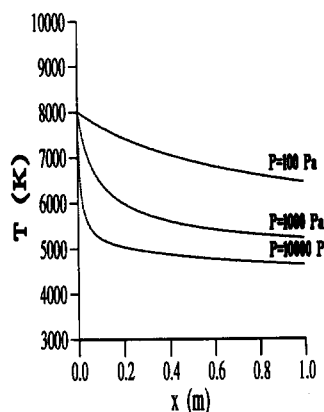


FIG. 41. Temperature along the plate.

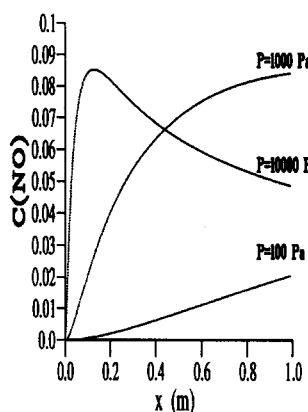


FIG. 42. NO mass fraction along the plate.

associated to a thicker boundary layer, hence a stronger leading edge shock wave. A comparison of the temperature profiles inside the boundary layer, 10 cm downstream the leading edge, is shown on Fig. 43, for case 3. A comparison of the wall heat fluxes is given on Fig. 44 for case 3: a similar agreement is obtained for the other two cases.

### 5.3.2. Double Ellipse

This second example has been proposed as a test case to validate computational methods for typical hypersonic reentry flow problems.<sup>(153)</sup> It consists of the hypersonic flow around a double ellipse at 30° angle of attack. The flow conditions are given in Table 2.

Park's chemical model is prescribed by the Workshop requirements. The diffusive terms are modelled using a constant Lewis number, equal to 1.2, the viscosity and conductivity coefficients being computed from Wilke formula<sup>(200)</sup> with Blottner<sup>(24)</sup> and Eucken relations<sup>(195)</sup> for the species coefficients. This test case involves several complex phenomena such as high nonequilibrium effects, strong shock wave, separation due to the compression near the canopy. A global description of the flowfield is given on Fig. 45, where the temperature contours are plotted. The large endothermic dissociation effects in the stagnation region result in large temperature gradients across the shock layer in this region. This is confirmed by looking at the temperature profile along the x-axis (see Fig. 46) where one can also notice the excellent shock-capturing capabilities of the scheme. The mass fraction

TABLE 2. FLOW CONDITIONS FOR THE DOUBLE ELLIPSE CASE

$M_\infty = 25$	$Re/m = 2.2 \cdot 10^4$	$\alpha = 30^\circ$
$P_\infty = 2.52 \text{ Pa}$	$T_\infty = 205.3 \text{ K}$	$H_\infty = 2.61 \cdot 10^7 \text{ J kg}^{-1}$
Half axis = 0.6 m	$T_w = 1500 \text{ K}$	non-catalytic wall

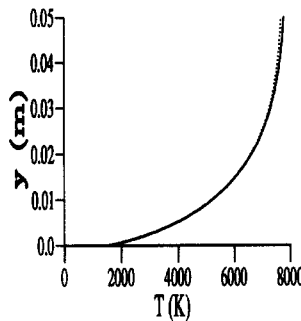


FIG. 43. Temperature profile: ... Boundary layer, — TLNS.

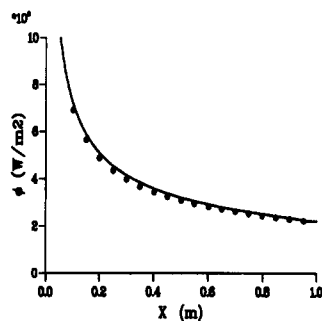


FIG. 44. Wall heat flux: ● Boundary layer, — TLNS.

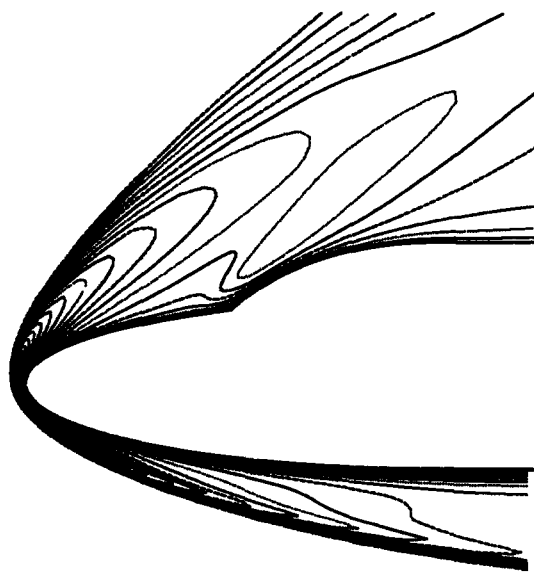


FIG. 45. Temperature contours.

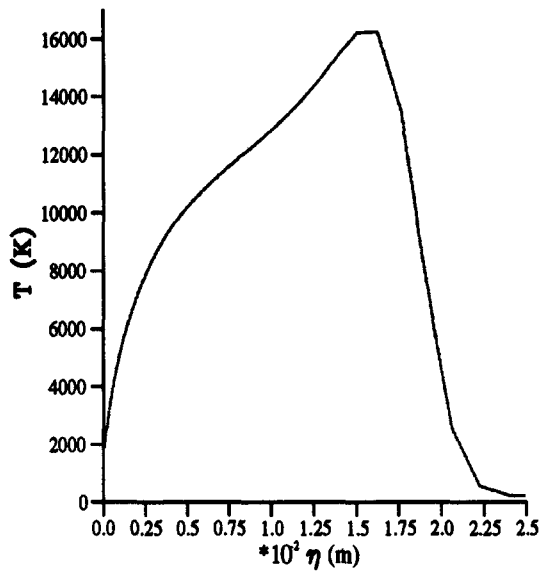


FIG. 46. Temperature profile along the x-axis.

profiles along the  $x$ -axis are shown in Fig. 47; almost all the oxygen is dissociated, against only 30% for the nitrogen. The evolution of the wall pressure coefficient  $C_p$ , skin-friction coefficient  $C_f$  and Stanton number  $S_t$  along the wall are plotted in Figs 48, 49 and 50. A small separation region near the canopy is noticeable from the  $C_f$  plot.

### 5.3.3. Hyperboloid

The hyperboloid geometry is chosen so as to model the flow over the windward symmetry plane of the American space shuttle. The half-angle  $\theta$  between the asymptotes is  $40.75^\circ$  and the nose radius  $R_n$  is 1.276 m. The free stream conditions and the geometry are taken from STS-2 flight,  $t = 460$  s (reentry time):  $M_\infty = 25.5$ ,  $U_\infty = 7200 \text{ m s}^{-1}$ ,

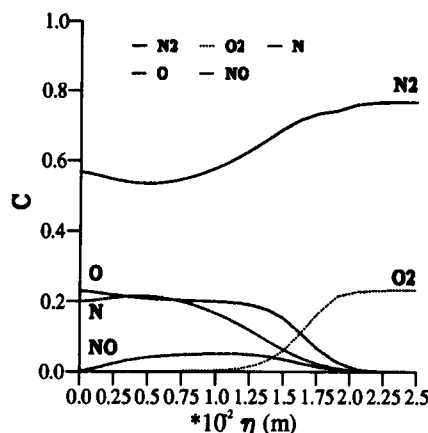


FIG. 47. Mass fraction profiles along the x-axis.

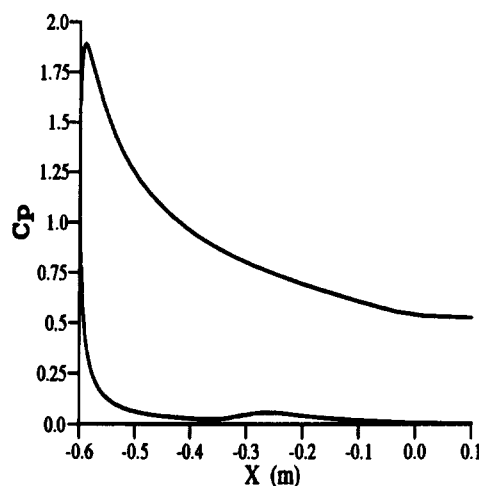


FIG. 48. Wall pressure coefficient.

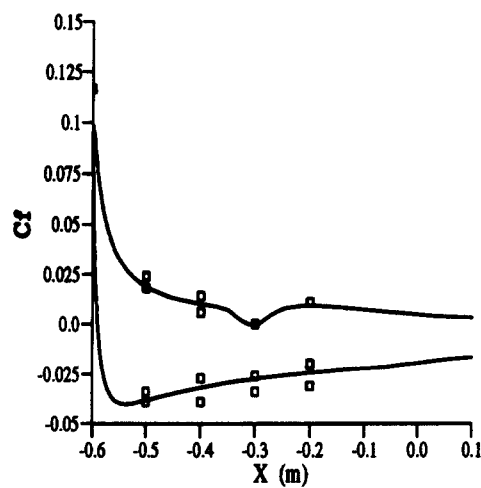


FIG. 49. Skin friction coefficient: □ Workshop results, — TLNS.

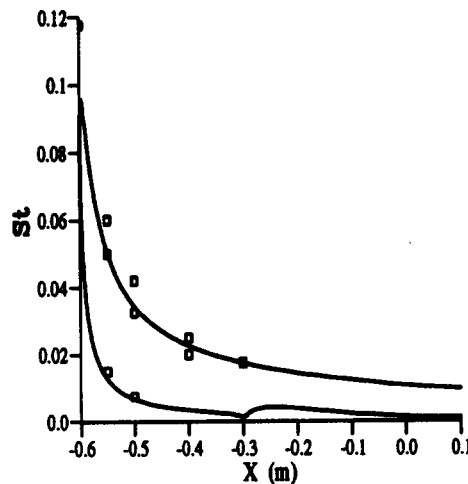


FIG. 50. Stanton number:  $\square$  Workshop results, — TLNS.

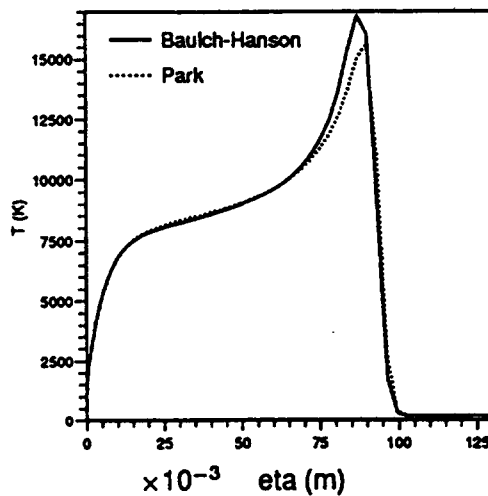


FIG. 51. Temperature profiles along the symmetry line.

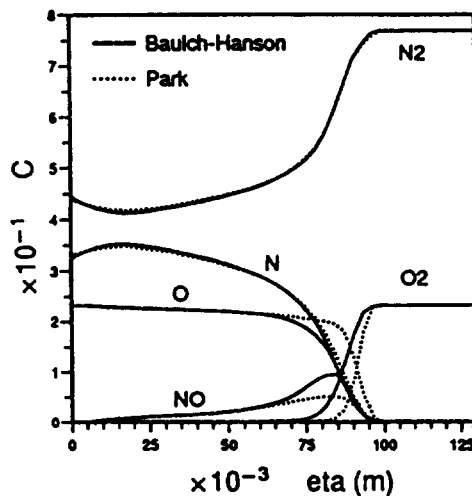


FIG. 52. Mass fraction profiles along the symmetry line.

$\rho_\infty = 3.815 \cdot 10^{-5} \text{ kgm}^{-3}$ ,  $Re = 2.7 \cdot 10^4$ . The same modeling for the diffusive terms as for the double ellipse case is chosen.

Comparisons between the present TLNS solver and a coupled Euler-second order boundary layer method developed by Sawley and Wütrich<sup>(202)</sup> are first presented. The temperature profiles normal to the wall at various locations along the hyperboloid are plotted in Fig. 53. Excellent agreement is found between the two methods throughout the shock layer. The only noticeable discrepancy occurs at the detached bow shock due to the fact that this shock wave is fitted in the Euler solver while it is captured with the present TLNS method. Good agreement is also found on the mass fraction profiles, the maximum discrepancies being observed for the NO mass fraction profiles (see Fig. 54).

Finally, to conclude this sample of results about shock layer computations, one would like to stress that a better understanding and prediction in hypersonic flowfields computations imply improvements in two major areas. The first area concerns further developments

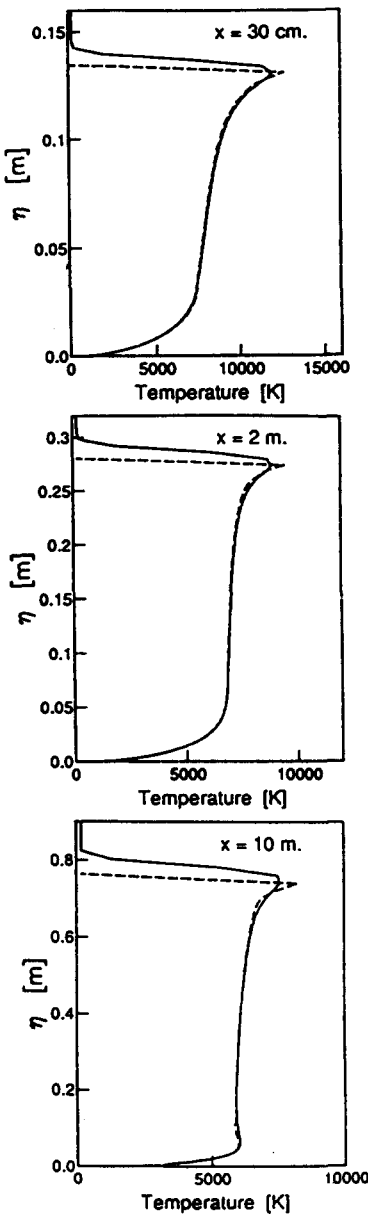


FIG. 53. Temperature profiles at  $x = 0.3 \text{ m}$ ,  $2 \text{ m}$ ,  $10 \text{ m}$ : — Euler/Boundary layer, — TLNS.

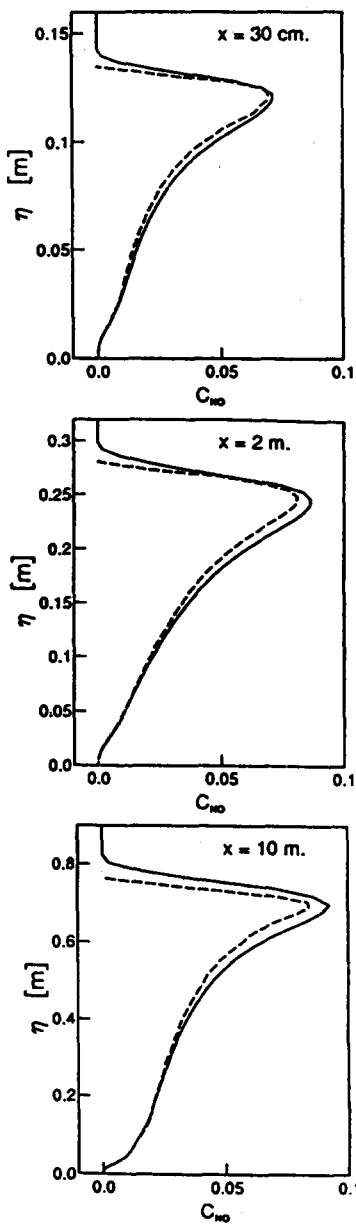


FIG. 54. NO mass fraction profiles at  $x = 0.3$  m, 2 m, 10 m: --- Euler/Boundary layer, —— TLNS.

in the field of computational methods in order to allow better efficiency and accuracy. One would like to point out here the specificity of hypersonic flow computations as compared to perfect gas computations due to the presence of stiff nonlinear source terms: for the moment the numerical treatment of these source terms has been largely ad-hoc. The second area that has strong consequences on the predictability of computational methods for hypersonic flows is linked to the validity of the models to be used to account for the real gas effects. To illustrate the importance of this aspect, results obtained for the hyperboloid geometry using two different chemistry models, namely Park and Baulch-Hanson models,<sup>(83)</sup> are shown. The temperature predicted by both models are quite similar and the discrepancy on the maximum temperature in the field is about 5% (see, in Fig. 51, the temperature profiles along the symmetry line). More significant effects are observed on the mass fraction profiles (see Fig. 52 where the mass fraction profiles along the symmetry line

are plotted). The maximum NO mass fraction with Baulch–Hanson's model is twice the one obtained using Park's model (see also Ref. 150).

## 6. TURBULENCE MODELS

### 6.1. FOREWORD

When the shuttle gets deeper into the atmosphere, the Reynolds number increases thanks to the rapid increase of the density. For a re-entry trajectory as shown in Fig. 1 and Table 1, the boundary layer becomes turbulent on the pressure side at altitudes about 40 km. Some high temperature gas phenomena may still be observed at the beginning of the turbulent regime. On the leeside, the density is lower due to the expansion so that transition occurs at lower altitudes.

Hypersonic turbulent boundary layers can also be encountered on hypersonic missiles or hypersonic air-breathing airplanes. High Mach numbers can be observed at the outer edge of the boundary layer but no reacting flow is encountered, except in the engine nozzle.

Large Mach numbers and large temperature gradients can be observed in hypersonic turbulent boundary layers. Such a situation affects the turbulent motion which may exhibit a compressible character. This section will be devoted to the present knowledge on compressible turbulence and turbulence modelling for hypersonic boundary layers. Unless otherwise mentioned, perfect gas flow will be assumed for the sake of simplicity.

### 6.2. MEAN AND TURBULENT MOTIONS

#### 6.2.1. *The Decomposition Problem*

For incompressible flows, values are split into a mean value (noted  $\bar{\cdot}$ ) and a fluctuation (noted  $'$ )

$$x = \bar{x} + x'; \quad \bar{x} = \langle x \rangle \quad (71)$$

where  $\langle \cdot \rangle$  denotes ensemble averaging. This is the usual Reynolds decomposition. For compressible flows, such a decomposition leads to complex equations for the mean motion. For example, the nonlinear part of the advection term in the momentum equation yields

$$\begin{aligned} \overline{\rho u \otimes u} &= (\bar{\rho} + \rho')(\bar{u} + u') \otimes (\bar{u} + u') = \overline{\rho u} \otimes \bar{u} + \overline{\rho u' \otimes u'} \\ &\quad + \overline{\rho' u' \otimes \bar{u}} + \bar{u} \otimes \overline{\rho' u'} + \overline{\rho' u' \otimes u'} \end{aligned} \quad (72)$$

where the last three terms of the right-hand-side are null for incompressible flows as  $\rho' = 0$ .

In order to obtain a simpler form for the mean flow equations, while using physically meaningful variables, Favre<sup>(64, 65)</sup> introduced mass-weighted averages, noted  $\tilde{\cdot}$  together with fluctuations noted  $\tilde{\cdot}'$ , defined as

$$x = \tilde{x} + x''; \quad \tilde{x} = \frac{\langle \rho x \rangle}{\langle \rho \rangle} = \langle x \rangle + \frac{\langle \rho' x' \rangle}{\langle \rho \rangle}. \quad (73)$$

#### 6.2.2. *Mean Flow Equations*

Otherwise mentioned, ensemble (Reynolds) averages will be used for the pressure and the density and mass-weighted (Favre) averages for the velocity field, the temperature, the gas internal energy and enthalpy ...

The mean flow equations are obtained by ensemble averaging of the Navier–Stokes equations. They are

$$\bar{p} = \bar{\rho} R \tilde{T} \quad (74)$$

$$\frac{\partial \bar{p}}{\partial t} + \operatorname{div}(\bar{\rho} \tilde{\mathbf{u}}) = 0 \quad (75)$$

$$\frac{\partial \bar{\rho} \tilde{\mathbf{u}}}{\partial t} + \operatorname{div}(\bar{\rho} \tilde{\mathbf{u}} \otimes \tilde{\mathbf{u}}) = \operatorname{div}(\bar{\tau} - \bar{p} \underline{\delta} - \overline{\rho \mathbf{u}'' \otimes \mathbf{u}''}) \quad (76)$$

$$\frac{\partial \bar{\rho} \tilde{H}}{\partial t} + \operatorname{div}(\bar{\rho} \tilde{\mathbf{u}} \tilde{H}) = \operatorname{div}(\bar{\tau} \cdot \bar{\mathbf{u}} - \bar{q}_t - \overline{\rho \mathbf{u}'' h''} - \tilde{\mathbf{u}} \cdot \overline{\rho \mathbf{u}'' \otimes \mathbf{u}''} - \frac{1}{2} \overline{\rho \mathbf{u}'' \cdot \mathbf{u}'' \otimes \mathbf{u}''}) + \frac{\partial \bar{p}}{\partial t} \quad (77)$$

where the energy Eq. 77 is here written for the stagnation enthalpy  $H$ . The viscous stress tensor  $\underline{\tau}$  and the heat flux  $\mathbf{q}_t$ , respectively read

$$\underline{\tau} = \mu \left[ \operatorname{grad} \mathbf{u} + ' \operatorname{grad} \mathbf{u} - \frac{2}{3} (\operatorname{div} \mathbf{u}) \underline{\delta} \right] \quad (78)$$

$$\mathbf{q}_t = -\lambda \operatorname{grad} T. \quad (79)$$

With this decomposition, the mean flow equations are similar to the equations governing a laminar flow. In incompressible flows, the only difference is the turbulent shear stresses. In compressible flows, on the one hand, turbulent stress and heat flux terms are added to the equations, and, on the other hand, the ensemble averages of the viscous stress or of the heat flux do not reduce to the laminar form because of fluctuations of the viscosity or of the thermal conductivity and because of differences between ensemble and mass-weighted averages as shown by Eq. 73. It is however often assumed that these terms can be approximated as

$$\begin{aligned} \bar{\tau} &\simeq \bar{\mu} \left( \operatorname{grad} \tilde{\mathbf{u}} + ' \operatorname{grad} \tilde{\mathbf{u}} - \frac{2}{3} (\operatorname{div} \tilde{\mathbf{u}}) \underline{\delta} \right) \\ \bar{q}_t &\simeq -\bar{\lambda} \operatorname{grad} \tilde{T} \\ \overline{\tau \cdot \mathbf{u}} &\simeq \bar{\tau} \cdot \tilde{\mathbf{u}}. \end{aligned}$$

### 6.2.3. Boundary Layer Equations

For boundary layer flows, the longitudinal velocity fluctuations are small compared to the longitudinal mean velocity and density fluctuations are weak. For a steady, two-dimensional boundary layer, the governing equations read, with the same notations as in Fig. 14

$$\bar{p} = \bar{\rho} R \tilde{T} \quad (80)$$

$$\frac{\partial \bar{\rho} \tilde{u} R^j}{\partial x} + \frac{\partial \bar{\rho} \tilde{v} R^j}{\partial y} = 0 \quad (81)$$

$$\bar{\rho} \tilde{u} \frac{\partial \tilde{u}}{\partial x} + \bar{\rho} \tilde{v} \frac{\partial \tilde{u}}{\partial y} = -\frac{d \bar{p}}{dx} + \frac{\partial \tau}{\partial y}; \quad \tau = \bar{\mu} \frac{\partial \tilde{u}}{\partial y} - \overline{\rho u'' v''} \quad (82)$$

$$0 = \frac{\partial \bar{p}}{\partial y} \quad (83)$$

$$\bar{\rho} \tilde{u} \frac{\partial H}{\partial x} + \bar{\rho} \tilde{v} \frac{\partial H}{\partial y} = \frac{\partial (\tilde{u} \tau - q_{ty})}{\partial y}; \quad q_{ty} = -\bar{\lambda} \frac{\partial \tilde{T}}{\partial y} + \overline{\rho v'' h''}. \quad (84)$$

Using Reynolds averaging, the same set of equations can be obtained with some reasonable simplifications.<sup>(37)</sup>

For hypersonic boundary layers, a better form for Eq. 83 is

$$\frac{\partial \bar{p}}{\partial y} = -\frac{\partial \overline{\rho v'' v''}}{\partial y} \quad (85)$$

which accounts for the normal pressure gradient induced by turbulence which can no longer be negligible.<sup>(103)</sup> Another plausible cause of normal pressure gradient in hypersonic boundary layers is the streamline curvature as pointed out by Fernholz and Finley.<sup>(68)</sup>

### 6.3. THE THREE MODES OF TURBULENCE

In incompressible flows, pressure fluctuations ensure the incompressibility. In compressible flow, the pressure fluctuates as other thermodynamic variables (e.g. density, temperature).

Kovasznay<sup>(65)</sup> brought into evidence three basic fluctuation modes, namely the vorticity, entropy and acoustic modes. When fluctuation levels are low, the equations for these modes are uncoupled. With viscous terms neglected, these equations read

$$\frac{\partial \omega_i''}{\partial t} = 0 \quad (86)$$

$$\frac{\partial s''}{\partial t} = 0 \quad (87)$$

$$\frac{1}{a^2} \frac{\partial^2 p'}{\partial t^2} - \frac{\partial^2 p'}{\partial x_k \partial x_k} = 0. \quad (88)$$

These equations state that the vorticity fluctuations  $\omega_i''$  and the entropy fluctuations  $s''$ , which are invariants in inviscid flows, are conserved while acoustic waves propagate at the speed of sound  $a$ .

For large fluctuation levels, a second order theory is needed to describe interactions between these modes.<sup>(65)</sup>

From experimental data analysis, Morkovin<sup>(135)</sup> brought into evidence that the entropy and acoustic modes are weak in a boundary layer if the external Mach number is smaller than five and the wall heat flux is moderate. No vorticity mode is generated from interactions between modes and the velocity fluctuations remain solenoidal.

Bradshaw<sup>(30)</sup> proposed to characterize the incompressible character of the turbulent motion by looking at the relative density fluctuation level  $\sqrt{\langle \rho'^2 \rangle / \langle \rho \rangle}$ . He suggested a limit of 10%, which corresponds to an external Mach number of five for flat plate boundary layers. Another proposed parameter to characterize the compressibility of the turbulent motion is the turbulent Mach number

$$M_t = \frac{\sqrt{\overline{u'' \cdot u''}}}{a}. \quad (89)$$

### 6.4. EXPERIMENTAL KNOWLEDGE OF COMPRESSIBLE TURBULENT FLOWS

In order to develop and validate good turbulence models, a large and reliable experimental database is required. Unfortunately, this is not so for compressible flows. An extensive review of compressible boundary layer data has been provided by Fernholz, Finley *et al.*<sup>(67-70)</sup> Few complete and reliable data are available for model validation as accurate measurements in high Mach number flows are very difficult to obtain. Moreover, more of the available boundary layer data are affected by low Reynolds number effects and memory of the transition region.

#### 6.4.1. Homogeneous Flows

Homogeneous turbulence, which is the simplest possible turbulent flow, has been widely studied in incompressible flows but not in compressible flows. Only Direct Numerical Simulations (DNS) of compressible turbulence are available for isotropic, sheared or

compressed turbulence.<sup>(22, 43, 164)</sup> Although such simulations are restricted to low Reynolds numbers flows, they give some important indications about the influence of the compressible character of the turbulent motion. For sheared turbulence, the asymptotic growing rate of the turbulent kinetic energy is decreased. This seems to be due both to a change in the turbulent stress tensor anisotropy and to an increase in the dissipation rate.

#### 6.4.2. Free Sheared Flows

A well-known example of the influence of the compressible character of the turbulent motion is the evolution of the spreading rate of a mixing layer which depends, as shown in Fig. 55, upon the convective Mach number, i.e. the Mach number based upon the difference between the free-stream velocity and the convection velocity of the coherent structures. When the same gas is used for both streams, the convective Mach number reduces to  $M_c = \frac{U_2 - U_1}{a_1 + a_2}$  where  $U$  is the velocity of the flow outside of the mixing layer,  $a$  its speed of sound and subscripts 1 and 2 refer to the two mixing streams.

From studies of mixing between gases of different density, Papamoschou and Roshko<sup>(142)</sup> evidenced that the variations of the mixing layer spreading rate depend weakly upon the mean density variations and are mainly due to the compressible character of the turbulent motion. In a mixing layer, the velocity fluctuation level is higher than in a boundary layer. Consequently, the density fluctuation level can be large, and hence the turbulent motion can have a significant compressible character for moderate convective Mach numbers.

The main effect of compressibility seems to be a stabilization of the turbulent motion, as shown by a stability analysis.<sup>(142)</sup>

Jets exhibit a similar decrease of the expansion rate versus Mach number.<sup>(19, 81)</sup> Concerning wakes, their spreading rate and mean velocity profiles are hardly affected by compressibility while the external Mach number significantly influences the turbulent stress anisotropy.<sup>(26)</sup>

#### 6.4.3. Boundary Layer Flows: The Wall Region

Van Driest<sup>(54)</sup> has proposed to transform the longitudinal velocity, in order to extend the incompressible law of the wall to compressible boundary layers, as

$$u^* = \int_0^y \sqrt{\frac{\rho}{\rho_w}} du; \quad u^+ = \frac{u^*}{u_t}; \quad y^+ = \frac{\rho_w u_t y}{\mu_w} \quad (90)$$

where  $u_t$  is the friction velocity and the subscript  $w$  denotes wall values. Investigations of compressible boundary layer data from early works showed that the wall values provide the

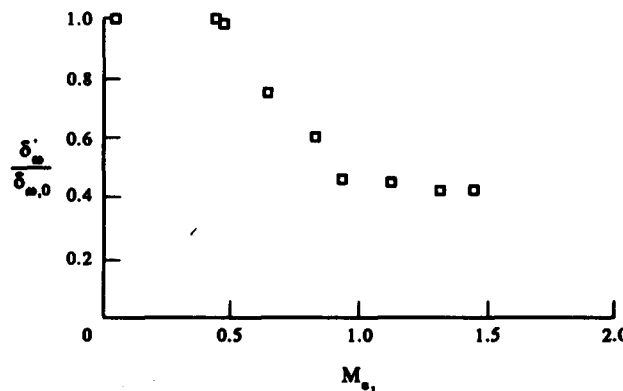


FIG. 55. Evolution of the mixing layer spreading rate versus convective Mach number (from Ref. 142).

correct scaling.<sup>(160)</sup> Van Driest transformation assumes that the mixing length still reads

$$l = \chi y; \quad \chi \sim 0.41. \quad (91)$$

Experimental data support the existence of the logarithmic law as shown in Fig. 56. It must be pointed out that this transformation is only valid in the logarithmic region; the viscous sublayer requires a different scaling to reduce to the incompressible form. According to Fernholz and Finley data survey, this law of the wall holds for cooled or adiabatic wall flows, provided that the pressure gradients are "moderate".

Similarly, experimental estimates of the mixing length<sup>(124)</sup> are in good agreement with the incompressible law Eq. 91. This shows that turbulence in the wall region is in equilibrium and that, since the velocity is small, compressibility effects are weak. This is in agreement with Bushnell's observation<sup>(36)</sup> that a turbulence model without any compressibility correction can give good predictions of the wall values but not of the complete boundary layer profiles.

As the external flow Mach number increases, the recovery temperature increases. This usually leads to an increase in the wall temperature. Since the kinematic viscosity  $\mu_w/\rho_w$  consequently increases, a given wall distance in wall units  $y^+$  corresponds to a higher altitude in the boundary layer. The wall region gets thicker and may occupy a significant part of the boundary layer. Low Reynolds number effects are therefore more and more important, as shown in Fig. 57 on which the boundary layer thickness  $\delta$  is expressed in wall units  $\delta^+ = \frac{\rho_w \delta u_t}{\mu_w}$  versus the Reynolds number for various Mach numbers and wall temperature/stagnation temperature ratios and regions of significant low Reynolds number effects are identified.

#### 6.4.4. Boundary Layer Flows: The Outer Region

As the turbulence is not modified by compressibility effects for external Mach numbers less than five for zero pressure gradient boundary layers, it is thus not really surprising to find the same shear stress distribution as for incompressible flows (Fig. 58) or the same mixing length profile (Fig. 59).

However, a fine comparison between low-speed and supersonic ( $M = 2.9$ ) flat plate boundary layers performed by Smits *et al.*<sup>(173)</sup> reveals differences in the turbulence structure, and some of them are known to amplify as the Mach number increases.

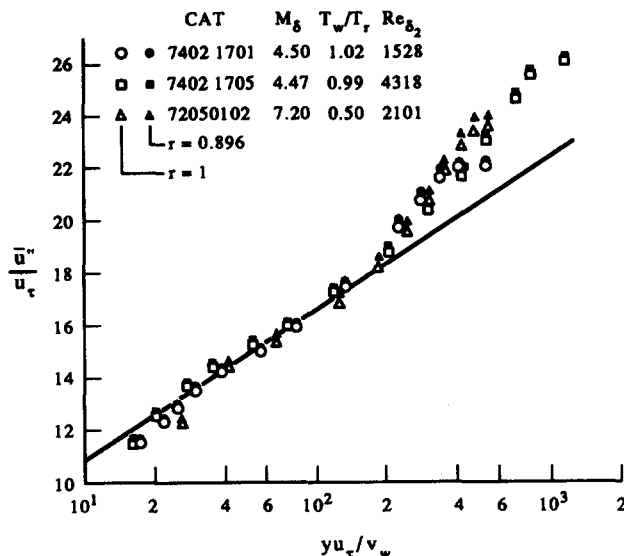


FIG. 56. Examples of logarithmic laws for compressible boundary layers (from Ref. 68).

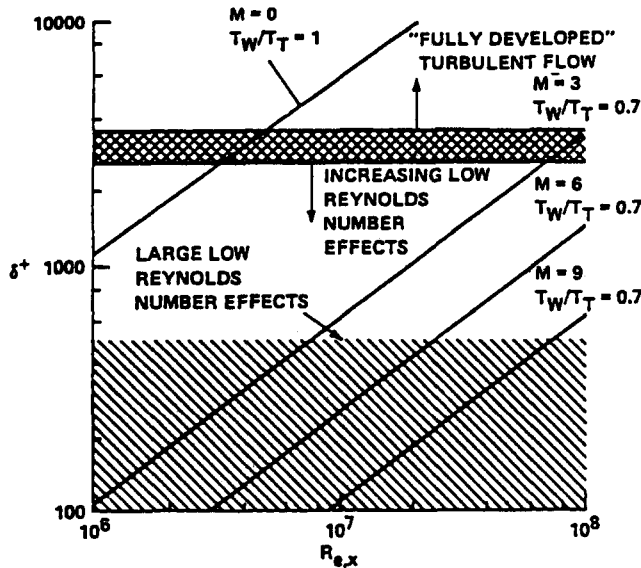


FIG. 57. Influence of low Reynolds number effects versus Mach number (from Ref. 35).

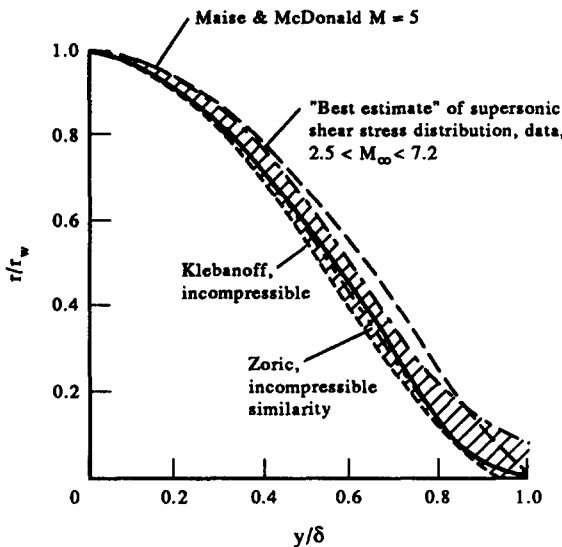


FIG. 58. Comparison of shear distributions in supersonic and incompressible flat plate boundary layers (from Ref. 124).

The longitudinal velocity fluctuations, normalized as  $\rho \overline{u''^2}/\tau_w$ , exhibit the same profile as in incompressible flows at this Mach number ( $M = 2.9$ ) but not at hypersonic Mach numbers.<sup>(1, 14)</sup> A more striking difference is the variation of the shear correlation coefficient

$$R_{uv} = \frac{-\widetilde{u''v''}}{\sqrt{\overline{u''^2}} \sqrt{\overline{v''^2}}} \text{ as shown in Fig. 60.}$$

The flatness distribution is different between incompressible and Mach 2.9 boundary layers, which can be linked to differences in the intermittency. For external Mach numbers larger than five, the intermittency region gets thinner for hypersonic flows as shown in Fig. 61.

Another striking behaviour of hypersonic boundary layers is the increase of the flow memory with the external Mach number. Mean and turbulent values profiles relax very

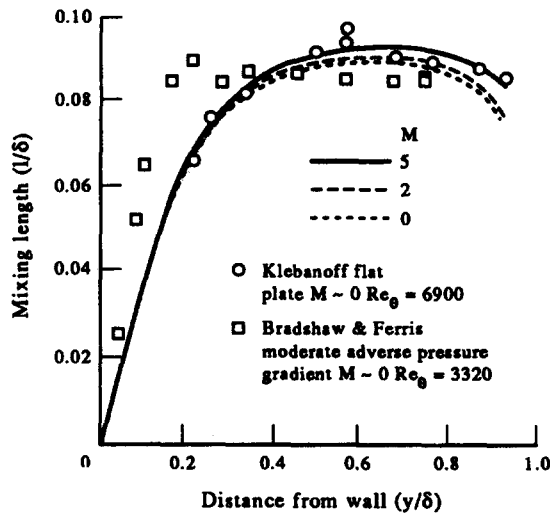


FIG. 59. Comparison of mixing length distributions in supersonic and incompressible boundary layers (from Ref. 124).

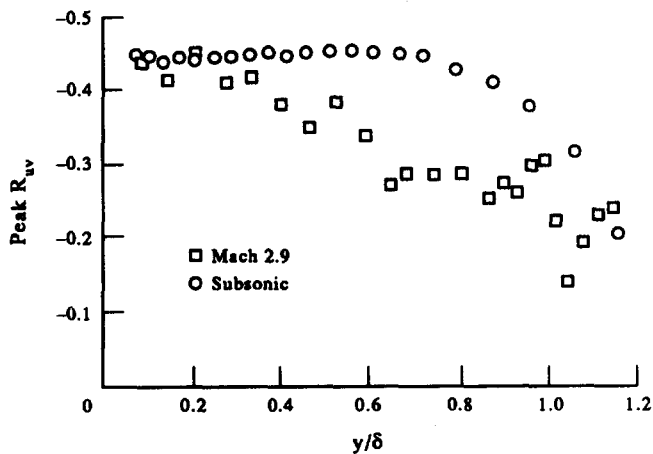


FIG. 60. Comparison of the shear correlation coefficient  $R_{uv}$  in supersonic and incompressible turbulent boundary layers (from Ref. 173).

slowly towards equilibrium solutions. This point has drastic consequences on available data as pointed out previously.

#### 6.4.5. Evolution of the Turbulent Prandtl Number

The turbulent Prandtl number is a convenient way to characterize the relative effectiveness of the turbulent motion to transport momentum and heat. For boundary layer flows, it reads

$$\mathcal{P}_t = \frac{\overline{\rho u'' v''}}{\overline{\partial \tilde{u}} / \partial y} \frac{\overline{\partial \tilde{h}} / \partial y}{\overline{\rho v'' h''}}. \quad (92)$$

There is unfortunately no universal value for the turbulent Prandtl number. An average value can be proposed for different kinds of flows, e.g. a value of about 0.5 for mixing layers

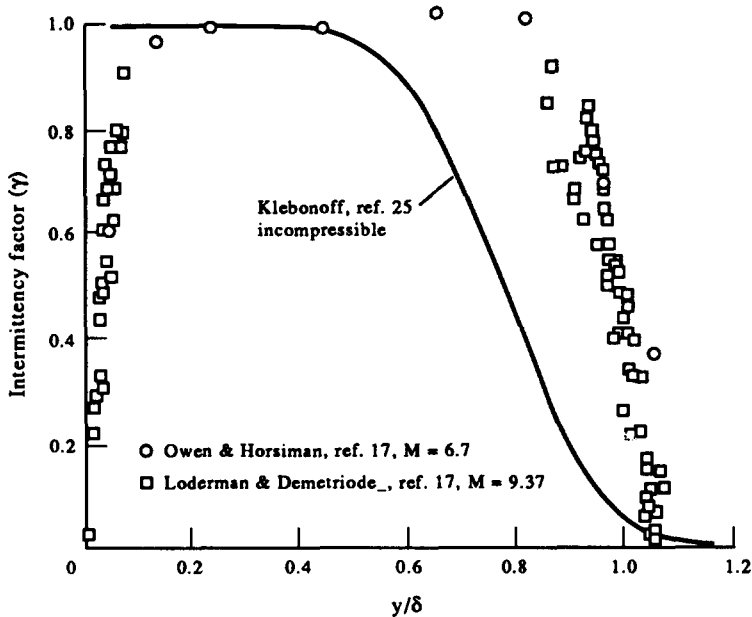


FIG. 61. Comparison of intermittency profiles in incompressible and hypersonic boundary layers (from Ref. 160).

or about 0.9 for boundary layer flows. Although a large plateau exists, the turbulent Prandtl number is not constant throughout the boundary layer: it exhibits a peak near the wall, and decreases in the outer part of the boundary layer as shown in Figs 62 and 63. While the increase near the wall or the decrease in the outer region do not have a universal shape, this profile with a plateau at a value close to 0.9 is observed whatever the Mach number, the pressure gradient ...

## 6.5. TURBULENCE MODELS FOR COMPRESSIBLE TURBULENT FLOWS

### 6.5.1. Model Classification

Mean flow Eqs 74 and 77 or boundary layer Eqs 80 and 84 form an open set as the turbulent stresses  $-\rho \bar{u}'' \otimes \bar{u}''$  and the turbulent heat fluxes  $-\rho \bar{u}'' h''$  require modelling.

Most of the models use the Boussinesq hypothesis which relates the turbulent stresses and heat fluxes to the mean flow properties

$$\overline{\rho \bar{u}'' \otimes \bar{u}''} - \frac{2}{3} \bar{\rho} k \underline{\delta} = - \mu_t (\text{grad } \bar{u} + ' \text{grad } \bar{u} - \frac{2}{3} (\text{div } \bar{u}) \underline{\delta}) \quad (93)$$

$$\overline{\rho \bar{u}'' h''} = - \lambda_t \text{grad } \tilde{T} \quad (94)$$

where  $k = \frac{1}{2} \widetilde{\bar{u}'' \cdot \bar{u}''}$  is the turbulent kinetic energy while  $\mu_t$  and  $\lambda_t$  are respectively the turbulent viscosity and the turbulent conductivity. They are related through the turbulent Prandtl number, since

$$\mathcal{P}_t = \frac{\mu_t C_p}{\lambda_t}. \quad (95)$$

The turbulent viscosity  $\mu_t$  can be linked to turbulent motion velocity and length scales as  $\mu_t = \rho U \mathcal{L}$ . A standard classification of the turbulence models, according to the number of transport equations added by the model is the following, for wall-bounded flows:

- Zero-equation models relate the turbulence length scale to the wall distance in the inner part of the boundary layer and to some boundary layer characteristic thickness in the outer part of the boundary layer (boundary layer thickness, displacement thickness ...). The

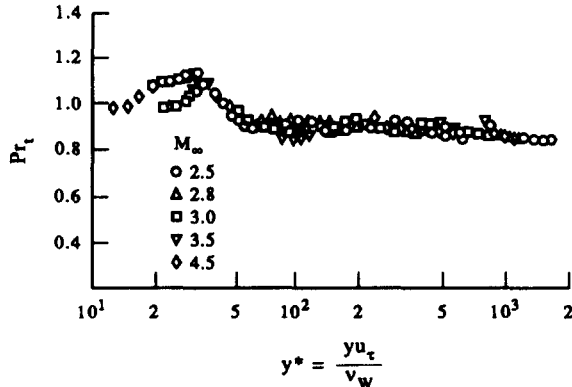


FIG. 62. Turbulent Prandtl number profile versus wall distance in wall units  $y^+$  for a zero pressure gradient boundary layer (from Ref. 131).

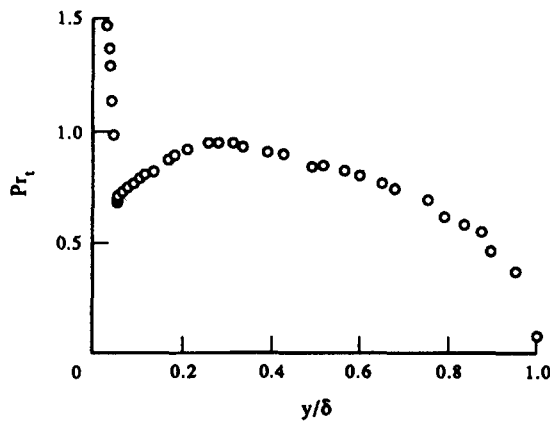


FIG. 63. Turbulent Prandtl number profile for a zero pressure gradient, Mach 7 boundary layer over a cold wall (from Ref. 141).

velocity scale is determined by assuming that the turbulent and mean motions are in equilibrium, i.e. have the same time scales. The turbulent motion time scale is  $\mathcal{L}/\mathcal{U}$  while the mean motion time scale reads  $\left(\frac{\partial \bar{u}}{\partial y}\right)^{-1}$  for boundary layers. Incompressible models are extended to compressible flows by using the local value of the density, often without extra compressibility terms.

- One-equation models usually take advantage of the good definition of the length scale with respect to the wall distance and the boundary layer thickness, and only determine the velocity scale with the help of a transport equation for the turbulent kinetic energy.

- Two-equation models are more general as they determine both the length and velocity scales. They can be used in any kind of flow and are thus very popular. The turbulent kinetic energy transport equation is usually solved to determine the velocity scale while various equations can be used to determine either the length scale  $\mathcal{L}$ , the turbulence time scale  $\mathcal{L}/\mathcal{U}$ , the turbulence dissipation rate  $\mathcal{U}^3/\mathcal{L}$  or any combination  $\mathcal{U}^m \mathcal{L}^n$ .

- Multiple transport equation models supercede the turbulent viscosity Eq. 93 and conductivity Eq. 94 hypothesis as they solve transport equations for the turbulent stresses and heat fluxes. However, they are more complex to implement and require about six to ten transport equations to compute the turbulent stresses and heat fluxes in two-dimensional flows, ten to thirteen in three-dimensional flows. Launder<sup>(107)</sup> points out that the turbulent heat flux level depends crucially upon the Reynolds stresses so that Reynolds stresses

transport equations must be solved but simpler models can be used for the turbulent heat fluxes, such as

$$\overline{\rho u_i'' T'} = - C_T \frac{k}{\varepsilon} \overline{\rho u_i'' u_j''} \frac{\partial \bar{T}}{\partial x_j}$$

which is a direct extension of Eq. 94 or

$$\overline{\rho u_i'' T'} = - C_T \frac{k}{\varepsilon} \left( \overline{\rho u_i'' u_j''} \frac{\partial \bar{T}}{\partial x_j} + \overline{\rho u_i'' T'} \frac{\partial \bar{U}_i}{\partial x_j} \right)$$

which is suggested by the turbulent heat flux transport Eq. 99.

### 6.5.2. Transport Equations for Compressible Turbulence

Except for zero-equation models which are derived on phenomenological grounds, the basic tools in turbulence model development are the turbulent quantities transport equations, derived from the Navier–Stokes equations. Only transport equations, the exact forms of which are used in turbulence modelling, i.e. turbulent stresses, turbulent kinetic energy and turbulent heat flux transport equations, are presented.

In a cartesian reference frame, the turbulent stress transport equation reads, with the standard Einstein notation

$$\begin{aligned} \underbrace{\frac{\partial \overline{\rho u_i'' u_j''}}{\partial t} + \frac{\partial \tilde{u}_k \overline{\rho u_i'' u_j''}}{\partial x_k}}_{(a)} &= - \underbrace{\overline{\rho u_i'' u_k''} \frac{\partial \tilde{u}_j}{\partial x_k} - \overline{\rho u_k'' u_j''} \frac{\partial \tilde{u}_i}{\partial x_k}}_{(b)} - \underbrace{\tau_{jk} \frac{\partial \bar{u}_j''}{\partial x_k} - \tau_{jk} \frac{\partial \bar{u}_i''}{\partial x_k}}_{(c)} \\ &\quad + \underbrace{p' \left( \frac{\partial \bar{u}_j''}{\partial x_i} + \frac{\partial \bar{u}_i''}{\partial x_j} \right) + \frac{\bar{\rho}' \bar{u}_i''}{\bar{\rho}} \frac{\partial \bar{p}}{\partial x_j} + \frac{\bar{\rho}' \bar{u}_j''}{\bar{\rho}} \frac{\partial \bar{p}}{\partial x_i}}_{(d)} \\ &\quad + \underbrace{\frac{\partial}{\partial x_k} \left[ - \overline{\rho u_i'' u_j'' u_k''} + \overline{u_i'' \tau_{jk}} + \overline{u_j'' \tau_{ik}} - p' (\bar{u}_i'' \delta_{jk} + \bar{u}_j'' \delta_{ik}) \right]}_{(e)}. \end{aligned} \quad (96)$$

This form is similar to the one obtained in incompressible flows, with advection (a), production (b), viscous dissipation (c), pressure/strain (d) and diffusion (e) terms. Compressibility gives rise to new terms, i.e.  $(\bar{\rho}' \bar{u}'' \otimes \text{grad } \bar{p})/\bar{\rho}$  and also modifies the other pressure terms. Indeed, the Poisson equation for the pressure in compressible flows is given by

$$-\frac{\partial^2 p'}{\partial x_i \partial x_i} = 2 \frac{\partial^2 \overline{\rho u_i'' \tilde{u}_m}}{\partial x_i \partial x_m} + \frac{\partial^2 (\overline{\rho u_i'' u_m''} - \overline{\rho u_i'' u_m''})}{\partial x_i \partial x_m} + \frac{\partial^2 \bar{\rho}' \tilde{u}_i \tilde{u}_m}{\partial x_i \partial x_m} - \frac{\partial^2 \bar{\rho}'}{\partial t^2} - \frac{\partial^2 (\tau_{lm} - \bar{\tau}_{lm})}{\partial x_i \partial x_m}. \quad (97)$$

The first two terms of the right-hand-side are similar to the ones obtained in incompressible flow but the fourth one corresponds to pressure waves. The pressure is no longer local in time and cannot be analytically expressed in terms of the velocity field at the same time. Viscous terms, which are small, will be discussed later.

The turbulent kinetic transport equation is obtained as half the trace of the turbulent stresses transport Eq. 96

$$\begin{aligned} \frac{\partial \bar{\rho} k}{\partial t} + \frac{\partial \bar{\rho} \tilde{u}_i k}{\partial x_i} &= - \overline{\rho u_i'' u_j''} \frac{\partial \tilde{u}_i}{\partial x_j} - \tau_{ij} \frac{\partial \bar{u}_i''}{\partial x_j} + p' \frac{\partial \bar{u}_i''}{\partial x_i} + \frac{\bar{\rho}' \bar{u}_i''}{\bar{\rho}} \frac{\partial \bar{p}}{\partial x_i} \\ &\quad + \frac{\partial}{\partial x_j} \left[ - \frac{1}{2} \overline{\rho u_i'' u_i'' u_i''} + \overline{u_i'' \tau_{ij}} - \frac{p' \bar{u}_i''}{2} \right]. \end{aligned} \quad (98)$$

By comparison with the incompressible form, a pressure/dilatation term, which is zero in incompressible flows, and a pressure gradient term are added.

In a cartesian reference frame, the turbulent heat flux transport equation reads

$$\begin{aligned} \frac{\partial \overline{\rho u_i'' h''}}{\partial t} + \frac{\partial \tilde{u}_k \overline{\rho u_i'' h''}}{\partial x_k} = & - \overline{\rho u_k'' h''} \frac{\partial \tilde{u}_i}{\partial x_k} - \overline{\rho u_i'' u_k''} \frac{\partial \tilde{h}}{\partial x_k} - \overline{\tau_{ik} \frac{\partial h''}{\partial x_k}} - \lambda \frac{\partial T}{\partial x_k} \frac{\partial u_i''}{\partial x_k} + \overline{u_i'' \varphi} \\ & + p' \frac{\partial h''}{\partial x_i} - \frac{\rho' h''}{\bar{\rho}} \frac{\partial \bar{p}}{\partial x_i} + \overline{u_i'' \frac{\partial p}{\partial t}} + \overline{u_i'' u_k \frac{\partial p}{\partial x_k}} \\ & + \frac{\partial}{\partial x_k} \left[ - \overline{\rho u_i'' u_k'' h''} - \overline{p' h''} \delta_{ik} + \overline{h'' \tau_{ik}} + \lambda \frac{\partial T}{\partial x_k} u_i'' \right] \end{aligned} \quad (99)$$

where  $\varphi = \tau_{ik} \frac{\partial u_i}{\partial x_k}$  is the viscous dissipation. The terms of advection, production due to the mean velocity and enthalpy gradients, viscous dissipation, pressure/enthalpy gradient and diffusion are easily identified. The term  $\rho' h''$  appears due to compressibility.

### 6.5.3. Strong Reynolds Analogy

Solving the transport equation for the turbulent kinetic energy  $k$  requires models for the pressure/dilatation term and for the turbulent mass flux  $\rho' u''$ .

Morkovin<sup>(135)</sup> took advantage of the fact that the entropy and acoustic modes are weak for boundary layers with external Mach numbers less than five. He assumed that the pressure fluctuations are weak. Thus, from the state equation, he obtained

$$\frac{p'}{\bar{p}} \ll 1 \Rightarrow \frac{\rho'}{\bar{\rho}} = - \frac{T''}{\tilde{T}} - \frac{\rho' T''}{\bar{\rho} \tilde{T}} \sim - \frac{T''}{\tilde{T}}. \quad (100)$$

Moreover, the assumption that stagnation enthalpy fluctuations are negligible leads, for flows with a preferred direction  $x_1$ , to

$$\frac{H''}{\tilde{H}} \ll 1 \Rightarrow C_P T'' = - \tilde{u}_i u_i'' \sim - \tilde{u}_1 u_1'' \quad (101)$$

or

$$\frac{T''}{\tilde{T}} = -(\gamma - 1) M^2 \frac{u_1''}{\tilde{u}_1} \quad (102)$$

hence,

$$\frac{\sqrt{\langle \rho'^2 \rangle}}{\bar{\rho}} = \frac{\sqrt{\langle T''^2 \rangle}}{\tilde{T}} = (\gamma - 1) M^2 \frac{\sqrt{\langle u_1''^2 \rangle}}{\tilde{u}_1}; \quad r_{u_1'' T''} = \frac{\langle u_1'' T'' \rangle}{\sqrt{\langle u_1''^2 \rangle \langle T''^2 \rangle}} = -1.$$

This set of relations gives the strong Reynolds analogy. Alternative arguments have been brought up by Gaviglio.<sup>(75)</sup> This gives good estimates as the experimental value of the correlation  $r_{u_1'' T''}$  is about  $-0.8$  for adiabatic boundary layer flows. With this analogy, the density/velocity correlation reads

$$\overline{\rho u_i''} = (\gamma - 1) M^2 \frac{\overline{\rho u_1'' u_i''}}{\tilde{u}_1}. \quad (103)$$

### 6.5.4. Alternatives to the Strong Reynolds Analogy

Rubesin<sup>(158)</sup> proposed a more general formulation than Eq. 100 assuming a polytropic behaviour of the turbulent motion

$$\frac{p'}{\bar{p}} = n \frac{\rho'}{\bar{\rho}} = \frac{n}{n-1} \frac{T''}{\tilde{T}}. \quad (104)$$

This hypothesis includes isobar ( $n = 0$ ), isothermal ( $n = 1$ ), isentropic ( $n = \gamma$ ) and incompressible ( $n = \infty$ ) behaviours. Rubesin initially proposed a value of about 1.2 for the polytropic coefficient  $n$  but strong deviations have been observed. Together with Eq. 102, the polytropic behaviour assumption yields

$$\overline{\rho' u_i''} = -\frac{\gamma-1}{n-1} M^2 \frac{\overline{\rho u_1'' u_i''}}{\tilde{u}_1}. \quad (105)$$

To evaluate the enthalpy fluctuations, Rubesin<sup>(159)</sup> suggested the use, instead of Eq. 101, of a first gradient hypothesis

$$h'' = -C_e \frac{k}{\varepsilon} u_i'' \frac{\partial \tilde{h}}{\partial x_i}. \quad (106)$$

The weak pressure fluctuations hypothesis Eq. 100 or the polytropic behaviour assumption Eq. 104 can be used to link the correlation  $\overline{\rho' u_i''}$  to the correlation  $\overline{T'' u_i''}$ , which can be approximated as  $\overline{\rho T'' u_i''}/\bar{\rho}$ , and evaluated with a model for the turbulent heat flux.

Other strategies have been proposed by Sarkar,<sup>(162)</sup> who used a first gradient hypothesis to express the density/velocity correlation in terms of the density gradient

$$\overline{\rho' u_i''} = -\frac{\mu_t}{\sigma_\rho} \frac{\partial \bar{\rho}}{\partial x_i}; \quad \sigma_\rho = 0.7 \quad (107)$$

or by Vandromme<sup>(189)</sup> who directly used transport equations for the correlations  $\overline{\rho' u_i''}$ .

Let us finally point out that these various approaches to modelling the density/velocity correlation can also be used to model the correlation  $\overline{\rho' h''}$  which appears in the turbulent heat flux transport Eq. 99.

#### 6.5.5. Modelling the Pressure/Dilatation Term

DNS of homogeneous sheared turbulence show that the pressure/dilatation term is not negligible in the turbulent kinetic energy budget and hence requires modelling.

Rubesin proposed to use the polytropic behaviour assumption Eq. 104 to express the pressure/dilatation term as

$$\left\langle p' \frac{\partial u_i''}{\partial x_i} \right\rangle = n \frac{\bar{p}}{\bar{\rho}} \left\langle \rho' \frac{\partial u_i''}{\partial x_i} \right\rangle$$

where the R.H.S. can be written, from the continuity equation, as

$$\left\langle \rho' \frac{\partial u_i''}{\partial x_i} \right\rangle = \frac{\langle \rho'^2 \rangle}{\bar{\rho}} \frac{\partial \tilde{u}_i}{\partial x_i}.$$

The density fluctuation variance is obtained with the help of the polytropic assumption Eq. 104 and the negligible stagnation enthalpy fluctuations hypothesis Eq. 101. Such a relation has been used, e.g. by Viegas,<sup>(192)</sup> as

$$\left\langle p' \frac{\partial u_i''}{\partial x_i} \right\rangle = A \bar{\rho} k M^2 \frac{\partial \tilde{u}_i}{\partial x_i}. \quad (108)$$

For homogeneous turbulence, a different approach has been introduced by Zeman,<sup>(208)</sup> using linear acoustics theory. Pressure, density and entropy are related, from the definition of the entropy, as

$$\frac{1}{\rho} \frac{D\rho}{Dt} = \frac{1}{\rho a^2} \frac{Dp}{Dt} - \frac{1}{C_p} \frac{Ds}{Dt}$$

where  $s$  is the entropy and  $a$  the speed of sound. Density fluctuations are obtained from the continuity equation as

$$\frac{1}{\bar{\rho}} \frac{D\rho'}{Dt} = -\frac{\partial u_i}{\partial x_i} - \frac{\partial \rho' u_i}{\partial x_i}.$$

Thus, neglecting terms of order  $\rho'/\bar{\rho}$  yields

$$\left\langle p' \frac{\partial u_i''}{\partial x_i} \right\rangle = - \frac{1}{2\bar{\rho}a^2} \frac{D\overline{p'^2}}{Dt} + \text{negligible terms.}$$

This equation links the pressure/dilatation correlation to the evolution of the pressure variance. The evolution of the pressure variance is modelled, from Erlebacher's works,<sup>(60)</sup> assuming a linear return towards an equilibrium value with an acoustic timescale

$$\frac{D\overline{p'^2}}{Dt} = \frac{p_{eq}^2 - \overline{p'^2}}{\tau_a}; \quad \tau_a \sim \frac{k^{3/2}}{\varepsilon a}; \quad p_{eq}^2 = \bar{\rho}^2 k a^2 \frac{\alpha M_t^2 + \beta M_t^4}{1 + \alpha M_t^2 + \beta M_t^4}; \quad M_t = \frac{\sqrt{2k}}{a}.$$

Zeman recently proposed a different model to link the pressure/dilatation term to the density gradient in order to recover Van Driest scaling in boundary layer flows.<sup>(207)</sup>

Another different approach has been proposed by Sarkar *et al.*<sup>(163)</sup> to model the pressure/dilatation term. It is based on DNS, Fourier analysis which is convenient for homogeneous flows and scaling arguments. The final form for the pressure/dilatation term reads

$$\left\langle p' \frac{\partial u_i''}{\partial x_i} \right\rangle = -\alpha_2 \bar{\rho} P M_t + \alpha_3 \bar{\rho} \varepsilon_s M_t^2 + \alpha_4 \bar{\rho} \frac{\partial \tilde{u}_i}{\partial x_i} k M_t, \quad (109)$$

where  $P$  stands for the turbulent kinetic energy production rate.

### 6.5.6. Modelling the Dissipation

In compressible flows, the viscous dissipation term can be written as

$$\bar{\rho}\varepsilon = \tau_{ij} \overline{\frac{\partial u_i''}{\partial x_j}} = \underbrace{\bar{\mu} \overline{\omega_i'' \omega_i''}}_{\bar{\rho}\varepsilon^s} + \underbrace{\frac{4}{3} \bar{\mu} \overline{\frac{\partial u_i''}{\partial x_i} \frac{\partial u_j''}{\partial x_j}}}_{\bar{\rho}\varepsilon^d} + \bar{\rho}\varepsilon_{fluc} + \bar{\rho}\varepsilon_{LowRe}. \quad (110)$$

The last two terms are respectively a viscosity fluctuation term and a low Reynolds number term which are both neglected. The first term, the solenoidal dissipation  $\varepsilon^s$  is due to vorticity fluctuations and is the only important term in high Reynolds number incompressible turbulence. The second term is the dilatational dissipation  $\varepsilon^d$  which is due to velocity divergence fluctuations and is specific to compressible turbulence. DNS show that the dilatational dissipation is small when compared to the solenoidal dissipation, but it is not negligible in the turbulent kinetic energy balance.

Sarkar uses a decomposition of the velocity field into an “incompressible” (solenoidal) and a “compressible” (irrotational) mode, which makes sense only for homogeneous flows. From an asymptotic analysis, he evidences an equilibrium partition of energy between the pressure fluctuation variance associated with the compressible mode and the compressible mode kinetic energy. Assuming that the incompressible and compressible modes have similar Taylor microscales, he gets

$$\varepsilon^d = \alpha M_t^2 \varepsilon^s. \quad (111)$$

The coefficient  $\alpha$  was initially set to one,<sup>(164)</sup> and later reduced to 0.5 when a model for the pressure/dilatation term has been introduced.<sup>(163)</sup>

Zeman<sup>(206, 208)</sup> postulated that the dilatational dissipation is due to shocklets within the large eddies. From Rankine–Hugoniot relations for shock waves, and assuming a Gramm–Charlier probability density function for the velocity fluctuations upstream of the shock wave, he gets

$$\varepsilon^d = c_D \varepsilon^s f(M_t, K) \quad (112)$$

where  $K$  is the kurtosis  $K = \overline{u'''^4} / \overline{u''^2}^2$ . For a mixing layer, i.e. for kurtosis between 6 and 8,

the function  $f$  reads

$$\begin{aligned} f &= 1 - \exp \left[ -\left( \frac{M_t - 0.1}{0.6} \right)^2 \right] && \text{when } M_t > 0.1 \\ f &= 0 && \text{when } M_t < 0.1. \end{aligned} \quad (113)$$

As Zeman recommended a value of  $c_D$  about 0.75, this function is very close to the one used by Sarkar<sup>(111)</sup> with  $\alpha = 1$  in the relevant range of turbulent Mach numbers ( $M_t < 0.6$ ).

Another approach has been suggested by Taulbee and Van Osdol.<sup>(179)</sup> If viscosity variations are neglected, the viscous term in the Poisson Eq. 97 can be written as

$$\frac{\partial^2 (\tau_{lm} - \bar{\tau}_{lm})}{\partial x_l \partial x_m} = -\frac{4}{3} \frac{\partial^2}{\partial x_i^2} \left( \mu \frac{\partial u_i''}{\partial x_l} \right)$$

so that they propose to model together the pressure/dilatation term and the dilatational dissipation term, with the help of the Poisson equation. The proposed modelled form reads

$$p' \frac{\partial u_i''}{\partial x_i} + \frac{4}{3} \mu \left( \frac{\partial u_i''}{\partial x_i} \right)^2 = -C_{k0} \rho \frac{k^{3/2} a}{\varepsilon} \frac{\rho'^2}{\rho^2} \left[ \frac{\partial u_i}{\partial x_i} \right]^2 + C_{k1} \rho a^2 \frac{\rho'^2}{\rho^2} \frac{\partial u_i}{\partial x_i} - C_{k2} \rho a^2 \frac{\varepsilon}{k} \frac{\rho'^2}{\rho^2}$$

and an auxiliary transport equation is required to determine the density variance.

As a mean flow dilatation term exists in the vorticity equation, a production term due to the mean flow dilatation appears in the solenoidal dissipation transport equation. This term is exact and does not require modelling. Otherwise, the incompressible closure for the solenoidal dissipation is generally used.

### 6.5.7. Closure of the Reynolds-Stress Transport Equations

One of the key modelling problems in the Reynolds-stress transport equation is the pressure/strain term. As pointed out previously, the nature of the Poisson equation is different in compressible flows compared to incompressible flows.

Vandromme<sup>(189)</sup> considered that incompressible models can be used as an approximation of the first term of a development with respect to the Reynolds-stress anisotropy, provided a model for the pressure/dilatation, i.e. the trace of the pressure/strain term, is added.

Bonnet<sup>(25)</sup> assumes small pressure fluctuations and uses the strong Reynolds analogy. The proposed pressure/strain term correlation model is an incompressible model with an extra return-to-isotropy term

$$-C_1 \left( 1 + C_B \frac{\widetilde{u''^2}}{a^2} \right) \rho \frac{k^2}{\varepsilon} \left( \widetilde{u_i'' u_j''} - \frac{2}{3} \delta_{ij} k \right)$$

in which a turbulent Mach number appears.

Dussauge and Quine<sup>(57)</sup> developed a closure for the pressure/strain term assuming weak density, pressure and velocity fluctuations and zero divergence for the velocity fluctuations. In the linearized form of the Poisson Eq. 97, only one new term appears, the gradient of relative density fluctuations times the mean pressure gradient.<sup>(56)</sup> For flows with a preferred direction  $x_1$ , the corresponding term in the pressure/strain term model is

$$u_1 \frac{\varepsilon}{k} \alpha \left[ \overline{\rho' u_1''} \delta_{ij} - \frac{3}{2} \left( \overline{\rho' u_i''} \delta_{1j} + \overline{\rho' u_j''} \delta_{1i} \right) \right].$$

Density/velocity correlations are expressed in terms of the turbulent stresses with the help of the strong Reynolds analogy as

$$\overline{\rho u_i''} = k_1 (\gamma - 1) M^2 \frac{\overline{\rho u_1'' u_i''}}{u_1}; \quad k_1 = 0.8; \quad k_2 = 1.5.$$

El Baz and Launder<sup>(15)</sup> also proposed a modified form for the pressure/strain term and the dissipation transport equation which yields some reduction in the anisotropy, a pres-

sure/dilatation term analogous to the one proposed by Sarkar and an increase in the dissipation due to a decrease of the dissipation sink term with the turbulent Mach number.

## 6.6. EXAMPLES OF MODEL PREDICTIONS

In order to give an idea of the problems encountered when turbulence models are extended from incompressible to compressible flows, only the very simple case of zero pressure gradient boundary layers will be addressed. More exhaustive reviews of the prediction capabilities of turbulence models for compressible flows can be found in Refs 46 and 190.

### 6.6.1. Evolution of the Skin Friction Coefficient Versus Mach Number

This test case is from the Stanford workshop.<sup>(31)</sup> It deals with the skin friction evolution versus Mach number for an adiabatic flat plate boundary layer at a Reynolds number based upon the momentum thickness  $R_\theta = 10,000$ . Attention has been paid to the influence of the initial conditions and of the grid in a boundary layer approach.

Computed skin-friction coefficients are compared with Van Driest II theory which gives a fair average of experimental results as shown e.g. by Bushnell.<sup>(34)</sup>

Results of various two-equation models, namely the  $k - \varepsilon$  models of Launder and Sharma,<sup>(108)</sup> Chien<sup>(40)</sup> and Nagano<sup>(138)</sup> and the  $k - \omega$  model of Wilcox<sup>(199)</sup> are compared.  $k - \varepsilon$  models exhibit a significant decrease of the skin-friction coefficient deviation with the Mach number as shown in Fig. 64. This seems to be due to the fact that  $k - \varepsilon$  models do not satisfy the compressible law of the wall as pointed out by Huang.<sup>(95)</sup> In agreement with Huang's analysis, Wilcox  $k - \omega$  model is less sensitive to the Mach number effect. However, an analysis of the boundary layer profiles has brought into evidence a strange behaviour of the  $k - \omega$  model which predicts a very long relaxation towards free-stream values in the outer region of the boundary layer.

Various models for the pressure/dilatation and dilatational dissipation have been introduced in different turbulence models. Figure 65 shows results for Nagano's  $k - \varepsilon$  model, with Zeman's correction for the dilatational dissipation and Sarkar's models for the dilatational dissipation (Sarkar 90) and for both the dilatational dissipation and the pressure/dilatation terms (Sarkar 91). Zeman's model has been tuned to reproduce the mixing layer spreading rate while Sarkar's models have been calibrated with respect to DNS data. All these models damp the turbulence too strongly and hence predict a drastic decrease of the skin friction as the Mach number increases. The same trends have been observed when the compressibility corrections have been applied to other turbulence models.

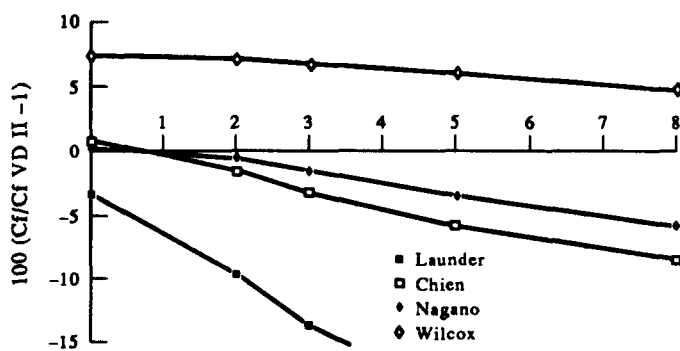


FIG. 64. Percentage deviation of computed skin friction from Van Driest II theory versus Mach number—Insulated plate—Two-equation models.

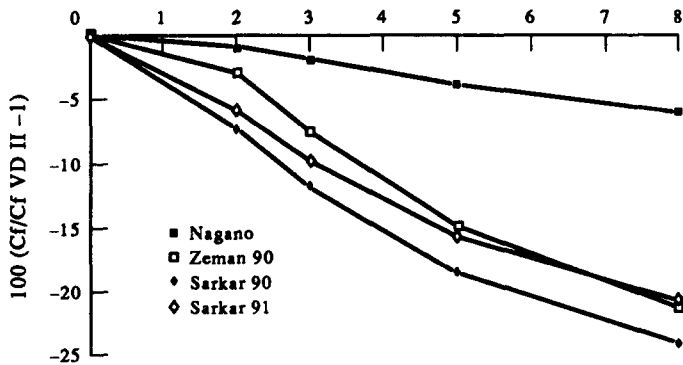


FIG. 65. Percentage deviation of computed skin friction from Van Driest II theory versus Mach number—Insulated plate—Two-layer models with compressibility corrections.

#### 6.6.2. Evolution of the Skin Friction Coefficient Versus Wall Temperature/Adiabatic Temperature Ratio

The second test is also from the Stanford workshop. It deals with the skin friction evolution versus wall temperature/adiabatic temperature ratio for a Mach 5 flat plate boundary layer at a Reynolds number based upon the momentum thickness  $R_\theta = 10,000$ .

This test case evidences another key problem with turbulence models, i.e. that a model must provide predictions in agreement with experimental knowledge but must also be numerically stable. Figure 66 shows that for very cold walls, some of the tested models were unable to converge.

While all  $k - \varepsilon$  models exhibited the same behaviour for the Mach number influence, no global trend can now be observed. Wilcox  $k - \omega$  model is rather insensitive to the wall temperature; as is Nagano's  $k - \varepsilon$  model, but it gives rise to numerical problems at low wall temperature ratios. Here again, "standard" compressibility corrections yield poor results.

#### 6.6.3. Prediction of the Mixing Layer Spreading Rate Evolution

The evolution of the mixing layer spreading rate with the convective Mach number shown on Fig. 55 cannot be predicted by incompressible turbulence models. A lot of turbulence models modifications have been proposed in order to reproduce it.

Dash<sup>(47)</sup> introduced an ad-hoc damping of the turbulent viscosity as function of the Mach number.

Kim<sup>(101)</sup> proposed a new mixing length, based upon the distance to points where the flow has a sonic relative speed, to limit the mixing length in high speed mixing layer.

Bonnet<sup>(25)</sup> and Dussauge and Quine<sup>(57)</sup> modified the pressure/strain term in the Reynolds stress transport equation. The effect of both modifications is to decrease the anisotropy, and hence the fluid entrainment.

Sarkar *et al.*<sup>(164)</sup> and Zeman<sup>(206)</sup> both modified the dissipation term to account for the dilatational dissipation. Their corrections were based upon different physical arguments but led to very similar corrections. They later proposed also to model the pressure/dilatation term.

The El Baz and Launder model<sup>(15)</sup> also yields fair predictions for the mixing layer spreading rate as well as for the Reynolds stresses. However, when its pressure/dilatation term and its modified dissipation equation are implemented into a low-Reynolds number  $k - \varepsilon$  model, it yields very strong compressibility effects in boundary layer flows.<sup>(10)</sup>

Finally, Ha Minh<sup>(81)</sup> was able to reproduce the evolution of the spreading rate by using a semi-deterministic approach in which the coherent structures are captured by solving unsteady Navier-Stokes equations and the turbulence model (presently  $k - \varepsilon$ ) only represents the more universal turbulent motion.

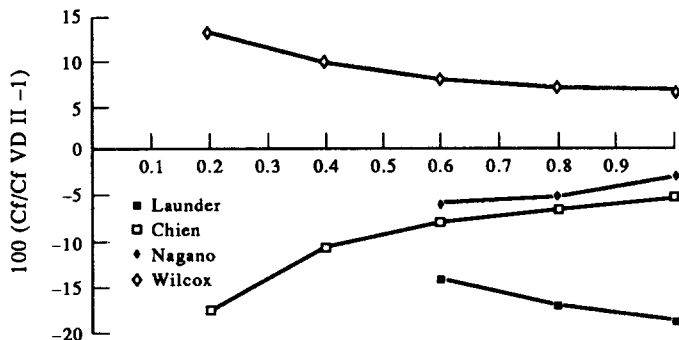


FIG. 66. Percentage deviation of computed skin friction from Van Driest II theory versus wall temperature/adiabatic temperature ratio at Mach 5—Two-equation models.

The use of so many and varied approaches to obtain somewhat similar results shows that the present knowledge of compressible turbulence and the modelling effort is far from complete. Moreover, the mixing layer, which is the most striking example of compressible turbulence effects cannot be solely used to validate turbulence models, as models which give good predictions for the mixing layer spreading rate evolution fail to reproduce the hypersonic boundary layer turbulence.

There is a dire need for experimental data. There are too few data available for hypersonic boundary layers, especially when looking at turbulent stresses and heat flux profiles.

## 7. TRANSITION

Since the classical experiments performed by Osborne Reynolds (1883), the instability of laminar flow and the transition to turbulence have maintained a constant interest in fluid mechanics problems. This interest results from the fact that transition controls important aerodynamic quantities such as drag or heat transfer. For example, the heating rates generated by a turbulent boundary layer may be several times higher than those for a laminar boundary layer, so that the prediction of transition is of great importance for hypersonic reentry spacecraft, because the thickness of the thermal protection is strongly dependent upon the altitude where transition occurs. Drag reduction for supersonic aircraft also requires a good knowledge of the transition mechanisms.

A laminar flow developing along a given body is strongly affected by various types of disturbances generated by the model itself (roughness, vibrations ...) or existing in the freestream (turbulence, noise, temperature fluctuations). These disturbances are the source of complex mechanisms which ultimately lead to turbulence. Two kinds of transition processes are usually considered:

(a) If the amplitude of the forced disturbances is large (high freestream turbulence level, large roughness elements ...), nonlinear phenomena are immediately observed and transition occurs a short distance downstream of the leading edge of the body. This mechanism is called a "bypass", in the sense that linear stages of the transition process are ignored. It will not be discussed in this section.

(b) If the amplitude of the forced disturbances is small, one can observe at first exponentially growing instabilities, the development of which are governed by linear equations (Tollmien-Schlichting waves, Görtler vortices ...). Three-dimensional and nonlinear effects occur subsequently, inducing secondary instabilities and then transition. In these cases of so-called "natural transition", the transition Reynolds numbers can be very large.

This section is devoted to a general description of the "natural transition" phenomena in supersonic and hypersonic flows. The subject is rather wide and several review papers have described the state-of-the-art in recent years, see Refs 4, 122, 136, 137, 147, 155 and 175. At first, the main features of the linear theory will be reviewed and typical results will be given.

After some brief comments related to the phenomena occurring before and after the region of linear amplification, the effects of factors acting on the stability properties are discussed. The last part of this section concentrates on the practical methods which can be used for transition prediction. It is to be noted that the linear theory will be presented for general three-dimensional flows but, due to space limitations, the applications will be restricted to two-dimensional flows.

### 7.1. LINEAR STABILITY THEORY

The instability leading to transition starts with the growth of sinusoidal disturbances, the existence of which was first demonstrated by the now classical experiments of Schubauer and Skramstad (1948,<sup>(167)</sup>), in incompressible flow. In fact, the development of small, regular oscillations travelling in the laminar boundary layer was postulated by Rayleigh (1887) and Prandtl (1921) many decades ago. Some years later, Tollmien worked out a complete theory of boundary layer instability (1929) and Schlichting calculated the total amplification of the most unstable frequencies (1933). For this reason, the instability waves are often referred to as "Tollmien-Schlichting waves" (TS waves). A complete description of this pioneering work can be found in Schlichting's book.<sup>(166)</sup> Nevertheless, the so-called "linear stability theory" received little acceptance, essentially because of the lack of experimental results. The experiments performed by Schubauer and Skramstad completely revised this opinion by demonstrating that TS waves constitute the first stage of the transition process. In the last forty years, a large amount of work was devoted to a more and more complete understanding of the linear mechanisms occurring at low speeds.

When considering compressible flows, the problem becomes more complex. The first attempt to develop a compressible linear stability theory was made by Küchemann (1938). One of the most important theoretical investigations was carried out by Lees and Lin (1946,<sup>(113)</sup>), who used an asymptotic theory and deduced from the inviscid equations some fundamental results concerning the "generalized inflection point" (see below, Section 7.1.5). Subsequent papers by Lees,<sup>(112)</sup> Dunn and Lin,<sup>(55)</sup> and Lees and Reshotko<sup>(114)</sup> were also based on asymptotic theories. However, as was pointed out by Mack, "some major differences between the incompressible and compressible theories were not uncovered until extensive calculations had been carried out on the basis of a direct numerical solution of the differential equations". From 1960 to the present time, Mack performed a thorough numerical investigation of the linear stability characteristics of compressible laminar boundary layers;<sup>(117-123)</sup> his most important finding is the discovery of the higher unstable modes at supersonic speeds. Due to the development of high speed computers, extensive stability computations have been performed during recent years. Some of the most significant results will be presented in the next paragraph. For a comprehensive account of the linear stability theory, the reader can refer to Mack's review papers.<sup>(118,122)</sup>

#### 7.1.1. Assumptions. Eigenvalue Problem

The principle of linear stability theory is to introduce small sinusoidal disturbances into the Navier-Stokes equations in order to compute the range of unstable frequencies. It is assumed that any fluctuating quantity  $r'$  (velocity, pressure, density or temperature) is expressed by

$$r' = r(y) \exp [i(\alpha x + \beta z - \omega t)] \quad (114)$$

$x, y, z$  is an orthogonal coordinate system, which can be either cartesian or curvilinear,  $y$  being normal to the surface. The complex amplitude function  $r$  depends on  $y$  only. In the general case,  $\alpha$ ,  $\beta$  and  $\omega$  are complex numbers.

The fluctuating quantities are very small, so that the quadratic terms of the disturbances can be neglected in the Navier-Stokes equations. It is also assumed that the mean flow quantities do not vary significantly over a wavelength of the disturbances; therefore  $U$  and

$W$  (mean flow components in the  $x$  and  $z$  directions) as well as the mean temperature  $T$  are functions of  $y$  alone, and the normal velocity  $V$  is equal to zero

$$U = U(y) \quad W = W(y) \quad T = T(y) \quad V = 0. \quad (115)$$

The implication of this *parallel flow approximation* is that the stability of the flow at a particular station ( $x, z$ ) is determined by the local conditions at that station independently of all others.

This leads to a system of homogeneous, ordinary differential equations for the amplitude functions  $r(y)$ . There are four equations for an incompressible flow (continuity + the  $x, y, z$  momentum equations) and six equations for a compressible flow (the four previous equations + energy equation + equation of state). Of course additional equations are needed for chemically reacting flows. For the simplest case of a two-dimensional, low speed flow with  $\beta = 0$ , the stability equations can be combined to obtain a single equation for the vertical component of the velocity fluctuation, which is often denoted as  $\varphi$ . This is the well known *Orr-Sommerfeld equation*

$$\varphi''' - 2\alpha^2\varphi'' + \alpha^4\varphi - iR [(\alpha U - \omega)(\varphi'' - \alpha^2\varphi) - \alpha U''\varphi] = 0 \quad (116)$$

with boundary conditions

$$\varphi(0) = 0 \quad \varphi'(0) = 0 \quad (117)$$

$$\varphi(y) \rightarrow 0 \quad \varphi'(y) \rightarrow 0 \quad \text{as} \quad y \rightarrow 0 \quad (118)$$

$R$  is the Reynolds number and the ' denotes differentiation with respect to  $y$ .

Due to the homogeneous boundary conditions (the disturbances must vanish at the wall and in the free stream, except the pressure fluctuations which have a non-zero amplitude at the wall), the problem is an eigenvalue one: when the mean flow is specified, non-trivial solutions exist only for certain combinations of the parameters  $\alpha, \beta, \omega$  and  $R$ . This constitutes the so-called *dispersion relation*.

### 7.1.2. Temporal and Spatial Theories

When considering the *temporal theory*,  $\alpha$  and  $\beta$  are real,  $\omega$  is a complex quantity:  $\omega = \omega_r + i\omega_i$ . Relation 114 then becomes

$$r' = r(y) \exp(\omega_i t) \exp[i(\alpha x + \beta z - \omega_r t)]. \quad (119)$$

Depending on the sign of the temporal amplification rate  $\omega_i$ , the disturbances are damped ( $\omega_i < 0$ ), amplified ( $\omega_i > 0$ ) or neutral ( $\omega_i = 0$ ).  $\omega_r$  represents a frequency.  $\alpha$  and  $\beta$  are the components of the wavenumber vector  $\vec{k}$  in the  $x$  and  $z$  directions, respectively (see Fig. 67a). The angle  $\psi$  between the  $x$  direction and  $\vec{k}$  is given by

$$\psi = \tan^{-1}(\beta/\alpha). \quad (120)$$

When the *spatial theory* is used,  $\omega$  is real,  $\alpha$  and  $\beta$  are complex:  $\alpha = \alpha_r + i\alpha_i$  and  $\beta = \beta_r + i\beta_i$ .  $r'$  is now expressed by

$$r' = r(y) \exp(-\alpha_r x - \beta_r z) \exp[i(\alpha_r x + \beta_r z - \omega t)]. \quad (121)$$

As can be seen in Fig. 67b, we define a wavenumber vector  $\vec{k} = (\alpha_r, \beta_r)$  and an amplification vector  $\vec{A} = (-\alpha_i, -\beta_i)$ , with angles  $\psi$  and  $\bar{\psi}$  with respect to the  $x$  direction

$$\psi = \tan^{-1}(\beta_r/\alpha_r) \quad (122)$$

$$\bar{\psi} = \tan^{-1}(\beta_i/\alpha_i). \quad (123)$$

If  $\beta_i$  is set equal to zero, the waves can be amplified ( $\alpha_i < 0$ ), neutral ( $\alpha_i = 0$ ) or damped ( $\alpha_i > 0$ ) in the  $x$  direction.

From these definitions, it is now clear that any eigenvalue problem involves five real parameters with the temporal theory ( $\alpha, \beta, \omega_r, \omega_i, R$ ) and six with the spatial theory

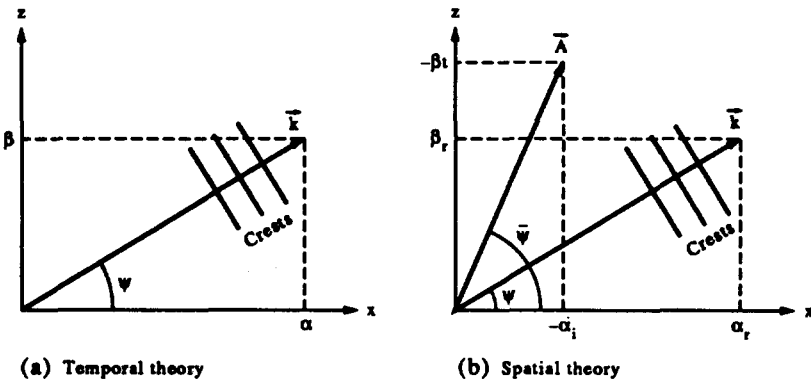


FIG. 67. Notations.

$(\alpha_r, \alpha_i, \beta_r, \beta_i, \omega, R)$ . The first set of parameters is often replaced by  $(\alpha, \psi, \omega_r, \omega_i, R)$ , while the second can be replaced by  $(\alpha_r, \alpha_i, \psi, \bar{\psi}, \omega, R)$ . Numerically, the input data are the mean velocity and mean temperature profiles, the free stream Mach number, the stagnation temperature, the fluid properties and all but two of the previous real parameters. The computation gives the values of the two remaining parameters (eigenvalues) as well as the disturbance amplitude profiles (eigenfunctions). Some examples of the numerical procedures are described in Ref. 122.

### 7.1.3. Relation Between Spatial and Temporal Theories

It is possible to convert a temporal to a spatial amplification rate by using the group velocity, which represents the velocity at which energy propagates in conservative systems. The general expression of the group velocity  $\vec{V}_g$  is

$$\vec{V}_g = \left( \frac{\partial \omega}{\partial \alpha}, \frac{\partial \omega}{\partial \beta} \right). \quad (124)$$

$\vec{V}_g$  is, in general, complex but its imaginary part is small and can therefore be neglected. To simplify the notations,  $\vec{V}_g$  will denote the real part of the group velocity. In the temporal theory,  $\vec{V}_g$  is expressed by

$$\vec{V}_g = \left( \frac{\partial \omega_r}{\partial \alpha}, \frac{\partial \omega_r}{\partial \beta} \right). \quad (125)$$

For two-dimensional waves ( $\beta = 0$ ), the group velocity reduces to a scalar which will be denoted as  $V_g$ . It can be demonstrated that the temporal growth rate  $\omega_i$  can be converted to a spatial growth rate  $-\alpha_i$  by the following relationship

$$-\alpha_i = \frac{\omega_i}{V_g} = \frac{\omega_i}{\partial \omega_r / \partial \alpha}. \quad (126)$$

This transformation was first used by Schlichting<sup>(165)</sup>. It was later derived formally by Gaster<sup>(74)</sup> and bears his name. In principle, relation 126 is only valid for small values of  $\omega_i$ , i.e. in the neighbourhood of the neutral curve.

For oblique waves ( $\beta \neq 0$ ),  $\vec{V}_g$  has a norm  $|V_g|$  and makes an angle

$$\psi_g = \tan^{-1} \left[ \frac{\partial \omega_r / \partial \beta}{\partial \omega_r / \partial \alpha} \right]$$

with respect to the  $x$  direction. The previous result can be generalized to compute the spatial growth rate  $\sigma_g$  along the group velocity trajectory  $x_g$

$$\sigma_g = \frac{\omega_i}{|V_g|}. \quad (127)$$

### 7.1.4. PSE Approach

A new formulation for the stability analysis was recently proposed by Herbert (see overview in Ref. 87). In this approach, the general expression of the disturbances is

$$r' = r(x, y) \exp [i(\theta(x) + \beta z - \omega t)] \quad \text{with} \quad \frac{d\theta}{dx} = \alpha(x). \quad (128)$$

In contrast to the local approach expressed by relation 114, the amplitude functions depend on  $y$  and  $x$ , and  $\alpha$  depends on  $x$ . Substituting the previous expression into the stability equations, neglecting  $\partial^2 r / \partial x^2$  and linearizing in  $r$  yield a partial differential equation of the form

$$Lr + M \frac{\partial r}{\partial x} + \frac{d\alpha}{dx} Nr = 0 \quad (129)$$

where  $L$ ,  $M$  and  $N$  are operators in  $y$  with coefficients that depend on  $x$  and  $y$  through the appearance of the basic flow profiles. When  $d\alpha/dx$  is computed from a so-called normalization condition, the previous equation can be solved using a marching procedure in  $x$  with prescribed initial conditions: this constitutes the PSE (Parabolized Stability Equations) approach. The interest of this procedure is that the nonparallel effects are taken into account. It is also possible to introduce the nonlinear terms. A comprehensive analysis of the PSE approach is given in Ref. 87. In this chapter, the discussion will be restricted to the results obtained using the classical method of local approximation based on the parallel flow assumption.

### 7.1.5. Inviscid Theory

In this theory, it is assumed that the viscosity acts only on the mean profiles. Furthermore, the terms of the order  $1/R$  are neglected in the stability equations. As a consequence of this simplification, a number of mathematical results can be established. This analysis demonstrates the importance of two parameters:

(a) The first one is the so-called “generalized inflection point”, which corresponds to the altitude  $y_s$  where

$$\frac{d}{dy} \left[ \rho \frac{dU}{dy} \right]_{y_s} = 0 \quad (130)$$

where  $\rho$  and  $U$  are the mean density and the mean velocity, respectively. It was demonstrated by Lees and Lin<sup>(113)</sup> that the presence of such a point is a sufficient condition for the appearance of unstable disturbances. It is also a necessary and sufficient condition for the existence of a neutral subsonic wave (the definition of a subsonic disturbance will be given below). The phase velocity of this wave is the mean velocity at  $y_s$ . These results are the generalization of Rayleigh’s condition for incompressible flows. However, they are valid only if

$$\frac{U}{U_e}(y_s) > 1 - \frac{1}{M_e}. \quad (131)$$

Let us consider the case of a flat plate. When the Mach number increases, the generalized inflection point goes from the wall ( $M_e = 0$ ) towards the outer edge of the boundary layer, and the numerical results indicate that the range of unstable frequencies is enlarged at high Reynolds numbers. It is clear that this “inflectional instability” plays a crucial role for instability and transition in hypersonics.

(b) The second parameter is the “relative Mach number”,  $\hat{M}$ , which is defined as

$$\hat{M} = M - \frac{c}{a} \quad (132)$$

where  $M$  is the local Mach number. For classical boundary layers, it increases from 0 to

$M_e$  between the wall and the free stream.  $c$  is the phase velocity of the waves; it does not depend on  $y$ . For two-dimensional waves ( $\beta = 0$ ),  $c = \omega_r/\alpha$  in temporal theory and  $c = \omega/\alpha$ , in spatial theory.  $a$  represents the local speed of sound, which depends on the mean temperature distribution. Obviously, it takes a non-zero value at the wall. The disturbances are subsonic if  $\hat{M}^2 < 1$ , sonic if  $\hat{M}^2 = 1$  and supersonic if  $\hat{M}^2 > 1$ .

If a wave is locally supersonic, say between  $y = 0$  and  $y = y_M$  (Fig. 68), the mathematical nature of the stability equations changes, and any eigenvalue problem admits an infinite sequence of neutral solutions. For instance, in the temporal theory and for two-dimensional disturbances, there is an infinity of neutral waves ( $\omega_i = 0$ ) having the same phase velocity  $\omega_r/\alpha$  but different wavenumbers  $\alpha$ . These multiple solutions (the higher modes) were first discovered by Mack for boundary layer flows.<sup>(117)</sup> In the case of adiabatic wall conditions, they appear when the free stream Mach number exceeds 2.2.

## 7.2. RESULTS FOR ZERO PRESSURE GRADIENT FLOWS ON ADIABATIC WALLS

The stability diagrams presented below were obtained by using a stability code developed at CERT/ONERA.<sup>(4)</sup> The basic profiles (mean velocity and mean temperature profiles) were obtained by solving the two-dimensional compressible similarity equations. The spatial theory is used and it is assumed that the amplification vector  $A$  is aligned with the mean flow direction, i.e.  $\bar{\psi} = 0$  or  $\beta_i = 0$ .

### 7.2.1. Two-Dimensional Waves, $\psi = 0$

Figure 69 shows examples of stability diagrams computed for two-dimensional waves ( $\psi = 0$ ) and for Mach numbers ranging from 0 to 10. For the sake of clarity, only some isoamplification curves ( $\alpha_i < 0$ ) are plotted in the (Reynolds number–wavenumber) plane. The Reynolds number is computed with the displacement thickness  $\delta_1$ , the free stream velocity  $U_e$  and the kinematic viscosity  $v_e$  of the outer flow,  $\alpha_r$  and  $\alpha_i$  are made dimensionless by the displacement thickness. For each Mach number, there is a critical Reynolds number  $R\delta_1 c_r$  below which all disturbances are damped.

The first observation is that the stability diagrams do not change very much when the Mach number increases from 0 to 1.3 (Fig. 69a and b). This can be explained by the fact that the generalized inflection point remains very close to the wall in this Mach number range, and the boundary layer is unstable essentially through the action of viscosity. This phenomenon, whereby the maximum amplification rate increases with decreasing Reynolds number at a fixed value of  $\omega$  or  $\alpha_r$ , is called viscous instability. Stability diagrams where viscous instability is present exhibit a local maximum of  $-\alpha_i$  at finite Reynolds numbers, and the curves of equal amplification rate are closed around this peak. Another important observation is that the amplification factors of the unstable waves are smaller in the transonic range than for incompressible flows, even if the critical Reynolds number is still of the same order.

At higher Mach numbers, the height of the generalized inflection point increases, and the inflectional instability plays a more and more important role. The inviscid theory shows

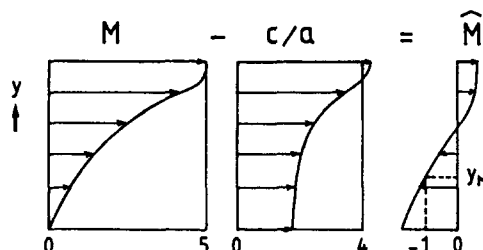


FIG. 68. Typical evolution of the relative Mach number.

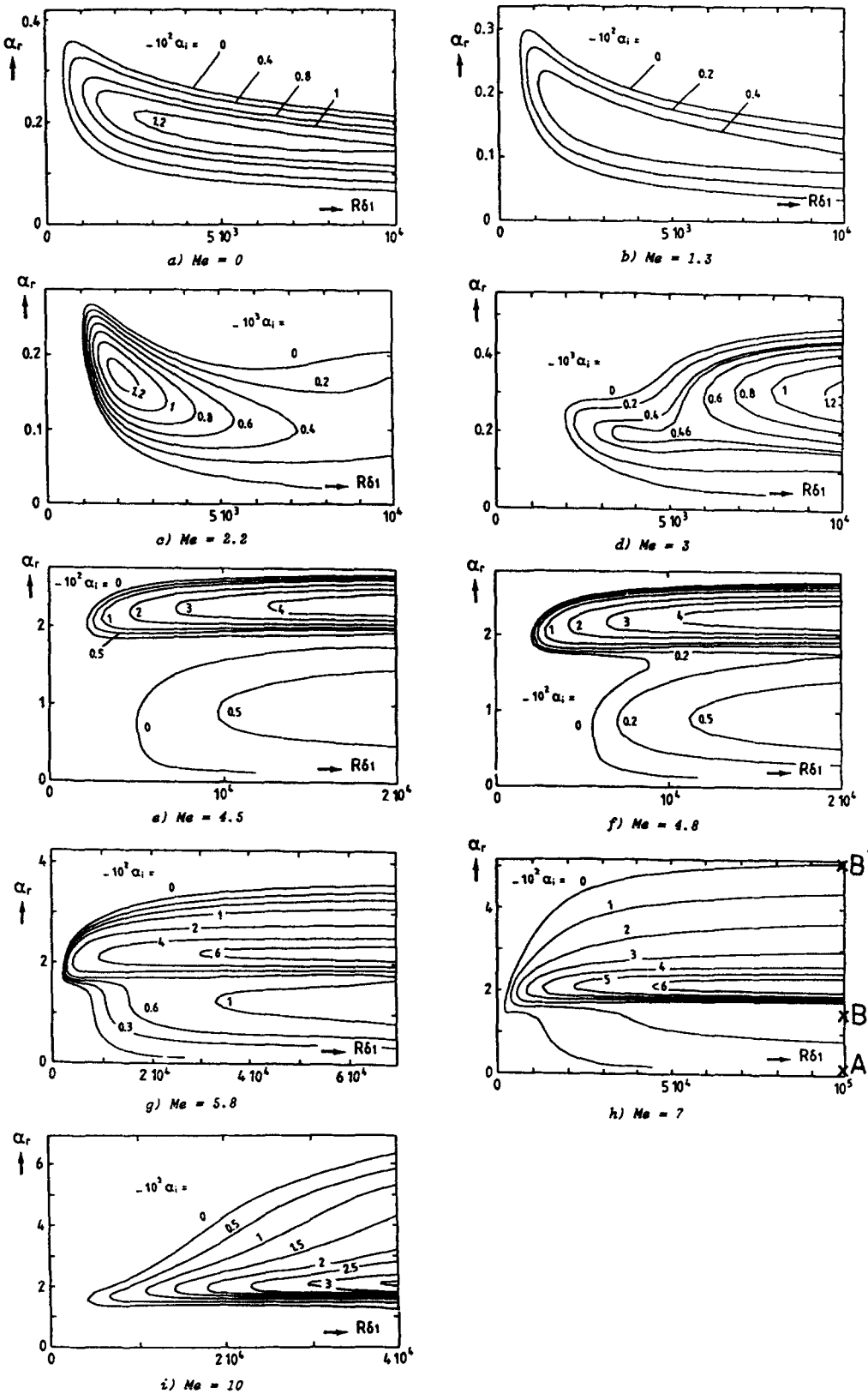


FIG. 69. Stability diagrams computed for two-dimensional waves (adiabatic wall).

that there is a range of unstable  $\alpha$ , or  $\omega$  at infinite Reynolds number and this range is enlarged with increasing Reynolds numbers. As a consequence, the curves of equal amplification rate tend to be parallel to the  $R\delta 1$  axis.

For  $M_e = 2.2$  (Fig. 69c), the stability diagram clearly shows the viscous instability (below  $R\delta 1 \approx 7000$ ) and the inflectional instability (beyond  $R\delta 1 \approx 7000$ ). The latter becomes predominant for  $M_e = 3$ .

It has been observed previously that higher modes could be computed for free stream Mach numbers larger than 2.2, but at first they are associated with very large wavenumbers. For this reason, only the first unstable mode is plotted in Fig. 69c and d for  $M_e = 2.2$  and 3. However, when the Mach number is increased, the second unstable mode appears at lower and lower wavenumbers. This is illustrated in Fig. 69e ( $M_e = 4.5$ ), where the first and second modes are close together. Let us observe that the second mode is more unstable than the first one: the ratio of the maximum amplification rates is of the order of four to five. At  $M_e = 4.8$  (Fig. 69f), the two unstable regions join each other and there is only one neutral curve at hypersonic conditions (Fig. 69g-i). However, when the phase velocity  $c = \omega/\alpha$ , is plotted as a function of  $\alpha_i$ , two well defined regions can be observed. As an example, the curve  $c(\alpha_i)$  is shown in Fig. 70 for  $M_e = 7$  and  $R\delta 1 = 10^6$ . The bump between points A and B corresponds to the first mode, and the loop between B and B' corresponds to the second mode. At larger Reynolds numbers, the growth rate at point B will tend to zero. At infinite Reynolds number, the phase velocity at points B and B' will be equal to the mean velocity at the generalized inflection point. Let us recall that the concept of higher modes deals essentially with the phase velocity of some particular neutral disturbances, independent of the number of separated neutral curves.

### 7.2.2. Oblique Waves ( $\psi \neq 0$ )

The previous results were obtained for two-dimensional waves. However, an important aspect of instability in compressible boundary layers is the effect of the wave direction  $\psi$  on the amplification rates. In incompressible flows, only the two-dimensional waves are usually considered because it can be demonstrated that they become unstable at lower Reynolds numbers than the oblique waves (for a given frequency): this is the celebrated Squire's theorem. This is no longer the case in compressible flows, even at moderate Mach numbers. When the Reynolds number and the frequency are prescribed, there is a non-zero value of  $\psi$  which corresponds to the maximum growth rate. This value will be denoted as  $\psi_M$ . For a given Mach number,  $\psi_M$  depends on the Reynolds number. Typically, it is around 50 deg. for transonic Mach numbers. In supersonic and hypersonic conditions, the situation is particularly complex, as can be seen in Fig. 71, where two stability diagrams are represented for  $M_e = 4.5$  and two values of  $\psi$ : 0 and 60 deg. Changing the wave orientation stabilizes the

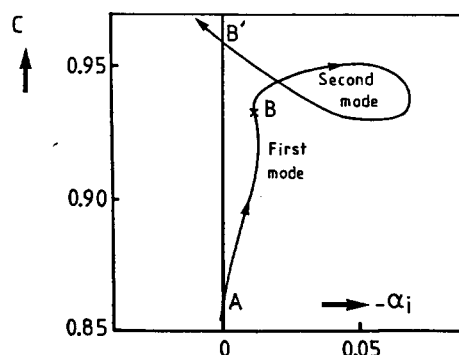


FIG. 70. Phase velocity as a function of the amplification rate. The points A, B and B' are reported in Fig. 69. The arrows indicate increasing frequencies.

second mode, but increases the instability of the first one, so that it becomes difficult to define "the most unstable direction".

### 7.3. RECEPTIVITY, SECONDARY INSTABILITY, NONLINEAR EFFECTS

#### 7.3.1. *Receptivity*

Some properties of the laminar boundary layer as a linear oscillator have been briefly discussed. But how are the unstable waves excited by the available disturbance environment? This question is a part of the problem which is usually addressed under the term "receptivity", introduced by Morkovin.<sup>(136)</sup> The receptivity describes the means by which the forced disturbances (free stream turbulence, sound field ...) enter the laminar boundary layer. It also describes their signature in the disturbed flow. It has previously been shown that a part of this signature is the development of unstable waves, which constitute the eigenmodes of the boundary layer.

Recent studies by Goldstein<sup>(77)</sup> and Kerschen<sup>(100)</sup> have demonstrated that the receptivity process occurs in regions of the boundary layer where the mean flow exhibits rapid changes in the streamwise direction. This happens near the body leading edge and/or in any region farther downstream where some local feature forces the boundary layer to adjust on a short streamwise lengthscale (sudden change in the wall slope or in the wall curvature, suction strip for instance).

These theoretical results were deduced from asymptotic approaches for incompressible flows. They have been more or less substantiated by low speed experiments, but there is no general receptivity theory applicable to high speed conditions. Mack<sup>(119)</sup> attempted to take into account the free stream noise effects by developing a modified linear stability theory. Choudhari and Street<sup>(41)</sup> presented an alternative to the asymptotic approach of Goldstein and Kerschen in order to predict the receptivity due to the interaction of a free stream acoustic wave with localized regions of short-scale variation in surface boundary conditions. This finite Reynolds number approach was applied to the generation of inviscid type instabilities in a two-dimensional supersonic boundary layer.

It is now established that the receptivity increases (i.e. the initial amplitude of the unstable waves increases for a fixed Mach number and for a given disturbance environment) when  $d\delta/dx$  increases,  $\delta$  being the boundary layer thickness. This could explain why the receptivity of a supersonic boundary layer on a cone is less than that of a supersonic boundary layer on a flat plate. On the other hand, changing the unit Reynolds number in a given wind tunnel modifies the level and the spectrum of the free stream disturbances; this constitutes one of the possible explanations for the "unit Reynolds number effect", which illustrates the importance of the receptivity process.

#### 7.3.2. *Nonlinear Evolution and Breakdown*

Let us assume now that unstable waves are generated through the action of a certain receptivity process. These waves grow according to the linear theory. When they reach a finite amplitude, the quadratic terms which are neglected in the theory become appreciable, and nonlinear effects appear. The problem is fairly well documented at low speeds, but very little is known about the nonlinear mechanisms in supersonic and hypersonic flows. It can be guessed that the nonlinearities are created by the temperature or density fluctuations, which have a very large amplitude around the location of the generalized inflection point. Interesting information can be deduced from direct numerical simulations, see Refs 61, 139 and 182 for instance, as well as from analytical theories.<sup>(130)</sup>

The question arises of the length of the nonlinear zone at high speeds. In incompressible flows, the distance between the end of the linear region and the breakdown to turbulence is rather short. This explains that practical prediction methods based on linear theory only (such as the  $e^n$ -method) provide us with good results for predicting the transition location,

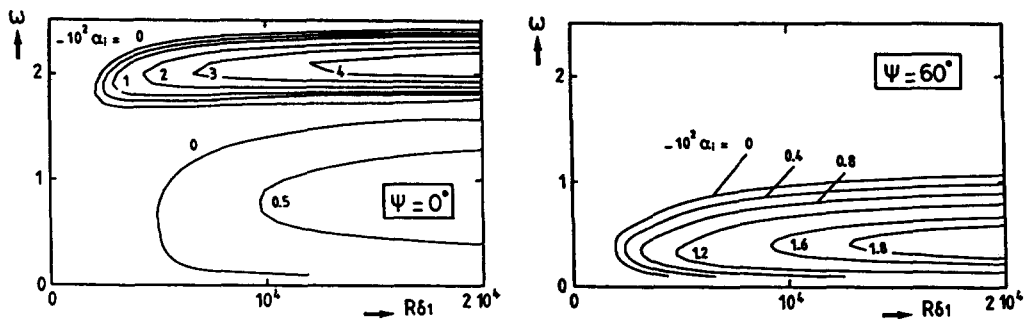


FIG. 71. Effect of the wave orientation on the growth rate ( $M_e = 4.5$ ).

at least for two-dimensional flows. Due to the lack of information, it is assumed that similar techniques can be used for compressible flows, as will be shown in Section 7.5.

#### 7.4. FACTORS ACTING ON THE STABILITY PROPERTIES

Linear stability theory makes it possible to study the influence of some parameters which can modify the stability properties of the flow. Some of these effects are discussed below.

##### 7.4.1. Streamwise Pressure Gradient

The effects of streamwise pressure gradients are well known for low speed flows. In a negative pressure gradient (accelerated flow), the mean velocity profile has no inflection point and the instability—if it exists—is very weak. In a positive pressure gradient (decelerated flow), the appearance of an inflection point gives rise to a strong inflectional instability.

The stability results showing the influence of streamwise pressure gradients at high speeds are not numerous. A major difficulty is that self-similar boundary layer profiles no longer exist, and it becomes necessary to deduce the basic profiles from non-similar boundary layer equations. Vignau,<sup>(193)</sup> for instance, analyzed the effects of positive pressure gradients for  $M_e$  decreasing linearly with  $x$ . For a local free stream Mach number equal to 5.8, it was found that the first mode was stabilized in comparison with the flat plate case, but that the instability of the second mode was increased. On the other hand, Malik<sup>(126)</sup> demonstrated that the second mode could be stabilized by favourable, i.e. negative, pressure gradients.

##### 7.4.2. Wall Temperature

To illustrate the influence of the wall temperature, Fig. 72 shows experimental results collected by Potter.<sup>(151)</sup> The ratio  $Rx_T/Rx_{T_0}$  is plotted as a function of  $T_w/T_{aw}$  for Mach numbers between 1.4 and 11.  $Rx_T$  is the transition Reynolds number computed with the free stream conditions and the transition location  $x_T$ .  $Rx_{T_0}$  is the value for  $Rx_T$  measured under adiabatic conditions.  $T_w$  and  $T_{aw}$  denote the wall temperature and the adiabatic wall temperature, respectively. Although there is some scatter in the data, it appears that cooling the wall delays the onset of transition. This effect is rather strong in the transonic range, but it is reduced when the Mach number increases. Another interesting feature which can be observed in Fig. 72 is the appearance of “transition reversals” and “transition re-reversals” ( $M_e = 3.54$  and  $8.2$ ). The origin of this behaviour has not yet been clearly established.

The stability of laminar boundary layers on cooled walls was studied by Mack,<sup>(118)</sup> Wazzan *et al.*,<sup>(197)</sup> Malik<sup>(126)</sup> and Vignau<sup>(193)</sup> for supersonic flows. The stability computations show a qualitative agreement with the experiments, in this sense that the growth rates

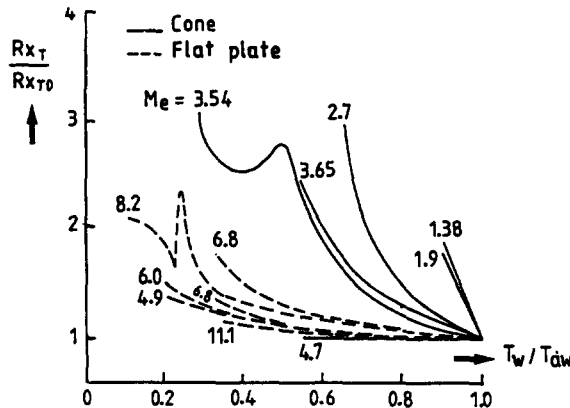


FIG. 72. Effect of wall cooling on the transition Reynolds number.

are reduced when the wall temperature decreases. This effect is linked with the evolution of the height  $y_s$  of the generalized inflection point. When  $y_s$  increases, the instability is enhanced for a fixed value of  $M_e$ . At high Mach numbers,  $y_s$  remains close to the outer edge of the boundary layer, and the stability properties become less sensitive to the wall temperature.

#### 7.4.3. Real Gas Effects

To date, most of the compressible stability analyses have assumed ideal gas behaviour. Real gas effects were studied by Malik,<sup>(127,128)</sup> Gasperas,<sup>(73)</sup> and Stuckert and Reed.<sup>(177)</sup> The latter study demonstrates that the amplification rates associated with the second mode do not change very much from the equilibrium to non-equilibrium and ideal gas models, but that there is a shift in the range of unstable frequencies. The first mode is usually more stable than the second one, although it is more strongly affected by real gas effects.

### 7.5. TRANSITION PREDICTION

For many practical applications, it is important to estimate the transition location. However, it is clear that a rigorous modelling of such a sequence of complicated phenomena appears to be a rather difficult task. The first problem is that in many circumstances the detailed characteristics of the forced disturbances are not very well known. Secondly, the receptivity theories cannot be used routinely for practical purposes, because the results are currently restricted to simple cases. Thirdly, many aspects of the last stages of the transition process are still unclear, especially for compressible flows.

A pessimistic conclusion could be that a "good" prediction of transition is impossible. In spite of this negative situation, transition predictions must be made. Some of the available transition prediction methods are reviewed in this section. Of course, these methods do not claim to reproduce the rich physics of the transition process; they must be considered as short term answers to practical problems.

#### 7.5.1. The $e^n$ -Method

This technique is widely used by people who are assigned the job of making transition prediction. It was first developed by Smith and Gamberoni<sup>(172)</sup> and by van Ingen<sup>(188)</sup> for low speed flows and then extended to compressible flows.

**Incompressible flows.** In this case, only two-dimensional waves ( $\beta = 0$ ) are considered. The growth rate is characterized either by  $-\alpha_i$  (spatial theory) or by  $\omega_i$  (temporal theory).

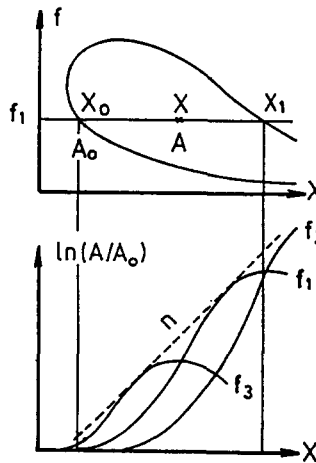


FIG. 73. Typical stability diagram in physical coordinates. Definition of the total growth rate and of the envelope curve.

For a given mean flow, it is possible to compute a stability diagram (upper part of Fig. 73) showing the range of unstable frequencies  $f$  as a function of the streamwise distance  $x$ . Let us now consider a wave which propagates downstream with a fixed frequency  $f_1$ . This wave passes at first through the stable region. It is damped up to  $x_0$ , then amplified up to  $x_1$ , and then it is damped again downstream of  $x_1$ . At a given station  $x$ , the total amplification rate of a spatially growing wave can be defined as

$$\ln(A/A_0) = \int_{x_0}^x -\alpha_i dx. \quad (133)$$

In the framework of the temporal theory, the temporal growth rate is converted to a spatial growth rate by using relation 126. In the previous expression,  $A$  is the wave amplitude, and the index 0 refers to the streamwise position where the wave becomes unstable. The envelope of the total amplification curves is

$$n = \max_f \left[ \ln \left( \frac{A}{A_0} \right) \right]. \quad (134)$$

In incompressible flow, with a low disturbance environment, it is assumed that transition occurs as soon as the  $n$  factor reaches a critical value in the range 7–10, i.e. when the locally most unstable frequency is amplified by a factor  $e^7$  to  $e^{10}$ .

**Extension to compressible flows.** When compressibility begins to play a role, the problem becomes more complex, because the most unstable waves are often oblique waves, see Section 7.2.2. As a consequence, a new parameter enters the dispersion relation: the angle  $\psi$  between the streamwise direction and the wavenumber vector.

It is usual to adopt the following procedure to compute the total amplification of a given frequency: at each streamwise location, the disturbance growth rate is maximized with respect to the wavenumber direction  $\psi$ , i.e. one has to compute  $\alpha_{iM} = \alpha_i(\psi_M)$  in the spatial theory or  $\omega_{iM} = \omega_i(\psi_M)$  in the temporal theory. The total amplification rates are then computed with the local values of  $\alpha_{iM}$  or  $\omega_{iM}$ . When the temporal theory is used, the spatial growth rate  $\sigma_g$  is deduced from relation 127 and the integration is performed along the group velocity trajectory  $x_g$ , which is usually very close to the free stream direction.

#### 7.5.2. First Application: Flat Plate with Adiabatic Wall

Figure 74 shows an application of the  $e^n$ -method for adiabatic flat plates. The stability results were used to compute the theoretical streamwise Reynolds numbers  $R_x$  which

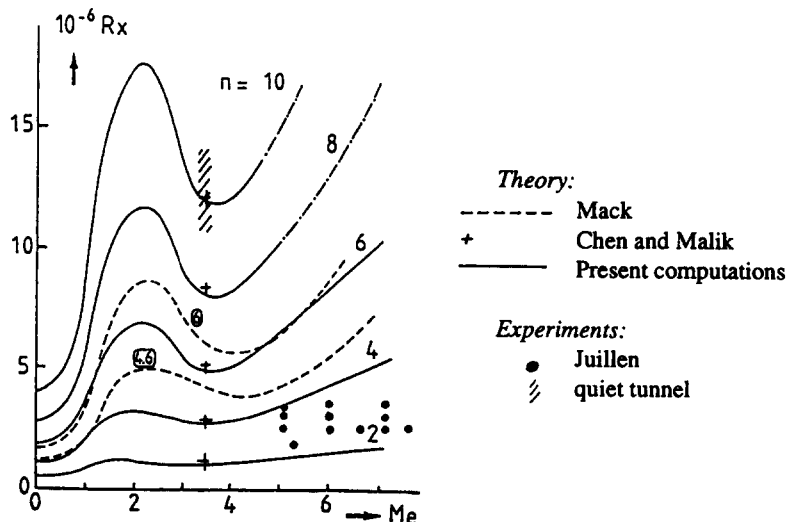


FIG. 74. Application of the  $e^n$ -method (flat plate, adiabatic wall).

correspond to different values of the  $n$  factor, as a function of the free stream Mach number. The dotted lines represent theoretical results given by Mack<sup>(119)</sup> for  $n = 4.6$  and  $6$ , and the crosses are computations performed by Chen and Malik<sup>(39)</sup> for  $M_e = 3.5$  and  $n = 2, 4, 6, 8$  and  $10$ . If it is assumed that transition occurs for a fixed value of the  $n$  factor, each curve represents the evolution of the transition Reynolds number with increasing  $M_e$ . It can be observed that compressibility has a strong stabilizing effect on transonic flows. It becomes destabilizing for Mach numbers between  $2$  and  $3.5$ , and stabilizing again at hypersonic conditions.

It has been previously observed that the value of  $n$  at the onset of transition is usually between  $7$  and  $10$  in "clean" subsonic wind tunnels. The problem is obviously to know if similar values of  $n$  are observed at high speeds. The solid symbols in Fig. 74 represent experimental data obtained at ONERA.<sup>(97)</sup> They correspond to low values of the  $n$  factor, between  $2$  and  $4$ . Numerous examples could be given to illustrate the fact that, in conventional hypersonic wind tunnels, the measured transition Reynolds numbers are rather low, say between  $2$  and  $3$  million. Possible origins of this behaviour are considered below.

### 7.5.3. Wind Tunnel Simulation. Empirical Criteria

It is well known that transition on a smooth surface can be triggered by disturbances which are present in the free stream: velocity fluctuations  $u'$  (free stream turbulence), pressure fluctuations  $p'$  (acoustic disturbances), temperature fluctuations  $T'$ . The problem is very complex, because the effects of these various disturbances depend on the Mach number range (see Pate<sup>(147)</sup>).

At low speeds, the transition Reynolds number is very sensitive to the free stream turbulence level, which is denoted as  $Tu$ . However, if  $Tu$  becomes very low, pressure fluctuations (fan noise in a wind tunnel for instance) can be of major importance for inducing transition.

In transonic flows, acoustical phenomena linked with slotted or perforated walls give rise to strong pressure disturbances, which cause early transition. Better results are obtained in transonic wind tunnels with solid walls.

In supersonic and hypersonic flows, the main factor affecting transition is also the noise, the origin of which lies in the pressure disturbances radiated by the turbulent boundary layers developing along the wind tunnel walls. The effects of  $u'$  and  $T'$  have not yet been firmly established for  $M_e > 3.5$ .

The strong effect of the wind tunnel noise on the transition Reynolds number is illustrated in Fig. 75 (Harvey,<sup>(86)</sup>), where values of  $Rx_T$  measured on cones and flat plates are given as a function of  $\tilde{p}'_\infty/q_\infty$  for  $4 < M_e < 23$ ;  $q_\infty$  is the mean dynamic pressure in the free stream and the  $\sim$  denotes a root mean square value. There are two separate mean curves for cones and flat plates, but the effect of Mach number disappears completely in this representation: transition is governed by  $\tilde{p}'_\infty$  rather than by  $M_\infty$ .

Pate also analysed available wind tunnel data and developed an empirical criterion for "natural" transitions measured in supersonic and hypersonic facilities. This criterion is a correlation between the transition Reynolds number  $Rx_T$  and the parameters acting on the noise intensity, i.e. the tunnel test section circumference  $P$ , and two characteristic parameters of the turbulent boundary layer on the nozzle walls: the mean skin friction coefficient  $C_F$  and the displacement thickness  $\delta_1$ .<sup>(147)</sup> If the free stream Mach number and the wall temperature ratio  $T_w/T_{aw}$  are constant, this criterion reduces to

$$Rx_T = \left( \frac{U_e}{v_e} \right)^{0.5} g(P) \quad (135)$$

where  $g$  is a function of  $P$  which increases as the test section circumference increases. This shows that the transition Reynolds number increases with increasing unit Reynolds number  $U_e/v_e$  and increasing wind tunnel size.

Another correlation, which was used during wind tunnel tests of a smooth model of the Columbia space shuttle, is expressed by the simple relationship

$$\left[ \frac{R\theta}{M_e} \right]_T = \text{constant}. \quad (136)$$

$R\theta$  is the momentum thickness Reynolds number of the laminar boundary layer which develops on the model. The constant is of the order of 200. The values of  $R\theta_T$  deduced from this expression are too low when compared with free flight data on smooth models.

Since the radiated noise is inherent in the presence of walls around the model, there is little doubt concerning the incapacity of wind tunnels to properly simulate free flight conditions. In order to reduce this noise level, it is necessary to delay transition on the nozzle walls, since a laminar boundary layer is less noisy than a turbulent one. This was done in the "quiet tunnel" built at NASA Langley with a free stream Mach number  $M_\infty = 3.5$ . A detailed description of the wind tunnel was given by Beckwith *et al.*<sup>(18)</sup> Notable features are the use of boundary layer bleed slots upstream of the throat, a careful

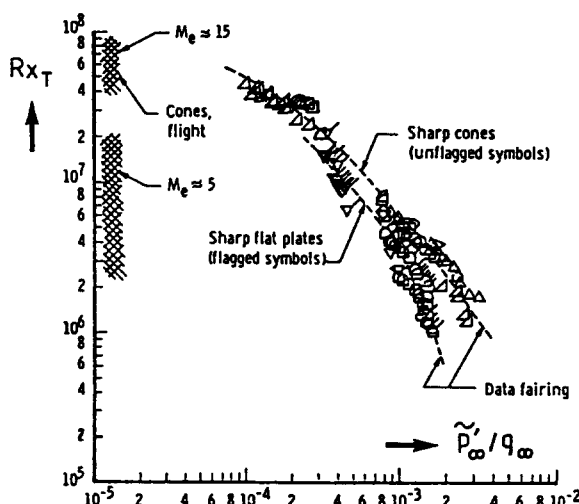


FIG. 75. Effect of wind tunnel noise on the transition Reynolds number.

polishing and a careful design of the nozzle walls' contour in order to minimize the amplification of Görtler vortices. With a laminar boundary layer on the nozzle walls, the measured pressure fluctuations can be one or two orders of magnitude below those measured in conventional facilities. Design and operational details of new low-disturbance wind tunnels are described in Ref. 17.

#### 7.5.4. Further Applications of the $e^n$ -Method

Several transition experiments were carried out in the "quiet tunnel". On a flat plate, transition Reynolds number as high as  $12 \cdot 10^6$  were measured. This value is nearly an order of magnitude larger than those obtained in conventional, noisy facilities.<sup>(39)</sup> It is interesting to notice that this result corresponds to the theoretical value of  $Rx_T$  given by the  $e^n$ -method for  $M_e = 3.5$  and  $n = 10$  (Fig. 74).

The flow on supersonic sharp cones constitutes a second case where the free stream Mach number is constant in the streamwise direction. Measurements performed in the "quiet tunnel" on a 5 deg. half angle sharp cone indicated values of  $Rx_T$  close to 7 or  $8 \cdot 10^6$ , two or three times greater than the values obtained in conventional wind tunnels. The predicted transition Reynolds number computed for  $n = 10$  is  $8 \cdot 10^6$ , in good agreement with experimental data.<sup>(39)</sup>

The problem is to know whether or not low disturbance level wind tunnels are representative of free flight conditions. As direct comparisons of the disturbance environment are difficult to perform, indirect comparisons are made by looking at the value of the  $n$  factor at the onset of transition. In this respect, the flight experiments on the so-called AEDC cone (Fisher and Dougherty<sup>(71)</sup>) provided some interesting information. This cone was mounted on the nose of an F-15 aircraft and flown at Mach numbers from 0.5 to 2 and at altitudes from 1500 to 15,000 m. Malik<sup>(125)</sup> computed the  $n$  factor for four supersonic Mach numbers and found that the transition Reynolds numbers at the onset of transition were correlated with  $n$  factors between 9 and 11. In the experiments, surface pressure fluctuations indicated the formation of TS waves, the frequency band of which was in agreement with linear theory.

Unfortunately, reliable and accurate free flight data are not numerous at higher, hypersonic Mach numbers. Figure 76 shows flight transition results which were collected for sharp cones by Beckwith.<sup>(16)</sup> The transition Reynolds numbers are plotted as a function of the free stream Mach number. The figure also contains a correlation for wind tunnel transition data, which lies much below the flight experiments. The range of results obtained in the "quiet tunnel" are shown for comparison. It is clear that there is a very important scatter in the free flight results, essentially for Mach numbers between 2 and 4. This is mainly due to the fact that these data have been obtained for various wall temperatures, the distribution of which is not known in many cases. Malik<sup>(125)</sup> calculated the transition Reynolds numbers corresponding to  $n = 10$  for a 5 deg. half cone and various Mach numbers up to 7. He made two series of computations: one by assuming that the wall was adiabatic and the other by assuming that the wall temperature depended on the free stream Mach number according to a purely empirical relationship

$$\frac{T_w}{T_{aw}} = 1 - 0.05 M_\infty - 0.0025 M_\infty^2. \quad (137)$$

The numerical results are reported in Fig. 76. Relation 137 makes it possible to reproduce the trends exhibited by the flight results.

The effect of nose bluntness on transition at high speed has been studied by many investigators due to its importance for many hypersonic configurations, see for instance Stetson *et al.*<sup>(176)</sup> The main result is that transition location moves downstream for small values of the nose radius. A linear stability analysis of this problem was performed by Malik *et al.*<sup>(128)</sup> In order to properly calculate the entropy layer effects, the basic flow was computed by solving the Parabolized Navier-Stokes (PNS) equations; the initial condition for the PNS solution was provided by solving the full compressible Navier-Stokes equations around the cone nose. By using the  $e^n$ -method, Malik *et al.* found that the predicted

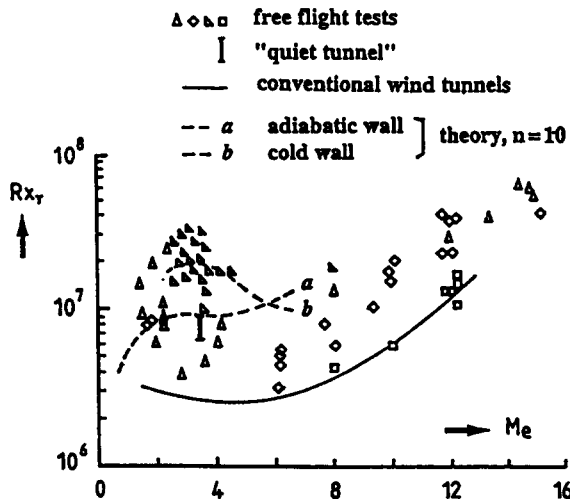


FIG. 76. Comparison between measured and predicted Reynolds numbers on sharp cones.

transition Reynolds number increased due to small nose bluntness, in qualitative agreement with Stetson's results. It was also demonstrated<sup>(128)</sup> that the nose bluntness effect constitutes one of the possible explanations for the unit Reynolds number effect.

The  $e^n$ -method was used by Malik *et al.*<sup>(127)</sup> for the rather complex reentry-F experiments. The reentry-F vehicle<sup>(96)</sup> consisted of a 5 deg. semi-vertex cone with an initial nose of 2.54 mm. Computations were carried out for an altitude of 30.48 km, where the free stream Mach number was close to 20. The base flow was calculated by equilibrium gas Navier-Stokes and PNS codes. At the measured transition location, the  $n$  factor was approximately 7.5. Roughness effects probably affected the transition mechanisms at the junction between the nose and the cone, and so the value of  $n$  would be somewhat larger for a perfectly smooth surface. These computations extend the  $e^n$ -method into the hypersonic, reacting gas regime.

## 7.6. CONCLUDING REMARKS

It has been shown that, even in the "simple" case of two-dimensional flows, the problems associated with boundary layer transition at high speeds are numerous and that many of them are far from solved.

From a theoretical point of view, the linear stability theory constitutes a very efficient tool to understand the fundamental mechanisms leading to turbulence. It can also explain, at least qualitatively, the influence of some parameters such as wall temperature or nose bluntness, but the key problem lies in the understanding of the receptivity mechanisms and of the nonlinear phenomena. In spite of these difficulties, the extension of the  $e^n$ -method to supersonic and hypersonic flows provides us with a reliable prediction of transition: for a low disturbance environment, the  $n$  factor has roughly the same value as in incompressible flow (around 10).

In the case of three-dimensional flows not considered here, the problems become more complex due to the appearance of a powerful cross-flow instability, and the validity of the  $e^n$ -method remains an open question, see for instance Refs 5, 161.

## 8. CONCLUSION

The calculation of shock layers and boundary layers has been described by using either the *boundary layer approach* or the solution of *Navier-Stokes equations*. In recent years,

decisive progress has been made to solve the Navier–Stokes equations and it is believed that accurate solutions can be obtained. However, these solutions are required to handle stiff problems, especially when non-equilibrium flows are involved. It is not always possible to claim that the numerical solution is a good approximation of the true solution. The behaviour of numerical solutions of strongly nonlinear equations involving different time scales has been studied for simple equations and surprising results have been demonstrated.<sup>(106,205)</sup> In addition, the capacity of present computers is often too small to use computational grids with a sufficient refinement. If a complete vehicle is considered, it is almost impossible to describe the boundary layer correctly, in particular when the flow is turbulent. Indeed, the accurate calculation of wall heat fluxes or of skin friction requires a large number of points near the wall. When the stability of laminar boundary layers is studied, the velocity and temperature profiles must also be described with an extreme accuracy, especially around the generalized inflection point. For simple geometries, the question is less severe and accurate solutions have been obtained. Nevertheless, even if the grid resolution is not fine enough, it is hoped that Navier–Stokes solutions give a good global picture of the flow around the vehicle. Numerical experience seems to indicate that the wall pressure distribution is not too sensitive to the grid refinement, except for phenomena like shock wave–boundary layer interactions.

For these reasons, the numerical solution of the *boundary layer equations* is still a valuable tool. The pressure distribution required for these solutions can be obtained either from the solution of Euler equations or from the solution of Navier–Stokes equations. In this latter case, the solution of boundary layer equations is useful to validate the Navier–Stokes solution or to improve the accuracy of the boundary layer characteristics (if the pressure distribution is good enough). Another good reason for using boundary layer solutions is the study of modelling (for example turbulence modelling), because these solutions are obtained in a small computer time and it is easier to test different models. In hypersonic flow around blunt bodies, the boundary layer is fed with a flow which crossed the curved front shock wave and entropy swallowing effects modify the development of the boundary layer. The defect boundary layer theory which has been presented is able to account for these effects while the simplicity of the standard boundary layer approach is retained.

The *modelling of hypersonic boundary layers* raises difficult questions: modelling of flow in chemical and thermal non-equilibrium, modelling of turbulence effects, modelling of the onset of transition and of the transition region. The last two questions are still open at low speeds and there is no reason that they are simpler to solve in hypersonic flow. There is no real theory to support the development of the engineering tools used to describe these effects, except direct numerical simulations (or large eddy simulations) obtained from solutions of three-dimensional unsteady Navier–Stokes equations. Nowadays, these simulations are able to give nice pictures of transitional or turbulent flows. In certain cases, the numerical simulations have been used to improve turbulence models.

In order to validate and to improve the physical models, *experimental results* are needed. Between global results around representative models of vehicles and detailed results on transition or on turbulence, different levels of results are required. Unfortunately, there are very few ground facilities able to reproduce the conditions of hypersonic flight, in particular the high temperature conditions. Strictly, it is even impossible to reproduce all the similarity parameters of hypersonic flight. To validate the models, flight data are extremely helpful. For example, flight data obtained on the shuttle have been used in this paper to assess calculations results. These flight data are invaluable even if one would like to know more details of the flow.

In no way can this paper pretend to be complete. Such important topics as shock wave–boundary layer interactions or experimental simulations have been excluded. Moreover, most of the presented topics have been only touched upon. We have tried to describe the main physical phenomena occurring in a shock layer and the associated modelling allowing us to simulate them. It is hoped that this paper gave a flavour of the flow in a shock layer which is a rich source of many fascinating research topics.

## ACKNOWLEDGEMENTS

Thanks to F. Thivet and K. Heffner who read the manuscript very carefully; they made many suggestions and helpful comments which greatly improved the text.

## REFERENCES

1. Acharya, M. (March 1977) Effect of compressibility on boundary-layer turbulence. *AIAA J.* **15**(3), 303–304.
2. Adams, J. C. (April 1968) Higher-order boundary-layer effects on analytic bodies of revolution. Technical Report AEDC-TR-68-57, Arnold Engineering Development Center, Arnold Air Force Station, Tennessee, U.S.A.
3. Anderson, Jr, J. D. (1989) *Hypersonic and High Temperature Gas Dynamics*. McGraw-Hill Book Company.
4. Arnal, D. (June 1989) Laminar-turbulent transition problems in supersonic and hypersonic flows. In *Special Course on Aerothermodynamics of Hypersonic Vehicles*, AGARD Report No. 761.
5. Arnal, D. (1993) Prediction based on linear theory. In *Progress in Transition Modelling*. AGARD Report No. 793.
6. AuPOIX, B. (10 May–3 June 1988) An introduction to real gas effects. In *Special Course on Aerothermodynamics of Hypersonic Vehicles*, AGARD-FDP VKI Lecture Series—AGARD Report 761.
7. AUPOIX, B., BONNET, S., GLEYZES, C. and COUSTEIX, J. (14–19 January 1989) Calculation of three-dimensional boundary layers including hypersonic flows. In *Fourth Symposium on Numerical and Physical Aspects of Aerodynamic Flows—Long Beach*.
8. AUPOIX, B., BRAZIER, J. P. and COUSTEIX, J. (7–10 January 1991) An asymptotic defect boundary layer theory applied to hypersonic flows. AIAA Paper 91-0026 29<sup>th</sup> Aerospace Sciences Meeting—Reno, Nevada.
9. AUPOIX, B. and COUSTEIX, J. (16–20 January 1989) Real gas effects in hypersonic laminar boundary layers for reentry flows. In *Second Joint Europe—US Short Course on Hypersonics—Colorado Springs*.
10. AUPOIX, B., DESMET, E. and VIALA, S. (20–23 June 1993) Hypersonic turbulent boundary layer modelling. In *Symposium on Transitional and Compressible Turbulent Flows*, Washington DC 1993 ASME Fluids Engineering Conference.
11. BALAKRISHNAN, A. (1986) Correlations for specific heats of air species to 50,000 K. AIAA paper 86-1277, Boston, Massachusetts.
12. LE BALLEUR, J. C. and GIRODROUX-LAVIGNE, P. (1992) Calculation of fully three-dimensional separated flows with an unsteady viscous-inviscid interaction method. *Fifth Symposium on Numerical and Physical Aspects of Aerodynamic Flows, Long Beach*.
13. BARRÈRE, M. and PRUDHOMME, R. (1973) *Équations fondamentales de l'aérothermochimie*. Masson et Cie.
14. BAULCH, D. L., DRYSDALE, D. D. and HORNE, D. G. (1973) *Evaluated Kinetic Data for High Temperature Reactions—Volume 2 Homogeneous Gas Phase Reactions of the H<sub>2</sub>-N<sub>2</sub>-O<sub>2</sub> System*. London, Butterworths.
15. EL BAZ A. M. and LAUNDER, B. E. Second-moment modelling of compressible mixing layers. In Elsevier Science Publishers, editor, *Engineering Turbulence Modelling and Experiments 2*, pages 63–72. W. Rodi and F. Martelli 1993.
16. BECKWITH, I. E. (1975) Development of a high Reynolds number quiet tunnel for transition research. *AIAA J* **13**(3).
17. BECKWITH, I. E., CHEN, F., WILKINSON, S., MALIK, M. and TUTTLE, D. (1990) Design and operational features of low-disturbance wind tunnels at NASA Langley for Mach numbers from 3.5 to 18. AIAA Paper 90-1391.
18. BECKWITH, I. E., CREEL, JR, T. R., CHEN, F. J. and KENDALL, J. M. (1983) Freestream noise and transition measurements on a cone in a Mach 3.5 pilot low-disturbance tunnel. TP 2180, NASA.
19. BIRCH, S. F. and EGGRERS, J. M. (January 1973) A critical review of the experimental data for developed free turbulent shear layers. Technical Report SP-312, NASA.
20. BIRD, G. A. (1976) *Molecular Gas Dynamics*. Oxford University Press, London.
21. BIRD, R. B., STEWART, W. E. and LIGHTFOOT, E. N. (1960) *Transport Phenomena*. John Wiley and Sons, New York.
22. BLAISDELL, G. A., MANSOUR, N. N. and REYNOLDS, W. C. (1991) Numerical simulations of compressible homogeneous turbulence. Report TF-50, Department of Mechanical Engineering Stanford University, Stanford, California.
23. BLOTTNER, F. G. (November 1964) Nonequilibrium laminar boundary-layer flow of ionized air. *AIAA J.* **2**(11) 1291–1297.
24. BLOTTNER, F. G., JOHNSON, M. and ELLIS, M. (1970) Chemically reacting viscous flow program for multicomponent gas mixture. Technical Report Sc-RR-70-754, Sandia Laboratories.
25. BONNET, J. P. (1981) Comparison of computation with experiments—Summary report. In S. J. Kline, B. J. Cantwell, and G. M. Lilley, editors, *Volume III—Comparison of Computation with Experiment, and Computers' Summary Reports*, pp. 1408–1410. 1980–81 AFOSR-HTTM-Stanford Conference on Complex Turbulent Flows.
26. BONNET, J. P. and YERU, R. (15–17 October 1990) Test d'un modèle de fermeture au second ordre pour la prévision de sillage turbulents hypersoniques. In *Colloque d'Aérodynamique Appliquée—Marseille*. AAAF.
27. BONNET, S. (17 June 1988) Couches limites laminaires tridimensionnelles avec effets de dissociation. PhD thesis, Ecole Nationale Supérieure de l'Aéronautique et de l'Espace, Toulouse.
28. BORTNER, M. H. (May 1969) A review of rate constants of selected reactions of interest in re-entry flow fields in the atmosphere. Technical Report 484, National Bureau of Standard.
29. BOUTIER, A. (ed.) (1993) *New Trends in Instrumentation for Hypersonic Research, Volume 224 NATO ASI Series—Series E: Applied Sciences*. Kluwer Academic Publishers.

30. BRADSHAW, P. (1977) Compressible turbulent shear layers. *Annu. Rev. of Fluid Mechanics* **9**, 33–54.
31. BRADSHAW, P., LAUNDER, B. E. and LUMLEY, J. L. (7–10 January 1991) Collaborative testing of turbulence models. AIAA Paper 91-0215 29<sup>th</sup> Aerospace Science Meeting Reno, Nevada.
32. BRUN, R. (1986) *Transport et relaxation dans les écoulements gazeux*. Masson—Physique fondamentale et appliquée.
33. BRUN, R. (1992) Problèmes d'écoulement posés par la rentrée dans les atmosphères planétaires. *Revue Scientifique et Technique de la Défense*.
34. BUSHNELL, D. M. (1981) Simple compressible strains. In S. J. Kline, B. J. Cantwell, and G. M. Lilley, editors, *Volume II—Taxonomies, Reporter's Summaries, Evaluation, and Conclusions*, pp. 812–836. 1980–81 AFOSR-HTM-Stanford Conference on Complex Turbulent Flows.
35. BUSHNELL, D. M., CARRY, JR, A. M. and HARRIS, J. E. (1977) Calculation methods for compressible turbulent boundary layers. Technical Report SP-422, NASA.
36. BUSHNELL, D. M. and MORRIS, D. J. (August 1971) Shear-stress, eddy-viscosity, and mixing-length distributions in hypersonic boundary layers. Technical Memorandum TM X-2310, NASA.
37. CEBEKI, T. and SMITH, A. M. O. (1974) *Analysis of Turbulent Boundary Layers*, Volume 15 of *Applied Mathematics and Mechanics*. Academic Press, New York.
38. CHAPMAN, S. and COWLING, T. G. (1939) *Mathematical Theory of Non Uniform Gases*. Cambridge University Press.
39. CHEN, F. J. and MALIK, M. R. (1988) Comparison of boundary layer transition on a cone and flat plate at Mach 3.5. AIAA Paper 88-0411.
40. CHIEN, K. Y. (January 1982) Predictions of channel and boundary-layer flows with a low-Reynolds-number turbulence model. *AIAA J.* **20(1)**, 33–38.
41. CHOUDHARI, M. and STRETT, C. L. (1991) A finite Reynolds number approach for receptivity due to rapid variations in surface boundary conditions. In D. C. Reda, H. L. Reed, and R. Kobayashi, editors, *1<sup>st</sup> ASME/JSME Fluids Eng. Conf., Portland*.
42. COFFEE, T. P. and HEIMERL, J. M. (1981) Transport algorithms for premixed, laminar, steady-state flames. *Comb. and Flame* **43**, 273–289.
43. COLEMAN, G. N. and MANSOUR, N. N. (9–11 September 1991) Simulation and modeling of homogeneous compressible turbulence isotropic mean compression. In *Eighth Symposium on Turbulent Shear Flows*—Munich, Germany.
44. COUSTEIX, J. (1988) *Couche Limite Laminaire*, Cepadues, Toulouse.
45. COUSTEIX, J. and AUPOIX, B. (7–11 December 1987) Calculation of hypersonic laminar boundary layers. In *First Joint Europe—US Short Course on Hypersonics*—Paris, Birkhäuser, Boston.
46. COUSTEIX, J. and AUPOIX, A. (8–12 May 1989) Turbulence models for compressible flows. In *Three-dimensional Supersonic and Hypersonic Flows Including Separation*. AGARD-FDP VKI Lecture Series—AGARD Report 764.
47. DASH, S. M., WEILERSTEIN, G. and VAGLIO-LAURIN, R. (1975) Compressibility effects in free turbulent shear flows. TR 75-1436, AFOSR.
48. DAVIS, R. T. (1970) Numerical simulation of the hypersonic viscous shock-layer equations. *AIAA J.* **8**, 843–851.
49. DAVIS, R. T. and FLÜGGE-LOTZ, I. (1964) Laminar compressible flow past axisymmetric blunt bodies. *J. Fluid Mechanics* **20(4)**, 593–623.
50. DAVIS, R. T. and FLÜGGE-LOTZ, I. (1964) The laminar compressible boundary-layer in the stagnation-point region of an axisymmetric blunt body including the second-order effect of vorticity interaction. *Int. J. Heat and Mass Transf.* **7**, 341–370.
51. DÉLERY, J. (1988) Shock/shock and shock-wave/boundary layer interactions in hypersonic flows. In *AGARD 761, Special Course on Aerothermodynamics of Hypersonics Vehicle*.
52. DÉLERY, J. and MARVIN, J. G. (1986) Shock-wave/boundary layer interactions. AGARDograph No. 280.
53. DORRANCE, W. H. (1962) *Viscous Hypersonic Flow*. McGraw-Hill Book Company.
54. VAN DRIEST, E. R. (1951) Turbulent boundary layer in compressible fluids. *J. Aer. Sci.* **18**.
55. DUNN, D. W. and LIN, C. C. (1955) On the stability of the laminar boundary layer in a compressible fluid. *J. Aer. Sci.* **22**, 455–477.
56. DUSSAUGE, J. P. and GAVIGLIO, J. (1987) The rapid expansion of a supersonic turbulent flow: Role of bulk dilatation. *J. Fluid Mechanics* **174**, 81–112.
57. DUSSAUGE, J. P. and QUINE, C. (October 1988) A second-order closure for supersonic turbulent mixing flows—Application to the supersonic mixing. In *The Physics of Compressible Turbulent Mixing*. Princeton University, New Jersey, Lecture Notes in Physics—Springer-Verlag.
58. ELEDÉM, C. (14 Décembre 1987) Couches limites hypersoniques avec effets de dissociation. PhD thesis, Ecole Nationale Supérieure de l'Aéronautique et de l'Espace, Toulouse.
59. EMANUEL, G. (1987) Advanced Classical Thermodynamics, Education Series. AIAA.
60. ERLEBACHER, G., HUSSAINI, M. Y., KREISS, H. O. and SARKAR, S. (February 1990) The analysis and simulation of compressible turbulence. Contract Report CR 181997 (ICASE Report No. 90-15), NASA.
61. ERLEBACHER, G. and HUSSAINI, M. Y. (1990) Second mode interactions in supersonic boundary layers. In D. Arnal and R. Michel, editors, *Laminar-Turbulent Transition, IUTAM Symp.*, Toulouse. Springer-Verlag.
62. FANNELØP, T. K. and FLÜGGE-LOTZ, I. (1965) Two-dimensional hypersonic stagnation flow at low Reynolds numbers. *Z. Flugwiss.* **13(8)**, 282–296.
63. FANNELØP, T. K. and FLÜGGE-LOTZ, I. (1966) Viscous hypersonic flow over simple blunt bodies; comparison of a second-order theory with experimental results. *J. de Mécanique* **5(1)**, 69–100.
64. FAVRE, A. (1956) Equations statistiques des gaz turbulents. In *Comptes Rendus de l'Académie des Sciences* **246**.
65. FAVRE, A., KOVASZNAY, L. S. G., DUMAS, R., GAVIGLIO, J. and COANTIC, M. (1976) *La turbulence en mécanique des fluides—Bases théoriques et expérimentales—Méthodes statistiques*, Bordas.
66. FAY, J. A. and RIDDELL, F. R. (February 1966) Theory of stagnation point heating in dissociated air. *J. Aer. Sci.* **25(2)**, 73–85, 121.

67. FERNHOLZ, H. H. and FINLEY, P. J. (June 1977) A critical compilation of compressible turbulent boundary layer data. AGARDograph AG-223, AGARD.
68. FERNHOLZ, H. H. and FINLEY, P. J. (May 1980) A critical commentary on mean flow data for two-dimensional compressible turbulent boundary layers. AGARDograph AG-253, AGARD.
69. FERNHOLZ, H. H., FINLEY, P. J., DUSSAUGE, J. P. and SMITS, A. J. (May 1989) A survey of measurements and measuring techniques in rapidly distorted compressible turbulent boundary layers. AGARDograph AG-315, AGARD.
70. FERNHOLZ, H. H., FINLEY, P. J. and MIKULLA, V. (November 1981) A further compilation of compressible turbulent boundary layer data with a survey of turbulence data. AGARDograph AG-263, AGARD.
71. FISHER, D. F. and DOUGHERTY, N. S. (1982) In-flight transition measurements on a 10 deg. cone at Mach numbers from 0.5 to 2. TP 1971, NASA.
72. GARDINER, JR, W. C. (1984) *Combustion Chemistry*. Springer-Verlag.
73. GASPERAS, G. (1990) Stability of the laminar boundary layer for an imperfect gas. In D. Arnal and R. Michel, editors, *Laminar-Turbulent Transition, IUTAM Symp., Toulouse*.
74. GASTER, M. (1962) A note on the relation between temporally increasing and spatially increasing disturbances in hydrodynamic stability. *J. Fluid Mechanics* 14, 222-224.
75. GAVIGLIO, J. (1989) Reynolds analogies and experimental studies of heat transfer in the supersonic boundary layer. *Int. J. Heat and Mass Transfer* 30(5), 911-926.
76. GODUNOV, S. (1959) A difference scheme for numerical computation of discontinuous solutions of equations of fluid dynamics. *Mat. Sb* 47(89), 271-306.
77. GOLDSTEIN, M. E. (1983) The evolution of TS waves near a leading edge. *J. Fluid Mechanics* 127, 59-81.
78. GORDON, S. and McBRIDE, B. J. (1971) Computer program for calculation of complex chemical equilibrium compositions, rocket performance, incident and reflected shocks and Chapman-Jauguet detonations. SP 73, NASA.
79. GOULARD, R. (November 1958) On catalytic recombination rates in hypersonic stagnation point heat transfer. *Jet Propulsion*, pp. 737-745.
80. GUPTA, R. N., YOS, J. M., THOMPSON, R. A. and LEE, K. P. (August 1990) A review of reaction rates and thermodynamic and transport properties for an 11-species air model for chemical and thermal nonequilibrium calculations to 30000 K. Technical Report Reference Publication 1232, NASA.
81. HA MINH, H. (15-17 Octobre 1990) Physique et modélisation des écoulements turbulents compressibles. In *Colloque d'Aérodynamique Appliquée—Marseille*, AAAF.
82. HANSEN, C. F. (1959) Approximations for the thermodynamic and transport properties of high-temperature air. Technical Report TR R-50, NASA.
83. HANSON, R. K. and SALIMIAN, S. (1984) Survey of rate constants in the N/H/O system. In *Combustion Chemistry*, W. C. Gardiner (ed.).
84. HARTEN, A. (1983) High resolution scheme for hyperbolic conservation laws. *J. Comp. Phys.* 49, 357-393.
85. HARTEN, A. (1984) On a class of high resolution total variation stable finite difference scheme. *SIAM J. Num. Anal.* 21, 1-23.
86. HARVEY, W. D. (1978) Influence of free stream disturbances on boundary layer transition. Technical Memorandum 78635, NASA.
87. HERBERT, T. (1993) Parabolized Stability Equations. In *Progress in Transition Modelling*, AGARD-FDP-VKI Special Course.
88. HIRSCH, C. (1990) *Numerical Computation of Internal and External Flows*. John Wiley & Sons.
89. HIRSCHEL, E. H. and KORDULLA, W. (1981) *Shear Flow in Surface-Oriented Coordinates*, volume 4 of *Notes on Numerical Fluid Mechanics*. Vieweg, Braunschweig/Wiesbaden.
90. HIRSCHFELDER, J. O., CURTISS, C. F. and BIRD, R. B. (1954) *Molecular Theory of Gases and Liquids*. John Wiley and Sons.
91. HIRSCHFELDER, J. O. and CURTISS, C. F. (1949) Flame propagation in explosive gas mixtures. In *3rd Symp. (Int.) on Combustion*, pp. 121-127. Rheinhold, New York.
92. HOLDEN, M. S. (1989) Shock-shock boundary layer interactions. In *AGARD Report No. 764, Special Course on Three-Dimensional Supersonic/Hypersonic Flows Including Separation*.
93. HORNUNG, H. G. (1988) 28th Lanchester memorial lecture—Experimental real-gas hypersonics. *L'Aéronautique et l'Astronautique* 133(6), 11-21.
94. HOWARTH, L. (1951) The boundary layer in three-dimensional flow. II: The flow near a stagnation point. *Phil. Mag.* 7, 1433-1440.
95. HUANG, P. G., BRADSHAW, P. and COAKLEY, T. J. (1991) Assessment of closure coefficients for compressible-flow turbulence models. Technical memorandum, NASA.
96. JOHNSON, C. B., STAINBACK, P. C., WIKER, K. C. and BONY, L. R. (1972) Boundary layer edge conditions and transition Reynolds number data for a flight test at Mach 20 (Reentry F). TM X-2584, NASA.
97. JUILLEN, J. C. (1969) Détermination expérimentale de la région de transition sur une plaque plane à  $M = 5$ , 6 et 7. Technical Report 10/2334 AN, ONERA.
98. KANG, S. W. and DUNN, M. G. (1972) Theoretical and measured electron density distributions for the RAM vehicle at high altitudes. AIAA Paper 72-689.
99. KEE, R. J., RUPLEY, F. M. and MILLER, J. A. (April 1987) The Chemkin thermodynamic data base. Sandia report Sand87-8215, Sandia National Laboratories.
100. KERSCHEN, E. J. (1989) Boundary layer receptivity. AIAA Paper 89-1109.
101. KIM, S. C. (November, 1990) New mixing-length model for supersonic shear layers. *AIAA J.* 28(11), 1999-2000.
102. KOPPENWALLNER, G. (1984) Fundamentals of Hypersonics. In *Hypersonic Aerothermodynamics, VKI Lecture Series 1984-01*.
103. LADERMAN, A. J. and DEMETRIADES, A. (1974) Mean and fluctuating flow measurements in the hypersonic boundary layer over a cooled wall. *J. Fluid Mechanics* 63(1), 121-144.
104. LAFON, A. (Mars 1990) Calcul d'écoulements visqueux hypersoniques. Rapport technique RT 32/5005.22, ONERA.

105. LAFON, A., DENIAU, H., MAMAN, P. and MOSCHETTA, J. M. (January 1994) A fully upwind implicit PNS solver for the computation of 3D supersonic flows with crossflow separation. To be presented at the 32nd Aerospace Sciences Meeting and Exhibit, Reno.
106. LAFON, A. and YEE, H. C. (July 1991) Dynamical approach study of spurious steady-state numerical solutions of nonlinear differential equations. III. The effects of nonlinear source terms and boundary conditions in reaction-convection equations. NASA TM 103877.
107. LAUNDER, B. E. (1993) Modelling convective heat transfer in complex turbulent flows. In Elsevier Science Publishers, *Engineering Turbulence Modelling and Experiments 2*, pp. 3–22. W. Rodi and F. Martelli (eds).
108. LAUNDER, B. E. and SHARMA, B. L. (1974) Application of energy-dissipation model of turbulence to the calculation of flow near a spinning disc. *Letters in Heat and Mass Transfer* 1, 131–138.
109. LAWRENCE, S. L. (March, 1992) Parabolized Navier–Stokes methods for hypersonic flows. In *VKI Lecture Series*.
110. LAWRENCE, S. L., CHAUSSEE, D. S. and TANNEHILL, J. C. Application of an upwind algorithm to the three-dimensional parabolized Navier–Stokes equations. AIAA Paper 87-1112-CP.
111. LE BALLEUR, J. C. (29 September–1 October 1980) Calcul des écoulements à forte interaction visqueuse au moyen de méthodes de couplage. In *Computation of Viscous-Inviscid Interactions, AGARD Conference Proceedings No. 291*, United States Air Force Academy—Colorado Springs.
112. LEES, L. (1947) The stability of the laminar boundary layer in a compressible fluid. TN 876, NACA.
113. LEES, L. and LIN, C. C. (1946) Investigation of the stability of the laminar boundary layer in a compressible fluid. TN 1115, NACA.
114. LEES, L. and RESHOTKO, E. (1962) Stability of the compressible laminar boundary layer. *J. Fluid Mechanics* 12(4), 555–590.
115. LENGRAND, J. C., ALLÈGRE, J. and RAFFIN, M. (26–28 Octobre 1987) Hypersonique et gaz raréfiés. 24ème Colloque d'Aérodynamique Appliquée, Poitiers.
116. LUBARD, S. C. and HELLIWELL, W. S. (1974) Calculation of the flow on a cone at high angle of attack. *AIAA J.* 12, 965–974.
117. MACK, L. M. (1965) Stability of the compressible laminar boundary layer according to a direct numerical solution. In *AGARDograph 97, Part 1*, pp. 329–362.
118. MACK, L. M. (November, 1969) Boundary layer stability theory (2 volumes). Jet Propulsion Laboratory, Calif. Inst. of Techn., Pasadena, California.
119. MACK, L. M. (1975) Linear stability and the problem of supersonic boundary layer transition. *AIAA J.* 13(3), 278–289.
120. MACK, L. M. (1977) Transition prediction and linear stability theory. In *AGARD Conf. Proc. No. 224, Paris*.
121. MACK, L. M. (1981) Compressible boundary layer stability calculations for sweptback wings with suction. *AIAA J.* 20, 363–369.
122. MACK, L. M. (1984) Boundary layer linear stability theory. In *AGARD Report No. 709*.
123. MACK, L. M. (1984) Remarks on disputed numerical results in compressible boundary layer stability theory. *Phys. Fluids* 27(2).
124. MAISE, G. and MACDONALD, H. (June 1968) Mixing length and kinematic eddy viscosity in a compressible boundary layer. *AIAA J.* 9(6), 73–79.
125. MALIK, M. R. (February 1984) Instability and transition in supersonic boundary layers. In *Laminar Turbulent Boundary Layers*, Energy Sources Technology Conf., New Orleans, Louisiana.
126. MALIK, M. R. (1987) Prediction and control of transition in hypersonic boundary layers. AIAA Paper 87-1414.
127. MALIK, M. R. (1990) Stability theory for chemically reacting flows. In D. Arnal and R. Michel, editors, *Laminar-Turbulent Transition, IUTAM Symp., Toulouse*, Springer-Verlag.
128. MALIK, M. R. (1990) Transition in hypersonic boundary layers. In T. Cebeci, (ed.), *Numerical and Physical Aspects of Aerodynamic Flows IV*, Springer-Verlag.
129. MARRONE, P. V. and TREANOR, C. E. (September 1963) Chemical relaxation with preferential dissociation from excited vibrational levels. *The Physics of Fluids*, 6(9).
130. MASAD, J. A. and NAYFEH, A. H. (1990) Subharmonic instability of compressible boundary layers. *Phys. Fluids A* 2(8), 1380–1392.
131. MEIER, H. U. and ROTTA, J. C. (November 1971) Temperature distributions in supersonic turbulent boundary layers. *AIAA J.* 9(11), 2149–2156.
132. MONNOYER, F., MUNDT, C. and PFITZNER, M. (8–11 January 1990) Calculation of the hypersonic viscous flow past reentry vehicles with an Euler-boundary layer coupling approach. AIAA Paper 90-417, 28<sup>th</sup> Aerospace Sciences Meeting, Reno, Nevada.
133. MONTAGNÉ, J. L., YEE, H. C. and VINOKUR, M. (July 1987) Comparative study of high resolution shock capturing schemes for a real gas. Technical Report TM 100004, NASA.
134. MOORE, F. K. (1964) *Theory of Laminar Flows*, High Speed Aerodynamics and Jet Propulsion. Princeton University Press.
135. MORKOVIN, M. V. (1961) Effects of compressibility on turbulent flows. Colloque International CNRS No. 108, Mécanique de la Turbulence, Editions CNRS.
136. MORKOVIN, M. V. (1968) Critical evaluation of transition from laminar to turbulent shear layers with emphasis on hypersonically travelling bodies. Report AFFDL-TR-68-149, Wright-Patterson Air Force Base, Ohio.
137. MORKOVIN, M. V. (1987) Transition at hypersonic speeds. Contractor Report 178 315, ICASE NASA.
138. NAGANO, Y. and TAGAWA, M. (March 1990) An improved  $k - \epsilon$  model for boundary layer flows. *J. of Fluids Engng—Trans. ASME* 112, 33–39.
139. NORMAND, X. (1990) Transition à la turbulence dans les écoulements cisaillés compressibles libres ou pariétaux. PhD thesis, Grenoble University.
140. OERTEL, H. (1966) *Stofbrohre*, Springer-Verlag.
141. OWEN, F. K., HORSTMAN, C. C. and KUSSOV, M. I. (1975) Mean and fluctuating flow measurements on a fully-developed, non-adiabatic, hypersonic boundary layer. *J. Fluid Mechanics* 70(2), 393–413.

142. PAPAMOSCHOU, D. and ROSHKO, A. (1988) The compressible turbulent shear layer: An experimental study. *J. Fluid Mechanics* **197**, 453–477.
143. PARK, C. (25–28 July 1984) Problems of rate chemistry in the flight regimes of aeroassisted orbital transfer vehicles. AIAA Paper 84-1730, *19<sup>th</sup> Thermophysics Conference*, Snowmass, Colorado.
144. PARK, C. (January 14–17, 1985) On convergence of computation of chemically reacting flows. AIAA Paper 85-247, *23<sup>rd</sup> Aerospace Sciences Meeting*, Reno, Nevada.
145. PARK, C. (1987) Assessment of a two-temperature kinetic model for ionizing air. *AIAA 87-1574*.
146. PARK, C. (1990) *Nonequilibrium Hypersonic Aerothermodynamics*, John Wiley & Sons.
147. PATE, S. R. (1980) Effects of wind tunnel disturbances on boundary layer transition with emphasis on radiated noise: a review. AIAA Paper 80-0431, Colorado Springs.
148. PENNER, S. S. (1955) *Introduction to the Study of Chemical Reactions in Flow Systems*, Butterworths Scientific Publications, London.
149. PERREL, F. (1991) Simulation numérique d'écoulements hypersoniques visqueux en déséquilibre chimique. PhD thesis, ENSAE, Toulouse, France.
150. PERREL, F. and LAFON, A. (September, 1992) Numerical simulation of hypersonic viscous flows in chemical nonequilibrium. In *IUTAM Symp. Aerothermochemistry of Spacecrafts and Associated Hypersonic Flows*, Marseille, France.
151. POTTER, J. L. (1980) Review of the influence of cooled walls on boundary layer transition. *AIAA J.* **18**(8).
152. PRABHU, D. K., TANNEHILL, J. C. and MARVIN, J. G. A new PNS code for three-dimensional chemically reacting flows. AIAA Paper 87-1472.
153. Proceedings of the INRIA-GAMNI/SMAI Workshop on hypersonic flows for Reentry Problems, Part II, Antibes, France, R. Abgrall, et al. (eds.). Springer-Verlag, 1991.
154. PULLIAM, T. H. and STEGER, J. L. (February 1980) Implicit finite difference simulations of three-dimensional compressible flow. *AIAA J.* **18**(2), 159–167.
155. RESHOTKO, E. (1976) Boundary layer stability and transition. *Annu. Rev. Fluid Mechanics* **8**.
156. ROE, P. The use of the Riemann problem in finite difference schemes. Lecture notes in Physics, Vol. 141, Springer-Verlag.
157. ROE, P. (1981) Approximate Riemann Solvers, Parameters Vectors and Differences Schemes. *J. Comp. Phys.* **43**, 357–372.
158. RUBESIN, M. W. (1976) A one-equation model of turbulence for use with the compressible Navier-Stokes equations. Technical Memorandum TM X-73-128, NASA.
159. RUBESIN, M. W. (1990) Extra compressibility terms for Favre-averaged two-equation models of inhomogeneous turbulent flows. Contractor Report CR 177556, NASA.
160. SANDBORN, V. A. (March 1974) A review of turbulence measurements in compressible flows. Technical Memorandum TM X-62337, NASA.
161. SARIC, W. S. (1992) Laminar-turbulent transition: fundamentals. Special Course on Skin Friction Reduction, AGARD-R-786.
162. SARKAR, S. and BALAKRISHNAN, L. (February 1990) Application of a Reynolds stress turbulence model to the compressible shear layer. Contract Report CR 182002 (ICASE Report No. 90-18), NASA.
163. SARKAR, S., ERLEBACHER, G. and HUSSAINI, M. Y. (9–11 September 1991) Compressible homogeneous shear: Simulation and modeling. In *Eighth Symp. on Turbulent Shear Flows*, Munich. Springer-Verlag.
164. SARKAR, S., ERLEBACHER, G., HUSSAINI, M. Y. and KREISS, H. O. (1991) The analysis and modeling of dilatational terms in compressible turbulence. *J. Fluid Mechanics* **227**, 473–493.
165. SCHLICHTING, H. (1933) Zur Entstehung der Turbulenz bei der Plattenströmungsgesellschaft der Wissenschaften. Göttingen, Math.-Phys. Klasse, pp. 181–208.
166. SCHLICHTING, H. (1968) *Boundary-Layer Theory*. McGraw-Hill Book Company.
167. SCHUBAUER, G. R. and SKRAMSTAD, H. K. (1948) Laminar boundary layer oscillations and transition on a flat plate. Report 909, NACA.
168. SCOTT, C. D. (14–16 July 1980) Catalytic recombination of nitrogen and oxygen on high-temperature reusable surface insulation. AIAA Paper 80-1477 *15<sup>th</sup> Thermophysics Conference*, Snowmass, Colorado.
169. SCOTT, C. D. (7–11 December 1987) The effects of thermochemistry, nonequilibrium and surface catalysis in the design of hypersonic vehicles. In *First Joint Europe—US Short Course on Hypersonics—Paris*, Birkhäuser, Boston.
170. SCOTT, D. S. (1–5 October 1990) Wall catalytic recombination and boundary conditions in nonequilibrium hypersonic flows—with applications. In *Third Joint Europe—US Short Course on Hypersonics—Aachen*, GAMNI/SMAI.
171. SHINN, J., MOSS, J. N. and SIMMONDS, A. L. (June 1982) Viscous shock-layer heating analysis for the shuttle windward symmetry plane with surface finite catalytic recombination rates. AIAA Paper 82-0842 *3<sup>rd</sup> AIAA/ASME Joint Thermophysics, Fluids, Plasma and Heat Transfer Conference*, Saint Louis, Missouri.
172. SMITH, A. M. O. and GAMBERONI, N. (1956) Transition, pressure gradient and stability theory. Rept. ES 26388, Douglas Aircraft Co., El Segundo, California.
173. SMITS, A. J., SPINA, E. F., ELVING, A. E., SMITH, R. W., FERNANDO, E. M. and DONOVAN, J. F. (November 1989) A comparison of the turbulence structure of subsonic and supersonic boundary layers. *The Physics of Fluids A* **1**(11), 1865–1875.
174. STALKER, R. J. (1989) Hypervelocity aerodynamics with chemical nonequilibrium. *Annu. Rev. Fluid Mechanics* **21**, 37–60.
175. STETSON, K. F. (1990) Hypersonic boundary layer transition. In *Third Joint Europe/US Short Course in Hypersonics—Aachen*.
176. STETSON, K. F., THOMPSON, E. R., DONALDSON, J. C. and SILER, L. G. (1984) Laminar boundary layer stability experiments on a cone at Mach 8—Part 2: blunt cone. AIAA Paper 84-0006.
177. STUCKERT, G. K. and REED, H. L. (1990) Stability of hypersonic, chemically reacting viscous flows. AIAA Paper 90-1529.
178. STURMAYR, A. M., MOSCHETTA, J. M. and LAFON, A. Comparison of ENO and TVD schemes for the parabolized Navier-Stokes equations. AIAA Paper 93-2970.

179. TAULBEE, D. and VAN OSDOL, J. (7–10 January 1991) Modeling turbulent compressible flows: The mass fluctuating velocity and squared density. AIAA Paper 91-0524, 29<sup>th</sup> Aerospace Sci. Meet., Reno, Nevada.
180. THIVET, F., CANDEL, S. and PERRIN, M. Y. (May 1991) Hypersonic viscous shock layer in thermochemical nonequilibrium. In *First European Symp. Aerothermodynamics for Space Vehicles*, ESA.
181. THIVET, F., PERRIN, M. Y. and CANDEL, S. (1991) A unified nonequilibrium model for hypersonic flows. *Physics of Fluids A* **3**(11), 2799–2812.
182. THUMM, A., WOLZ, W. and FASEL, H. (1990) Numerical simulation of spatially growing three-dimensional disturbance waves in compressible boundary layers. In D. Arnal and R. Michel, editors, *Laminar–Turbulent Transition, IUTAM Symp.* Toulouse, Springer-Verlag.
183. TREANOR, C. E. and MARRONE, P. V. (September 1962) Effect of dissociation on the rate of vibrational relaxation. *The Physics of Fluids*, **5**(9), 1022–1026.
184. VAN DYKE, M. (1962) Higher approximations in boundary-layer theory—part 1: General analysis. *J. Fluid Mechanics*, **14**, 161–177.
185. VAN DYKE, M. (1962) Higher approximations in boundary-layer theory—part 2: Application to leading edges. *J. Fluid Mechanics* **14**, 481–495.
186. VAN DYKE, M. (1962) Second-order compressible boundary layer theory with application to blunt bodies in hypersonic flow. In F. R. Riddell (ed.), *Hypersonic Flow Research*, Volume 7, pp. 37–76. Academic Press.
187. VAN DYKE, M. (1975) *Perturbation Methods in Fluid Mechanics*. The Parabolic Press, Stanford, California.
188. VAN INGEN, J. L. (1956) A suggested semi-empirical method for the calculation of boundary layer transition region. Rept. UTH-74, Univ. of Technn., Dept. of Aero. Eng., Delft.
189. VANDROMME, D. (16 September 1963) Contribution à la modélisation et la prédition d'écoulements turbulents à masse volumique variable. PhD thesis, Université des Sciences et Techniques de Lille.
190. VANDROMME, D. and HA MINH, H. (18–20 May 1987) Turbulence modeling for compressible flows. In *Introduction to the Modeling of Turbulence*, VKI Lecture Series 1987-06.
191. VEUILLOT, J. P. (1989) Calcul de l'écoulement axisymétrique autour d'un corps de rentrée. Rapport technique RT 31/1285 AY, ONERA.
192. VIEGAS, J. R. and HORSTMAN, C. C. (10–12 July 1978) Comparison of multiequation turbulence models for several shock separated boundary-layer interaction flows. AIAA Paper 78-1165 11<sup>th</sup> Fluid and Plasma Dynamics Conf., Seattle, Washington.
193. VIGNAU, F. (1989) Etude théorique et expérimentale de la transition en écoulement bidimensionnel compressible. PhD thesis, ENSAE, Toulouse.
194. VIGNERON, Y. C., RAKICH, J. V. and TANNEHILL, J. C., Calculation of supersonic viscous flow over delta wings with sharp subsonic leading edges. AIAA Paper 78-1137.
195. VINCENTI, W. G. and KRUGER, JR., C. H. (1965) *Introduction to Physical Gas Dynamics*. Robert E. Krieger Publishing Company, Malabar, Florida.
196. VINOGRAD, M. and MONTAGNE, J. L. (1990) Generalized flux vector splitting and Roe average for an equilibrium real gas. *J. Comp. Phys.* **89**(2), 276–300.
197. WAZZAN, A. R. and TAGHAVI, H. (1982) The effect of heat transfer on three-dimensional spatial stability and transition on flat plate boundary layer at Mach 3. *Int. J. Heat Mass Transfer* **25**(9), 1321–1331.
198. WESTLEY, F. (April 1980) Table of recommended rate constants for chemical reactions occurring in combustion. Technical Report NSRDS-NBS 67, National Bureau of Standard.
199. WILCOX, D. C. (November 1988) Reassessment of the scale-determining equation for advanced turbulence models. *AIAA J.* **26**(11), 1299–1310.
200. WILKE, C. R. (April 1950) A viscosity equation for gas mixtures. *J. Chem. Phys.* **18**(4), 517–519.
201. WÜTHRICH, S. and SAWLEY, M. (1992) Coupled Euler/boundary layer method for nonequilibrium, chemically reacting hypersonic flows. *AIAA J.* **30**, 2836–2844.
202. WÜTHRICH, S., PERREL, F., SAWLEY, M. and LAFON, A. (September 1991) Comparison of thin layer Navier-Stokes and coupled Euler/boundary layer computations of non-equilibrium hypersonic flows. In *Ninth GAMM Conf. on Numerical Methods in Fluid Mechanics*, Lausanne, Suisse.
203. YEE, H. C. (May 1987) Upwind and symmetric shock capturing schemes. Technical Report TM 89464, NASA.
204. YEE, H. C. and SHINN, J. L. Semi-implicit and fully implicit shock-capturing methods for hyperbolic conservation laws with stiff source terms. AIAA Paper 87-1116-CP.
205. YEE, H. C., SWEBY, P. K. and GRIFFITHS, D. F. (December 1991) Dynamical approach study of spurious steady-state numerical solutions of nonlinear differential equations. I. The dynamics of time discretization and its implications for algorithm development in Computational Fluid Dynamics. *J. Comp. Phys.* **97**(2), 249–310.
206. ZEMAN, O. (February 1990) Dilatation dissipation: The concept and application in modeling compressible mixing layers. *The Physics of Fluids A* **2**(2), 178–188.
207. ZEMAN, O. (11–14 January 1993) A new model for super/hypersonic turbulent boundary layers. AIAA Paper 93-0897 29<sup>th</sup> Aerospace Sci. Meet., Reno, Nevada.
208. ZEMAN, O. and BLAISDELL, G. A. (July 1990) New physics and models for compressible turbulent flows. European Turbulence Conference—Stockholm.